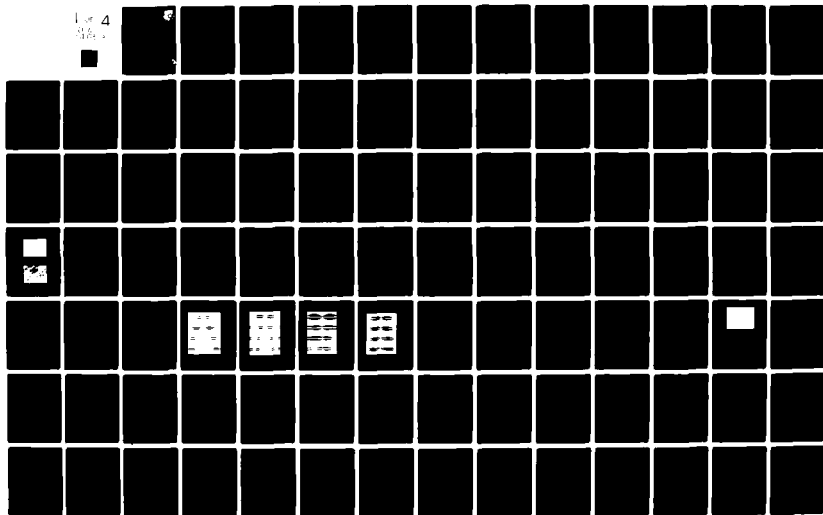


F/6 11/4

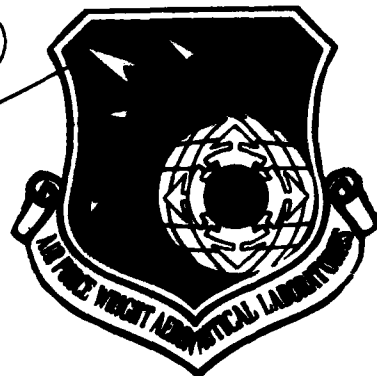
DEC 81 D ASKINS, A BEHME, A BIERMANN, W CLICK F33615-78-C-5102

NL

1 of 4



AFWAL-TR-81-4154



IMPROVED MATERIALS FOR COMPOSITES AND ADHESIVES

J. T. Grant, R. Y. Kim, S. R. Soni, et al
University of Dayton Research Institute
Dayton, Ohio 45469

December 1981

Final Report for Period 16 May 1980 - 31 August 1981

Approved for public release; distribution unlimited.

DTIC FILE COPY

MATERIALS LABORATORY
AIR FORCE WRIGHT AERONAUTICAL LABORATORIES
AIR FORCE SYSTEMS COMMAND
WRIGHT-PATTERSON AIR FORCE BASE, OHIO 45433



82 05 03 014


NOTICE

When Government drawings, specifications, or other data are used for any purpose other than in connection with a definitely related Government procurement operation, the United States Government thereby incurs no responsibility nor any obligation whatsoever; and the fact that the government may have formulated, furnished, or in any way supplied the said drawings, specifications, or other data, is not to be regarded by implication or otherwise as in any manner licensing the holder or any other person or corporation, or conveying any rights or permission to manufacture use, or sell any patented invention that may in any way be related thereto.

This report has been reviewed by the Office of Public Affairs (ASD/PA) and is releasable to the National Technical Information Service (NTIS). At NTIS, it will be available to the general public, including foreign nations.

This technical report has been reviewed and is approved for publication.


J. M. WHITNEY, Project Engineer
Mechanics & Surface Interactions Branch
Nonmetallic Materials Division


S. W. TSAI, Chief
Mechanics & Surface Interactions Branch
Nonmetallic Materials Division

FOR THE COMMANDER:


F. D. CHERRY, Chief
Nonmetallic Materials Division

"If your address has changed, if you wish to be removed from our mailing list, or if the addressee is no longer employed by your organization, please notify AFWAL/MLBM, WPAFB, OH 45433 to help us maintain a current mailing list."

Copies of this report should not be returned unless return is required by security considerations, contractual obligations, or notice on a specific document.

UNCLASSIFIED

SECURITY CLASSIFICATION OF THIS PAGE (When Data Entered)

REPORT DOCUMENTATION PAGE		READ INSTRUCTIONS BEFORE COMPLETING FORM	
1. REPORT NUMBER AFWAL-TR-81-4154	2. GOVT ACCESSION NO. AD-A114 069	3. RECIPIENT'S CATALOG NUMBER	
4. TITLE (and Subtitle) IMPROVED MATERIALS FOR COMPOSITES AND ADHESIVES		5. TYPE OF REPORT & PERIOD COVERED Final Report - 16 May 1980 - 31 August 1981	
		6. PERFORMING ORG. REPORT NUMBER UDR-TR-81-108	
7. AUTHOR(s) D. Askins, A. Behme, A. Biermann, W. Click, C. Fowler, J. Grant, T. Grossman, D. Hall, J. Hartness, G. Jones, R. Kim, M. Koenig, (cont'd)		8. CONTRACT OR GRANT NUMBER(s) F33615-78-C-5102	
9. PERFORMING ORGANIZATION NAME AND ADDRESS University of Dayton Research Institute 300 College Park Avenue Dayton, Ohio 45469		10. PROGRAM ELEMENT, PROJECT, TASK AREA & WORK UNIT NUMBERS 24190311	
11. CONTROLLING OFFICE NAME AND ADDRESS Materials Laboratory (AFWAL/MLBM) Air Force Wright Aeronautical Laboratories, AFSC Wright-Patterson Air Force Base, Ohio 45433		12. REPORT DATE December 1981	
		13. NUMBER OF PAGES 315	
14. MONITORING AGENCY NAME & ADDRESS (if different from Controlling Office)		15. SECURITY CLASS. (of this report) Unclassified	
		15a. DECLASSIFICATION/DOWNGRADING SCHEDULE	
16. DISTRIBUTION STATEMENT (of this Report) Approved for public release; distribution unlimited.			
17. DISTRIBUTION STATEMENT (of the abstract entered in Block 20, if different from Report)			
18. SUPPLEMENTARY NOTES			
19. KEY WORDS (Continue on reverse side if necessary and identify by block number)			
Composites	Dielectrometry	Formulation	Moisture
Epoxy	Rheology	Cure	Thermal Analysis
Matrix	Adhesives	Fatigue	Chemical Composition
Fiber	Interfacial	Environmental	Interlaminar Stresses
Thermoplastic	Processing	Electrode	Fibrous Materials
20. ABSTRACT (Continue on reverse side if necessary and identify by block number)			
<p>This report presents a summary of the work performed by the University of Dayton Research Institute under Contract No. F33615-78-C-5102 during the period of 16 May 1980 through 31 August 1981. Research was conducted in the following areas: Structural Composites, Surface Energetics, Adhesives, Durability/Life Prediction of Composites and Adhesives, Traveling Wave Tubes, and Surface Analysis. The work was performed at the Air Force Wright Aeronautical Laboratories, Materials Laboratory, Wright-Patterson Air Force Base, Ohio, with Dr. J. M. Whitney as project engineer.</p>			

DD FORM 1 JAN 73 1473 EDITION OF 1 NOV 65 IS OBSOLETE

UNCLASSIFIED

SECURITY CLASSIFICATION OF THIS PAGE (When Data Entered)

UNCLASSIFIED

SECURITY CLASSIFICATION OF THIS PAGE(When Data Entered)

7. Contributors: (Concluded)

R. Kuhbander, K. Lindsay, M. Rich, J. Solomon, and S. Soni

19. Key Words: (Concluded)

Acetylene Terminated
Delamination
Life Prediction
Gas Permeability
Bonded Joint
Failure Analysis
Corrosion
Flammability
Aging
Adherends
Shear Strength
Photoelastic
Surface Analysis
Auger Electron Spectroscopy

Photoelectron Spectroscopy
Traveling Wave Tubes
Secondary Ion Mass Spectroscopy
Dispenser Cathode
Graphite Fibers
Anodization
Surface Treatment
Adhesive Bonding
Aluminum Alloys
Sputter Profile Analysis
Adsorption
Surface Area

Accession For	
DTIC GRA&I	<input checked="checked" type="checkbox"/>
DTIC TAB	<input type="checkbox"/>
Unannounced	<input type="checkbox"/>
Justification	
By	
Distribution/	
Availability Codes	
Dist	Avail and/or Special
A	



UNCLASSIFIED

SECURITY CLASSIFICATION OF THIS PAGE(When Data Entered)

FOREWORD

This report was prepared by the University of Dayton Research Institute under Air Force Contract No. F33615-78-C-5102, Project No. 2419, Task No. 24190311. The work was administered under the direction of the Nonmetallic Materials Division, Air Force Wright Aeronautical Laboratories, Materials Laboratory, Air Force Systems Command, with Dr. J. M. Whitney (AFWAL/MLBM) as contract monitor.

This report was submitted in October 1981 and covers work conducted from 16 May 1980 through 31 August 1981.

Personnel who contributed to this research are: D. Askins, A. Behme, A. Biermann, W. Click, C. Fowler, J. Grant, T. Grossman, D. Hall, J. Hartness, G. Jones, R. Kim, M. Koenig, R. Kuhbänder, K. Lindsay, M. Rich, J. Solomon, and S. Soni.

Two interim progress reports have been published on this contract. They are: AFML-TR-79-4176 covering work conducted from 16 May 1978 through 15 May 1979, and AFWAL-TR-80-4132 covering work during period 16 May 1979 through 15 May 1980.

TABLE OF CONTENTS

Section	Page
I	
STRUCTURAL COMPOSITES	1
1. REINFORCED PLASTIC COMPOSITES	1
A. Resin Characterization	1
(1) Acetylene Terminated Sulfone	1
(2) High Vinyl Modified Epoxy	7
B. Failure Mechanisms of Composites	11
C. Thermoplastic Polyester Matrix Composites	15
(1) Experimental Discussion and Results	15
(a) Resin properties	15
(b) Composite processing	18
(c) Composite properties	20
(d) Hot-moist aging	23
(2) Conclusions	23
2. MECHANICAL TESTING	24
II	
SURFACE ENERGETICS	25
1. INTERPHASE PHENOMENA	25
A. Carbon Fiber-Epoxy Matrix Interphase	25
(1) Experimental	25
(2) Materials	26
(3) Results and Discussion	26
(a) Interfacial shear strength	26
(b) Failure mode	35
(c) Interfacial response to water	41
B. Aluminum Oxide/Epoxy Interphase	43
(1) Materials	43
(2) Experimental	43
(a) Wire preparation	43
(b) Anodization	44
(c) Sample fabrication and testing	44
(d) Oxide thickness measurement	44
(3) Results and Discussion	44
2. VOLUMETRIC ADSORPTION/DESORPTION OF CARBON FIBERS	47
A. AS1-C Surface Area Results	47
B. AS1-C Surface Thermodynamics	47

TABLE OF CONTENTS (Continued)

Section	Page
II SURFACE ENERGETICS (Concluded)	
C. AS1-C Desorption Studies	50
D. AS4 Surface Area Results	53
E. AS4 Surface Thermodynamics	53
F. AS4 Desorption Studies	55
3. X-RAY PHOTOELECTRON STUDIES OF GRAPHITE FIBERS	55
A. Graphite Single Crystal	59
B. HM Fibers	59
C. High Modulus Fibers + Polyvinyl Alcohol	63
D. AU Fibers	67
E. AS Fibers	70
F. AS + Cyclohexane	70
G. AS + Water	70
H. AS + Hydrogen	75
I. AS + Epoxy	75
III ADHESIVES	77
1. EXPERIMENTAL ADHESIVES	77
A. BATQH/ATP - An Acetylene-Terminated Sulfone with Reactive Plasticizer	77
B. BADABA - An Acetylene-Terminated Quinoxaline	77
C. Acetylene-Terminated Sulfone	79
D. HR600 and MC600 - An Acetylene-Terminated Polyimide	84
E. Epoxy Model Material	84
F. Equipment	94
2. FABRICATION OF THERMID 600/TREATED GRAPHITE COMPOSITES	94
3. NYLON FILAMENT WINDING	95
4. MOISTURE PICKUP OF M-16 MATERIALS	97
5. MECHANICAL PROPERTIES OF FILLED AND UNFILLED EPOXIES	97

TABLE OF CONTENTS (Continued)

Section		Page
III	ADHESIVES (Concluded)	
	6. ANTIOXIDANTS FOR HIGH-TEMPERATURE POLYMERS	97
	7. FORMULATION OF THERMID 600	104
	8. ADHESIVE BONDING	108
	A. The Influence of Interfacial Copper on Anodic Oxide Growth by Phosphoric Acid Anodization of 2024-T3 Aluminum	108
	(1) Introduction	108
	(2) Experimental	110
	(3) Results	112
	(a) Scanning electron microscope	112
	(b) Auger sputter profile analysis	112
	(c) Rutherford backscattering	116
	(4) Discussion	120
	(a) Interfacial phenomena	120
	(b) Oxide thickness	124
	(c) Oxide morphology	126
	(5) Conclusions	127
	B. Phosphate-Fluoride Etching Effects on Titanium Alloy Surfaces	128
	(1) Introduction	128
	(2) Experimental	129
	(3) Results	129
	(4) Discussion	131
	(5) Conclusion	134
	C. The Effect of Surface Treatment on Bond Line Performance of Adhesively Bonded Ti-6Al-4V	136
	(1) Introduction	136
	(2) Experimental	136
	(3) Results and Discussion	138
	(4) Conclusion	146
IV	DURABILITY/LIFE PREDICTION OF COMPOSITES AND ADHESIVES	148
	1. STRENGTH OF MULTIDIRECTIONAL LAMINATES	148
	2. DELAMINATION	149
	A. Initiation of Delamination	149
	B. Transverse Crack and Delamination	154

TABLE OF CONTENTS (Continued)

Section	Page
IV	DURABILITY/LIFE PREDICTION OF COMPOSITES AND ADHESIVES (Concluded)
	C. Effect of Matrix Properties 154
	D. Prevention of Delamination 156
	E. Free-Edge Analysis: Global-Local Laminate Variational Principle 160
	(1) Introduction 160
	(2) Numerical Results 165
3.	FATIGUE STUDY 168
4.	ADHESIVE BONDED JOINT 172
V	TRAVELING WAVE TUBES 174
1.	CHARACTERIZATION OF CATHODES 174
	A. Evaporation Rates 177
	B. Scanning Low Energy Electron Probe 187
	C. BaCO_3 , BaO , and Ba Metal Studies 190
	D. SEM Studies 193
	E. Phase 1 193
	F. Phase 2 198
	G. Phase 3 198
2.	STUDIES OF COMPONENTS OF TRAVELING WAVE TUBES 210
VI	SURFACE ANALYSIS 217
1.	PRATT AND WHITNEY NICKEL ALLOY SPECIMENS 217
	A. Fracture Specimens 217
	B. Nickel Alloy Wafers 218
	(1) Specimen #1 220
	(2) Specimen #2 220
	(3) Specimens #3 and #4 221
2.	ULTRAPURE SILICON WAFER 221
3.	TITANIUM CARBIDE 223
	A. Graphoil Cover Plates 223
	B. Titanium Carbide Fracture Specimen 224

TABLE OF CONTENTS (Concluded)

Section		Page
VI	SURFACE ANALYSIS (Concluded)	
	4. SiO ₂ SPUTTER RATE DETERMINATION	224
	5. ALUMINUM PANELS	227
	6. ALUMINUM ALLOY (7075) PANELS AND TITANIUM-6ALUMINUM-4VANADIUM ALLOY PANELS	229
	7. GAS BEARINGS USED IN THE GUIDANCE SYSTEM OF THE MX MISSILE	229
VII	LIST OF PUBLICATIONS AND PRESENTATIONS	231
	REFERENCES	233
	APPENDIX A	239
	APPENDIX B	271
	APPENDIX C	289

LIST OF ILLUSTRATIONS

Figure		Page
1	Photomicrograph PET/T-300 Bidirectional Cloth	19
2	Photomicrograph PBT/T-300 Bidirectional Cloth	19
3	Tensile Strength versus Gauge Length for AS4 Single Filaments	27
4	Histogram of AS1 L/D Data	30
5	Histogram of AS4 L/D Data	30
6	Histogram of AS1-C L/D Data	31
7	Histogram of AS4-C L/D Data	31
8	Histogram of AS4-70% Surface Treatment L/D Data	32
9	Histogram of AS4-85% Surface Treatment L/D Data	32
10	Histogram of AS4-100% Surface Treatment L/D Data	33
11	Histogram of AS4-120% Surface Treatment L/D Data	33
12	Histogram of AS1-C/MPDA by Aldrich L/D Data	34
13	AS1/Epon 828-mpDA Photoelastic Stress Pattern as a Function of Strain	36
14	AS4/Epon 828-mpDA Photoelastic Stress Pattern as a Function of Strain	37
15	AS1-C/Epon 828-mpDA Photoelastic Stress Pattern as a Function of Strain	38
16	AS4-C/Epon 828-mpDA Photoelastic Stress Pattern as a Function of Strain	39
17	Water Absorption at Different Temperatures in AS/Epon 828-mpDA Test Coupons	41
18	Pure Aluminum Wire Radial Oxide Fractures	45
19	Isosteric Heat of Krypton Adsorption on AS1-C Fiber Sample Following a 75°C VHT	48
20	Differential Entropy of Krypton Adsorption on AS1-C Fiber Sample Following a 75°C VHT	48

LIST OF ILLUSTRATIONS (Continued)

Figure		Page
21	Isosteric Heat of Krypton Adsorption on AS1-C Fiber Sample Following a 150°C VHT	49
22	Differential Entropy of Krypton Adsorption on AS1-C Fiber Sample Following a 150°C VHT	49
23	Total and Incremental Amounts of Volatiles Desorbed from AS1-C Fiber Sample	51
24	Composition vs. Temperature for AS1-C Volatiles	52
25	Isosteric Heat of Krypton Adsorption on AS4 Fiber Sample Following a 75°C VHT	54
26	Differential Entropy of Krypton Adsorption on AS4 Fiber Sample Following a 75°C VHT	54
27	Isosteric Heat of Krypton Adsorption on AS4 Fiber Sample Following a 150°C VHT	56
28	Differential Entropy of Krypton Adsorption on AS4 Fiber Sample Following a 150°C VHT	56
29	Total and Incremental Amounts of Volatiles Desorbed from AS4 Fiber Sample	57
30	Composition vs. Temperature for AS4 Volatiles	58
31	Carbon 1s XPS Spectra from: (1) F035, High Modulus Fiber Specimen; (2) F033, Fiber with Small Amount of PVA Adsorbed; and (3) F031, Fiber with Larger Amount of PVA Adsorbed Presented in (a) Pulse-Counting and (b) Differentiated Modes	66
32	Oxygen 1s XPS Spectra from: (1) F031, High Modulus Fiber with PVA Adsorbed; (2) F029, AS Fiber Exposed to Water; and (3) F036, AS Fiber Presented in (a) Pulse-Counting and (b) Differentiated Modes	68
33	SEM Micrograph of Oxides on Aluminum Anodized in Room Temperature 0.05M H_3PO_4 at 60 Volts for 1 Hour	113
34	SEM Micrograph of Oxide on 2024-T3 Anodized in Room Temperature 1.0M H_3PO_4 at 10 Volts for 20 Minutes	113

LIST OF ILLUSTRATIONS (Continued)

Figure		Page
35	Oxide Film Thickness on Aluminum and 2024-T3 Plotted as a Function of Anodization Time at 10 Volts in Room Temperature 1.0M H_3PO_4	114
36	Oxygen, Aluminum, and Copper Auger Sputter Profiles of the Surface Oxide Layer of Oakite Deoxidized 2024-T3 Aluminum	115
37	Auger Sputter Profiles of Copper in Anodic Oxide Films on Oakite-Etched 2024-T3 Anodized at 10 Volts in Room Temperature 1.0M H_3PO_4	116
38	RBS Spectrum from Oakite-Etched 2024-T3 with a 2MeV $^4He^+$ Beam	117
39	RBS Spectrum from Oakite-Etched 2024-T3 Anodized in Room Temperature 1.0M H_3PO_4 at 10 Volts for 20 Minutes Obtained Using a 2MeV $^4He^+$ Beam	117
40	RBS Spectra of the Cu and P Peaks from Oakite-Etched 2024-T3 Anodized in Room Temperature 1.0M H_3PO_4 at 10 Volts for Times in Minutes, as Specified for Each Spectra, Using a 2MeV $^4He^+$ Beam	118
41	Depth Resolution $\Delta t/t$ (where t is Sputtering Time in Minutes) versus Anodic Oxide Thickness Sputtered on Al and 2024-T3 Anodized in Room Temperature 1.0M H_3PO_4 at 10 Volts	122
42	Real Charge on the Titanium Atom versus $Ti_{2p_{3/2}}$ Shift for Several Compounds	135
43	Illustrations of a Three-Point Flexure Test Configuration Using a Single Adherend-Epoxy Adhesive Test Specimen: (a) with No Applied Stress, (b) with Applied Stress, (c) Delamination of the Adhesive, and (d) Yielding of Thin Metal Adherend with Application of Stress	137
44	Specimen Preparation Fixture	139
45	Bonded Single Metal Adherend Specimen (a) and Specimen Mounted in a Model 1102 Instron Tester Fitted with a Light Polarizer (b)	140

LIST OF ILLUSTRATIONS (Continued)

Figure		Page
46	Photoelastic Isochromatic Fringes Recorded During the Testing of a Single Ti-6Al-4V Adherend Specimen	143
47	Examples of Possible Stress-Strain Curve that Could Result from Various Interfacial Failure Mechanisms	145
48	Microphotograph Showing Delamination of a Specimen of $[0/\pm 45/90]_s$ Laminate Under Static Tension	152
49	Microphotograph Showing Delamination of a Specimen of $[0/90_3/\pm 45]_s$ Laminate Under Static Compression	152
50	Distribution of Interlaminar Normal Stress in the Free-Edge Region	153
51	Crack Density vs. Applied Stress for 90-Degree Layer; Composite Data of Three Specimens for Each Material System	155
52	Details of Reinforced Specimen	157
53	Microphotographs Showing Delamination of $[0/\pm 45/90]_s$ Laminate Under Static Tension	157
54	Comparison of Acoustic Emission Signal of an Unreinforced Specimen to a Reinforced Specimen for $[0/\pm 45/90]_s$ Laminate	158
55	Stress vs. Strain for the Unreinforced and Reinforced Specimen of the $[0/\pm 45/90]_s$ Laminate	159
56	Microphotographs Showing Delamination of $[0/\pm 45/90]_s$ Laminate Under Fatigue Loading at $S_{max} = 50$ ksi	161
57	X-ray Pictures Showing Extension of Delamination Toward the Middle of $[0/\pm 45/90]_s$ Specimen Width Under Fatigue Loading	161
58	Stress vs. Strain Prior to and After Fatigue of $[0/\pm 45/90]_s$ Laminate	162
59	Coordinate System Used for the Free-Edge Stress Analysis	166

LIST OF ILLUSTRATIONS (Continued)

Figure		Page
60	Distribution of Interlaminar Normal Stress in the Free-Edge Region	167
61	Distribution of Interlaminar Normal Stress in the Free-Edge Region	169
62	X-ray Picture Showing Delamination of a [0/90/ \pm 45] _s Laminate Under Fatigue Loading	171
63	Schematic of Combined AES and SIMS Instrument for the Characterization of TWT Components	175
64	Model of Impregnated Tungsten Cathode According to Forman	178
65	Three Possible Growth Mechanisms of Adsorbate on Substrate	179
66	Assumed Collector - Cathode Configuration	179
67	Ratio of Adsorbate to Substrate versus Deposition Time for a Cathode Temperature of 1050°C	184
68	Ratio of Adsorbate to Substrate versus Deposition Time for a Cathode Temperature of 1100°C	184
69	Ratio of Adsorbate to Substrate versus Deposition Time for a Cathode Temperature of 1150°C	185
70	Ratio of Adsorbate to Substrate versus Deposition Time for a Semicon 1:1:1	185
71	Schematic of Electron-Beam Scanning Tube and Associated Circuitry	188
72	Idealized Potential Profile Over the Electron-Beam Path in the Electron-Beam Scanning Tube	189
73	Vacuum Mounting Hardware for Scanning Low Energy Electron Probe (SLEEP)	191
74	Electron Gun Configuration for SLEEP	191
75	Micrograph of G.E. Tungsten Powder As Received, 5000X	195
76	Micrograph of G.E. Tungsten Powder After Sorting and Deconglomeration 5.5-6.5 μ m Nominal Size	195

LIST OF ILLUSTRATIONS (Continued)

Figure		Page
77	Micrograph of Sylvania Tungsten Powder As Received	196
78	Micrograph of Sylvania Tungsten Powder After Sorting and Deconglomeration 5.5-6.5 μ m Nominal Size	196
79	Particle Size Distribution Plot of Sample #1 Sorted Tungsten Powder	199
80	Particle Size Distribution Plot of Sample #2 Sorted Tungsten Powder	199
81	Particle Size Distribution Plot of Sample #3 Sorted Tungsten Powder	200
82	Particle Size Distribution Plot of Sample #4 Sorted Tungsten Powder	200
83	Particle Size Distribution Plot of Sample #5 Sorted Tungsten Powder	201
84	Particle Size Distribution Plot of Sample #6 Sorted Tungsten Powder	201
85	Particle Size Distribution Plot of Sample #7 Sorted Tungsten Powder	202
86	Particle Size Distribution Plot of Sample #8 Sorted Tungsten Powder	202
87	Particle Size Distribution Plot of Sylvania Sorted Powder 5.5-6.5 μ m Nominal Size	203
88	Particle Size Distribution Plot of G.E. Sorted Tungsten Powder 5.5-6.5 μ m Nominal Size	203
89	Particle Size Distribution Plot of Sample #21 Sorted Tungsten Powder	204
90	Particle Size Distribution Plot of Sample #22 Sorted Tungsten Powder	204
91	Particle Size Distribution Plot of Sample #23 Sorted Tungsten Powder	205
92	Particle Size Distribution Plot of Sample #24 Sorted Tungsten Powder	205

LIST OF ILLUSTRATIONS (Continued)

Figure		Page
93	Particle Size Distribution Plot of Sample #25 Sorted Tungsten Powder	206
94	Tungsten Billet of Sample #3 Sorted Powder	207
95	Tungsten Billet of Sample #6 Sorted Powder	208
96	Micrograph of Sample #3 Tungsten Sorted Powder	209
97	Micrograph of Sample #6 Tungsten Sorted Powder	209
98	Semicon 5:3:2 Dispenser Cathode Near Center 5.0 kX 1 μ m	211
99	Semicon 1:1:1 Dispenser Cathode Near Center 5.0 kX 1 μ m	211
100	Typical Auger Scan from Collector 263 HA S/N 242	212
101	Auger Spectrum of Spot Approximately 1 mm from Edge of a Telefunken Anode	215
102	Auger Spectrum of Spot Approximately 5 mm from Edge of a Telefunken Anode	215
103	Auger Spectrum of Spot Approximately 8 mm from Edge of a Telefunken Anode	216
104	Auger Scan of Fracture Surface of Nickel Alloy Specimen RSR 533	219
105	Auger Scans of Nickel Alloy Specimen RSR 533 Taken from Two Different Regions on the Fracture Surface	219
106	SEM of Fracture Surface on Nickel Alloy Rod	220
107	Auger Scan of Burnt Area on Ultrapure Silicon Wafer Before Ion Bombardment	222
108	Auger Scan of Burnt Area on Ultrapure Silicon Wafer After 30 Seconds of Ion Bombardment	222
109	Auger Scan Graphoil Standard	225

LIST OF ILLUSTRATIONS (Concluded)

Figure		Page
110	Auger Scan Graphoil Specimen HP-25	225
111	Auger Scan Graphoil Specimen HP-26	226
112	Auger Scan Graphoil Specimen HP-27	226
113	Auger Scan of Phosphoric Acid Anodized 2024 Aluminum Alloy Panel P190-1A, (a) Before Ion Bombardment and (b) After 30 Seconds Ion Bombardment	228
114	Auger Scan of Scab Area on Corroded 2024 Aluminum Alloy Panel AP190-21A	228
115	Auger Scan of Typical Area on Gas Bearing Number ML-33	230

LIST OF TABLES

Table		Page
1	ATS/AS	3
2	Flexure, 3 Point, 0°	5
3	ATS/AS	6
4	Physical Properties	16
5	PET and PBT Neat Resin Chemical Resistance	17
6	Radel Neat Resin Chemical Resistance	18
7	Composite Processing	20
8	PET/T-300 Bidirectional Cloth	21
9	PBT/T-300 Bidirectional Cloth	21
10	PET/T-300 Bidirectional Cloth	22
11	PBT/T-300 Bidirectional Cloth	22
12	Tensile Strength of One-Inch Gauge Length Filaments	27
13	Interfacial Shear Strength of Single Carbon Filaments in an Epoxy Matrix	29
14	Mechanical Properties of Epoxy Compositions	40
15	Approximate Oxide Thickness of Phosphoric Acid Anodized Wires	45
16	Aluminum Oxide Mean Fracture Length	46
17	AS1-C BET Surface Area Results	50
18	Total and Incremental Amounts of Volatiles Desorbed from the AS1-C Fiber Sample	51
19	Composition vs. Temperature for AS1-C Volatiles	52
20	AS4 BET Surface Area Results	53
21	Total and Incremental Amounts of Volatiles Desorbed from the AS4 Fiber Sample	57
22	Composition vs. Temperature for AS4 Volatiles	58

LIST OF TABLES (Continued)

Table		Page
23	Energies and Widths of the Carbon 1s and Oxygen 1s Photoelectron Peaks of the Fibers Analyzed in this Study	60
24	Surface Composition of Type HM and High Modulus Fiber Specimens Obtained Using XPS	64
25	Surface Composition of AU Fiber Specimens Obtained Using XPS	69
26	Surface Composition of AS Fiber Specimens Obtained Using XPS	71
27	Surface Composition of AS Fiber Specimens Obtained Using XPS	73
28	Tensile Testing - BATQH/ATP	78
29	Tensile Testing - ATS Dogbones XIII 18-A	80
30	Tensile Testing - ATS Dogbones XIII-20 with Initiator Added	81
31	Tensile Testing - ATS Dogbones XIII-35 and XIII-36	82
32	Tensile Testing - ATS Dogbones XIII-37 (Cure Initiated)	83
33	Tensile Testing - ATS (Gulf) Dogbones Cured at 350°F (176°C) for 16 Hrs in Air	85
34	Tensile Testing - ATS (Gulf) Dogbones Cured at 350°F (176°C) for 16 Hrs in N ₂	86
35	Tensile Testing - ATS (Gulf) Dogbones Cured at 300°F (149°C) for 16 Hrs in N ₂	87
36	Tensile Testing - ATS (Gulf) Dogbones Cured at 100°C for 24 Hrs in N ₂ , 200°C for 1 Hr in N ₂	88
37	TH-600 Cure #1 290°C - 40 Hrs in Air - Tensile Dogbone	89
38	TH-600 Cure #2 340°C - 40 Hrs in Air - Tensile Dogbone	90

LIST OF TABLES (Continued)

Table		Page
39	TH-600 Cure #3 372°C - 3.5 Hrs in Air - Tensile Dogbone	91
40	TH-600 Cure #4 372°C - 1 Hr in N ₂ - Tensile Dogbone	92
41	TH-600 Cure #5 372°C - 40 Hrs in N ₂ - Tensile Dogbone	93
42	Percent Moisture Pickup of M-16 Candidate Materials	98
43	Percent Weight Pickup of M-16 Candidate Materials After 13 Days in Various Fluids and Solvents	99
44	Tensile Properties of M-16 Candidate Materials	100
45	Compressive Properties of M-16 Candidate Materials	100
46	Flexure Properties of M-16 Candidate Materials	101
47	Impact Strength of M-16 Candidate Materials	101
48	Tensile Properties of Neat Adhesives at 200°F (93°C)	102
49	Secant Modulus Values for Adhesives "Wet" Aged for 12 Months	103
50	Percent Weight Loss of Thermid MC-600 and Candidate Antioxidants at 600°F (316°C)	105
51	Effect of Postcure on Flexural Properties	107
52	Effect of Carrier Glass Fabric Finish on Room Temperature Lap Shear Strength of Thermid 600 Titanium-to-Titanium Joints	107
53	Sputter Rates for Anodic Oxides on Al and 2024-T3 Using a 2keV 1.9uA/mm ² Argon Ion Beam	114
54	Rutherford Backscattering Data from Oakite-Etched and 10 Volt 1.0M H ₃ PO ₄ Anodized 2024-T3 with a 2MeV ⁴ He ⁺ Beam	119

LIST OF TABLES (Concluded)

Table		Page
55	Summary of AES, SIMS, and ASPA Data from Chemically Etched Titanium and Titanium Alloys	130
56	XPS Binding Energy Difference from Chemically Etched Ti-6Al-4V Alloy	133
57	Surface Chemical Treatments for Titanium and Titanium Alloys	141
58	AES Elemental I.D. of Treated Ti-6Al-4V	142
59	Three-Point Flexure Test Data and Oxide Thicknesses for Chemically Treated Ti-6Al-4V Adherend-Epoxy Structures	147
60	Static Strength of Multidirectional Laminates	150
61	Experimental Results of Delamination	153
62	Summary of Test Results	155
63	Tensile Strength: Mean of 10 Specimens	160
64	Static Test Results	171
65	Fatigue Test Results	172
66	Evaporation Rates	182
67	Particle Size Distributions of 15 Sorted Tungsten Powders and Expected Size for 10 of the Powders	197

SECTION I
STRUCTURAL COMPOSITES

1. REINFORCED PLASTIC COMPOSITES

A. Resin Characterization

(1) Acetylene Terminated Sulfone

The major effort of work involving acetylene terminated sulfone (ATS) during the past year was to understand and improve the brittle nature of neat ATS resin.

An additional short study was completed to look at the effect of curing and postcuring in nitrogen versus air. There was some scattering in the data, and the results were not conclusive. Work on the transmission microscope shows some promise. It appears that microtoming is a successful technique for preparing samples. Resin castings containing 5 and 10 percent polysulfone with ATS were treated with methylene chloride, while another set was treated with osmium tetroxide fumes, both after microtoming. The methylene chloride treatment brought about the best results as far as being able to see any possible phasing out between the two materials. An analysis was done on the ATS/P-1800 (polysulfone) specimens. Transmission microscopy on microtomed specimens shows a reverse phasing at 10 percent polysulfone, the polysulfone being the continuous phase. This portion of work turned out to be very successful as well as offering a reasonable explanation as to the appearance of two Tg's on the 10 percent polysulfone.

Another approach was tried using 5000 mw polysulfone as a toughening agent. This material was supplied to us from Union Carbide Company. Transmission microscopy indicated a favorable morphology that is best described as an interpenetrating polymer network (IPN). Blends of 10 percent and 15 percent were cast into tensile bars and given standard cure and postcure [16 hours at 500°F (260°C)] in air. An overall improvement in

strain to failure was noticed at room temperature and 350°F (177°C) for the 10 percent and 15 percent blend. The strengths were significantly improved at elevated temperature as is to be expected with an improvement in strain to failure.

An effort was initiated to look at the large Gulf batch of ATS. Work was of a nature as to complement the contractual work of the University of Dayton Research Institute (UDRI) under Dr. Chartoff. Analysis of the resin by differential scanning calorimetry (DSC), dynamic mechanical analysis (DMA), and Haake viscometer indicated that this resin is very similar to previous batches evaluated. Analysis also indicated a ratio of 73 percent monomer to 27 percent oligomer. Although the resin was somewhat glassy at room temperature (RT), it possessed tack and drape with a small application of heat at approximately 100°F (38°C). Our main effort was to understand processing and to look at the application of using P-1800 (5000 mw) as a toughening agent.

Initial work looked at the ease of hot-melt prepregging with our new hot-melt prepregger. Prepregging was accomplished easily using AS graphite fiber. Resin content was easily maintained across the width of the tape. The tape prepregged was 6" wide and possessed a resin content of 45 weight percent. This is optimum for the ATS system with controlled bleed in the composite fabrication stage. The tape was easily removed from the winder. The cutting up of individual plies presented some problem in that there was occasional tow separation. The prepreg does not possess the same qualities to be able to handle it exactly like an epoxy prepreg. It was thought that a slight lowering of the RT viscosity should relieve this problem. Four composites were fabricated, and all used Celgard to prevent excess bleed. All composites possessed satisfactory fiber to resin ratios with no evidence of voids.

All composites were fabricated by the vacuum bag technique with vacuum pressure being the only pressure used. Processing conditions were based primarily on the viscosity

profile obtained by Rheometrics. The processing conditions are outlined below:

1. RT to 212°F (100°C) at 5°F (-15°C)/min under full vacuum (30 psi).
2. Hold for one hour at 212°F (100°C) under full vacuum.
3. 212°F (100°C) to 350°F (177°C) at 5°F (-15°C)/min.
4. Hold for one hour at 350°F (177°C) under full vacuum.
5. Cool to below 150°F (65.5°C) under full vacuum and remove.
6. Post cure: 16 hours at 500°F (260°C) circulating air oven.

Panels were cut up after postcure, and some mechanical properties were obtained. A "new" four-point shear test was used to generate shear numbers. The span-to-depth ratio was 16 to 1, and all composites failed in a true shear failure. Three-point flexure and modulus was run. The flex strength and modulus was good, but the shear strength was low. The low shear strength was thought to be due to a brittle resin matrix. There was visual evidence also for this conclusion as the matrix forms somewhat of a powder upon failure. Mechanical properties are shown in Table 1 below.

TABLE 1

ATS/AS

0° - 6 ply

<u>Temperature</u>	<u>3-pt. Flex Strength x10³ psi</u>	<u>Modulus x10⁶ psi</u>	<u>Failure Mode</u>
RT	240.0	13.3	tensile
350°F (177°C)	219.5	13.8	tensile
400°F (204°C)	211.4	13.5	tensile

4-pt. Shear Strength

RT	9.5x10 ³ psi	shear
----	-------------------------	-------

Composite density = 1.59 gm/cc.

In an attempt to improve composite shear properties, a new tape was fabricated using a 10 percent loading of 5000 mw polysulfone. A solution of methylene chloride was used to blend the ATS and polysulfone. The solvent was removed using the Roto evaporator. The resin pot temperature (100°C) was increased on the hot melt prepregger due to a higher inherent viscosity. A good tape was wound possessing a resin content of 45 weight percent. The tape was cut and stacked as usual and processed with just vacuum bag pressure. The resulting composite was visually inferior to previous composites with voids being present parallel to the fiber direction. The composite density obtained was 1.51 gm/cc versus 1.59 gm/cc. The void content was calculated to be about three percent. The four-point shear properties were low. An additional composite was fabricated in the autoclave using 100 psi instead of just vacuum bag pressure.

The resulting 90 percent ATS/10 percent polysulfone (5000 mw)/AS composite possessed a higher composite density (1.57 gm/cc) and was of a high quality. The four-point shear properties were not significantly improved over the unmodified ATS composite. An additional ATS/AS composite was processed using the vacuum bag technique as has been the case. The resulting composite was of lower quality as indicated by range of composite densities (1.53 to 1.57 gm/cc) and a calculated void content. The composite was fabricated from a stack of six plies that had been at RT for approximately 30 days. It is thought that possible aging or environmental effects resulted in an inferior composite.

Because of this problem, a new 6"-wide tape was wound using AS graphite fiber. The tape had a satisfactory resin content of 45 percent. A six-ply 6"x8-1/4" panel was fabricated using vacuum bag pressure only. The panel was of high quality with an average density of 1.60 gm/cc and a calculated fiber volume of 56.69 percent. A modified cure cycle was used based on information gathered from Dr. Chartoff. The cure and postcure is as follows.

1. RT \rightarrow 260°F (6-7°F/min) full vacuum.
2. Hold for one hour at 260°F (125°C).
3. Run up 260°F (125°C) \rightarrow 332°F (168°C).
4. Hold for one hour and 37 minutes.
5. Cool slowly to RT and remove.
6. Postcure (circulating air oven).
7. RT \rightarrow 572°F (300°C) over a one hour and 10 minute period.
8. Cool slowly to RT and remove.
9. Additional postcure was given 16 hours at 425°F (219°C).

Additional postcure was given because the composites were failing in compression at 350°F. The additional postcure helped the mode of failure, but the composites were still not as brittle as earlier composites reported. This panel was cut up into flexure specimens for moisture aging. The data is shown in Table 2. The equilibrium moisture gain was 0.83 percent at 160°F underwater for 16 days. Long-term moisture aging is ongoing.

TABLE 2
FLEXURE, 3 POINT, 0°

<u>Temperature</u>	<u>Condition</u>	<u>Avg. Strength x10³ psi</u>	<u>Avg. Modulus x10⁶ psi</u>
RT	dry	218.7	13.26
350°F (177°C)	dry	190.0	13.20
350°F (177°C)	wet	155.6	13.06

In a continuing effort to improve the brittle nature of the neat ATS resin, as well as to improve layup, a modified ATS was received from the Polymer Branch. The sample was ATS/mono acetylene terminated polymer (ATP) (95/5). The attempt was made to bring about tack and drape in the prepreg form. The sample was analyzed with the differential scanning

calorimeter and Rheometrics (parallel plate) and looked very similar to the Gulf ATS. A 3"-wide tape was made with the hot melt prepregger. The resulting tape possessed tack and drape in that the tape could be formed into a circle across its width and, with finger pressure and temperature, be joined or tacked to itself. This prepreg was vacuum bag cured and given the standard cure and postcure. It was hoped that the mono ATP would improve the shear properties of the composites. The composite possessed a good density (1.60 gm/cc) and good fiber volume. The four-point shear properties were low.

In order to evaluate the nature of the brittle resin in the composite, transverse tensile and transverse flexure properties were run on an ATS/AS composite given the standard cure and postcure. Results indicated that the material is very brittle as has been observed in the neat resin. Results are shown in Table 3 below. The transverse flexure numbers are probably more realistic, as the tensile test is more sensitive to specimen imperfections. Work was started to try to bring about tack and drape in the ATS/AS prepreg system. Ethanol has been added first to the neat resin, and amounts less than one percent lower the Tg to -7°C. A five percent ethanol solution was prepregged with success. The final tape possessed approximately two percent volatiles and 40 percent weight resin with tack and drape. A piece of prepreg was left out in the lab unwrapped to observe changes in tack and drape.

TABLE 3
ATS/AS

	<u>Strength psi</u>	<u>Modulus x10⁶ psi</u>	<u>% Strain to Failure</u>
RT-transverse tensile	721	1.04	0.063
RT-transverse flexure	3521	1.41	0.240

A composite was fabricated from the ethanol solution (five percent) with the standard vacuum bag processing. This composite possessed a good fiber to resin ratio but also contained a three percent void content, with voids visible on the photomicrographs and a composite density of 1.55 to 1.57 gm/cc. Work will continue to solve the void problem.

Additional work was done to look at the effect of adding a monofunctional ATP at a five percent level. The composite was processed using the vacuum bag procedure. The composite possessed a good density (1.60 gm/cc) and good fiber volume. The four-point shear properties were low, and work will continue on this project with the additional analysis on the neat resin.

Work has also been ongoing to look at the effect of a monofunctional ATS as a toughening agent. Dogbone tensile specimens showed some slight improvement in strength and strain-to-failure over the unmodified ATS at a level of five percent. An increased loading to 10 percent brought about a lowering of those properties. It was also determined by thermal gravimetric analysis (TGA) that the monofunctional ATS is somewhat volatile and thus may be a problem as an additive.

Work is continuing to understand and improve the nature of these various toughening agents, as well as to assist in the fabrication of composites containing the large Gulf ATS system from U.S. Polymeric.

(2) High Vinyl Modified Epoxy (HME)

Much effort was given to develop a resin system that had good neat resin properties that were transferred into a matrix resin in the composite.

The following resin formulations were prepared for the HME development program.

Resin DesignationFormulation

Con #11-2	C-1000, 200 gms AMC-2, 20 drops Epon 826 epoxy, 21 gms
Con #10-TBS-2	C-1000, 100-4 gms AMC-2, 10 drops Epon 826 epoxy, 15.8 gms Test-Butylstyrene (TBS), 15 gms
Con #11-3	C-1000, 200 gms AMC-2, 20 drops Epon 826 epoxy, 21 gms
Con #11-4	C-1000, 100 gms AMC-2, 10 drops Epon 826 epoxy, 10.5 gms
Con #11-TBS	C-1000, 100 gms AMC-2, 10 drops Epon 826 epoxy, 10.5 gms TBS, 15 gms
Con #4-4-N	C-1000, 200 gms ERE 1359 epoxy ingredient, 14.4 gms AMC-2, 20 drops
Con #11-5	C-1000, 200.4 gms AMC-2, 0.5 gms Epon 826 epoxy, 21.1 gms
Con #11-6	C-1000, 200.1 gms AMC-2, 0.5 gms Epon 826 epoxy, 21.1 gms
Con #11-7	C-1000, 200.1 gms AMC-2, 0.5 gms Epon 826 epoxy, 21 gms
Con #10-TBS-3	C-1000, 100.2 gms AMC-2, 0.5 gms Epon 826 epoxy, 15.8 gms TBS, 116.5 gms
Con #11-TBS-4V	C-1000, 200 gms AMC-2, 20 drops Epon 826 epoxy, 21 gms TBS, 30 gms Vul-Cup catalyst, 4 gms
Con #11-8	C-1000, 200 gms AMC-2, 20 drops Epon 826 epoxy, 21 gms Vul-Cup catalyst, portions catalyzed

Two of the formulations, Con #11-2 and Con #4-4-N, were prepared for experimental use as an adhesive material. Con #11-4 has provided the highest mechanical properties to date - four-point flex data averaged 11,000 psi (75.790 MPa). This higher strength level was attributed to a new supply of carboxy-terminated butadiene (C-1000) used in the formulation. This new supply does not

contain an antioxidant or inhibitor which, in the past, seemed to have been affecting the chain reaction during cure.

Viscosity measurements were run on two nylon materials and two polydimethyl siloxane materials to determine their compatibility with the HME formulations. The nylon material could be somewhat more compatible due to its lower viscosity and could have a toughening effect, while the siloxane may accelerate the reaction during cure.

Resin casting Con #11-4, Con #10-TBS-2, and Con #11-A were prepared into test specimens.

The Con #11-5 and #11-6 formulations were prepared for use in the experimental composite work utilizing a hot melt prepregger. Two nylon materials and two polydimethyl siloxane materials are presently being added to the other formulations at various concentrations in an attempt to improve toughness. Castings made using these different formulations were tested.

Work was concentrated on the development of a prepreg and composite utilizing various HME resin formulations. Because our hot-melt prepregger device is a fairly new piece of equipment, a control prepreg tape using AS graphite fiber and 5208 resin was made in order to test a new die that was made for the AS type fiber and to gain additional knowledge about the operation of the equipment. A resin content of 43 percent was obtained from the prepreg made. A six-ply, 0° composite was then cured using a standard AS/5208 cure cycle. Mechanical properties (flex and SBS) were very close to what was expected of the material, although there was evidence of excess voids throughout the composite. At this point it was decided to go ahead and wind an HME prepreg tape. The tape contained the HME Con #11 resin and AS graphite fiber. The resin content of this tape was around 37 percent, so every effort was taken to contain the resin during the cure cycle. The 4 in. x 4 in., 0°, 12-ply composite was sealed in a vac pac envelope using an electrical bag sealer. The top of this envelope was punctured with 8 to 10 pin holes for

volatile release. After the cure cycle was completed, the vacuum bag lay-up indicated excess resin bleed from what we thought was a sealed system. The composite contained numerous voids and, therefore, was not tested. The problem indicated above is an example of the problems we have encountered in containing the resin in this resin system and in others.

Three other HME panels were made. The three panels were made from prepreg supplied by Hercules Company. The resin in the prepreg is HME Con #11 which was originally formulated in this laboratory. The fiber is AS graphite. Flex and SBS tests were conducted on the first panel which was cured using a standard vacuum bag lay-up. The data obtained were below desired properties sought in this material. The other two panels were not tested due to delamination and numerous voids. Again this problem has been attributed to the vacuum bag lay-up which was allowing too much resin bleed in a system that cannot afford the resin loss.

Test results of HME and Celion 6000 are as follows:

Panel #2	SBS 2.2×10^3 psi (15.2 MPa)	3 pt flex 145×10^3 psi (999 MPa)
Panel #3	6.9×10^3 psi (47.5 MPa)	161×10^3 psi (1109 MPa)
Panel #4	6.1×10^3 psi (47.5 MPa)	165×10^3 psi (1136 MPa)

A total of four HME composites were made from the prepreg material made for us by Hercules Company. Each laminate contained 12 plies of prepreg layed in a unidirectional configuration. Three of the panels were made from Con #11, HME prepreg. Different vacuum bag lay-ups were used for each panel in order to try and develop a bag lay-up which will contain the resin cure. The lay-up which seemed to work best utilized a microporous polypropylene film (Celguard) blanket which was sealed around the laminate with double-faced tape. The Celguard blanket is designed to be permeable to any volatile release while, at the same time, acts as a barrier to contain the resin. Even though resin bleed was minimal, mechanical properties were below ideal. The fourth panel was made from Hercules Con #10-TBS-HME prepreg. This panel's

mechanical properties were also somewhat lower than ideal. Photomicrographs indicate the fiber is not wetting out properly. This could be due to a problem in the prepreg itself or insufficient pressure. Several batches of HME resin were prepared for composition experimentation. A 100-gram batch of HME-Con #11-TBS resin was prepared so that a different catalyst could be tried. It is hoped that the catalyst, namely Vul-Cup, will improve the reactivity of the resin during cure.

Additional thermal analysis indicated no improvement in the HME system. At this time no additional work is planned on the HME resin development.

B. Failure Mechanisms of Composites

A new work project was initiated during this contractual period. The objective of this work was to investigate the role of the matrix in composite failure mechanisms. The first phase of the work consisted of preparing two resin systems having substantially different mechanical performance characteristics. One resin was to have ductile characteristics, while the other was to be brittle. Both were to have characteristics that made them amenable to processing into cast plates as well as processing into high quality laminates. The ductile resin was defined as:

Epon 828 - 100 pbw
Diaminodiphenyl sulfide (DDS) - 33 pbw

The brittle resin was defined as:

MY-720 100 pbw
Diaminodiphenyl sulfide (DDS) - 50 pbw

Both resin systems were debulked prior to casting. Once cast, the Epon 828 system was cured two hours at 250°F plus one hour at 350°F.

The first task of Phase I involved a preliminary evaluation of the processing and properties of these two systems to validate the acceptability of the technical direction.

One 1/16 in. thick, 828 epoxy resin/eporal (DDS) hardener casting, two 1/8 in. thick, 828/DDS castings, and one 1/8 in. thick

MY720 epoxy resin/DDS casting were prepared for the program. Dog-bone tensile specimens provided the needed baseline data on each candidate resin system before further work was begun.

During the mixing procedure, viscosity was recorded as a function of time in order to determine when full chain extension of the uncatalyzed resin occurs.

Much work was involved in trying to cast void-free 828 epoxy/DDS hardener specimens. Air seemed to become entrapped during the casting procedure with debulking not solving the problem due to increased viscosity. Initially, seven 828/DDS castings were made, each time altering the cure cycle or preparing the mold in a different manner. One casting made utilized a mirror-finish stainless steel mold polished with a silicon lubricant for release instead of the standard Frekote release agent. We were getting a near-perfect release from the stainless steel mold, but air was still entrapped throughout the casting. A vacuum was not pulled on the resin in the mold, so the entrapped air was caused by the agitation during the pouring process.

One attempt employed pyrex plates polished with silicon. A vacuum was applied so one can observe if the silicon is preventing the adhesion of the air bubbles to the inside surface of the mold.

The resin was debulked in a beaker prior to pouring into the glass mold.

Usually at this point the resin is debulked in the glass mold; however, this step was eliminated so that the chances of entrapping any air that adheres to the sides and the bottom of the mold are eliminated. The resin is cured directly after pouring into the mold.

The only possibility of entrapping air is during the pouring process from the beaker to the mold. If agitation of the resin is avoided and it is poured into the mold in one step, it has been noted that few bubbles are created that could become entrapped during cure.

Testing was completed on dogbone specimens which were debulked and not debulked in the mold. Data indicates mechanical properties are insignificantly influenced by not debulking in the mold. Casting #12 was cured the same way. However, stainless steel plates were used rather than pyrex glass to eliminate glass breakage. Also, the plates were sprayed with a teflon coating release agent in order to eliminate possible contamination by the silicon gel release agent.

Several thermoplastic polysulfone/AS graphite composites were fabricated as part of the study. One composite was a 12-ply, 0°, 9 in. x 6 in. The other was an angle ply, 12 plies, [90°, 90°, +30°, +30°, -30°, -30°]_g. Neat resin properties were generated on Radel, polyphenylsulfone.

A release agent, namely Dow 20, was tested on our stainless steel mold. This release agent supposedly gives a heat-stable, nonoily silicone parting film that will not contaminate the castings. One 828 epoxy/DDS hardener resin casting and one MY720 epoxy/DDS hardener resin casting were made using this release agent. Both castings released from the mold effortlessly and intact; however, both castings revealed severe stress patterns due to shrinkage. Both had shrinkage patterns that begin on one side of the casting, dip down towards the bottom, and rise to the opposite side thus forming a sort of half-moon configuration. This phenomenon has been observed in the past but was never investigated at length. The cause could be one of several things: the expansion or contraction of the teflon dam, the adherence of the resin to the mold at some point during the cure, or a heat gradient from one side of the mold to the other in the air circulating oven used for the cure. These possible causes will be investigated through the process of elimination.

Stress-free castings were made from both the 828 and MY720 systems by altering the cure cycle and method of cure. This was done first by determining how long it takes the resin to gel at 250°F (121°C) which is the first dwell temperature for both resin systems; and how long we need to dwell at that temperature

before we can remove the partially-cured casting and continue the cure unrestricted by the stainless steel mold. This restriction by the steel mold evidently was the major cause of the stress patterns. Although it is not fully understood why the steel mold induced these stresses, by removing the casting and continuing the cure outside the mold, the problem is completely eliminated.

One casting from each system was made using this method. Dogbone tensile specimens and slotted tensile specimens were cut from each casting and were tested.

Two 828/DDS epoxy resin castings were prepared to be used in the program. Approximately 60, three-inch dogbone tensile specimens were machined from both castings. These tensile specimens were tested using three different strain rates at room temperature, 175°F, and 250°F. Five specimens per data point were tested.

We have prepared several MY720/DDS castings from an older batch of resin in order to establish a workable cure cycle; however, a new batch of MY720 resin, which was recently obtained to supply us with our testable castings, has reacted much differently during the initial phase of cure.

Three MY720/DDS epoxy resin castings were prepared for the program. Approximately 50 dogbone tensile specimens were machined out for evaluation at room temperature and various elevated temperatures. The testing of these specimens completes the preliminary evaluation of the ductile resin system and the brittle resin system.

Batches of MY720/DDS resin were prepared for prepregging operations as we prepared for Phase II of the program. This involved altering the standard MY720/DDS formulation with the addition of ATBN, a liquid rubber additive. This material is being added to act as a toughening agent for the brittle resin system. The first rubber-toughened formulation contained 10 parts ATBN per 10 grams MY720 resin. The finished casting contained many nonhomogeneous areas and air voids. The voids were entrapped

in the casting during the pouring process due to the high viscosity of the resin.

We are presently experimenting with a series of epoxy resins from Nippon-Soda as possible candidates to toughen the MY720/DDS system.

The composite end of the program now includes the preparation of resin formulations for winding prepreg tapes and the winding itself. Prepregs for two 828/DDS composites have been made to date.

C. Thermoplastic Polyester Matrix Composites

Continuous fiber graphite reinforced thermoplastic composites have been under development and evaluation for several years, and the potential advantages of thermoplastic matrix composites for aircraft structures are well documented.^(1,2,3) These advantages usually include major reductions in fabrication costs, improved repairability, reduced moisture degradation, and less variability in matrix resin constituents. In the past these advantages have been somewhat offset by certain problems. The problems in the past have included lack of chemical resistance as far as the amorphous thermoplastics are concerned and lack of toughness in the semicrystalline materials such as polyphenylene sulfide. The processing of thermoplastic composites has been successfully demonstrated by interlaying film and reinforcement with high temperature (600-700°F) compression molding (100-200 psi).^(4,5) The use of this technique has allowed the continued evaluation of the potential of these materials as composite matrix resins.

(1) Experimental Discussion and Results

(a) Resin properties

The resins evaluated in this study were poly(ethylene terephthalate), trade name Tenite PET Polyester 7970 from Eastman Chemical Products, and poly(butylene terephthalate), trade name Tenite PBT Polyester 6P4D. These materials represent current thermoplastic polyesters in production. Both materials

were supplied in the amorphous state in 10 mil film. Basic mechanical properties have been generated on both materials. Although both resins revert to their crystalline form upon melt and cool down, there are some differences between the two. Physical properties are shown in Table 4 for both materials in their crystalline form as supplied by Eastman.

TABLE 4
PHYSICAL PROPERTIES
Crystalline Form

Property, Units	Value	
	PET	PBT
Crystallinity, %	35-40	50
Density, gm/cm ³	1.45	1.31
Temperature Characteristics, °C		
Glass Transition	110±10	40
Softening Point by TMA	245-252	
Crystalline Peak M.P.	<255	--
Melting Point	<257	225

Polyethylene terephthalate (PET) crystallizes somewhat slower than polybutylene terephthalate (PBT), but since the material is taken above its melt point and slowly cooled, there seems to be no problem with the material crystallizing. Both materials must be used in their crystalline form in order to obtain good chemical resistance. A good deal of chemical resistance data is reported by Eastman. In our study additional chemicals of interest were evaluated. The test procedure involved dead weight loading 10 mil thick dogbone specimens and exposing them continuously to the agent for a prescribed amount of time or until

failure. All specimens were crystallized first by dipping in methylene chloride prior to loading. No failures occurred under the conditions and agents used. Table 5 shows these conditions. No etching or stress cracking of any of the specimens was observed. Table 6 shows the results on polyphenylsulfone (Radel), an engineering thermoplastic that has superior chemical resistance to polysulfone (UDEL) and polycarbonate. Polyethylene terephthalate possesses a low Tg of 110°C (230°F) and a high melt temperature of 260°C (500°F). Polybutylene terephthalate also possesses a low Tg of 40°C (104°F) and a high melt point of 225°C (442°F). As with other semicrystalline polymers, the modulus-temperature behavior is believed to be significantly different from that of amorphous polymers. In the glass transition region, the shear modulus drops to a much less extent. This drop in modulus usually occurs over a broader temperature range. The modulus first exhibits a plateau, then drops slowly up to the melting temperature and drops rapidly thereafter. The composite flexural tests support this conclusion.

TABLE 5
PET AND PBT NEAT RESIN
CHEMICAL RESISTANCE

<u>Chemical</u>	<u>Stress (psi)</u>	<u>Time at Stress</u>
MIL-H-5606C ¹	1000	1 week
Skydrol 500B ²	1000	1 week
JP-4 AF-Fuel	1000	1 week
Dichloromethane	1000	1 week
MEK	1000	1 week
Acetone	1000	1 week
T-5351 Al ³	1000	1 week

1 Air Force Hydraulic Fluid

2 Commercial Aircraft Hydraulic Fluid

3 Air Force Paint Stripper

TABLE 6
RADEL NEAT RESIN CHEMICAL RESISTANCE

<u>Chemical</u>	<u>Stress (psi)</u>	<u>Rupture Time</u>	<u>Immersion</u>
+MIL-H-5606C	500	No Failure	No Swelling
++Skydrol 500B	500	30 min.	No Swelling
++Skydrol 500B-4	500	15 min.	No Swelling
++Skydrol LD	500	20 min.	No Swelling
++Skydrol LD-4	500	10 min.	No Swelling
Dichloromethane	500	3 min.	--
	1000	10 sec.	--
MEK	500	1 sec.	--
Toluene	500	15 sec.	--
Trichloroethylene	500	1 sec.	--
Acetone	500	20 min.	--
+++T-5351 Al(PS)	500	4 min.	--

+ Air Force Hydraulic Fluid
 ++ Commercial Aircraft Hydraulic Fluid
 +++ Air Force Paint Stripper

(b) Composite processing

As with earlier thermoplastic matrix composites, amorphous film was interleaved with bidirectional Thornel 300-8 satin harness graphite cloth with a UC307 finish (thermoplastic finish). The same technique of spot welding the film to the cloth, thus holding the cloth together, was again successful and allowed easily the cutting of any geometric ply orientation. Both resin systems were processed the same. The stack was placed in a matched die mold and compression molded in a press at 273°C (525°F) and 100 psi for 30 minutes. The composite was allowed to cool slowly under pressure to approximately 200°F before removal. Sufficient bleedout of resin resulted in composites with 50-55% fiber volume. Photomicrographs indicate good fiber wetting (Figures 1 and 2). Composite processing parameters were not

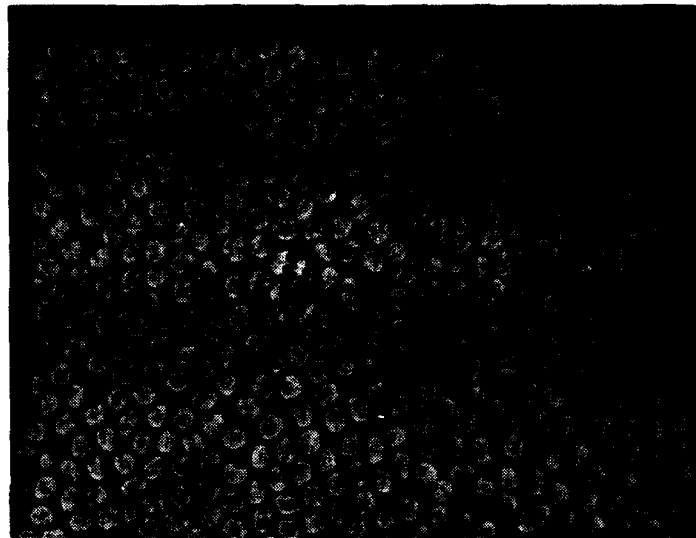


Figure 1. Photomicrograph PET/T-300 Bidirectional Cloth.

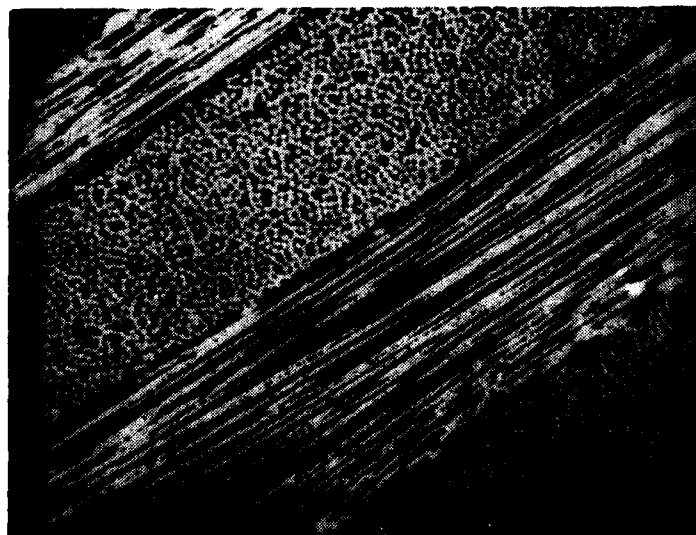


Figure 2. Photomicrograph PBT/T-300 Bidirectional Cloth.

optimized, although it is expected that no significant changes can be made with respect to temperature. It is possible that shorter times at temperature and pressure may be successful. It is expected that thermoforming should be successful, as the resin is capable of repeated cycles of melting and cooling. Table 7 shows the processing conditions. Consideration should be given to the rate and degree of crystallization for each material. The PBT crystallizes very rapidly and to a greater extent than does the PET.

TABLE 7
COMPOSITE PROCESSING

- Heat to 525°F (275°C) as fast as possible using contact pressure.
- Apply 100 psi and hold for 30 min.
- Cool slowly under pressure to 200°F.
- Remove from mold.

(c) Composite properties

A series of mechanical property tests were performed on composite laminates to determine the resin performance as a matrix material. All composite properties were generated on bidirectional Thornel 300-8 satin harness graphite cloth with a UC307 finish. It was hoped that a unidirectional cloth with a polyester fill could also be evaluated, but cloth data could not be obtained in time to include in this paper. Flexural and tensile properties were evaluated at room and elevated temperature. Tables 8 through 11 show these results. As can be seen the material maintains its properties with an approximate 50% dropoff at 300°F. The flexural modulus holds up well at 300°F and is not significantly affected even at 350°F. The differences

TABLE 8
PET/T-300 BIDIRECTIONAL CLOTH
(UC307 Finish) (8H Satin)

<u>Property</u>	<u>Condition</u>	<u>Strength x10³ psi</u>	<u>Modulus x10⁶ psi</u>	<u>Strain to Failure %</u>	<u>Poisson Ratio</u>
Tensile 0° warp direction	RT	61	10.38	.60	0.046
"	200°F	57	11.67	.57	--
"	250°F	43	10.16	.44	--
"	300°F	46	10.47	.56	--
"	350°F	50	8.69	.78	--
Tensile ±45° warp direction	RT	16	2.93	2.37	0.716

TABLE 9
PBT/T-300 BIDIRECTIONAL CLOTH
(UC307 Finish) (8H Satin)

<u>Property</u>	<u>Condition</u>	<u>Strength x10³ psi</u>	<u>Modulus x10⁶ psi</u>	<u>Strain to Failure %</u>	<u>Poisson Ratio</u>
Tensile 0° warp direction	RT	59	11.39	.67	.051
"	250°F	34	9.02	.57	.084
"	350°F	33	8.82	.61	.363
Tensile ±45° warp direction	RT	7.61	2.47	.58	.766

TABLE 10
 PET/T-300 BIDIRECTIONAL CLOTH
 (UC307 Finish) (8H Satin)

<u>Property</u>	<u>Temp.</u>	<u>Strength x 10³ psi</u>	<u>Modulus x 10⁶ psi</u>
3 pt. Flexure	RT	84.59	7.12
0° warp dir.	200°F	60.09	6.81
	250°F	49.40	5.84
	300°F	46.17	6.06
	350°F	35.31	5.61

55% Fiber Volume

TABLE 11
 PBT/T-300 BIDIRECTIONAL CLOTH
 (UC307 Finish) (8H Satin)

<u>Property</u>	<u>Temp.</u>	<u>Strength x 10³ psi</u>	<u>Modulus x 10⁶ psi</u>
3 pt. Flexure	RT	87.94	6.62
0° warp dir.	200°F	63.36	6.38
	250°F	50.06	5.81
	300°F	43.55	5.58
	350°F	33.83	5.63

60% Fiber Volume

between the two materials in the $\pm 45^\circ$ tensile strengths may be explained by the rate and degree of crystallization between PBT and PET. Although it is somewhat unfair to compare directly the mechanical properties of a thermoset, such as an epoxy, with those of a thermoplastic, the properties are somewhat similar. There is a greater dropoff at elevated temperature due to the nature of the polyester, but useful properties are observed due to the semicrystalline nature of the materials.

(d) Hot-moist aging

It has been well documented that a hot humid environment brings about a decrease in the mechanical properties of thermoplastic polyesters.⁽⁶⁾ Evaluating three grades of PBT, Gardner and Martin have shown that hydrolysis occurs rapidly at high temperature and relative humidities, and progressively slows as the temperature and/or humidity are decreased. According to the evaluation equations for making life-cycle predictions at any combination of temperature and humidity were derived from Arrhenius plots. "If a 50% loss in tensile strength constitutes failure, then the PBT examined should be expected to last only three to four years at 50°C (120°F) and 100% relative humidity. Reducing the humidity level to 50% extends the useful life at this temperature to 10-20 years. Predictions based on the tensile strength half-life should not be used where toughness or impact properties are important because PBT embrittles long before the tensile strength half-life is reached." Exactly how and to what degree this study applies to graphite-reinforced thermoplastic polyesters remains to be evaluated. There is every reason to expect that there would be an effect. Serious consideration should be given to any application where possible hot and humid environments may be encountered for any length of time.

(2) Conclusions

In general, the polyesters appear to have good properties as matrix resins for composites. The ability to form

high-quality laminates by interleaving polymer film and cloth indicates potential for a variety of product forms and fabrication procedures for producing low-cost structures. Polyesters are both cheap and plentiful. The resin offers excellent chemical resistance, thermal stability, and mechanical properties up to at least 300°F. One major problem with polyesters is their sensitivity to a hot/moist environment.

2. MECHANICAL TESTING

Work in the area is supportive of all the various materials developed and evaluated. Specific tests that are run include micro dogbone tensile testing using the DSST microextensometer, strain-gaged four-point flexure on resin castings, regular composite tensile testing using either a strain gage or extensometer at ambient and elevated temperature, stress analysis studies to determine fracture toughness of center-notched tensile specimens of various materials, regular three-point flexural and four-point flexural testing on composite materials.

Design and modification was completed on the four-point flexural fixture in order to make it more stable at higher loads as well as better aligned. This fixture will be used to test composite materials in a newly developed test called a four-point shear. The span-to-depth ratio is changed to 16 to 1 and resulting tests have consistently given a shear failure. This has not been the case with the short beam shear test. It is hoped that this new four-point shear test will replace the short beam shear as a reliable test to determine shear properties in a composite.

SECTION II

SURFACE ENERGETICS

1. INTERPHASE PHENOMENA

Interactions that occur at the adhesive-adherend interface are an important parameter governing the performance of bonded systems. Also affected by these interactions is the near interface region forming an interphase of unique material properties. An understanding of the interactions that occur in this region would permit tailoring the interphase to meet specific design criteria. This study was conducted to evaluate the interphase of two bonded systems, namely, the carbon-epoxy interphase and the aluminum oxide-epoxy interphase.

A. Carbon Fiber-Epoxy Matrix Interphase

(1) Experimental

The carbon fiber-epoxy matrix interphase was investigated using the single filament composite technique.^(7,8) This test involves fabricating "critical length" specimens enabling an average interfacial shear strength to be calculated according to the expression

$$\tau = \frac{\sigma_f}{2\beta} \Gamma\left(1 - \frac{1}{\alpha}\right) \quad (1)$$

where σ_f is the fiber tensile strength, β and α are, respectively, the Weibull scale and shape parameters of the length to diameter aspect ratio distribution, and Γ is the Gamma function. This permits a ranking of the shear adhesion strength for different fibers tested in the same matrix. Additionally, valuable information on the failure mode can be obtained by in situ microscopic observation of the fiber during the straining process.

The carbon-epoxy interfacial response to moisture was investigated by performing the single filament technique on specimens subjected to high humidity environments at different temperatures. Test coupons were mounted onto holders designed

to minimize contact with the specimen and were suspended above distilled/deionized water in a sealed container, thereby effectively making a 100 percent relative humidity (RH) chamber. Tests were conducted at room temperature, 70°C, and 125°C. Sample weight measurement, as well as in situ microscopic observation of the fiber, was made periodically. After sample weight maximized specimens were either tested for interfacial shear strength or dehydrated until weight minimized before placing the coupon under tensile load.

(2) Materials

All fibers used in this study were Type II fibers fabricated from polyacrylonitrile (PAN) precursor. Fibers were supplied with a proprietary surface treatment and/or finish designed to enhance adhesion to an epoxy matrix.⁽⁹⁾

The epoxy matrix used was Epon 828,⁽¹⁰⁾ a diglycidyl ether of bisphenol A (DGEBA) cured with 14.5 phr meta-phenylene diamine (mPDA).^(11,12) The cure cycle was two hours at 75°C followed by a two-hour postcure at 125°C.

(3) Results and Discussion

(a) Interfacial shear strength

The tensile strengths of one-inch gauge length single filaments were measured on a table-top Instron⁽¹³⁾ and are reported in Table 12. Because fiber tensile strength increases with decreasing fiber length,⁽¹⁴⁾ measurement of fiber strength at the "critical length" would enable a more accurate value of τ to be calculated.

Tensile strengths of AS4 filaments were determined for gauge lengths ranging from one inch to 0.01 inch. Lengths shorter than 1/2 inch were measured on a Tecam microtensile testing device,⁽¹⁵⁾ whereas the 1/2-inch and one-inch lengths were measured on an Instron. An image splitting eyepiece was used to measure fiber diameters. A plot of the logarithm of gauge length versus tensile strength (Figure 3) illustrates the significant

TABLE 12
TENSILE STRENGTH OF ONE-INCH GAUGE LENGTH FILAMENTS

<u>Fiber</u>	<u># Tested</u>	<u>Tensile Strength</u> <u>(x10³ psi)</u>	<u>Modulus</u> <u>(x10⁶ psi)</u>
AS-original lot	5	381	32.7
AS1	9	390	28.5
AS1-C	22	387	29.0
AS4	12	393	28.7
AS4-C	10	411	28.2

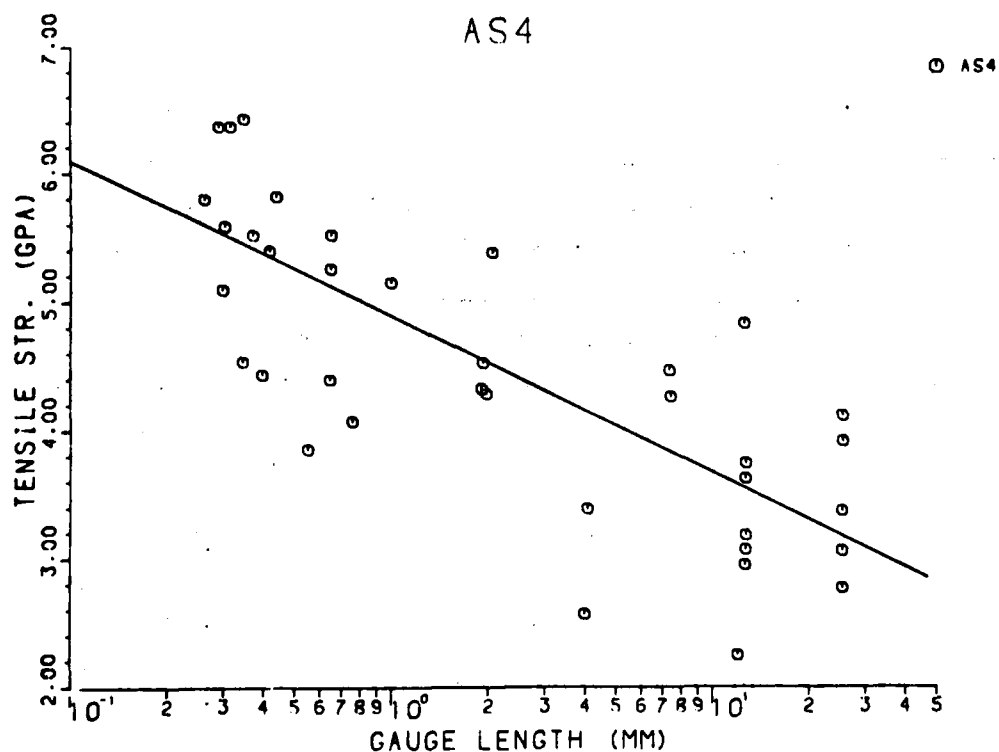


Figure 3. Tensile Strength versus Gauge Length for AS4 Single Filaments. Solid line is simple linear regression of data.

increase in strength from $\sim 480 \times 10^3$ psi (3.3 GPa) at one inch to $\sim 770 \times 10^3$ psi (5.3 GPa) at the critical length of 0.018 in. (.46 mm). Hence, using tensile strengths measured at the critical length will increase the value of τ , the average interfacial shear strength.

The interfacial shear strengths of a variety of fibers were calculated according to equation (1) using one-inch gauge length tensile strengths and are reported in Table 13. Histograms of the l/d frequency distribution along with a two-parameter Weibull and normal fit are provided in Figures 4-12.

A fiber designated "AS-original lot" that was previously studied⁽⁷⁾ was retested using recently-received resin and curing agent. The interfacial shear strength is greater in the system employing the new matrix materials. All other systems studied in this report were fabricated using the new supplies of both resin and curing agent.

Type AS1 are fibers that were recently (1980) fabricated and surface treated under the same processing conditions as the AS-original lot fibers which were manufactured in 1974. Two sets of AS1/Epon 828-mPDA specimens were fabricated and tested. As can be seen from Table 13, the results of the two-parameter Weibull analysis of the l/d aspect ratio of each set are virtually the same. Additionally, the calculated interfacial shear strength is approximately that of the AS-original lot/Epon 828-mPDA system.

The AS4/Epon 828-mPDA system was also tested. The most significant differences between AS1 and AS4 fibers are that the PAN precursor for each fiber is from a different source and that the AS4 fiber has a smooth surface, whereas the AS1 surface is marked with long, shallow axial grooves. Although the one-inch gauge length tensile strengths are equal, the calculated interfacial shear strength of the AS4 fiber is much lower than the AS1/Epon 828-mPDA system.

TABLE 13
INTERFACIAL SHEAR STRENGTH OF SINGLE CARBON FILAMENTS
IN AN EPOXY MATRIX

<u>Fiber</u>	<u>Matrix</u>	<u>Total Fragments</u>	<u>β</u>	<u>α</u>	<u>τ (psi)</u>
AS-original lot	Epon 828-mPDA	669	48.50	3.07	5260
AS-original lot	New Epon 828 New mPDA	745	41.54	3.26	6010
AS1-Set A	Epon 828-mPDA	408	38.13	3.55	6450
Set B	Epon 828-mPDA	415	39.41	3.49	6320
Set A+B	Epon 828-mPDA	825	38.78	3.51	6340
AS1-C	Epon 828-mPDA	776	30.29	3.77	7985
AS1-C: Cold Mold	Epon 828-mPDA	585	29.03	3.62	8400
AS1-C	Epon 828 mPDA by Aldrich	602	26.56	3.91	9325
AS4	Epon 828-mPDA	860	57.24	3.07	4600
AS4-C	Epon 828-mPDA	378	43.77	4.07	5760
AS4-70% S.T.	Epon 828-mPDA	370	70.85	2.98	-
AS4-85% S.T.	Epon 828-mPDA	256	69.00	2.91	-
AS4-100% S.T.	Epon 828-mPDA	327	68.88	2.67	-
AS4-120% S.T.	Epon 828-mPDA	339	68.24	3.31	-
AS-original lot 100% RH at 70°C	Epon 828-mPDA	95	53.48	3.21	-
AS-original lot 125°C - 5 days	Epon 828-mPDA	243	36.17	3.62	6640

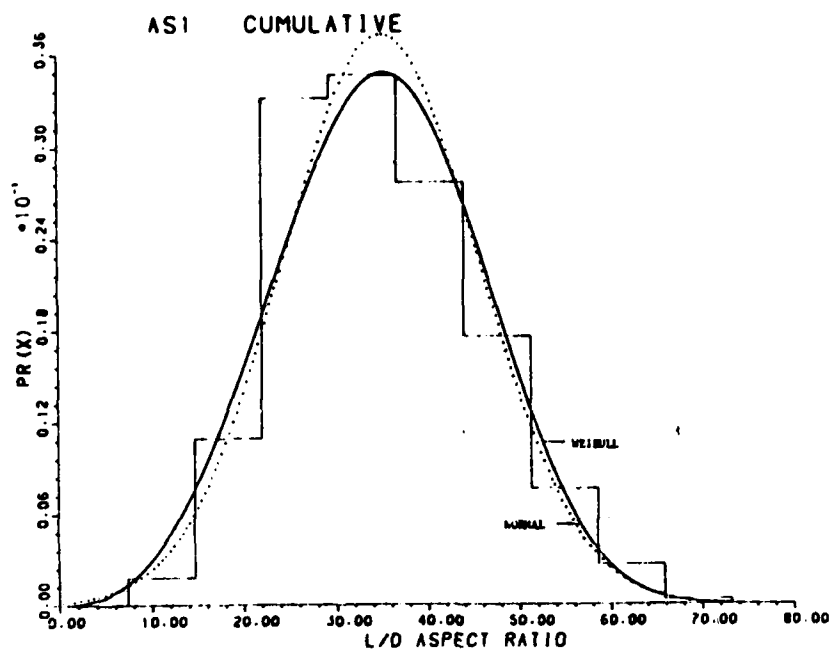


Figure 4. Histogram of AS1 L/D Data.

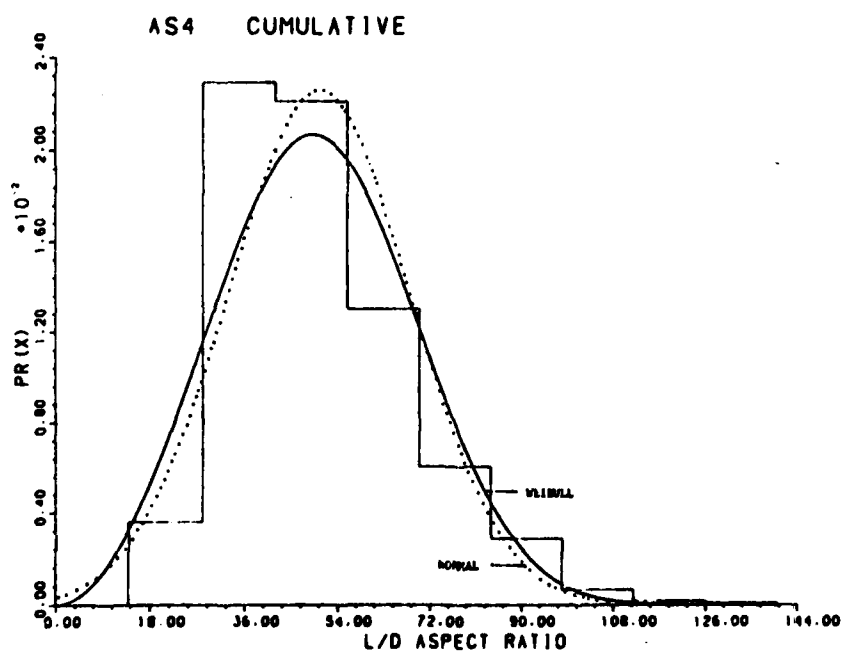


Figure 5. Histogram of AS4 L/D Data.

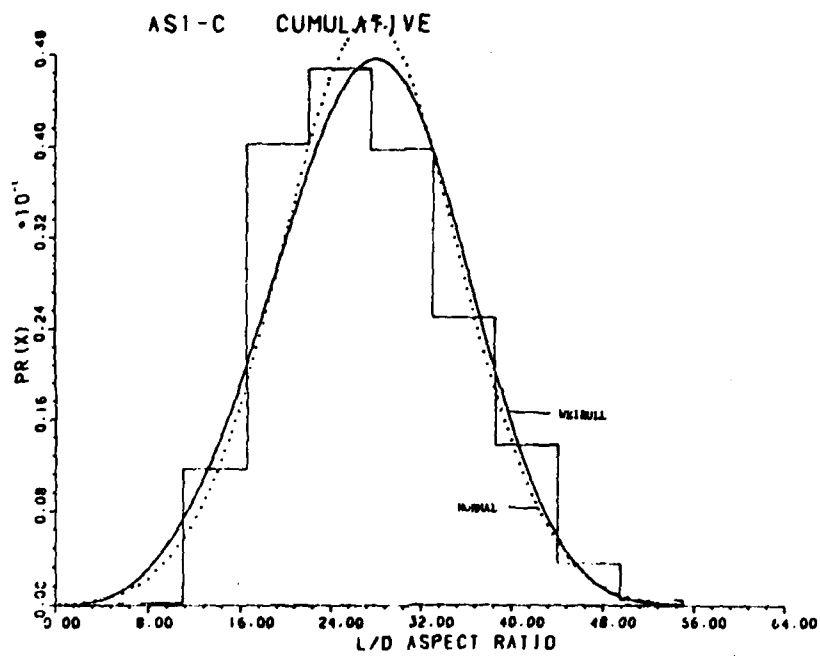


Figure 6. Histogram of AS1-C L/D Data.

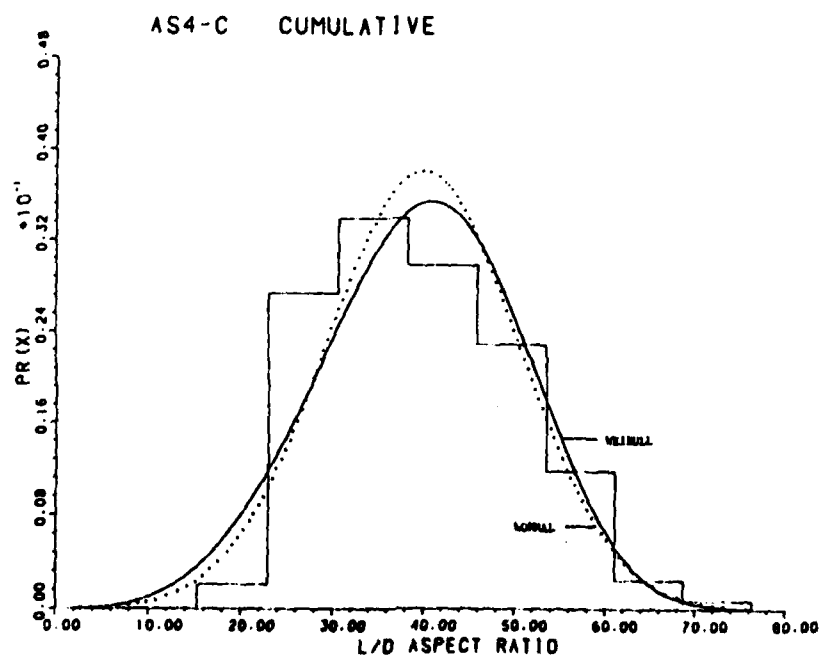


Figure 7. Histogram of AS4-C L/D Data.

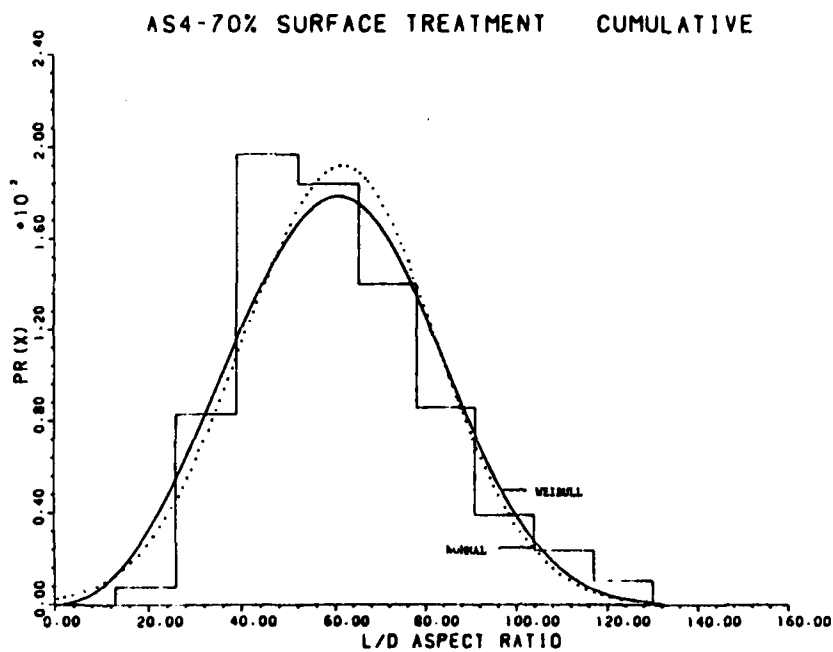


Figure 8. Histogram of AS4-70% Surface Treatment L/D Data.

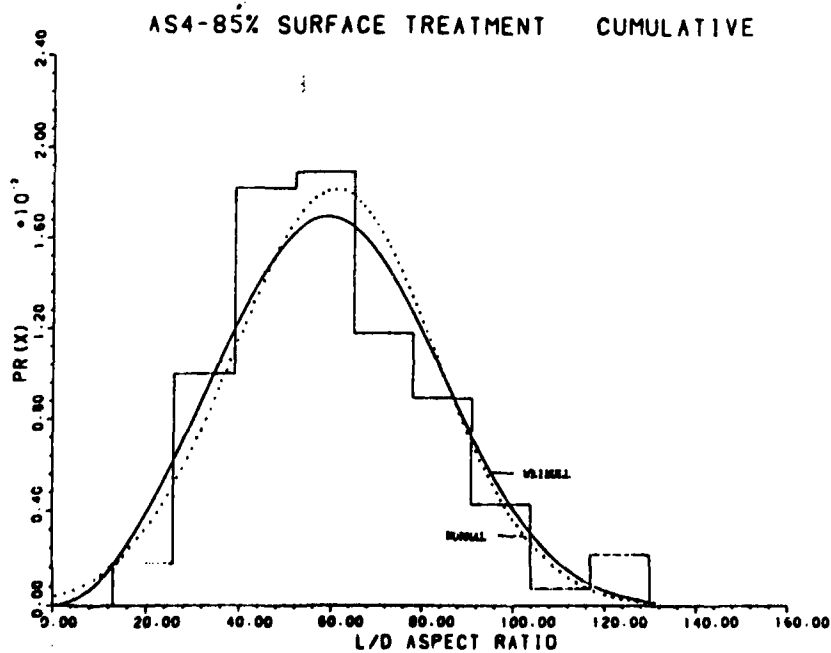


Figure 9. Histogram of AS4-85% Surface Treatment L/D Data.

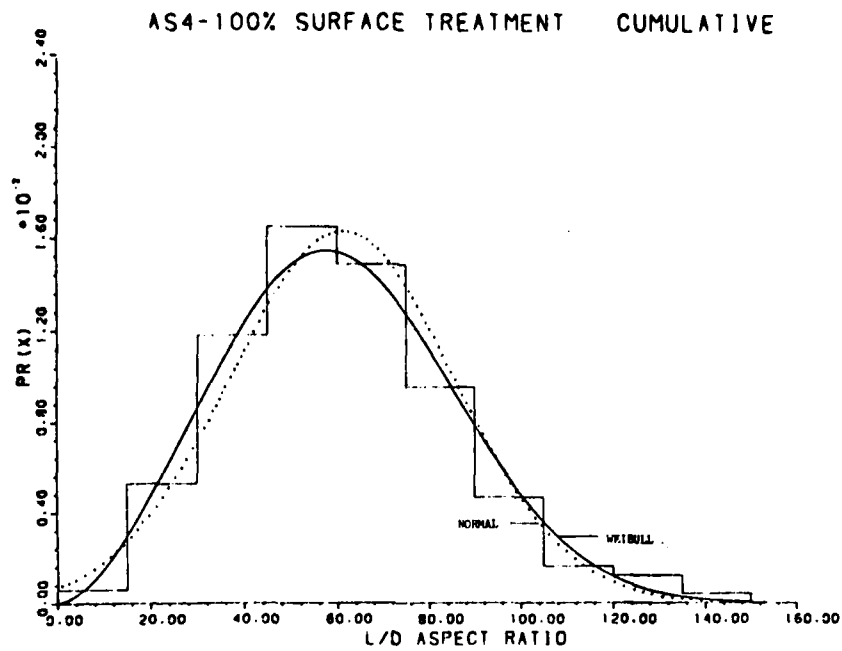


Figure 10. Histogram of AS4-100% Surface Treatment L/D Data.

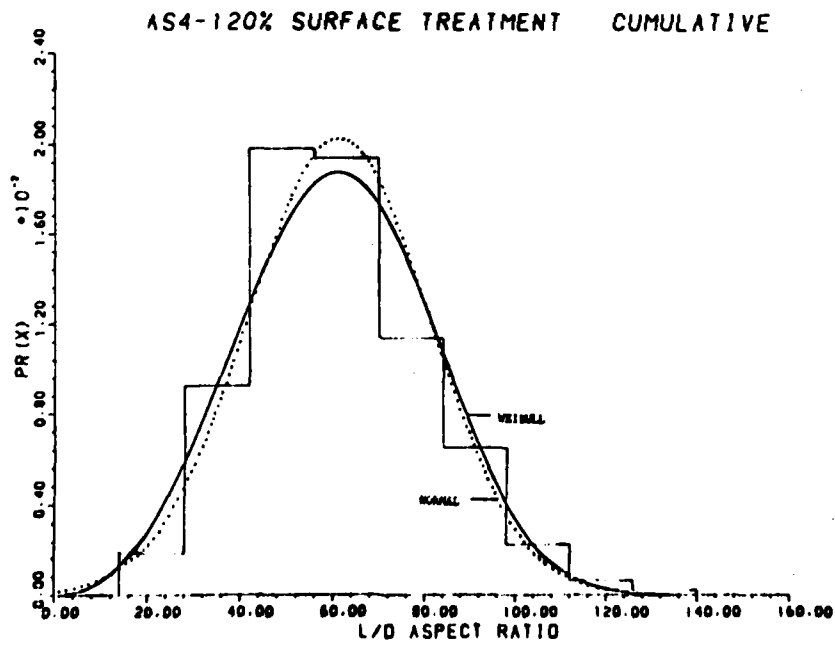


Figure 11. Histogram of AS4-120% Surface Treatment L/D Data.

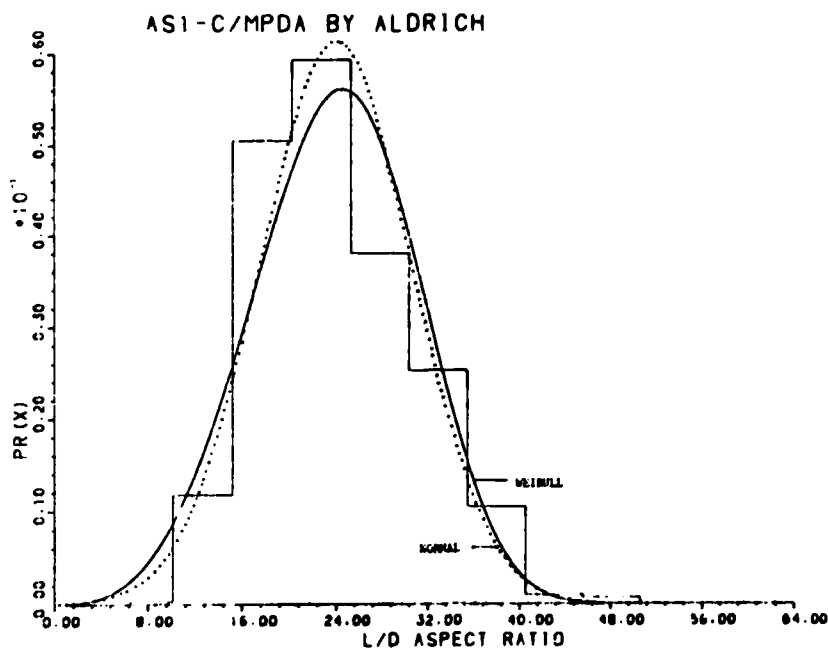


Figure 12. Histogram of AS1-C/MPDA by Aldrich L/D Data.

The interfacial shear strengths of both AS1 and AS4 fibers that had been given a surface finish by the manufacturer were evaluated. The finish consists of pure diglycidyl ether of bisphenol A applied by a solvent extraction process to one weight percent. These coated fibers are designated AS1-C and AS4-C in this study. The finish has enhanced interfacial adhesion as indicated by ~25% increase of τ for both the AS1-C and AS4-C fibers above their respective unfinished fibers.

Additionally, four sets of AS4 fibers having different degrees of the same proprietary surface treatment were tested using the single filament technique. The fibers were given 70, 85, 100, and 120% of normal surface treatment by the manufacturer at a laboratory facility. From Table 13 it can be seen that little variation exists among the Weibull scale and shape parameters for these four fibers. However, a large discrepancy of the scale parameter exists between the AS4 fiber manufactured at the

production facility and the AS4 given a 100% surface treatment at a laboratory. Interfacial shear strength cannot be calculated for the laboratory surface-treated fibers due to insufficient tensile strength data.

Standard procedure entails placing the mold containing the fibers in the oven as the resin is being debulked. To evaluate how this preliminary heating might affect the interfacial properties of the finished fiber, a set of specimens was fabricated without the mold being preheated (AS1-C/Epon 828-mPDA: cold mold). No significant change in performance was observed.

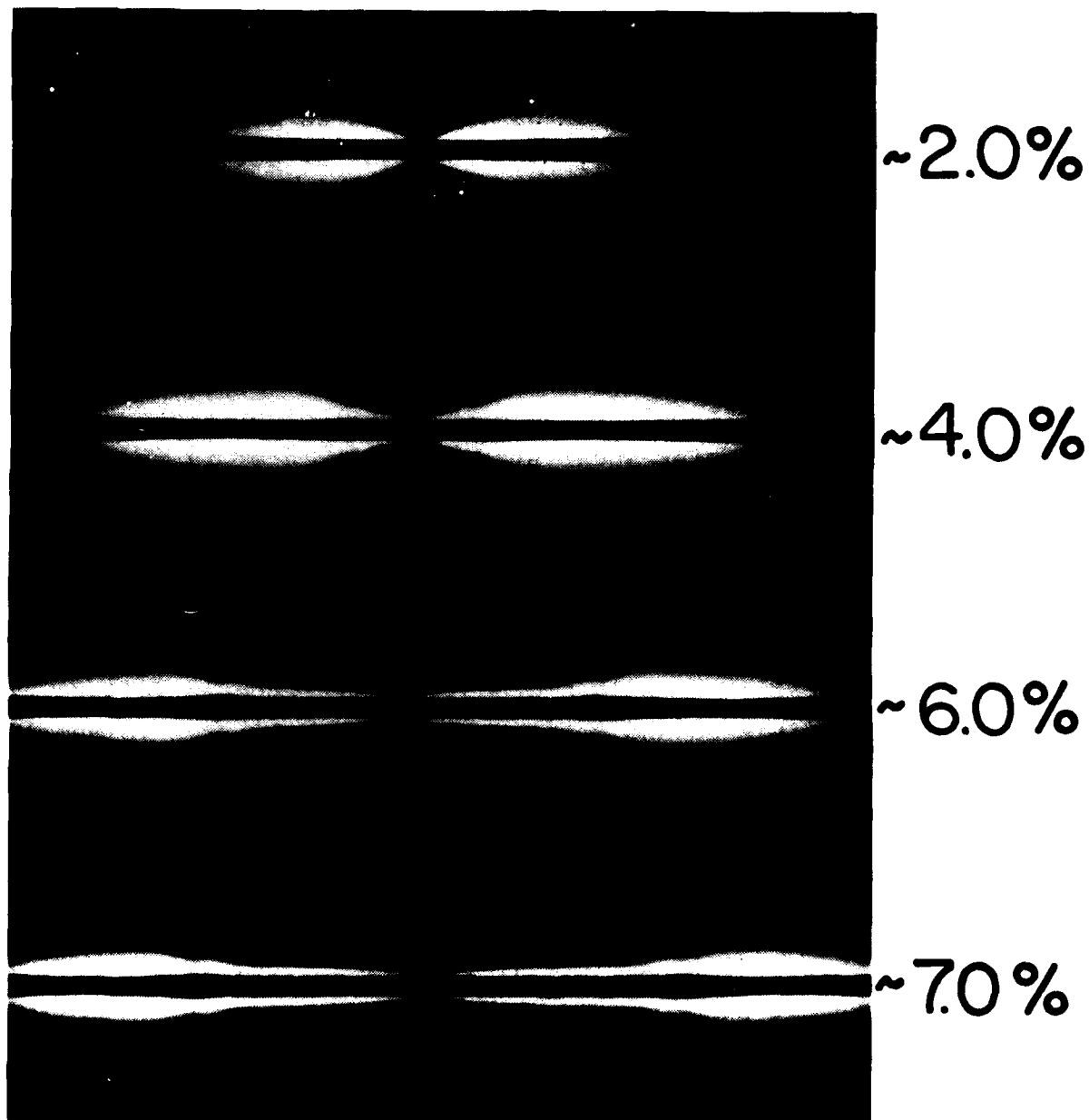
AS1-C/Epon 828-mPDA specimens were fabricated using curing agent manufactured by Aldrich Chemical Company. Pfaltz and Bauer, Inc. supplied the mPDA in all other systems evaluated. The interfacial shear strength is greater in the AS1-C/Epon 828-mPDA by Aldrich system than the AS1-C/Epon 828-mPDA by Pfaltz and Bauer.

(b) Failure mode

In situ microscopic observation of the fiber during load application reveals a dramatic difference in failure mode between the finished and unfinished fibers. Figures 13 and 14 show representative photoelastic stress patterns of the unfinished AS1 and AS4 fibers loaded in the epoxy matrix. In both cases a highly stressed region is initially concentrated at the tip of the fractured fiber. With increasing strain this region moves toward the center of the fiber fragment as a crack between the fiber and matrix is propagated.⁽¹⁶⁾ The result of this process is a thin, highly stressed area remaining at the interface.

Application of an epoxy finish to these same fibers greatly alters the fracture mode. As can be seen from Figures 15 and 16, a crack normal to the fiber axis is generated into the matrix in the AS1-C and AS4-C systems. Furthermore, this crack grows with increasing strain. The finish has changed the failure mode from fiber-matrix separation to matrix crack propagation.

AS1 / EPON 828 - mPDA



100 μm

Figure 13. AS1/Epon 828-mPDA Photoelastic Stress Pattern as a Function of Strain.

AS4 / EPON 828 - mPDA

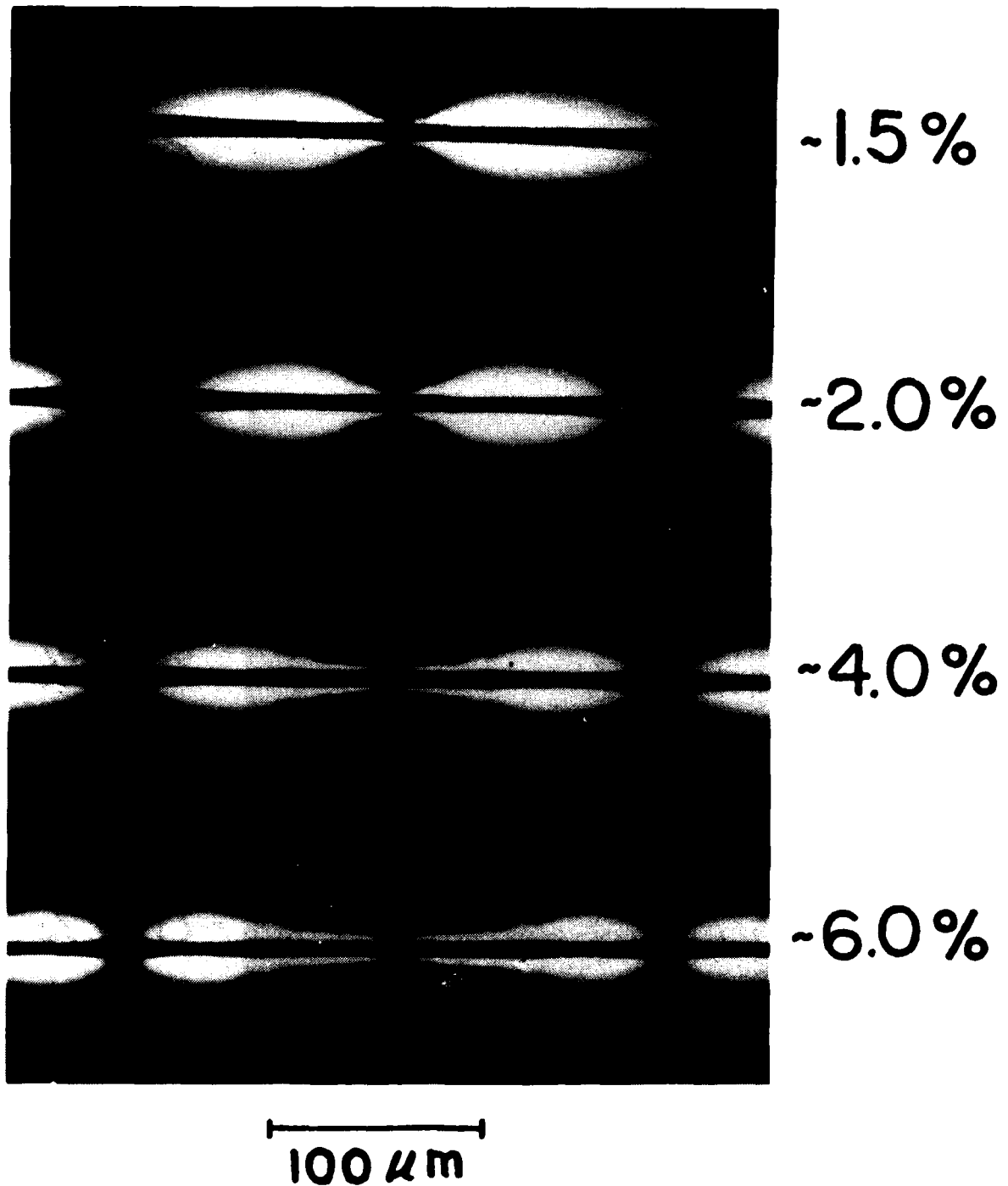


Figure 14. AS4/Epon 828-mPDA Photoelastic Stress Pattern as a Function of Strain.

AS1-C / EPON 828 - mPDA

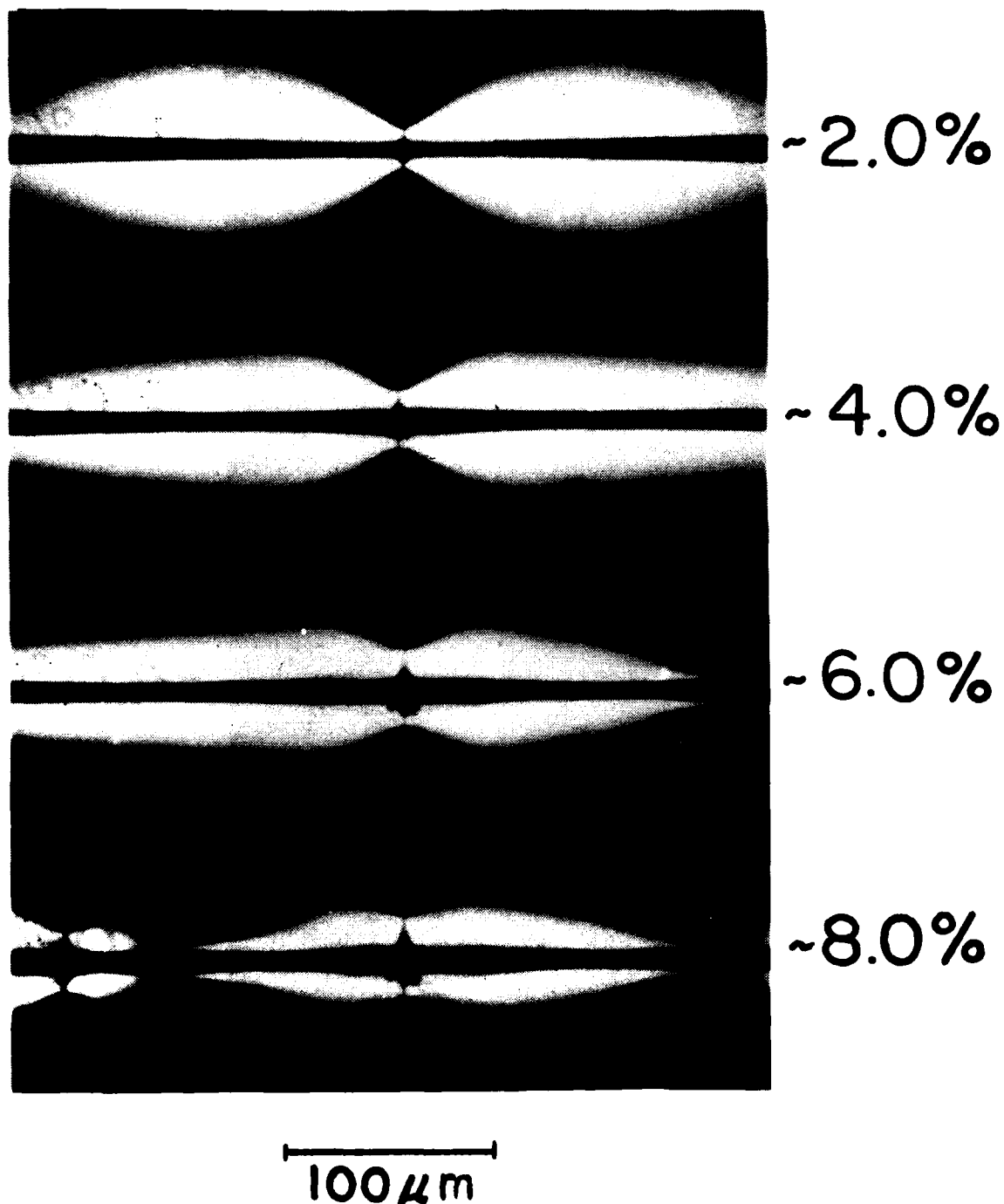
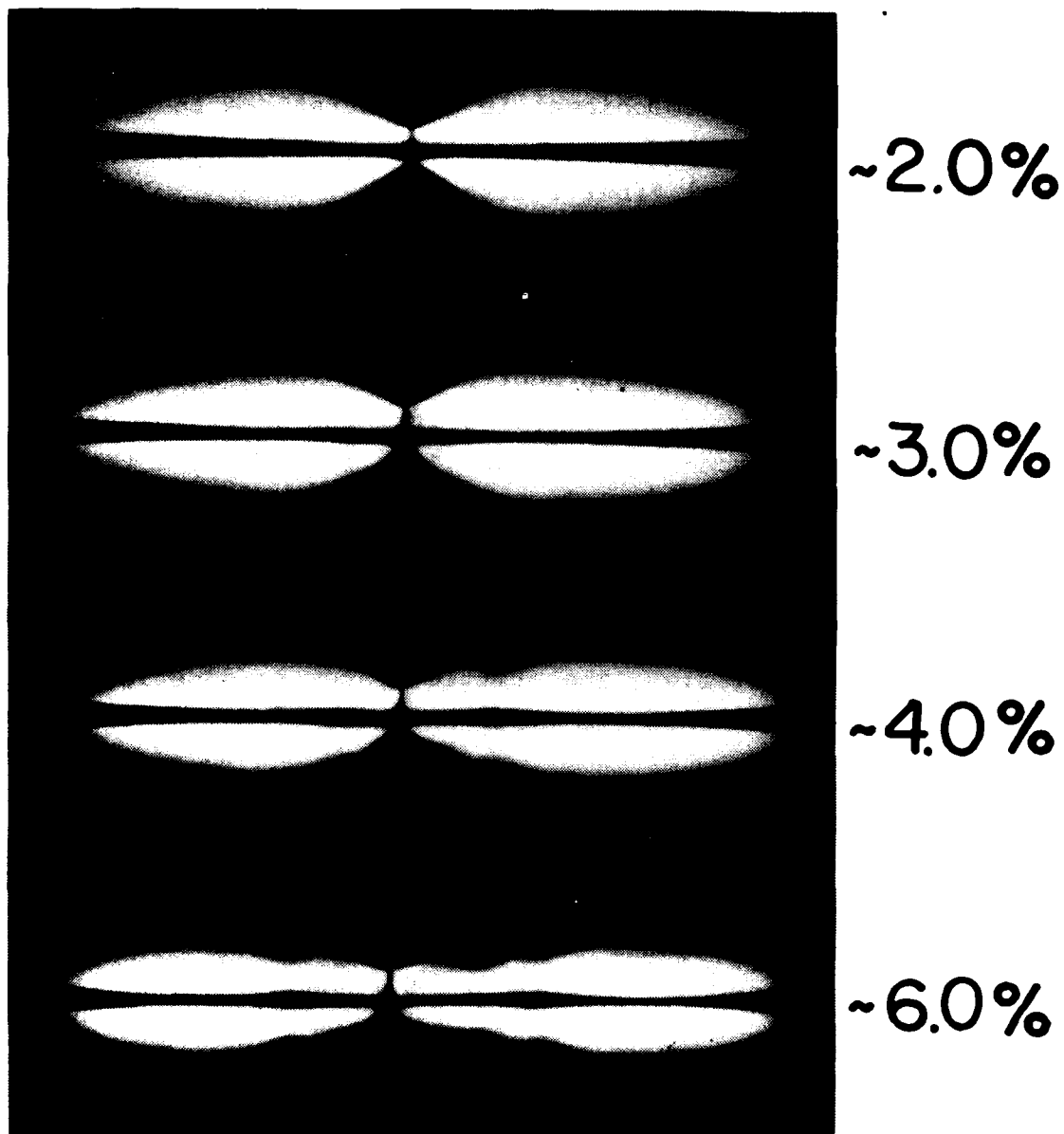


Figure 15. AS1-C/Epon 828-mPDA Photoelastic Stress Pattern as a Function of Strain.

AS4-C / EPON 828 - mPDA



100 μm

Figure 16. AS4-C/Epon 828-mPDA Photoelastic Stress Pattern as a Function of Strain.

The structure of the interphase can account for this change of failure mode. During sample fabrication, resin with the stoichiometric amount of curing agent is placed around the finished fiber. Before gelation of the matrix, the curing agent would be free to diffuse into the resin coating. This would result in a gradient of mPDA from low concentrations near the fiber surface to stoichiometric concentrations in the bulk matrix. This gradient of curing agent would be expected to be thicker than the original fiber finish.

Neat tensile coupons of Epon 828 were fabricated with mPDA concentrations from well below to well above stoichiometric. Measurement of the mechanical properties reveals that the ultimate tensile strength decreases and Young's modulus increases as mPDA concentrations decrease from the stoichiometric amount of 14.5 weight percent (see Table 14). This implies that the formulations deficient in mPDA behave in a more brittle fashion. Similar results have been reported by others.^(17,18) Additionally, it has been shown that in a system where the modulus changes from elastic-plastic to brittle, the critical length to diameter ratio decreases; i.e., the brittle system is superior at shear transfer of load onto the fiber surface.⁽¹⁹⁾

TABLE 14
MECHANICAL PROPERTIES OF EPOXY COMPOSITIONS

<u>wt. % mPDA</u>	<u>Young's Modulus ($\times 10^3$ psi)</u>	<u>Ultimate Tensile Strength (psi)</u>
7.5	695	5,000
10.0	642	12,000
14.5	525	13,700
20.0	527	13,200
25.0	581	13,900

These properties of the different resin formulations can thus explain the observed difference in performance of the finished and unfinished fibers. During specimen fabrication, the finish causes the formation of an interphase deficient in curing agent. Because this interphase is weaker and has a higher modulus than the bulk matrix, the failure mode is changed from interfacial to matrix crack propagation and the critical length is reduced, resulting in an increase of the interfacial shear strength, τ . (20)

(c) Interfacial response to water

AS-original lot/Epon 828 specimens were subjected to 100 percent RH at either room temperature, 70°C, or 125°C. Figure 17 presents a plot of weight gain versus the square root of time for the three test temperatures, illustrating that the rate of water absorption increases with temperature. The type and degree of interfacial degradation is also temperature-dependent.

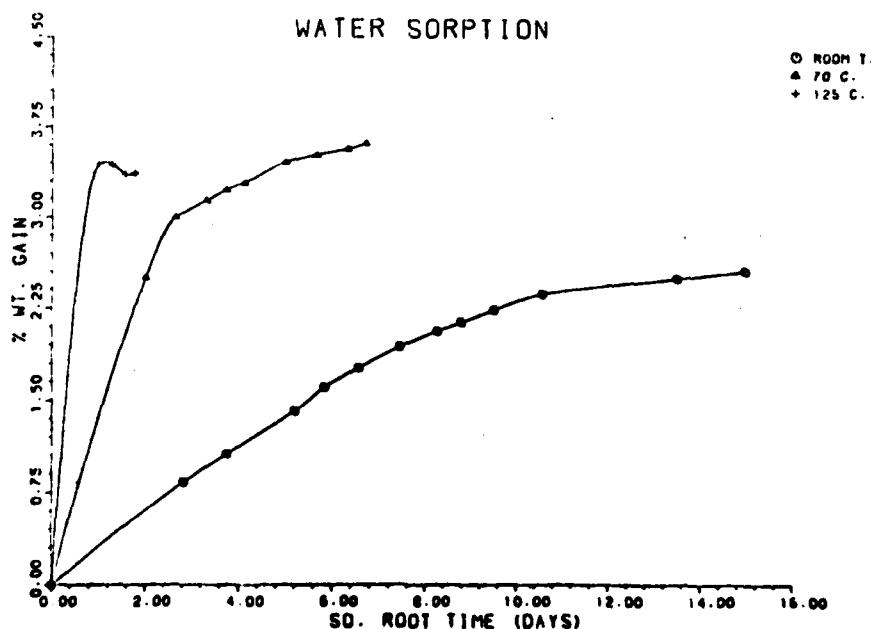


Figure 17. Water Absorption at Different Temperatures in AS/Epon 828-mpDA Test Coupons.

At room temperature specimens are still absorbing water after 200 days of exposure. No interfacial degradation can be observed using polarizing light microscopy.

Interfacial damage was found to begin at ~2.5-3.0 percent weight gain for the 100 percent RH/70°C test conditions. Approximately four to six fiber failures were observed in each of four specimens. With continued exposure up to eight fractures per specimen were sustained, each accompanied with a long photoelastic stress pattern. The specimens were subsequently dehydrated at 70°C until sample weight minimized before loading in tension. Approximately two weeks were needed for sample weight to equilibrate at ~.013 percent above their original weight. The photoelastic stress patterns persisted following dehydration. Furthermore, fiber failures did not occur in these areas when the specimens were loaded in tension. Critical length data are reported in Table 13. The larger l/d aspect ratio indicates a weaker interfacial shear strength than the same system not subjected to the elevated humidity and temperature environment.

At 125°C, sample weight reached a maxima at 24 hours followed by a slight loss of weight. Severe interfacial damage was induced and can be grouped into three categories.

The first category consists of fiber fractures that are accompanied by a diffuse photoelastic stress pattern that radiates into the matrix. A prominent gap exists between the failed fiber ends.

The second group consists of fiber fractures that induce conical voids that radiate three to five fiber diameters into the matrix. These are accompanied by bold photoelastic stress patterns.

The last category consists of regions of apparent reduced fiber diameter. These areas are associated with small yet bold photoelastic stress patterns.

A total of 10 to 12 of these three types of anomalies occurred in the gauge area. Further exposure to 100 percent RH at 125°C did not induce more damage.

A control group of test specimens subjected to 125°C (AS/Epon 828-mpDA: 125°C) for five days did not exhibit any interfacial degradation. The calculated interfacial shear strength of this system is slightly greater than the AS/Epon 828-mpDA system (see Table 13).

B. Aluminum Oxide/Epoxy Interphase

The single filament composite technique⁽⁷⁾ was used to evaluate the aluminum oxide/epoxy interphase. Phosphoric acid anodized wires were bonded in an epoxy test coupon and loaded in tension causing the anodic oxide to fracture. With increasing load a point is reached whereby no further oxide fractures are induced. An aluminum oxide/epoxy interfacial shear strength (τ) can be calculated by modifying equation (1) to

$$\tau = \frac{\sigma_o t}{2l} \quad (2)$$

where σ_o is the oxide tensile strength, t is the oxide thickness, and l is the mean distance between oxide failures.

(1) Materials

Pure aluminum wires plus two alloy wires marketed as 2024-T3 and 6061-T6 were used.^(21,22) Wire diameters were 0.005 in. before anodization.

The matrix used was Epon 828.⁽¹⁰⁾ Also, a purified DGEBA designated X-22 was used in a few trials. Both resins were cured with 14.5 phr mpDA⁽¹¹⁾ for two hours at 75°C followed by a two-hour postcure at 125°C.

(2) Experimental

(a) Wire preparation

In preparation for anodization, all wires were subjected to the following cleansing sequence.

- 1) acetone rinse
- 2) ultrasonic cleaning in carbon tetrachloride
- 3) 3 min. in 0.1 N NaOH
- 4) deionized water rinse
- 5) 2 min. in 5:1 $\text{HNO}_3:\text{HF}$
- 6) 0.5 min. in 1:1 $\text{HNO}_3:\text{H}_2\text{O}$
- 7) deionized water rinse
- 8) oven dry at 80°C

(b) Anodization

All wires were anodized in one molar phosphoric acid at 60 volts for various lengths of time. The anodizing bath was maintained at $23 \pm 1^\circ\text{C}$. Following anodization the wires were rinsed in deionized water and oven dried at 80°C .

(c) Sample fabrication and testing

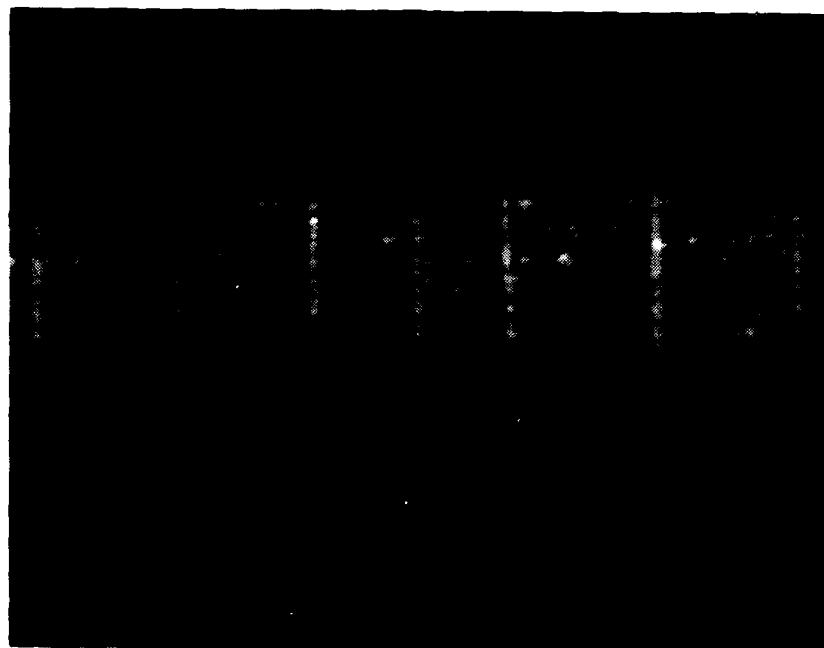
Specimen fabrication and testing procedures are the same as described elsewhere^(7,8) except that aluminum wires are substituted for carbon fibers.

(d) Oxide thickness measurement

Using standard metallographic techniques, the cross section of test specimens was polished to permit microscopic examination of the oxide layer. Distinct substrate oxide-matrix boundaries have been achieved by using magnesium oxide polishing compounds on the final polishing steps.

(3) Results and Discussion

Tensile loading of the test coupon induces radial fractures in the oxide as pictured in Figure 18. Only a limited amount of data are available to date for oxide thickness on tested wires (see Table 15). A trend to thicker oxides with longer anodization time was observed during the first hour of anodization. Table 16 reports the mean distance between oxide



0.005 in.

Figure 18. Pure Aluminum Wire Radial Oxide Fractures.

TABLE 15
APPROXIMATE OXIDE THICKNESS OF
PHOSPHORIC ACID ANODIZED WIRES

Anodization Time	Pure Aluminum	No. Measured	2024-T3	No. Measured	6061-T6	No. Measured
5	0.63 μm	1				
20	1.25	1	1.87 μm	1	1.80 μm	3
30	2.40	5	2.43	3	2.38	2
45			3.12	1		

TABLE 16
ALUMINUM OXIDE MEAN FRACTURE LENGTH

Sample	Anodization Time (min.)	Resin	Specs. Tested	Total Fragments	Mean Fracture Length (in.)	Standard Deviation (in.)
Al	5	Epon 828	6	1290	3.92×10^{-4}	0.9×10^{-4}
Al	5	X-22	2	502	5.90×10^{-4}	1.5×10^{-4}
Al	20	Epon 828	6	1488	9.21×10^{-4}	2.4×10^{-4}
Al	20	X-22	4	1015	1.63×10^{-3}	0.4×10^{-3}
Al	30	Epon 828	9	1936	2.63×10^{-3}	0.7×10^{-3}
Al	30	X-22	4	800	2.59×10^{-3}	0.7×10^{-3}
2024-T3	20	Epon 828	1	200	3.85×10^{-4}	1.0×10^{-4}
2024-T3	30	Epon 828	3	684	5.80×10^{-4}	1.8×10^{-4}
2024-T3	30	X-22	1	200	4.46×10^{-4}	1.2×10^{-4}
2024-T3	45	Epon 828	3	600	6.57×10^{-4}	2.0×10^{-4}
6061-T6	20	Epon 828	3	600	4.82×10^{-4}	1.4×10^{-4}
6061-T6	30	Epon 828	4	800	5.95×10^{-4}	1.7×10^{-4}

fractures for the three systems studied. For each oxide/resin system, the mean fracture length increases with anodization time and oxide thickness. A thicker oxide would be expected to be stronger than a thinner oxide formed on the same substrate. Consequently, a longer length would be required for sufficient shear transfer of load to occur capable of fracturing the oxide. Hence, wires with thicker oxides have longer mean fracture lengths.

Calculation of an average oxide-epoxy shear strength requires measurement of the oxide tensile strength and thickness. With improved methods for measuring these two parameters, this technique has the potential to become a valuable tool to evaluate the oxide-epoxy adhesive bond.

2. VOLUMETRIC ADSORPTION/DESORPTION OF CARBON FIBERS

The Volumetric Adsorption and Desorption System (VADS) has been used to characterize high strength carbon reinforcing fibers. Information on surface areas, surface thermodynamics, and surface volatiles has been obtained. Details on VADS operation and methods of data reduction may be found elsewhere.⁽²³⁾

During the reporting period, two types of carbon fibers have been characterized using the VADS. The first sample, designated AS1-C, is a type A surface-treated carbon fiber with a polymer coating applied to improve handling characteristics. The second type of fiber, designated AS4, is an uncoated type A surface-treated fiber. Both fiber samples were manufactured from a polyacrylonitrile precursor and provided by Hercules Inc.⁽⁹⁾

A. AS1-C Surface Area Results

Adsorption isotherms were determined for krypton on a 6.3861-gram sample of AS1-C fibers. Isotherms were obtained on the fiber sample in the "as-received" (A-R) condition and following vacuum heat treatment (VHT) at two temperatures. A method of surface area analysis developed by Brunauer, Emmett, and Teller⁽²⁴⁾ was applied to the isotherm data. The results of this analysis are included in Table 17.

B. AS1-C Surface Thermodynamics

The isosteric heat and differential entropy of krypton adsorption on the AS1-C carbon fiber sample were determined following both a 75°C, 130 minute vacuum heat treatment and a 150°C, 120 minute vacuum heat treatment. These thermodynamic parameters were calculated with the integrated Claussius-Clapyron equation using data collected at different adsorption temperatures. Four combinations of isotherm data were compared for each thermal treatment to insure reproducibility. Representative plots of the results are included. The isosteric heat curve and differential entropy plots for the sample following a 75°C vacuum heat treatment are included as Figures 19 and 20. Figures 21 and 22 show the isosteric heat curve and differential entropy of adsorption following a 150°C vacuum heat treatment.

AS1-C/75°C VHT

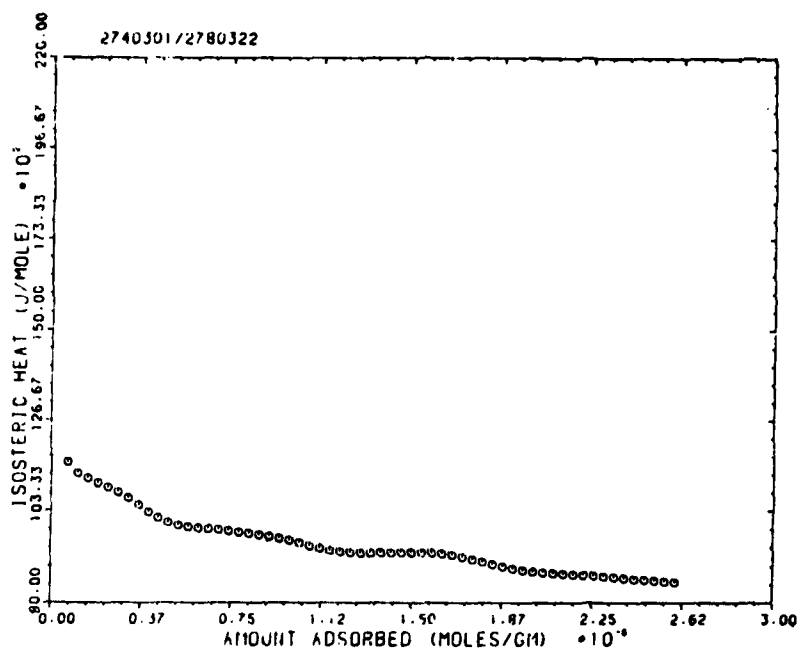


Figure 19. Isosteric Heat of Krypton Adsorption on AS1-C Fiber Sample Following a 75°C VHT.

AS1-C/75°C VHT

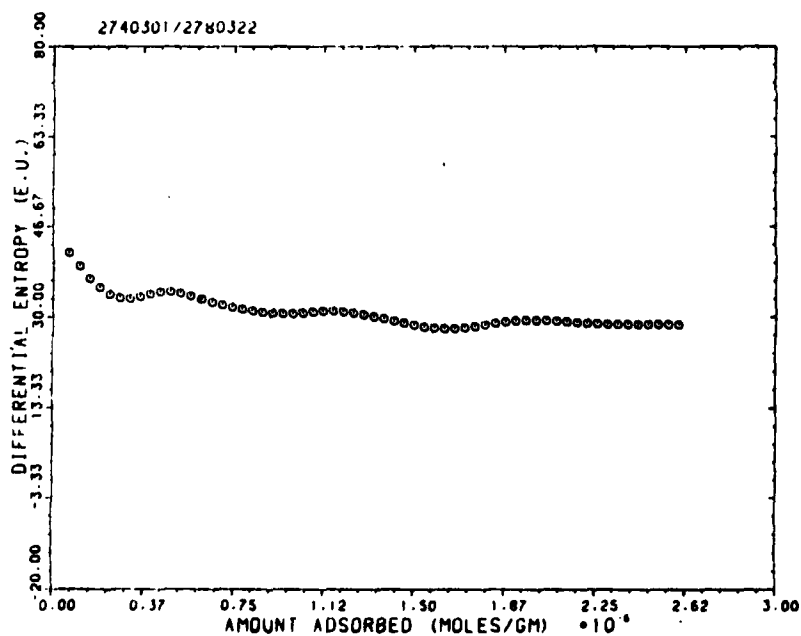


Figure 20. Differential Entropy of Krypton Adsorption on AS1-C Fiber Sample Following a 75°C VHT.

AS1-C/150°C VHT

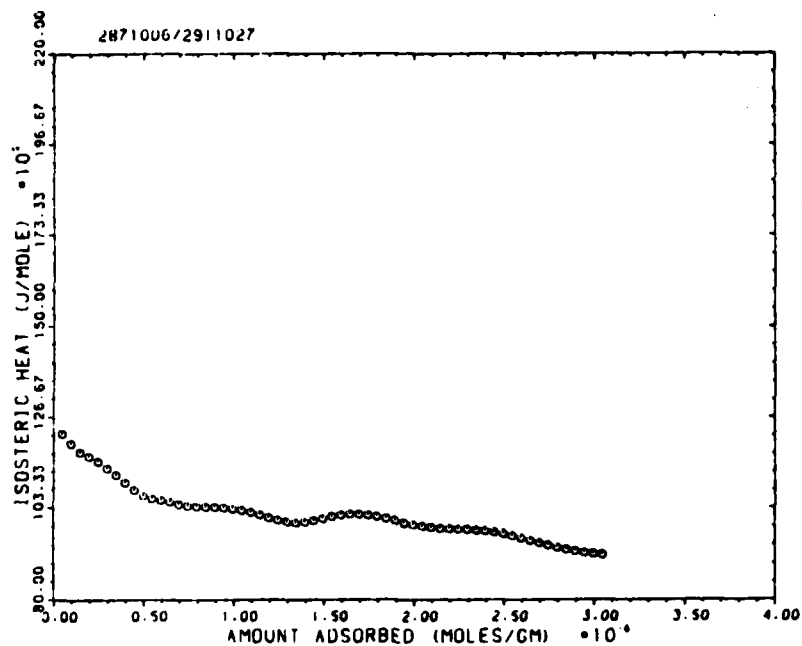


Figure 21. Isosteric Heat of Krypton Adsorption on AS1-C Fiber Sample Following a 150°C VHT.
AS1-C/150°C VHT

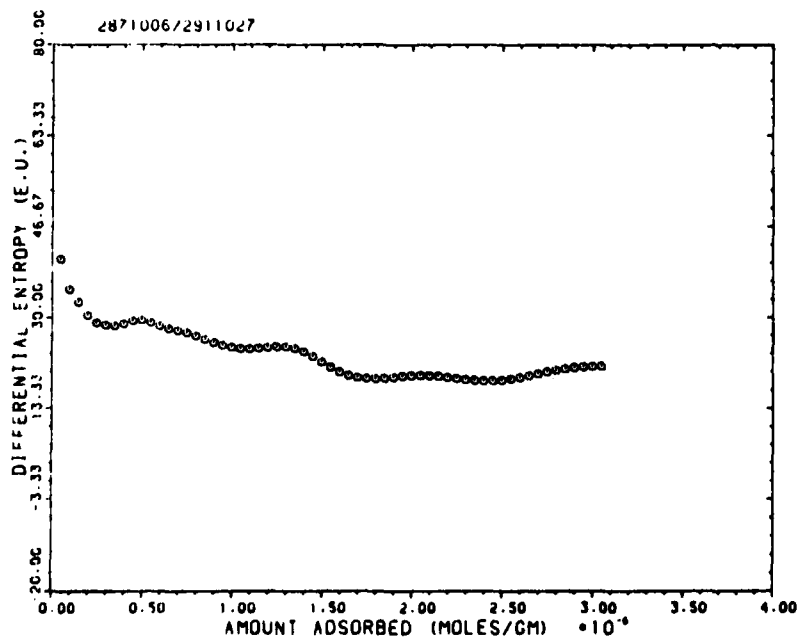


Figure 22. Differential Entropy of Krypton Adsorption on AS1-C Fiber Sample Following a 150°C VHT.

TABLE 17
AS1-C BET SURFACE AREA RESULTS

<u>Run #</u>	<u>Adsorption Temp. °K</u>	<u>Sample Treatment</u>	<u>"C"</u>	<u>V_m (cc/gm)</u>	<u>n_m (moles/gm)</u>
2680266	95.63	A-R	9.09	3.49×10^{-2}	1.56×10^{-6}
2700273	95.54	A-R	8.95	3.54×10^{-2}	1.58×10^{-6}
2740301	95.43	75°C VHT/130 min	9.07	3.43×10^{-2}	1.53×10^{-6}
2760308	95.48	75°C VHT/130 min	9.46	3.44×10^{-2}	1.53×10^{-6}
2780322	105.90	75°C VHT/130 min	7.85	4.18×10^{-2}	1.86×10^{-6}
2810337	105.88	75°C VHT/130 min	8.21	4.13×10^{-2}	1.84×10^{-6}
2850350	95.62	150°C VHT/120 min	9.31	3.81×10^{-2}	1.70×10^{-6}
2871006	95.65	150°C VHT/120 min	9.29	3.79×10^{-2}	1.69×10^{-6}
2891020	106.05	150°C VHT/120 min	8.71	4.23×10^{-2}	1.89×10^{-6}
2911027	106.02	150°C VHT/120 min	9.06	4.12×10^{-2}	1.84×10^{-6}
2941040	95.67	177°C VHT/100 min	11.82	3.69×10^{-2}	1.65×10^{-6}
2961049	95.65	177°C VHT/100 min	11.43	3.92×10^{-2}	1.75×10^{-6}

C. AS1-C Desorption Studies

Volatile species adsorbed on the surface of carbon fibers will desorb when heated. The AS1-C sample was thermally treated in vacuum to desorb the volatile species on its surface for analysis.

The sample was heat treated in three stages. The initial vacuum heat treatment was for 130 minutes at 75°C, the second vacuum heat treatment was for 120 minutes at 150°C, and the final heat treatment was for 100 minutes at 177°C. The volatiles desorbed during each of these treatments were trapped and analyzed. Pressure measurements were recorded to quantify the volatiles prior to analysis with a mass spectrometer. The total and incremental amounts adsorbed are listed in Table 18 and plotted in Figure 23. A zero-order analysis of the mass data is included in Table 19 and plotted in Figure 24.

TABLE 18
TOTAL AND INCREMENTAL AMOUNTS OF VOLATILES
DESORBED FROM THE ASI-C FIBER SAMPLE

<u>Treatment</u>	<u>Incremental Amount (monolayers)</u>	<u>Total Amount (monolayers)</u>	<u>Monolayer Capacity (moles/gm)</u>
75°C VHT/130 min	8.5×10^{-3}	8.5×10^{-3}	1.57×10^{-6}
150°C VHT/120 min	4.8×10^{-1}	4.9×10^{-1}	1.69×10^{-6}
177°C VHT/100 min	4.1×10^{-1}	9.0×10^{-1}	1.78×10^{-6}

Type ASI-C Fiber

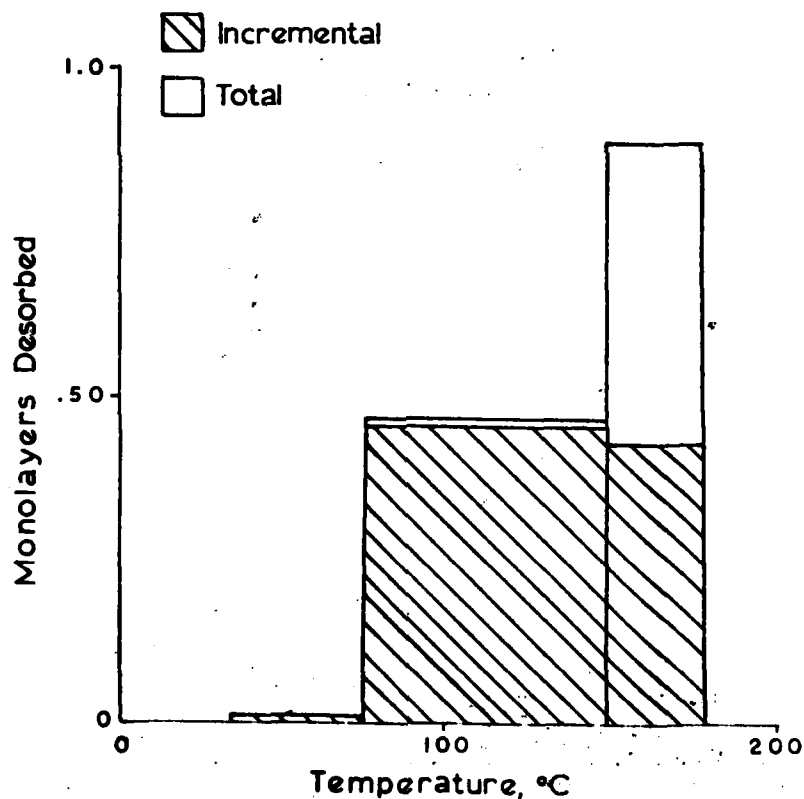


Figure 23. Total and Incremental Amounts of Volatiles Desorbed from ASI-C Fiber Sample.

TABLE 19
COMPOSITION VS. TEMPERATURE FOR ASI-C VOLATILES

<u>Symbol</u>	<u>75°C VHT/130 min</u> <u>mole %</u>	<u>150°C VHT/120 min</u> <u>mole %</u>	<u>177°C VHT/100 min</u> <u>mole %</u>
H ₂	10	13	19
CH ₄	1	4	4
NH ₃	3	9	4
H ₂ O	75	17	25
CO	9	32	16
N ₂	-	9	12
CO ₂	2	16	20

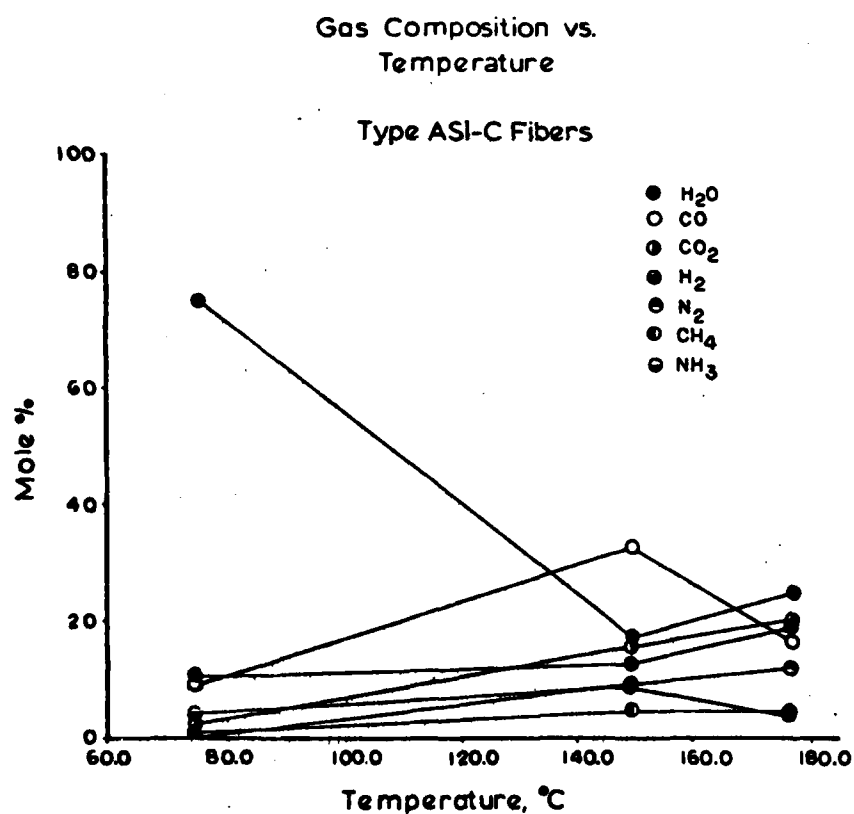


Figure 24. Composition vs. Temperature for ASI-C Volatiles.

D. AS4 Surface Area Results

Krypton adsorption isotherms were obtained on a 7.6781-gram sample of the uncoated AS4 carbon fibers. Prior to the adsorption studies the sample was thermally treated in vacuum at 75°C for 130 minutes. Adsorption isotherms were obtained on this surface as well as after a 150°C heat treatment that followed.

A BET surface area analysis was completed on the isotherm data, and the results are included in Table 20. As shown by the results, the 150°C vacuum heat treatment had a significant effect on both the surface area and the "C" constant. The deviation exhibited by the "C" constant for run number 3201125 is unexplained.

TABLE 20
AS4 BET SURFACE AREA RESULTS

Run #	Adsorption Temp. °K	Sample Treatment	"C"	V _m (cc/gm)	n _m (moles/gm)
3041069	95.68	75°C VHT/130 min	19.21	.0539	2.40x10 ⁻⁶
3061076	95.64	75°C VHT/130 min	20.46	.0548	2.44x10 ⁻⁶
3081083	105.99	75°C VHT/130 min	15.90	.0627	2.80x10 ⁻⁶
3101090	106.00	75°C VHT/130 min	16.25	.0630	2.81x10 ⁻⁶
3191118	95.64	150°C VHT/60 min	92.64	.0741	3.31x10 ⁻⁶
3201125	95.63	150°C VHT/60 min	186.41	.0705	3.15x10 ⁻⁶
3221132	106.00	150°C VHT/60 min	73.64	.0822	3.67x10 ⁻⁶
3241195	106.03	150°C VHT/60 min	77.43	.0800	3.57x10 ⁻⁶

E. AS4 Surface Thermodynamics

The adsorption thermodynamics for krypton on the AS4 fiber were determined using the integrated Claussius-Clapyron equation. The isosteric heat of adsorption and the differential entropy of adsorption were determined following a 75°C vacuum heat treatment and are represented in Figures 25 and 26, respectively.

AS4/75°C VHT

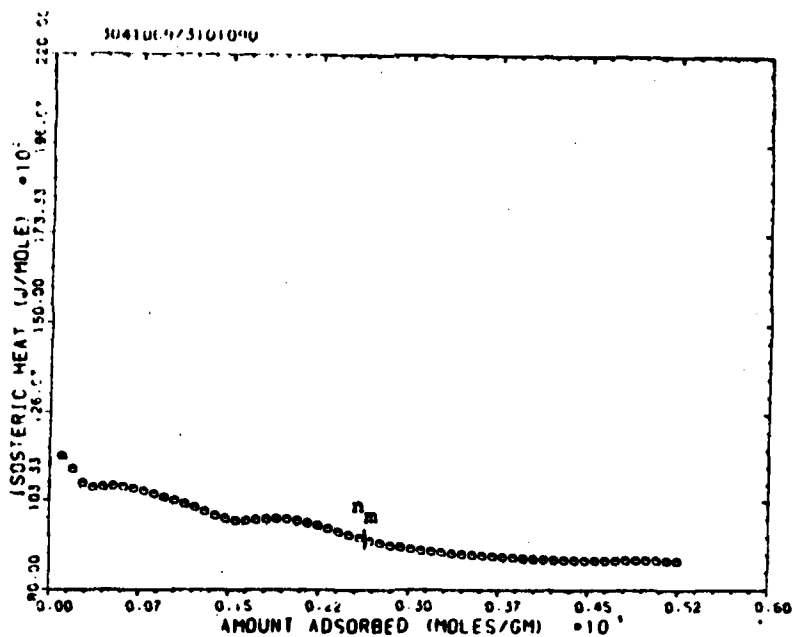


Figure 25. Isosteric Heat of Krypton Adsorption on AS4 Fiber Sample Following a 75°C VHT.

AS4/75°C VHT

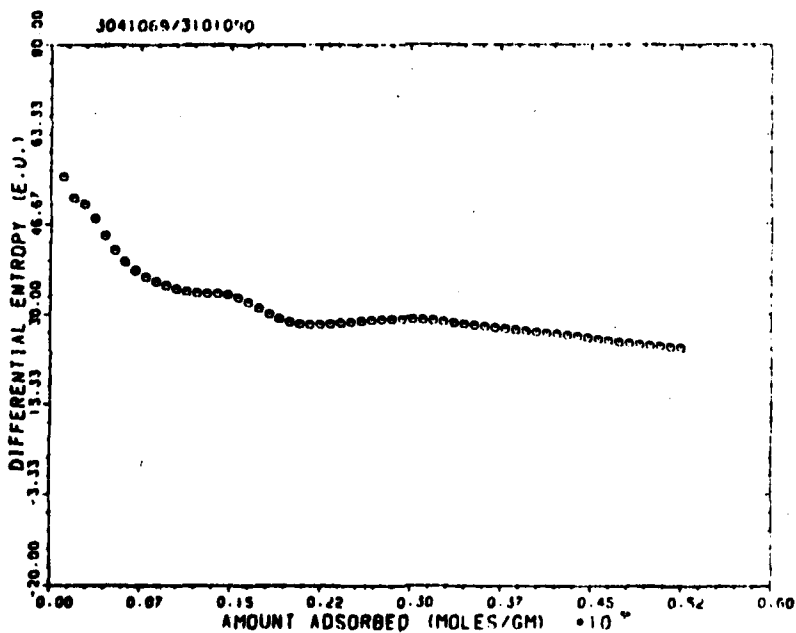


Figure 26. Differential Entropy of Krypton Adsorption on AS4 Fiber Sample Following a 75°C VHT.

Figure 27 illustrates the isosteric heat curve following the 150°C vacuum heat treatment, while Figure 28 represents the differential entropy of adsorption on the 150°C vacuum heat-treated surface.

F. AS4 Desorption Studies

The AS4 sample was subjected to four thermal treatments to enable analysis of surface volatiles. The initial vacuum heat treatment was for 130 minutes at 75°C, the second treatment was for 60 minutes at 150°C, and the third and fourth treatments at 177°C and 204°C, respectively, were for 90 minutes each. The volatiles desorbed during each of the above vacuum heat treatments were trapped and analyzed. Pressure measurements were recorded to enable quantification of the incremental and total amounts of volatiles desorbed. This data is listed in Table 21 and plotted in Figure 29. The volatiles were also analyzed with a mass spectrometer. A zero-order reduction of the mass data is listed in Table 22 and plotted in Figure 30.

3. X-RAY PHOTOELECTRON STUDIES OF GRAPHITE FIBERS

Carbon and graphite fibers are being used in composite structures for a wide variety of applications. Two types of fibers have been characterized by x-ray photoelectron spectroscopy. These two types, A and HM, are polyacrylonitrile fibers which have been graphitized at $\approx 1500^\circ\text{C}$ and $\approx 2600^\circ\text{C}$, respectively. The HM-type fibers are, hence, more graphitic and less reactive than the A-type fibers. These fibers are further labeled with an S or U, indicating, respectively, whether the fibers have undergone an oxidizing surface treatment by the manufacturer or are untreated. The main constituents of the fibers (carbon, oxygen, and nitrogen), along with the two major impurities due to manufacturing processes (sodium and sulfur), were the peaks of interest for these analyses. The fibers were analyzed using MgK α radiation ($h\nu = 1253.6 \text{ eV}$), and the kinetic energy scale was calibrated by assigning the C_{1s} peak of graphite the value 284.6 eV binding energy.⁽²⁵⁾

AS4/150 °C VHT

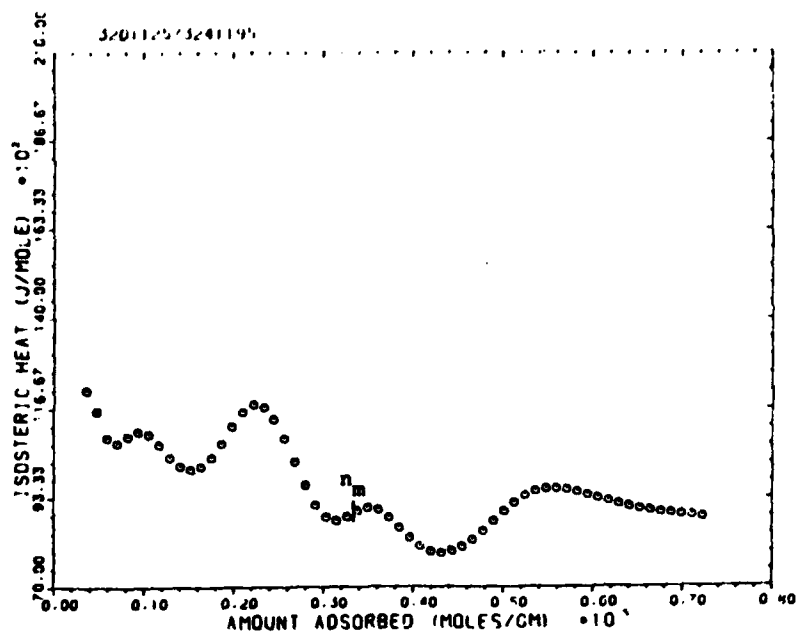


Figure 27. Isosteric Heat of Krypton Adsorption on AS4 Fiber Sample Following a 150°C VHT.

AS4/150 °C VHT

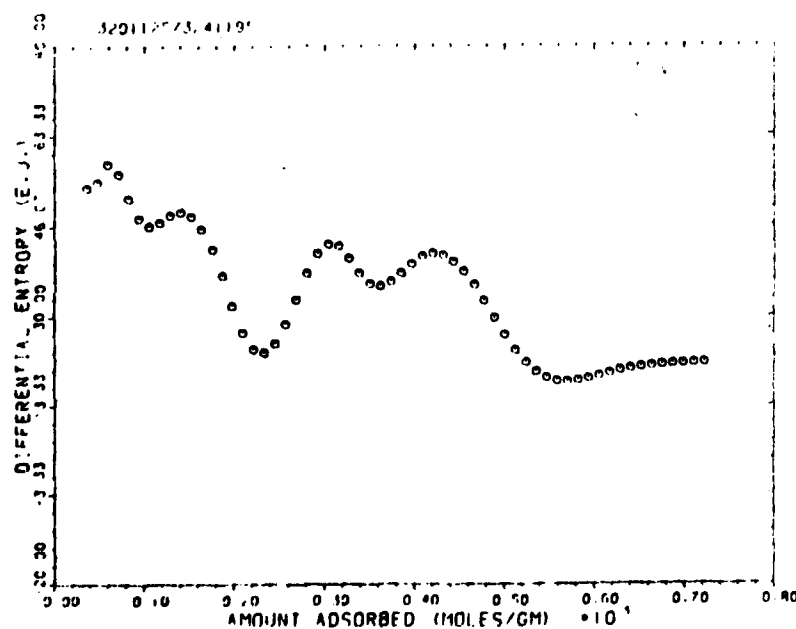


Figure 28. Differential Entropy of Krypton Adsorption on AS4 Fiber Sample Following a 150°C VHT.

TABLE 21
TOTAL AND INCREMENTAL AMOUNTS OF VOLATILES
DESORBED FROM THE AS4 FIBER SAMPLE

<u>Treatment</u>	<u>Incremental Amount (monolayers)</u>	<u>Total Amount (monolayers)</u>	<u>Monolayer Capacity (moles/gm)</u>
75°C VHT/130 min	1.6×10^{-2}	1.6×10^{-2}	2.61×10^{-6}
150°C VHT/60 min	4.6	4.62	2.61×10^{-6}
177°C VHT/90 min	3.8×10^{-3}	4.62	3.43×10^{-6}
204°C VHT/90 min	1.1×10^{-3}	4.63	3.43×10^{-6}

Type AS4 Fiber

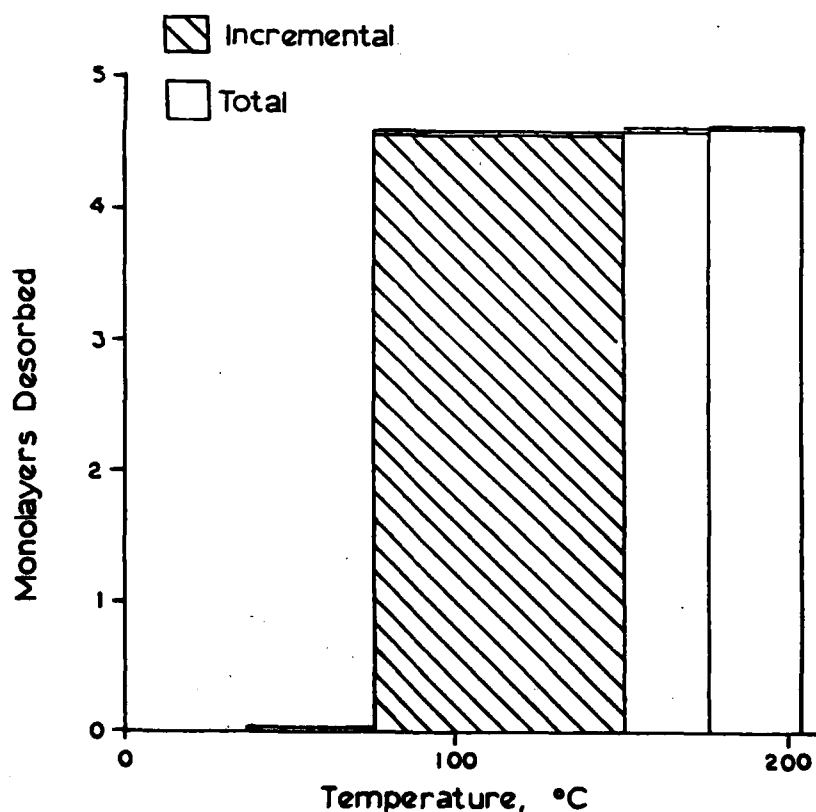


Figure 29. Total and Incremental Amounts of Volatiles Desorbed from AS4 Fiber Sample.

TABLE 22
COMPOSITION VS. TEMPERATURE FOR AS4 VOLATILES

Symbol	75°C VHT/130 min mole %	150°C VHT/60 min mole %	177°C VHT/90 min mole %	204°C VHT/90 min mole %
H ₂	13	6	28	14
CH ₄	3	2	6	-
NH ₃	6	15	27	11
H ₂ O	25	18	14	-
CO	28	42	6	40
N ₂	12	8	9	-
CO ₂	13	9	10	35

Gas Composition vs.
Temperature

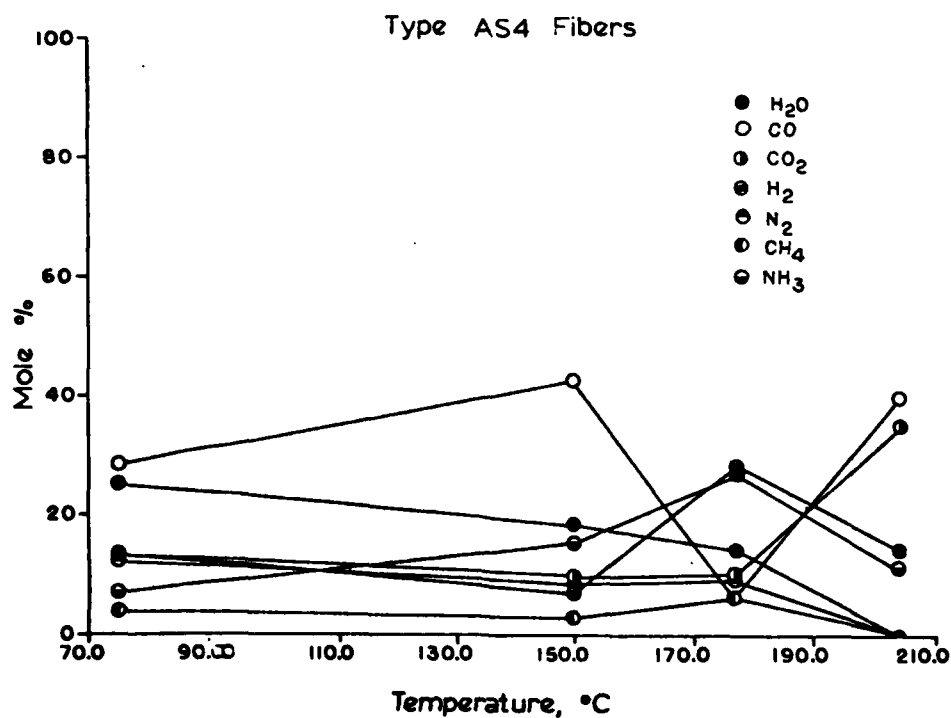


Figure 30. Composition vs. Temperature for AS4 Volatiles.

This study focuses mainly on the AS-type fiber because it is the most reactive of those studied and, hence, undergoes the greatest changes. These fibers were analyzed "as received" from the manufacturer and also after various compounds were adsorbed on the fiber surface to observe how the fibers interact with these adsorbates. The results of this work are summarized below.

A. Graphite Single Crystal (freshly cleaved in air)

A fairly symmetrical C_{1s} peak was obtained with a slight tail on the low kinetic energy (KE) side. This peak is comparable to the narrowest of the C_{1s} peaks obtained from the fiber specimens; its full width at half maximum (FWHM) was measured to be 1.7 eV. A small loss feature is visible in the spectrum at approximately 6.6 eV lower KE than the main peak. The O_{1s} peak is also symmetric, and its FWHM measured to be 2.9 eV. Oxygen comprised about one atomic percent of the freshly-cleaved surface and can be attributed mainly to the interstitial water of the graphite structure. If the C_{1s} peak position is adjusted to appear at the commonly accepted value of 284.6 eV binding energy (BE), then the O_{1s} peak is positioned at 532.9 eV BE. Table 23 contains the peak position and FWHM values of the C_{1s} and O_{1s} peaks obtained from the specimens reported in this work.

B. HM Fibers

HMU fibers were found to have about two percent oxygen on their surface compared with three to three-and-one-half percent oxygen on the HMS fiber. Surface concentration values for the major constituents of these fibers can be found in Table 24. The C_{1s} peak from each is slightly broader than that of graphite (1.9 eV versus 1.7 eV FWHM) but has a very similar shape. The O_{1s} peak is very similar from the two fibers, the FWHM ranging from 3.0 to 3.2 for HMU and 3.2 to 3.4 for HMS. The O_{1s} peaks for both the fibers are broadened slightly from that of the graphite single crystal towards lower BE.

TABLE 23

ENERGIES AND WIDTHS OF THE CARBON 1s AND OXYGEN 1s
PHOTOELECTRON PEAKS OF THE FIBERS ANALYZED IN THIS STUDY

Specimen	C _{1s}		O _{1s}	
	Peak Energy* eV	FWHM** eV	Peak Energy eV	FWHM eV
Graphite crystal	285.1	1.7	533.4	2.9
<u>HMU fibers</u>				
HM02	284.8	1.6	532.7	2.8
F013	285.1	1.9	533.0	3.0
F053	284.5	1.8	532.5	3.2
<u>HMS fibers</u>				
F006	284.9	1.5	532.4	3.1
F012	285.1	1.9	532.9	3.2
F052	284.6	1.9	532.4	3.3
F026	285.1	1.9	533.0	3.4
F030	284.7	1.9	532.4	3.2
<u>HM fibers + PVA</u>				
F031	286.0	3.8	533.9	2.4
F034	285.0	2.9	533.5	2.3
F032	284.7 289.2	2.3	533.0 530.8	2.8
F033	285.0 289.7	2.9	533.1	2.6
<u>AU fibers</u>				
F016	285.6 288.7	2.2	532.9	2.8
F017	285.4 289.4	2.1	532.8	2.9
F050	284.6	2.2	532.4	2.8
F051	284.8	2.2	532.6	2.9
F040	284.5	2.2	532.3	3.0
F042	284.5	2.2	532.1	3.1
F043	284.5	2.2	532.3	3.1

TABLE 23

ENERGIES AND WIDTHS OF THE CARBON 1s AND OXYGEN 1s
PHOTOELECTRON PEAKS OF THE FIBERS ANALYZED IN THIS STUDY

(Continued)

Specimen	C _{1s}		O _{1s}	
	Peak Energy* eV	FWHM** eV	Peak Energy eV	FWHM eV
<u>AS fibers</u>				
F001	285.2 288.9	2.2	532.6	3.3
F007	285.0 288.7	2.1	532.3	3.2
F008	285.0 288.6	2.1	532.4	3.2
F009	285.1 288.6	2.0	532.2	3.2
F010	285.0 288.7	2.1	532.1	3.2
F002	285.0 288.6	2.1	532.5	3.1
F003	284.9 288.7	2.2	532.4	3.1
F004	285.0 288.5	2.1	532.4	3.2
F024	285.4 288.9	2.3	533.1	3.2
F035	284.8	2.5	532.6	3.4
F036	285.1	2.0	532.9	3.2
F037	284.7	2.4	532.5	3.3
F038	284.8	2.3	532.5	3.2
F021	285.6 289.2	2.4	532.9	3.3
F027	285.3 289.1	2.6	533.0	3.6
F028	285.2 288.4	2.3	532.8	3.3

TABLE 23
ENERGIES AND WIDTHS OF THE CARBON 1s AND OXYGEN 1s
PHOTOELECTRON PEAKS OF THE FIBERS ANALYZED IN THIS STUDY
(Concluded)

Specimen	C _{1s}		O _{1s}	
	Peak Energy* eV	FWHM** eV	Peak Energy eV	FWHM eV
<u>AS fibers</u>				
F022	285.5 288.9	2.2	532.7	3.6
F044	284.4	2.2	532.1	3.8
F045	284.8	2.3	532.7	2.8
F025	285.3 289.5	2.6	532.8	3.7
F029	285.1 288.8	2.6	532.9	3.6
F014	285.4 288.9	2.4	533.2	3.2
F015	285.7 288.9	2.5	533.2	3.1
F019	285.5	2.2	532.6	3.2
F020	285.5	2.1	532.6	3.2
F048	284.9 289.0	2.9	533.0	2.6
F049	284.6 288.7	3.0	532.8	2.7
F046	284.8	2.8	533.0	2.7
F047	284.9	2.8	533.0	2.7

*Measured values, reported in binding energy. No corrections are made for possible sample charging.

**Spectra from specimens HM02, single crystal graphite, and F001 through F011 were taken under higher resolution conditions than the remaining spectra, hence the smaller values for FWHM.

C. High Modulus Fibers + Polyvinyl Alcohol (PVA)

This fiber is a special high-modulus fiber. No other samples of this type, either treated or untreated, were submitted for analysis to compare with this data, and so the data has been compared with the AS fiber.

These four samples contain varying amounts of adsorbed PVA. Two of the samples, F032 and F033, were heated after exposure to the PVA-containing solution which tended to reduce the amount of PVA remaining on the surface of the fiber. This is evident in the spectra by an increase of the O_{1s} peak intensity on the low BE side and a decrease of the C_{1s} peak intensity on the high BE side of the peak after heat treatment. Further support for this interpretation comes from the data obtained from specimen F031. When first analyzed, the main C_{1s} peak was positioned at 286.0 eV, and the O_{1s} peak was found at 533.9 eV BE with a FWHM of only 2.4 eV. These facts are indicative of a large number of C-OH bonds on the surface of the fibers. The spectra from these fibers gradually changed as the specimen remained in the vacuum of the analysis chamber. Over several days, the oxygen peak broadened toward lower BE, and the peak intensity of the C_{1s} peak diminished at 286.0 eV and increased at 285 eV BE, until finally resembling the spectra from F033 which had undergone heat treatment. Results of these analyses are contained in Table 24 as surface concentration values.

Figure 31 shows narrow scans of the C_{1s} photoelectron peak of three samples which contained different amounts of adsorbed PVA. Slight differences can be seen between these spectra, but the individual components of the peaks are not discernible from these scans. If these spectra are differentiated, however, the differences are much more striking. It is now evident that the major component of F031 is different from that of F035, and that F033 is a mixture of these two components. Deconvolution of these peaks using the Kratos computer package supplied with the instrument consistently showed peaks at 284.8 and 286.0 eV binding energies, which are what would be expected for the

TABLE 24
SURFACE COMPOSITION OF TYPE HM AND HIGH MODULUS FIBER SPECIMENS
OBTAINED USING XPS

Specimen	Photoelectron Peak	Peak Area	Surface Concentration (atomic percent)	Specimen	Photoelectron Peak	Peak Area	Surface Concentration (atomic percent)
Graphite single crystal	C _{1s}	7.0 x 10 ⁶	99	<u>HMS Fibers</u> F006	C _{1s}	2.7 x 10 ⁶	96
	O _{1s}	2.6 x 10 ⁵	1.0		O _{1s}	2.7 x 10 ⁵	3.0
					N _{1s}	7.1 x 10 ⁴	1.5
					S _{2p}	--	-- ^a
					Na _{KLL}	--	-- ^a
<u>HMU Fibers</u> HM02	C _{1s}	2.7 x 10 ⁶	92	F012	C _{1s}	3.6 x 10 ⁶	95
	O _{1s}	5.9 x 10 ⁵	6.0		O _{1s}	4.7 x 10 ⁵	3.5
	N _{1s}	5.4 x 10 ⁴	1.0		N _{1s}	8.2 x 10 ⁴	1.0
	S _{2p}	--	1.5 ^b		S _{2p}	1.7 x 10 ⁴	<0.5
	Na _{KLL}	--	-- ^a		Na _{KLL}	--	-- ^a
F013	C _{1s}	4.3 x 10 ⁶	97	F052	C _{1s}	4.9 x 10 ⁶	95
	O _{1s}	3.0 x 10 ⁵	2.0		O _{1s}	5.6 x 10 ⁵	3.5
	N _{1s}	3.3 x 10 ⁴	0.5		N _{1s}	1.2 x 10 ⁵	1.3
	S _{2p}	1.7 x 10 ⁴	<0.5		S _{2p}	1.5 x 10 ⁴	<0.2
	Na _{KLL}	--	-- ^a		Na _{KLL}	6.9 x 10 ⁴	0.5
F053	C _{1s}	3.9 x 10 ⁶	97	F026 (HMS + H ₂ O)	C _{1s}	3.7 x 10 ⁶	94
	O _{1s}	2.6 x 10 ⁵	2.0		O _{1s}	5.5 x 10 ⁵	4.0
	N _{1s}	2.8 x 10 ⁴	<0.5		N _{1s}	7.0 x 10 ⁴	1.0
	S _{2p}	1.1 x 10 ⁴	<0.2		S _{2p}	2.4 x 10 ³	<0.5
	Na _{KLL}	5.1 x 10 ⁴	0.5		Na _{KLL}	7.6 x 10 ⁴	1.0

TABLE 24
SURFACE COMPOSITION OF TYPE HM AND HIGH MODULUS FIBER SPECIMENS
OBTAINED USING XPS
(Concluded)

Specimen	Photoelectron Peak	Peak Area	Surface Concentration (atomic percent)	Specimen	Photoelectron Peak	Peak Area	Surface Concentration (atomic percent)
F030 (HMS + cyclohexane)	C _{1s}	4.0 x 10 ⁶	94	F032 (high modulus + PVA + heat treatment)	C _{1s}	4.2 x 10 ⁶	88
	O _{1s}	5.8 x 10 ⁵	4.0		O _{1s}	1.7 x 10 ⁶	11
	N _{1s}	1.0 x 10 ⁵	1.3		N _{1s}	8.6 x 10 ⁴	1.0
	S _{2p}	1.6 x 10 ⁴	0.2		S _{2p}	9.0 x 10 ³	<0.2
	Na _{KLL}	5.6 x 10 ⁴	<1.0		Na _{KLL}	7.9 x 10 ⁴	<1.0
High Modulus Fibers + PVA F031	C _{1s}	2.8 x 10 ⁶	82	F033 (high modulus + PVA + heat treatment)	C _{1s}	4.1 x 10 ⁶	83
	O _{1s}	1.7 x 10 ⁶	15		O _{1s}	2.3 x 10 ⁶	14
	N _{1s}	1.4 x 10 ⁴	<0.5		N _{1s}	8.3 x 10 ⁴	1.0
	S _{2p}	5.2 x 10 ³	<0.2		S _{2p}	1.6 x 10 ⁴	<0.2
	Na _{KLL}	1.8 x 10 ⁵	2.7		Na _{KLL}	1.4 x 10 ⁵	1.5
F034	C _{1s}	4.0 x 10 ⁶	88				
	O _{1s}	1.7 x 10 ⁶	11				
	N _{1s}	-- ^c					
	S _{2p}	6.8 x 10 ³	<0.2				
	Na _{KLL}	7.7 x 10 ⁴	<1.0				

^a High resolution scans not taken of these peaks.

^b Estimated from broad scan.

^c Nitrogen not measurable in narrow scan; concentration less than 0.2 atom percent.

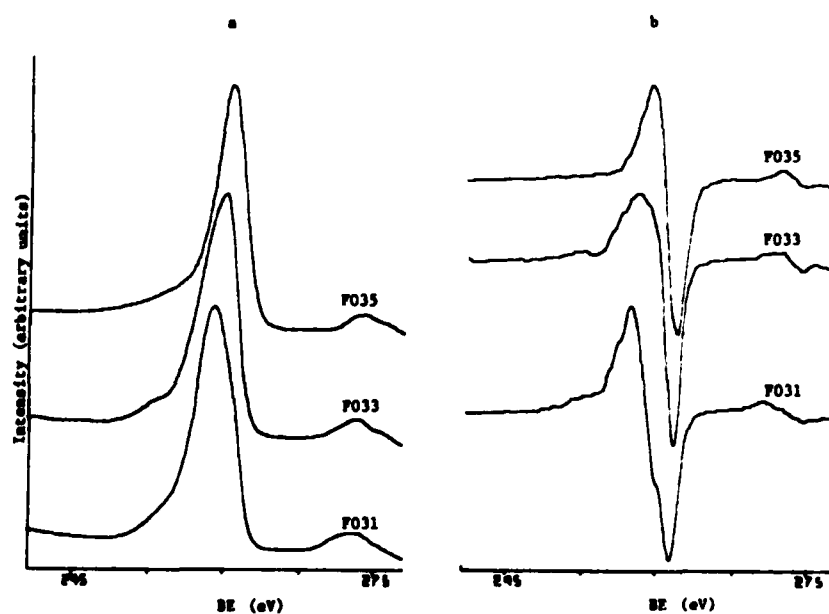


Figure 31. Carbon 1s XPS Spectra from: (1) F035, High Modulus Fiber Specimen; (2) F033, Fiber with Small Amount of PVA Adsorbed; and (3) F031, Fiber with Larger Amount of PVA Adsorbed Presented in (a) Pulse-Counting and (b) Differentiated Modes. Peaks are displaced vertically for clarity.

carbonized surface of the fiber and the shift due to the influence of -OH groups attached to the carbon atoms of PVA, respectively.

The O_{1s} spectrum of a high-modulus fiber after exposure to PVA can be seen in Figure 32, the binding energy being 533.3 eV. This spectrum is compared in Figure 32 with oxygen spectra from an AS fiber (F036) and an AS fiber which had been exposed to water (F029). The difference in O_{1s} binding energy between these peaks and that from the fiber exposed to PVA is about 1 eV. The O_{1s} peak of the PVA-coated fiber is also narrower than the other two peaks, indicating that the other two peaks may contain more than one component. The differentiated spectra, however, exhibit no additional information about these peaks. A deconvolution of the PVA O_{1s} peak resulted in only one component at the same binding energy. The signal-to-noise ratio of the other two O_{1s} spectra was inadequate to obtain accurate deconvolution results with the deconvolution program used in this work.

D. AU Fibers

The AU fibers which were analyzed had widely varying surface compositions with oxygen contents ranging between four and nine atom percent as can be seen in Table 25. The C_{1s} peaks (2.15 to 2.25 eV FWHM) are broader than the HM fibers and narrower than the AS "as received". This confirms the expectation that the AU fibers are less graphitic than the HM fibers and less oxidized than the AS fibers.

The O_{1s} peaks had FWHM values between 2.85 and 3.10 eV and positioned at ≈ 532.3 eV BE. This is similar to the oxygen peaks obtained from the HMU fibers.

Like the AS fibers, the AU fibers differed from the AU-1 and AU-4 lots mainly in the increased levels of sodium (4.6 percent vs. 1 to 1.5 percent) and sulfur (0.5 to 1 percent vs. ≤ 0.2 percent) contamination. Since the sulfur is present mainly in its oxidized form, i.e. $-SO_3^-$ and $-SO_4^{2-}$ groups, this also accounts for most of the difference in oxygen levels between the AU fiber lots.

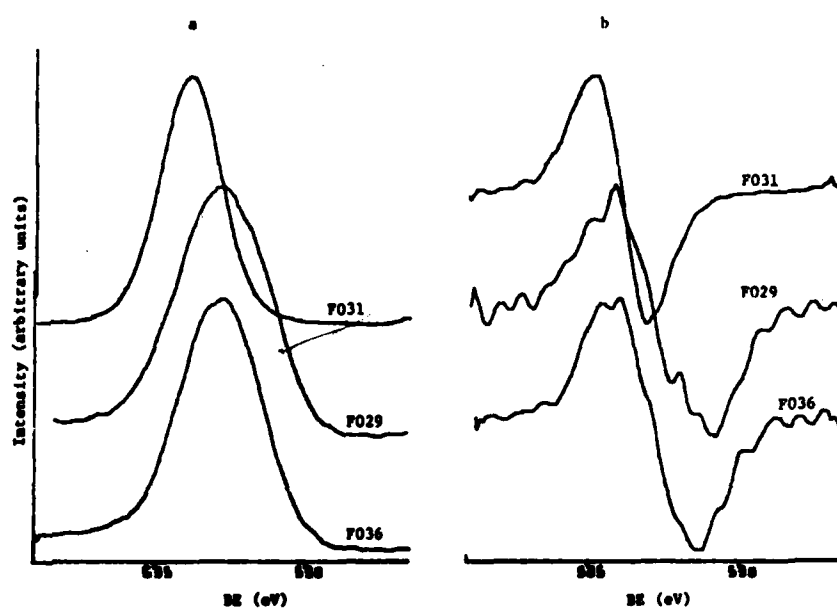


Figure 32. Oxygen 1s XPS Spectra from: (1) F031, High Modulus Fiber with PVA Adsorbed; (2) F029, AS Fiber Exposed to Water; and (3) F036, AS Fiber Presented in (a) Pulse-Counting and (b) Differentiated Modes. Peaks are displaced vertically for clarity.

TABLE 25
SURFACE COMPOSITION OF AU FIBER SPECIMENS OBTAINED USING XPS

Specimen	Photoelectron Peak	Peak Area	Surface Concentration (atomic percent)	Specimen	Photoelectron Peak	Peak Area	Surface Concentration (atomic percent)
F016	C _{1s}	3.5 x 10 ⁶	84	F040 (AU-1)	C _{1s}	3.2 x 10 ⁶	92
	O _{1s}	1.3 x 10 ⁶	9.0		O _{1s}	5.4 x 10 ⁵	4.5
	N _{1s}	1.4 x 10 ⁵	2.0		N _{1s}	1.1 x 10 ⁵	1.5
	S _{2p}	4.2 x 10 ⁴	0.5		S _{2p}	5.5 x 10 ³	<0.2
	Na _{KLL}	3.7 x 10 ⁵	4.5		Na _{KLL}	1.2 x 10 ⁵	1.5
F017	C _{1s}	1.7 x 10 ⁶	88	F042 (AU-1)	C _{1s}	3.1 x 10 ⁶	92
	O _{1s}	3.9 x 10 ⁵	6.0		O _{1s}	4.7 x 10 ⁵	4.5
	N _{1s}	5.4 x 10 ⁴	1.5		N _{1s}	1.6 x 10 ⁵	2.5
	S _{2p}	2.0 x 10 ⁴	0.5		S _{2p}	1.5 x 10 ⁴	0.2
	Na _{KLL}	1.6 x 10 ⁵	4.0		Na _{KLL}	9.0 x 10 ⁴	1.5
F050	C _{1s}	3.4 x 10 ⁶	84	F043 (AU-4)	C _{1s}	2.5 x 10 ⁶	92
	O _{1s}	8.8 x 10 ⁵	6.8		O _{1s}	4.4 x 10 ⁵	5.0
	N _{1s}	1.0 x 10 ⁵	1.5		N _{1s}	1.1 x 10 ⁵	2.0
	S _{2p}	6.0 x 10 ⁴	1.0		S _{2p}	5.2 x 10 ³	<0.2
	Na _{KLL}	5.2 x 10 ⁵	6.5		Na _{KLL}	4.7 x 10 ⁴	1.0
F051	C _{1s}	3.2 x 10 ⁶	85				
	O _{1s}	8.5 x 10 ⁵	6.8				
	N _{1s}	1.2 x 10 ⁵	1.5				
	S _{2p}	5.2 x 10 ⁴	1.0				
	Na _{KLL}	4.5 x 10 ⁵	6.0				

E. AS Fibers

These fibers were analyzed over a period of a year and placed in the following groups by common results. This data comprises Table 26 and is summarized below:

- 1st group	C 82 ± 2	atom %	AS
	O 11 ± 1	"	
	N 4.3 ± 0.3	"	
- 2nd group	C 85.7 ± 0.7	"	AS1, AS4 100%
	O 9.5 ± 1.0	"	
	N 4.0 ± 0.6	"	
- 3rd group	C 88 ± 1.0	"	AS4 120%, AS4 70%
	O 7 ± 1.0	"	
	N 3.4 ± 1.0	"	

The main difference between the groups is the amount of oxygen on their surfaces. Peak shapes and positions are all very similar, except that the C_{1s} spectra of the 3rd group show less carboxyl and ester type groups along with the reduction in oxygen content. This is indicated by decreased intensity of the component of the carbon peak found at ≈ 289.3 eV BE. C_{1s} FWHM are generally in the range 2.1 to 2.4 eV, while O_{1s} FWHM are about 3.1 to 3.4 eV.

F. AS + Cyclohexane

The fiber specimens were soaked in cyclohexane for several days at 70°C. No changes due to this cyclohexane exposure were found. This data and the data for the following three sections is contained in Table 27.

G. AS + Water

Fiber specimens were soaked in water at 70°C and 120°C for several days. Nitrogen and sulfur decreased significantly following exposure to water. This indicates that these impurities may largely be present as salts. Sodium decreased slightly and the O_{1s} peak occurred on the low BE side of the peak. This indicates that the O_{1s} peak seen is a composite of at least two

TABLE 26
SURFACE COMPOSITION OF AS FIBER SPECIMENS OBTAINED USING XPS

Specimen	Photoelectron Peak	Peak Area	Surface Concentration ^a (atomic percent)	Specimen	Photoelectron Peak	Peak Area	Surface Concentration ^a (atomic percent)
<u>Group 1</u> F001	C _{1s}	2.9×10^6	84	F009	C _{1s}	1.9×10^6	82
	O _{1s}	1.1×10^6	10		O _{1s}	8.1×10^5	11
	N _{1s}	2.5×10^5	4.0		N _{1s}	2.0×10^5	4.5
	S _{2p}	--	0.5		S _{2p}	4.1×10^4	1.0
	Na _{KLL}	--	2.0		Na _{KLL}	--	2.0
F007	C _{1s}	2.3×10^6	84	F010	C _{1s}	1.7×10^6	82
	O _{1s}	8.8×10^5	10		O _{1s}	7.2×10^5	11
	N _{1s}	2.3×10^5	4.5		N _{1s}	1.7×10^5	4.5
	S _{2p}	--	0.5		S _{2p}	3.5×10^4	1.0
	Na _{KLL}	--	2.0		Na _{KLL}	--	2.0
F008	C _{1s}	1.8×10^6	80				
	O _{1s}	9.1×10^5	12				
	N _{1s}	1.9×10^5	4.5				
	S _{2p}	--	1.0				
	Na _{KLL}	--	2.0				

TABLE 26
SURFACE COMPOSITION OF AS FIBER SPECIMENS OBTAINED USING XPS
(Concluded)

Specimen	Photoelectron Peak	Peak Area	Surface Concentration ^a (atomic percent)	Specimen	Photoelectron Peak	Peak Area	Surface Concentration (atomic percent)
<u>Group 2</u> F002 (AS-1)	C _{1s}	3.0 x 10 ⁶	85	<u>Group 3</u> F035 (AS-4 120%)	C _{1s}	2.6 x 10 ⁶	84
	O _{1s}	1.1 x 10 ⁶	9.5		O _{1s}	8.9 x 10 ⁵	9.0
	N _{1s}	3.0 x 10 ⁵	4.5		N _{1s}	2.3 x 10 ⁵	4.0
	S _{2p}	3.2 x 10 ⁴	0.5		S _{2p}	3.3 x 10 ⁴	0.5
	Na _{KLL}	--	≤1.0		Na _{KLL}	1.2 x 10 ⁵	2.0
F003 (AS-1)	C _{1s}	2.6 x 10 ⁶	85	F036 (AS-4 120%)	C _{1s}	2.1 x 10 ⁶	89
	O _{1s}	9.9 x 10 ⁵	9.5		O _{1s}	5.2 x 10 ⁵	6.5
	N _{1s}	2.8 x 10 ⁵	4.5		N _{1s}	1.5 x 10 ⁵	3.5
	S _{2p}	3.2 x 10 ⁴	0.5		S _{2p}	3.0 x 10 ³	<0.2
	Na _{KLL}	--	≤1.0		Na _{KLL}	4.1 x 10 ⁴	<1.0
F004 (AS-4 100%)	C _{1s}	2.1 x 10 ⁶	86	F037 (AS-4 70%)	C _{1s}	6.5 x 10 ⁶	88
	O _{1s}	6.9 x 10 ⁵	9.0		O _{1s}	1.9 x 10 ⁶	7.5
	N _{1s}	2.1 x 10 ⁵	4.5		N _{1s}	4.5 x 10 ⁵	3.0
	S _{2p}	1.1 x 10 ⁴	<0.5		S _{2p}	9.7 x 10 ³	<0.2
	Na _{KLL}	--	≤1.0		Na _{KLL}	1.3 x 10 ⁵	1.0
F024 (AS-4 100%)	C _{1s}	2.8 x 10 ⁶	85	F038 (AS-4 70%)	C _{1s}	3.7 x 10 ⁶	89
	O _{1s}	1.1 x 10 ⁶	10		O _{1s}	1.0 x 10 ⁶	7.5
	N _{1s}	2.1 x 10 ⁵	3.5		N _{1s}	2.3 x 10 ⁵	3.0
	S _{2p}	1.4 x 10 ⁴	<0.5		S _{2p}	6.8 x 10 ³	<0.2
	Na _{KLL}	7.4 x 10 ⁴	1.0		Na _{KLL}	5.6 x 10 ⁴	0.5

^a S_{2p} and Na_{KLL} concentrations were calculated from peak heights on the wide scan where no peak areas are listed.

TABLE 27
SURFACE COMPOSITION OF AS FIBER SPECIMENS OBTAINED USING XPS

Specimen	Photoelectron Peak	Peak Area	Surface Concentration (atomic percent)	Specimen	Photoelectron Peak	Peak Area	Surface Concentration (atomic percent)
AS Fibers + Cyclohexane F021	C _{1s}	1.5 x 10 ⁶	78	AS + Water F044	C _{1s}	2.0 x 10 ⁶	83
	O _{1s}	7.0 x 10 ⁵	11		O _{1s}	8.5 x 10 ⁵	11
	N _{1s}	1.3 x 10 ⁵	3.5		N _{1s}	9.0 x 10 ⁴	2.0
	S _{2p}	1.7 x 10 ⁴	0.5		S _{2p}	7.2 x 10 ³	<0.2
	Na _{KLL}	2.2 x 10 ⁵	6.0		Na _{KLL}	2.1 x 10 ⁵	4.5
F027 (AS-4 120%)	C _{1s}	2.2 x 10 ⁶	85	F045	C _{1s}	2.9 x 10 ⁶	89
	O _{1s}	9.5 x 10 ⁵	11		O _{1s}	8.8 x 10 ⁵	8.5
	N _{1s}	1.7 x 10 ⁵	3.5		N _{1s}	7.3 x 10 ⁴	1.0
	S _{2p}	6.5 x 10 ³	<0.5		S _{2p}	9.4 x 10 ³	<0.2
	Na _{KLL}	4.3 x 10 ⁴	1.0		Na _{KLL}	6.4 x 10 ⁴	1.0
F028 (AS-4 70%)	C _{1s}	4.2 x 10 ⁵	89	F025 (AS-4 120%)	C _{1s}	3.1 x 10 ⁶	85
	O _{1s}	1.0 x 10 ⁵	6.5		O _{1s}	1.3 x 10 ⁶	11
	N _{1s}	2.7 x 10 ⁴	3.0		N _{1s}	2.0 x 10 ⁵	3.0
	S _{2p}	2.2 x 10 ³	<0.5		S _{2p}	1.6 x 10 ⁴	<0.5
	Na _{KLL}	9.4 x 10 ³	1.0		Na _{KLL}	7.3 x 10 ⁴	1.0
AS + Water F022	C _{1s}	2.9 x 10 ⁶	86	F029 (AS-4 70%)	C _{1s}	1.6 x 10 ⁶	87
	O _{1s}	1.1 x 10 ⁶	10		O _{1s}	6.0 x 10 ⁵	10
	N _{1s}	1.7 x 10 ⁵	2.5		N _{1s}	1.0 x 10 ⁵	3.0
	S _{2p}	5.5 x 10 ³	<0.5		S _{2p}	8.3 x 10 ³	<0.5
	Na _{KLL}	7.1 x 10 ⁴	1.0		Na _{KLL}	1.6 x 10 ⁴	0.5

TABLE 27
SURFACE COMPOSITION OF AS FIBER SPECIMENS OBTAINED USING XPS
(Concluded)

Specimen	Photoelectron Peak	Peak Area	Surface Concentration (atomic percent)	Specimen	Photoelectron Peak	Peak Area	Surface Concentration (atomic percent)
<u>AS + H₂</u> F014	C _{1s}	3.2 x 10 ⁶	79	<u>AS + epoxy</u> F048 (AS-1)	C _{1s}	1.8 x 10 ⁶	83
	O _{1s}	1.9 x 10 ⁶	14		O _{1s}	9.8 x 10 ⁵	13
	N _{1s}	2.3 x 10 ⁵	3.0		N _{1s}	1.3 x 10 ⁵	3.0
	S _{2p}	4.4 x 10 ⁴	0.5		S _{2p}	4.1 x 10 ³	<0.2
	Na _{KLL}	3.1 x 10 ⁵	4.0		Na _{KLL}	4.0 x 10 ⁴	1.0
F015	C _{1s}	3.3 x 10 ⁶	76	F049 (AS-1)	C _{1s}	2.6 x 10 ⁶	82
	O _{1s}	2.4 x 10 ⁶	16		O _{1s}	1.4 x 10 ⁶	13
	N _{1s}	2.8 x 10 ⁵	3.5		N _{1s}	1.8 x 10 ⁵	3.0
	S _{2p}	7.0 x 10 ⁴	1.0		S _{2p}	5.3 x 10 ³	<0.2
	Na _{KLL}	3.6 x 10 ⁵	4.0		Na _{KLL}	5.8 x 10 ⁴	1.0
F019	C _{1s}	3.4 x 10 ⁶	91	F046 (AS-4)	C _{1s}	2.4 x 10 ⁶	83
	O _{1s}	3.8 x 10 ⁵	3.0		O _{1s}	1.3 x 10 ⁶	13
	N _{1s}	1.8 x 10 ⁵	2.5		N _{1s}	1.3 x 10 ⁵	2.5
	S _{2p}	2.5 x 10 ⁴	0.5		S _{2p}	6.3 x 10 ³	<0.2
	Na _{KLL}	2.0 x 10 ⁵	2.5		Na _{KLL}	6.0 x 10 ⁴	1.0
F020	C _{1s}	3.5 x 10 ⁶	92	F047 (AS-4)	C _{1s}	2.1 x 10 ⁶	83
	O _{1s}	3.7 x 10 ⁵	3.0		O _{1s}	1.1 x 10 ⁶	13
	N _{1s}	1.8 x 10 ⁵	2.5		N _{1s}	1.2 x 10 ⁵	2.5
	S _{2p}	3.0 x 10 ⁴	0.5		S _{2p}	4.2 x 10 ³	<0.2
	Na _{KLL}	2.1 x 10 ⁵	2.5		Na _{KLL}	4.3 x 10 ⁴	1.0

F/G 11/4

DAYTON UNIV OH RESEARCH INST
IMPROVED MATERIALS FOR COMPOSITES AND ADHESIVES. (U)

DEC 81 D ASKINS, A BEHME, A BIERMANN, W CLICK F33615-78-C-5102

UNCLASSIFIED

UDR-TR-81-108

AFWAL-TR-81-4154

NIL

204

peaks, the component on the low BE side being attributable to carbonyl-type oxygen (C=O).

H. AS + Hydrogen

These specimens were outgassed at 600°C in a vacuum system typically operating at 1×10^{-8} Torr (1.3×10^{-6} Pa). After being cooled overnight to room temperature, they were heated to 750°C in the presence of hydrogen gas, the amount equivalent to two monolayers coverage. After one hour the hydrogen was pumped out and the sample cooled. The samples were stored in a desiccator filled with argon gas. Much less oxygen and a slightly reduced amount of nitrogen were found on the surface of these fibers. C_{1s} peaks are still broader than the HM fibers, indicating the presence of carbon groups singly-bonded to oxygen (FWHM 2.1 to 2.2 eV). The oxygen peak is similar to that of the HM fibers. The N_{1s} and S_{2p} peaks are doublets on this surface, indicating that amine groups and elemental sulfur are present in addition to the oxidized forms of both elements.

I. AS + Epoxy (2,2-diphenylpropane-p,p'-diglycidyl ether)

These samples were prepared by soaking the fibers in a one percent solution of this epoxy in methyl ethyl ketone. The C_{1s} peaks for these specimens are, like the PVA-coated specimens, much broader than the C_{1s} peaks of the AS fibers in the "as received" condition (2.8 to 3.0 eV FWHM vs. 2.1 to 2.4 eV). This is mainly due to the large component of the peak at 286.3 eV BE, which is due to carbon singly-bound to oxygen. There is also some intensity at 289.3 eV BE which could be from the underlying AS fiber. The fiber does not, therefore, seem to be as completely covered as it was with the PVA. The amount of nitrogen seen, 2.5 to 3.0 atom percent, is less than the AS "as received" fibers (3.0 to 4.5 percent). This further indicates incomplete coverage of the fiber surface by the epoxy. This may be due to the method of sample preparations or due to an intrinsic difference between the two systems.

The O_{1s} peaks are narrower than on the AS fiber "as received" (2.6 to 2.7 eV FWHM vs. 3.1 to 3.4 eV) and in the same position as the O_{1s} peaks on the PVA-exposed specimens. This indicates that most of the oxygen is singly-bound to carbon which agrees with the C_{1s} data.

SECTION III ADHESIVES

1. EXPERIMENTAL ADHESIVES

A. BATQH/ATP - An Acetylene-Terminated Sulfone with Reactive Plasticizer

Tensile dogbone and beam specimens were molded of BATQH blended with 30 percent acetylene-terminated reactive plasticizer (ATP) by weight. ATP is of very low molecular weight and, when it is added to a compatible high molecular weight oligomer such as BATQH, it should increase the mobility of the material and decrease the melt point temperature. The viscosity of the BATQH was reduced to a point that it could readily be used as a composite matrix material, or to wet out carrier cloth for adhesive applications.

The BATQH/ATP (30 percent) dogbones were tested in tensile at room temperature and elevated temperatures before and after humid aging to moisture equilibrium. Humid aging was done at 200°F (93.3°C). Data is reported in Table 28.

B. BADABA - An Acetylene-Terminated Quinoxaline

BADABA dogbone tensile and beam specimens were molded from neat oligomer synthesized and purified in the laboratory. In addition, formulations of BADABA + one percent cure initiator were molded into dogbone tensile specimens. Data on those specimens have been reported previously. Since that time another batch of BADABA was synthesized by Midwest Research Institute (MRI), and many attempts were made to process that material without much success. Processing problems were caused by solvent retained in the oligomer that were probably introduced during synthesis. Removal of the solvent by vacuum at various temperatures was tried, and later the material was precipitated from a dilute solution in order to purify it. Bubbles caused by volatiles were persistent, so the oligomer was again dissolved and then freeze-dried. The freeze-dried BADABA seemed to process more readily.

TABLE 28
TENSILE TESTING
BATOH/ATP

Specimen Number	Condition of Test	Ult. Strength (psi)	ΔL_f	Ult. Strength MPa	Modulus of Elast. (10 psi) M	MPa
1	R.T. Dry	8,822	.046	62	190,528	1,264
2	" "	7,162	.052		176,187	
3	300°F Dry	9,634	.087	65.7	110,735	827
4	" "	9,432	.073		127,214	
5	400°F Dry	6,993	.070	47.7	99,902	708.1
6	" "	6,857	.065		105,493	
7	450°F Dry	5,223	.093	35.8	56,165	416.5
8	" "	5,173	.080		64,661	
9	500°F Dry	2,574	.049	21.6	52,528	304
10	" "	3,707	.104		35,644	
11	R.T. Wet	10,186	.057	61.8	178,711	1,506
12	" "	7,743	.03		258,096	
13	300°F Wet	8,779	.058	55.1	151,361	1,019
14	" "	7,214	.05		144,276	
15	400°F Wet	5,585	.043	39.3	129,879	811.6
16	" "	5,804	.055		105,533	
17	450°F Wet	4,914	.049	35	100,278	596.6
18	" "	5,240	.072		72,779	
19	500°F Wet	2,575	.07	18.5	36,790	323.5
20	" "	2,796	.049		57,059	

Due to the amount of time and effort required to freeze-dry the oligomer, the previously precipitated material was again dried at 106°C for three days in an attempt to clean it up. Initial results indicate that a sufficient amount of the volatiles was removed to process dogbones, although it is still uncertain whether beams can be molded from that material.

C. Acetylene-Terminated Sulfone (ATS)

Several formulations of ATS were processed. The spectrum ran from pure monomer to monomer plus dimer and trimer. The monomer to oligomer ratio changed in some formulations, and also cure initiator was added to ATS monomer in order to reduce the cure temperature requirement. It is desirable to accomplish complete cure of the ATS at 350°F (176°C) or lower so that it may be used as an adhesive for aluminum structures. Temperatures in excess of 350°F (176°C) would adversely affect the heat treatment properties of the structural aluminum alloys.

All ATS monomer tensile dogbones were fabricated by casting in silicone rubber (G.E. RTV 664) molds including the cure initiated ATS monomer. Tensile data dry and after humid aging at 200°F, 95% RH to moisture equilibrium are reported in Tables 29 and 30 for formulations XIII-18-A and XIII-20. Dry data for ATS monomer, initiated and uninitiated with a 350°F (176°C) final cure temperature are reported in Tables 31 and 32. Formulation XIII-35 and XIII-36 are uninitiated monomer and XIII-37 is initiated.

An ATS material manufactured by Gulf which was 73% monomer and 27% by weight higher molecular weight oligomers (predominantly dimer and trimer) was cast in silicone rubber molds to dogbone and beam configurations.

Several cure cycles were done on the Gulf ATS to determine which would be the most satisfactory and, in addition, to determine the effects of the temperature/time/atmosphere relationship on the mechanical behavior of the material. Four cure cycles were used: (a) 16 hrs @ 350°F (177°C) in air; (b) 16 hrs @ 350°F (177°C) in N₂; (c) 16 hrs @ 300°F (149°C) in N₂; and (d) 24 hrs @ 212°F (100°C) and 1 hr @ 392°F (200°C) in N₂.

TABLE 29
TENSILE TESTING
ATS DOGBONES XIII 18-A

Specimen Number	Condition of Test	Ult. Strength (psi)	ΔL_f	Ult. Strength MPa	Modulus of Elast. (10 psi) M	MPa
18A-1	R.T. Dry	4,203	.022		191,037	
18A-2	" "	6,586	.044	33.3	149,695	1,210
18A-3	" "	3,715	.020		185,749	
18A-4	300°F	4,086	.027	35.2	151,339	1,125
18A-5	"	6,120	.035		174,850	
18A-6	450°F	4,544	.038	35.4	119,593	907
18A-7	"	5,726	.05		114,514	
18A-8	500°F	4,679	.049	32.3	95,498	743
18A-9	"	4,690	.039		120,266	
18A-10	600°F	1,733	.031	14.2	55,915	354
18A-11	"	2,387	.051		46,812	
18A-12	R.T. Wet	4,781	.018	34.4	265,617	1,812
18A-13	"	5,198	.02		259,881	
18A-14	300°F Wet	4,947	.023	26.6	215,088	1,424
18A-15	"	2,773	.014		198,059	
18A-16	450°F Wet	4,580	.031	27.3	147,737	1,010
18A-17	"	3,341	.023		145,256	
18A-18	500°F Wet	4,616	.045	30.3	102,590	732
18A-19	"	4,171	.038		109,766	
18A-20	600°F Wet	2,238	.048	15.4	46,626	321.5

TABLE 30
TENSILE TESTING
ATS DOGBONES XIII-20 WITH INITIATOR ADDED

Specimen Number	Condition of Test	Ult. Strength (psi)	ΔL_f	Ult. Strength MPa	Modulus of Elast. (psi) M	MPa
XIII-20-1	R.T.	6,583	.041		160,561	
XIII-20-2	"	6,600	.042	45	157,143	1,204
XIII-20-3	"	6,386	.031		206,000	
XIII-20-4	300°F	4,212	.03		140,400	
XIII-20-5	"	4,020	.025	28.4	160,800	1,038
XIII-20-6	450°F	2,934	.022		133,380	
XIII-20-7	"	3,207	.027	21.2	118,763	869
XIII-20-8	500°F	2,600	.03		86,668	
XIII-20-9	"	2,858	.028	18.9	102,878	653
XIII-20-10	600°F	604	.046		13,127	
XIII-20-11	"	632	.046	4.3	13,748	92.6
XIII-20-12	300°F Wet	2,883	.016	19.9	180,180	1,242
XIII-20-13	500°F Wet	NOT LOADED-----				
XIII-20-14	R.T. Wet	4,112	.015	24.6	274,131	1,890
XIII-20-15	"	3,022	.014		215,848	

TABLE 31
TENSILE TESTING
ATS DOGBONES XIII-35 AND XIII-36

Specimen Number	Condition of Test	Ultimate Strength (psi)	ΔL_f	Ultimate Strength (MPa)	Modulus of Elast. (psi)	Modulus of Elast. (MPa)
35-1	RT	4667	.018	32.15	259,259	1786
35-2	RT	5121	.018	35.28	284,507	1960
35-3	200°F	1976	.008	13.6	247,025	1702
35-4	200°F	1758	.008	12.1	219,780	1514
35-5	300°F	3503	.015	24.1	233,567	1609
35-6	300°F	4000	.022	27.6	181,818	1253
35-7	350°F	5378	.032	37.1	168,080	1158
35-8	350°F	6948	.033	47.9	210,563	1451
*36-1	RT	3922	.018	27.0		
*36-2	RT	4665	.018	32.1		

*Specimens were high pressure molded rather than cast in silicone rubber molds.

TABLE 32
TENSILE TESTING
ATS DOGBONES XIII-37 (CURE INITIATED)

Specimen Number	Condition of Test	Ultimate Strength (psi)	ΔL_f	Ultimate Strength (MPa)	Modulus of Elast. (psi)	Modulus of Elast. (MPa)
37-1	RT	6344	.024	43.7	264,346	1821
37-2	RT	5580	.020	38.4	279,014	1922
37-3	200°F	4904	.019	33.8	258,116	1779
37-4	200°F	6375	.025	43.9	254,986	1757
37-5	300°F	5530	.028	38.0	197,498	1361
37-6	300°F	5304	.026	36.5	203,995	1406
37-7	350°F	5680	.044	39.1	129,081	889
37-8	350°F	5801	.045	40.0	128,913	888

Data from dogbone tensile testing is reported in Tables 33, 34, 35, and 36.

In addition to dogbone moldings, 1/2" (12.7 mm) x 2" (50.8 mm) x .1" (2.54 mm) beam specimens were cast in silicone rubber molds and machined into compact tension (CT) specimens for fracture spectra determination.

D. HR600 and MC600 - An Acetylene-Terminated Polyimide

HR600 (Hughes) and MC600 (Gulf) are identical materials synthesized by the two different manufacturers. The material is 100 percent solids and was purified in the laboratory.

This polymer was chosen for study because it is in the acetylene-terminated (AT) family and is available in relatively large quantities; in addition, it is commercially produced.

Considerable tensile, rheometric and kinetic data have previously been produced in the laboratory and are available for baseline information.

A program to determine effects of time, temperature, atmosphere and strain rate on the cure on the polymer was done.

Tensile dogbones and beam specimens were molded from HR600 and cured at five conditions. Those conditions were: (1) 290°C, 40 hrs, air; (2) 340°C, 40 hrs, air; (3) 372°C, 3.5 hrs, air; (4) 372°C, 1 hr, N₂; and (5) 372°C, 40 hrs, N₂.

Tensile dogbone data is reported in Tables 37 to 41.

The molded HR600 beams were machined into CT specimens and tested at the same temperatures and strain rates as the tensile dogbones after each set had been cured along with the representative dogbones.

Fracture data was obtained from the CT specimens and is reported elsewhere.

E. Epoxy Model Material

Compact tension specimens were machined from resin castings of E828/Versamid 140 and Narmco 5208 resins and were

TABLE 33
TENSILE TESTING
ATS (GULF) DOGBONES
CURED AT 350°F (176°C) FOR 16 HRS IN AIR

Specimen Number	Condition of Test	Ultimate Strength (psi)	ΔL_f	Ultimate Strength (MPa)	Modulus of Elast. (psi)	Modulus of Elast. (MPa)
1	RT	7668	.037	52.8	210,082	1447
2	RT	9072	.041	62.5	221,266	1525
3	200°F	6704	.029	46.2	231,189	1593
4	200°F	5978	.025	41.2	239,130	1648
5	300°F	7504	.039	51.7	192,415	1326
6	300°F	7058	.036	46.6	196,065	1351
7	350°F	6679	.040	46.0	166,970	1150
8	350°F	7217	.049	49.7	147,290	1015

TABLE 34
TENSILE TESTING
ATS (GULF) DOGBONES
CURED AT 350°F (176°C) FOR 16 HRS IN N₂

Specimen Number	Condition of Test	Ultimate Strength (psi)	ΔL_f	Ultimate Strength (MPa)	Modulus of Elast. (psi)	Modulus of Elast. (MPa)
1	RT	7981	.032	55.0	249,401	1718
2	RT	6675	.024	46.0	278,103	1916
3	200°F	4848	.020	33.4	242,424	1617
4	200°F	6780	.024	46.7	282,499	1946
5	300°F	6497	.034	44.8	191,078	1317
6	300°F	7494	.039	51.6	192,158	1324
7	350°F	5352	.028	36.9	191,145	1317
8	350°F	5080	.030	35.0	169,331	1167

TABLE 35
TENSILE TESTING
ATS (GULF) DOGBONES
CURED AT 300°F (149°C) FOR 16 HRS IN N₂

Specimen Number	Condition of Test	Ultimate Strength (psi)	ΔL_f	Ultimate Strength (MPa)	Modulus of Elast. (psi)	Modulus of Elast. (MPa)
1	RT	6021	.022	41.5	273,676	1886
2	RT	5523	.020	38.0	276,151	1903
3	200°F	3517	.015	24.2	234,476	1616
4	200°F	4675	.024	32.2	194,798	1342
5	300°F	5221	.029	35.9	180,044	1241
6	300°F	5181	.024	35.7	215,880	1487
7	350°F	4837	.032	33.3	151,159	1041
8	350°F	4546	.039	31.3	156,756	1080

TABLE 36
TENSILE TESTING
ATS (GULF) DOGBONES
CURED AT 100°C FOR 24 HRS IN N₂, 200°C FOR 1 HR IN N₂

Specimen Number	Condition of Test	Ultimate Strength (psi)	ΔL_f	Ultimate Strength (MPa)	Modulus of Elasticity (psi)	Modulus of Elasticity (MPa)
1	RT	6011	.024	41.4	250,455	1726
2	RT	4493	.018	31.0	249,612	1720
3	200°F	5914	.026	40.7	227,448	1567
4	200°F	3508	.015	24.2	233,869	1611
5	300°F	4875	.025	33.6	195,005	1344
6	300°F	3198	.017	22.0	188,102	1296
7	350°F	6324	.040	43.6	158,099	1089
8	350°F	4533	.030	31.2	133,338	918.7

TABLE 37

TH-600

CURE #1 290°C - 40 HRS IN AIR

TEST: TENSILE DOGBONE

Spec. No.	Test Temp. (°C)	Load Rate (in/min)	Max. Load (lbs.)	Ultimate Strength (psi.)	Elong. (%)	Mod. Elast.-3 (psi)x10 ⁻³
1-1	RT	.02	75.2	14,484	6.2	233.6
1-2	RT	.02	40.8	7,436	2.7	275.4
1-3	200	.02	40.2	8,775	8.7	100.9
1-4	200	.02	42.9	7,235	4.8	150.7
1-5	250	.02	27.7	4,890	15.9	30.76
1-6	250	.02	26.7	4,503	10.6	42.5
1-7	250	.002	24.3	4,224	15.5	27.3
1-8	250	.002	25.6	4,545	17.6	25.8
1-9	290	.02	8.0	1,614	14.5	11.1
1-10	290	.02	7.4	1,274	13.6	9.4
1-11	290	.002	8.8	1,563	19.0	8.2
1-12	290	.002	6.0	1,065	12.4	8.6

TABLE 38

TH-600

CURE #2 340°C - 40 HRS IN AIR

TEST: TENSILE DOGBONE

Spec. No.	Test Temp. (°C)	Load Rate (in/min)	Max. Load (lbs.)	Ultimate Strength (psi.)	Elong. (%)	Mod. Elast.-3 (psi)x10
2-1	RT	.02	42.3	7,109	2.9	245.1
2-2	RT	.02	50.6	7,566	3.3	229.3
2-3	200	.02	34.9	7,344	4.3	170.8
2-4	200	.02	31.4	6,152	3.3	186.4
2-5	250	.02	15.3	2,690	1.8	149.5
2-6	250	.02	20.3	3,625	2.6	139.4
2-7	250	.002	25.3	4,252	4.2	101.2
2-8	250	.002	18.7	3,504	3.3	106.2
2-9	300	.02	9.7	1,584	3.0	52.8
2-10	300	.02	5.7	1,017	2.0	50.9
2-11	300	.002	8.3	1,317	3.3	39.9
2-12	300	.002	4.3	883	2.0	44.2

TABLE 39
TH-600
CURE #3 372°C - 3.5 HRS IN AIR
TEST: TENSILE DOGBONE

Spec. No.	Test Temp. (°C)	Load Rate (in/min)	Max. Load (lbs.)	Ultimate Strength (psi.)	Elong. (%)	Mod. Elast. -3 (psi)x10 ⁻³
3-1	RT	.002	61.1	12,860	4.9	263.5
3-2	RT	.002	73.3	13,015	6.1	213.4
3-3	200	.02	46.1	7,484	6.0	124.7
3-4	200	.02	40.0	7,331	5.3	138.3
3-5	250	.002	25.7	4,450	6.0	74.2
3-6	250	.002	22.4	3,939	4.6	85.6
3-7	250	.02	28.8	4,987	5.5	90.7
3-8	250	.02	24.6	4,535	4.4	103.1
3-9	300	.002	7.1	1,193	6.5	18.4
3-10	300	.002	6.3	1,155	5.5	21.0
3-11	300	.02	6.2	1,356	5.8	23.4
3-12	300	.02	6.4	1,254	3.6	34.8

TABLE 40

TH-600

CURE #4 372°C - 1 HR IN N₂

TEST: TENSILE DOGBONE

Spec. No.	Test Temp. (°C)	Load Rate (in/min)	Max. Load (lbs.)	Ultimate Strength (psi.)	Elong. (%)	Mod. Elast.-3 (psi)x10 ⁻³
4-1	RT	.002	116.6	18,351.	10.0	183.5
4-2	RT	.002	103.4	17,230	9.7	177.6
4-3	200	.02	37.6	7,121	7.3	97.6
4-4	200	.02	41.8	7,917	10.5	75.4
4-5	250	.002	18.8	3,231	14.3	22.6
4-6	250	.002	18.7	3,211	17.2	18.7
4-7	250	.02	18.9	3,206	11.7	27.4
4-8	250	.02	21.1	3,736	14.7	25.4
4-9	300	.002	4.1	799	13.3	6.0
4-10	300	.002	3.4	493	10.4	4.7
4-11	300	.02	4.6	788	11.1	7.1
4-12	300	.02	4.9	868	12.1	7.2

TABLE 41

TH-600

CURE #5 372°C - 40 HRS IN N₂

TEST: TENSILE DOGBONE

Spec. No.	Test Temp. (°C)	Load Rate (in/min)	Max. Load (lbs.)	Ultimate Strength (psi.)	Elong. (%)	Mod. Elast.-3 (psi)x10 ⁻³
5-1	RT	.02	50.2	7,506	3.0	250.2
5-2	RT	.02	89.4	13,444	6.4	210.1
5-3	200	.02	39.5	7,281	4.5	161.8
5-4	200	.02	47.0	8,092	5.6	144.5
5-5	250	.002	27.2	5,329	6.5	82.0
5-6	250	.002	35.6	5,812	7.2	80.7
5-7	250	.02	32.3	6,152	6.6	93.2
5-8	250	.02	24.8	4,724	3.8	124.3
5-9	300	.002	20.2	3,038	8.1	37.5
5-10	300	.002	9.2	1,658	3.8	43.6
5-11	300	.02	17.8	2,890	5.4	53.5
5-12	300	.02	16.0	3,030	6.2	48.9

used for model CT specimens for developing fracture evaluation parameters and techniques that will be employed on other materials.

Specimens were machined in various sizes [$1/2$ " x $1/2$ " (12.7 mm x 12.7 mm), 1" x 1" (25.4 mm x 25.4 mm), 2" x 2" (50.8 mm x 50.8 mm)] and thicknesses [0.1" (2.54 mm), 0.2" (5.08 mm) and 0.5" (12.7 mm)] in order to determine the most suitable configuration for maximum data per sample. Many materials that will be evaluated will be restricted to the smaller volume specimens because of limited material available.

F. Equipment

A small volume isothermal aging oven was designed and fabricated in the laboratory. The oven has very accurate temperature control and has the capability to have air and other selected gases introduced into the heat chamber. The oven is used for short and long-term aging, heats of reaction of polymers, and determination of cure extent.

Silicone rubber molds for resin casting have been made, and the mold masters were designed in the laboratory and machined in an outside machine shop.

A Buehler Isomet precision saw was modified in the laboratory to accommodate accurate machining of CT specimens. Drill guides were also designed to drill precision holes in CT specimens.

2. FABRICATION OF THERMID 600/TREATED GRAPHITE COMPOSITES

A request was received to fabricate composites with Thermid 600 resin and two treated spools of graphite fibers. The fibers were supplied by Ashland Chemical, and the panels were to be returned to them for evaluation. Two composites were fabricated from each spool and returned as requested.

3. NYLON FILAMENT WINDING

This project consisted of a feasibility study of filament winding with graphite fiber and nylon. The object was to develop techniques which would enable a Naval Ordnance Laboratory (NOL) ring to be filament wound with monomeric nylon as the starting matrix material.

A starting monomer mix composition by weight of 100 gms caprolactam, 0.054 gm sodium hydroxide (NaH) catalyst and 1.054 gms methylenediisocyanate (MDI) was melted together at 100-120°C and heated to 175°C. Although this was a stoichiometric ratio, it did not react and polymerize. This was felt to be due to absorption of moisture from the atmosphere. Additional NaH was added by hand in unmeasured quantities, and the mix eventually reacted and polymerized.

A second beaker experiment was conducted with four times the catalyst ratio (0.22 gms) used in the original experiment. This mix was melted at 110°C and remained very fluid for five minutes. It was then heated to about 135-140°C and, after only a few minutes, became quite thick and polymerized.

Several attempts were subsequently made to filament wind an NOL ring. Each attempt incorporated several changes in technique or winding set-up which were indicated by the previous attempt. A good quality NOL ring has not yet been achieved. Two principal problems appear to be responsible for this. The first is the extreme sensitivity of the resin ingredients to moisture. The second is the inability to achieve adequate monomer infiltration into the filament tow.

The ambient humidity during the period in which the winding attempts were made usually fell in the 50-60 percent RH range, with a few days falling as low as 40-45 percent RH. The only time the resin mix ever reacted was on the days with the very lowest humidity. Using predried starting materials, enough moisture was absorbed during melting and winding (a total of perhaps 30-45 minutes) that the catalyst (NaH) was severely compromised

converted to NaOH). It would appear that all activities should be conducted in a low humidity environment. Even using catalyst ratios as high as 0.44 gms/100 gms, caprolactam failed to overcome this problem on humid days. If a low humidity environment is inconvenient, the catalyst ratio will have to be increased substantially.

Although the monomer melt was very fluid and appeared to wet the fiber tow, all NOL rings, after heating to the polymerization temperature (175°C) for a short period (10-15 minutes), were very dry and resin starved, even those that did appear to polymerize on the days with low humidity. Since previous filament winding experience with epoxy resins having both lower and higher viscosities resulted in adequate resin pick-up and wet-out, the melt viscosity of the nylon is not the problem. What appears to be occurring is that as the room temperature fiber tow is drawn through the melt, the monomer is both coagulating on or near the tow surface and not penetrating throughout the fiber. The tow appears to be wet and to have picked up sufficient monomer, but one only observes the surface and this is apparently a misleading appearance. It would thus appear that the fiber will have to be preheated before passage through the monomer melt bath and kept warm until wound onto the mandrel.

Other steps which must be taken include the following.

- (1) All rollers over which the impregnated tow passes must be heated to prevent coagulation and monomer buildup with accompanying fiber fraying.
- (2) The mandrel must be kept warm to prevent coagulation.

Our efforts involved the use of heat lamps and hot air blowers to warm the rollers and mandrel during winding. We also shortened the fiber path as much as possible to prevent cooling and to gain fiber heating from the heat lamps and heat guns. This was insufficient to warm the fiber enough to permit thorough wetting, but it was satisfactory for the rollers and mandrel.

No further effort on this task can be performed due to a termination of funding. It is felt, however, that enough has been learned that the chances of winding a good NOL ring would be excellent with additional effort.

4. MOISTURE PICKUP OF M-16 MATERIALS

The objective of this investigation was to measure moisture absorption, impact, flexural, tensile, and compressive properties, heat distortion temperatures, and the weight gain after aging in nine different fluids and solvents of various different candidate plastic materials for use as M-16 stocks. A total of 12 different materials were tested for various properties during the program.

The humidity agings were conducted at 140°F and 95-100 percent relative humidity for up to 59 days. The fluid and solvent agings were conducted at room temperature for 13 days.

Tables 42 to 47 present the results obtained for each of the tests described above on the various materials.

5. MECHANICAL PROPERTIES OF FILLED AND UNFILLED EPOXIES

Tensile tests on epoxy adhesive material which had been "wet" aged for 12 months at 160°F (71°C) and 95-100 percent RH have been completed. The tensile tests were conducted at 200°F (93°C) on three different adhesive systems. The data from these tests are presented in Tables 48 and 49.

6. ANTIOXIDANTS FOR HIGH-TEMPERATURE POLYMERS

The objective of this investigation was to evaluate nontoxic compounds which might have the potential to act as an antioxidant in high-temperature polymers. Thermid 600 was the base polymer selected for the study. The experimental technique utilized to evaluate the candidate antioxidants was to blend the candidate materials with Thermid 600, mold buttons one inch in diameter by 1/8-inch thick, and then age the resulting samples in air at 600°F (316°C) for periods up to 1,000 hours. A total of six

TABLE 42
PERCENT MOISTURE PICKUP OF M-16 CANDIDATE MATERIALS

Material	Days at 140°F & 95-100% R.H.									
	3	7	14	21	28	35	42	49	59	
Fiberite 16801	1.32	2.13	3.13	3.79	4.22	4.19	4.48	4.66	4.71	
Dupont	3.10	3.69	4.05	4.21	4.28	4.36	4.38	4.38	4.43	
Premix	0.52	0.71	0.97	1.21	1.44	1.64	1.87	2.00	2.20	
EXI	2.94	3.63	3.94	4.04	4.10	4.13	4.37	4.17	4.17	
Allied	5.25	5.92	5.64	5.45	5.41	5.31	5.20	5.28	5.23	
Allied XNP	5.25	5.93	5.91	5.48	5.35	5.30	5.32	5.17	5.15	
Lytex 6093	0.42	0.60	0.83	0.94	1.06	1.14	1.21	1.28	1.39	

TABLE 43
PERCENT WEIGHT PICKUP OF M-16
CANDIDATE MATERIALS AFTER 13 DAYS IN
VARIOUS FLUIDS AND SOLVENTS

Candidate Material	Aging Fluid								JP-4
	10W40 Oil	Trichloro-ethane	Chloroform	Toluol	Ethylene Glycol	Acetone	5606	Brake Fluid	
Allied	-0.21	-0.42	1.05	-0.41	0.06	-0.49	-0.27	-0.66	-0.04
Allied XNP	-0.23	-0.45	0.98	-0.40	0.02	-0.55	-0.28	-0.65	-0.39
Premix	0.13	0.40	14.97	1.10	-0.08	6.83	0.25	0.10	0.11
EXI	-0.09	9.62	2.98	0.46	-0.05	-0.13	-0.09	-0.32	-0.05
Lytex 6093	0.25	-0.02	2.53	-0.02	-0.13	1.03	0.01	0.03	0.01
Dupont	-0.07	-0.02	3.35	0.23	-0.03	-0.04	-0.09	-0.47	-0.13
I-9968	0.17	0.86	18.91	1.31	0.25	6.65	0.23	0.38	0.28
I-9873	-0.97	7.07	7.40	5.37	-8.79	-2.81	0.71	3.09	1.26
Fiberite 16801	1.00	1.35	1.57	0.79	-0.84	0.99	1.24	0.37	0.99

TABLE 44
TENSILE PROPERTIES OF M-16 CANDIDATE MATERIALS

Material Designation	Room Temperature		250°F	
	Ult. Strength (10 ³ psi)	Modulus (10 ⁶ psi)	Ult. Strength (10 ³ psi)	Modulus (10 ⁶ psi)
L-9968	7.9	0.9	--	--
8130-E	9.2	1.8	--	--
L9873	5.2	1.0	--	--
D-514-E47	41.0	2.9	33.4	2.3
SL-702-50-E6	19.2	1.5	11.5	1.1

TABLE 45
COMPRESSIVE PROPERTIES OF M-16 CANDIDATE MATERIALS

Material Designation	Room Temperature		250°F	
	Ult. Strength (10 ³ psi)	Modulus (10 ⁶ psi)	Ult. Strength (10 ³ psi)	Modulus (10 ⁶ psi)
L-9968	10.8	2.4	4.0	0.9
8130-E	24.0	4.1	15.6	1.2
L9873	6.7	0.7	2.3	0.4
D-514-E47	10.4	2.7	6.6	2.6
SL-702-50-E6	17.4	2.0	3.5	1.5

TABLE 46
FLEXURE PROPERTIES OF M-16 CANDIDATE MATERIALS

Material Designation	Room Temperature		250°F	
	Ult. Strength (10 ³ psi)	Modulus (10 ⁶ psi)	Ult. Strength (10 ³ psi)	Modulus (10 ⁶ psi)
L-9968	21.5	1.1	7.4	0.6
8130-E	16.9	1.9	22.8	2.0
L9873	8.0	0.7	5.3	0.5
D-514-E-47	66.7	2.9	32.4	2.1
SL-702-50-E6	33.7	1.8	15.2	1.2

TABLE 47
IMPACT STRENGTH OF M-16 CANDIDATE MATERIALS

Material Designation	Impact Strength, ft.lbs.
D-514-E47 (longitudinal)	6.80
D-514-E47 (transverse)	1.87
L-9968	1.65
L-9873	0.83
8130-E	1.13
SL-702-50-E6	3.48

Sonntag Universal Impact Machine Model S1-1P

TABLE 48
TENSILE PROPERTIES OF NEAT ADHESIVES AT 200°F (93°C)

Material	R-398	AF-143	AF-147
Ult. Tensile Strength(psi)	991 (90)	2320 (280)	1640 (70)
Initial Modulus(ksi)	227.8 (25.2)	140.5 (15.6)	76.6 (4.1)
Ultimate Strain (in/in)	0.010 (0.002)	0.025 (0.005)	0.080 (0.009)
Wt. Gain During Aging (%)	1.2 (0.4)	0.95 (0.10)	1.5 (0.6)

- NOTES: 1. Values in parentheses represent standard deviations. Values for R398, AF-143, and AF-147 represent averages of five, four, and three specimens, respectively.
2. All specimens aged 12 months at 160°F (71°C) and 95-100% R.H. prior to testing.

TABLE 49
SECANT MODULUS VALUES FOR ADHESIVES "WET" AGED FOR 12 MONTHS

Time (minutes)	0.25	0.50	0.75	1.00	1.25	1.50	2.00	2.50	3.00	4.00	5.00	6.00
Adhesive	Secant Modulus (10^5 psi)											
Reliabond 398	1.97	1.89	1.53	1.15	1.26							
AF143	1.48	1.41	1.37	1.29	1.28	1.19	1.07					
AF147	0.70	0.70		0.66	0.59	0.48	0.43	0.36	0.29	0.24	0.21	

- NOTES: 1. All specimens aged for 12 months at 160°F (71°C) and 95-100% R.H. before testing.
2. Tensile tests after aging were conducted at 200°F (93°C).
3. Data for R398, AF143, and AF147 represent average of five, four, and three specimens, respectively.

materials were tested. None of the candidates, when blended with the base Thermid 600, produced a reduction in the weight loss rate during thermal aging, as compared to the pure base Thermid 600 itself. Table 50 presents the results obtained. Four of the five candidates other than hydroquinone (HQ) were used in addition to HQ. The HQ was added as a cure inhibitor. The fifth candidate, hydroquinone mono-methyl ether (HQMME), acted as a cure inhibitor itself, so no additional HQ was added to this blend.

It can be seen from the data in Table 50, that HQ, while acting as a cure inhibitor and a valuable processing aid, decreases the oxidative stability of the Thermid MC-600 resin significantly. Three of the four candidate antioxidant materials tried in addition to the HQ produced greater weight losses than the Thermid-HQ blend alone. The fourth candidate, Groodrite 3125, produced a significantly lower weight loss rate than the Thermid-HQ blend alone. This material should be investigated further. A fifth candidate (HQMME) was used without the additional HQ and also produced weight losses only slightly higher than the pure Thermid material, while simultaneously acting as a cure inhibitor. This material should be further investigated also.

7. FORMULATION OF THERMID 600

The objective of this investigation was to develop a Thermid 600 resin formulation that could be used as a high-temperature matrix resin or adhesive, with good processing characteristics and good property levels. Initial efforts were with the LR-600 version of Thermid, which incorporates nadic methyl pyrrolidine (NMP). This solvent is very difficult to completely remove and can give rise to porosity in the cured products. Later activities utilized the alcohol version of Thermid (AL-600).

The best laminates were obtained by winding our own unidirectional graphite tapes onto a drum winder and B-staging the tape. This produced fiber bundles which were well wetted and tapes which had good resin pickup. Void-free laminates were produced which

TABLE 50
PERCENT WEIGHT LOSS OF THERMID MC-600 AND
CANDIDATE ANTIOXIDANTS AT 600°F (316°C)

Antioxidant	Specific Gravity	100 Hr. Aging (% Wt. Loss)	250 Hr. Aging (% Wt. Loss)	500 Hr. Aging (% Wt. Loss)	750 Hr. Aging (% Wt. Loss)	1000 Hr. Aging (% Wt. Loss)
Thermid MC-600 alone	1.35	1.6	2.4	3.0	4.4	5.5
	1.35	1.5	2.1	2.6	3.8	4.7
	1.35	1.4	2.1	2.8	3.9	4.9
10% Hydroquinone	1.32	4.9	7.0	9.7	10.3	13.6
	1.33	2.8	4.7	7.1	7.8	11.1
	1.30	2.9	4.6	7.3	8.1	11.3
3% Cyanox 1790 ¹	1.31	5.1	8.0	12.2	13.2	18.2
	1.35	4.8	7.6	10.8	11.9	16.2
	1.35	2.9	5.7	10.3	12.2	18.2
3% Antioxidant 330 ¹	1.30	3.9	6.0	9.8	11.3	16.0
3% AA-406 ¹	1.37	2.6	4.7	7.1	10.2	13.6
3% HQME ²	1.35	1.5	2.4	3.3	4.5	5.7
	1.35	1.5	2.3	3.1	4.3	5.3
	1.35	1.2	2.3	3.5	4.8	6.2
3% Goodrite 3125 ¹	1.37	2.6	3.8	5.0	6.8	8.4

¹Contains an additional 10% hydroquinone.

²Does not contain any additional hydroquinone.

exhibited very good mechanical properties. It was found that the laminates could be cured at temperatures as low as 450°F if the proper subsequent postcure times and temperatures were used. A study was undertaken to identify a better postcure schedule than the simple four hours at 650°F which was used for the adhesive bonds and tried initially on the laminates as well. Table 51 identifies the postcure schedules which were investigated and the flexural properties which resulted from each postcure. It is readily apparent that dramatic improvements in elevated temperature properties are achieved by going to longer postcures and/or higher postcure temperatures. Additional work on the effects of long-term exposure to elevated temperature is warranted.

The initial adhesive bonding work was performed on titanium adherends, but the expense and scarcity of this metal occasioned a switch to steel adherends. Adhesive bonds cured at 50 psi (344 KPa) and 450°F (232°C) and subsequently postcured for four hours at 650°F (343°C) gave room temperature properties only 14 percent less than those obtained with a 600°F (316°C) cure. The use of other postcures may have eliminated even this difference. Elevated temperature properties, where postcure effects were found most significant on the laminate properties, have not yet been tested for these adhesive bonds. Another study undertaken with the use of Thermid 600 as an adhesive involved an evaluation of the effect of carrier fabric surface treatment on strength retention after humidity aging. While heat cleaned 112 glass cloth was found to be a satisfactory carrier fabric, the results obtained after humidity aging of lap shear bonds were low, and the failure locus was along the glass-resin interface. A silane finish was consequently tried after consulting with Dow Corning. Table 52 presents the results. It can be seen that property retention after aging is considerably better with the silane finish than with the heat cleaned finish.

TABLE 51
EFFECT OF POSTCURE ON FLEXURAL PROPERTIES

Postcure	Test Temperature					
	72°F(22°C)		550°F(288°C)		600°F(316°C)	
	Ult.Str. (10 ³ psi)	Modulus (10 ⁶ psi)	Ult.Str. (10 ³ psi)	Modulus (10 ⁶ psi)	Ult.Str. (10 ³ psi)	Modulus (10 ⁶ psi)
4 hrs. @ 650°F (343°C)	202.5	14.4	64.4	6.8	---	---
	205.0	14.3	67.4	8.6	---	---
8 hrs. @ 700°F (371°C)	215.0	17.8	144.5	12.7	---	---
16 hrs. @ 650°F (343°C)	227.0	19.8	---	---	108.0	13.7
4 hrs. @ 650°F (343°C) + 4 hrs. @ 750°F (399°C)	251.0	25.6	---	---	114.0	14.4
4 hrs. @ 650°F (343°C) + 16 hrs. @ 750°F (399°C)	---	---	143.0	11.5	---	---

TABLE 52
EFFECT OF CARRIER GLASS FABRIC FINISH ON
ROOM TEMPERATURE LAP SHEAR STRENGTH OF THERMID
600 TITANIUM-TO-TITANIUM JOINTS

Specimen Aging Condition	Carrier Fabric Finish	Lap Shear Strength	
		(psi)	(MPa)
None	Heat-cleaned	3700	25.5
2 wks. @ 160°F (71°C) & 95% R.H.	Heat-cleaned	2050	14.1
None	Silane	3400	23.4
2 wks. @ 160°F (71°C) & 95% R.H.	Silane	2860	19.7

8. ADHESIVE BONDING

A. The Influence of Interfacial Copper on Anodic Oxide Growth by Phosphoric Acid Anodization of 2024-T3 Aluminum

(1) Introduction

The surface preparation of the adherend is an important step in the optimization of bond strength and durability. The primary structural materials which are candidates for adhesive bonding in modern aircraft are the aluminum alloys 2024-T3, 6061-T6, and 7075-T6. At present, the surface preparation of 2024-T3 for adhesive bonding receiving the highest attention in the aircraft industry is the so-called "Boeing Process", BAC 1544,⁽²⁶⁾ which involves a chemical deoxidation to remove original surface oxides followed by the growth of a new surface oxide by electrochemical anodization in phosphoric acid.⁽²⁷⁾

The importance of phosphoric acid anodization as a surface prebonding treatment is related to both the corrosion resistance provided by the anodic oxide films and its porous morphology. The corrosion resistance is attributed to the thin, dense underlying barrier layer which protects the reactive metal from corrosive agents; while the porous nature of the outer oxide layer provides excellent mechanical interlocking sites with the adhesive.

The anodic oxide growth mechanism for 2024-T3 is essentially the same as aluminum;^(28,29) however, the morphology of the oxide has been reported to differ from that of the pure metal in that it does not have the well-defined characteristic columnar structure or intermediate barrier layer.^(30,31) If alloying affects anodic oxide structure, the question arises as to oxide morphological influences on adhesive bond strength and durability.

Recent data reported by Schwartz⁽³²⁾ from bonded structures of chemically etched and phosphoric acid anodized 2024-T3 and 7075-T6 panels bonded with thermosetting epoxy

adhesives exposed to high humidity, elevated temperatures and salt spray was not very conclusive on the effect of the chemically etched versus anodized surface. The data showed that anodized panels provided greater bond line durability with 121°C cure adhesives, while chemically etched panels were slightly superior with 177°C cure adhesives.

A better test of the influence of anodic oxide morphology on adhesive bond performance would be one which compares the bond strength of structures fabricated with anodized alloy sheets versus anodized aluminum. Although no data was found comparing aluminum alloys to the pure metal, Hennemann did compare bond strength data from clad versus bare phosphoric acid anodized and chemically etched 2024-T3 and 7075-T6 bonded structures subjected to high humidity temperature environments as well as typical room environment.⁽³¹⁾ Since the clad alloy has a layer of aluminum covering the alloy surface, the anodization process would behave the same as that for the pure metal; and the resultant anodic oxide should have the same morphology as that formed on the pure metal. Hennemann showed that the clad specimens had higher shear strength under normal, as well as adverse, environments. This implies that the strength of the bond joint is related to the morphology of the anodic oxide. In all cases the anodized structures were superior in strength to the chemically etched structures.

The adoption of phosphoric acid anodization of 2024-T3 as a prebonding surface treatment by the aircraft industry was primarily based on empirical evaluations of bond joint performance. Consequently, the nature of the bonding forces at work and the role of individual components in the bond joint was of secondary concern. However, because the chemical and physical properties of the adherend surface are vital to strength and durability characteristics of adhesively bonded structures, their control and predictability throughout the prebonding treatments is extremely important. Also, if the performance of a bonded structure is to be improved or tailored to a particular set of operational requirements without extensive reliance on empiricism

it becomes necessary to be able to predict which material properties involved in the bond joint must be adjusted, modified, or changed.

In the case of 2024-T3 the importance of the morphology of the anodic oxide surface has been established for strong and durable adhesive bonding. The oxide structure is affected by anodization conditions and by the bulk properties of the material being anodized. Therefore, before attempts are made to adjust adhesive bond performance of 2024-T3 structures, it is essential to understand the mechanisms at work during anodization and the parameters which affect morphology. In addition, it is important to know the distribution of alloying and electrolyte material throughout the oxide layer and the oxide-metal interface since the presence of certain elements may influence bond joint performance. For example, as discussed above, the presence of copper in 2024-T3 makes the alloy highly vulnerable to environmental corrosive attack. During anodization of copper containing aluminum alloys, copper can migrate to the oxide-metal interface forming a copper-enriched layer.^(30,33-35) At the same time the presence of copper in the bulk reduces the anodization efficiency of copper containing aluminum alloys, which means a thinner anodic oxide layer.^(29,36) Since the anodic oxide offers limited corrosion resistance, the amount of protection is diminished with thinner films⁽³⁷⁾ and further reduced with the presence of copper at the oxide-metal interface.⁽³⁵⁾

(2) Experimental

Pieces of 2024-T3 aluminum were deoxidized in Oakite and anodized at constant potential conditions in room-temperature phosphoric acid. After anodization the specimens were rinsed with room-temperature distilled water and hot air dried. The elemental distribution within the anodic oxide was characterized by Rutherford backscattering (RBS) and Auger sputter profile analysis (ASPA). The thickness of the anodic oxides was determined from scanning electron microscope (SEM) micrographs and ASPA.

ASPA is a technique which couples AES with in-situ ion milling or sputtering. As the material on a surface is removed by ion sputtering, any change in elemental content of the freshly formed surface will be reflected in the Auger spectrum. The principal requirement for the ion gun is that it be capable of precise and stable ion sputter rates on the order of a few nanometers per minute. This is necessary in order to establish sputter rate versus depth calibration curves.

The ion gun used for sputter profiling in this work was a Physical Electronics Model 94-191 sputter ion gun operated with a beam energy of 2keV and an ion current density of approximately 3 uA/mm^2 in a partial pressure of argon of $6.6 \times 10^{-3} \text{ Pa}$.

Because this work involved both aluminum and copper, only Al_{KLL} and Cu_{LMM} (920eV) were used for profile construction since the low energy Cu_{MNN} (60eV) and Al_{LMM} (67eV) peaks partially overlap. Sputter rates were determined from sputter times to reach the oxide-metal interface (which was defined as the average of the times to reach the artifact minimum in the Al_{KLL}) and the mid-point of the negative slope of the oxygen profile between 84 percent and 16 percent levels. Oxide thickness of sputtering standards was obtained from SEM micrographs.

High energy backscattering (MeV), commonly referred to as Rutherford backscattering or RBS, provides a means of identifying different species of atoms in thin film specimens and the concentration of each as a function of depth in the film. Ion backscattering spectroscopy makes use of the energy loss suffered by the elastic collision of a probing light element ion with a heavier atom in a target material. The information provided by this technique primarily concerns atomic concentration and distribution but not chemical. When low energy ions (keV) are used, the technique is surface-sensitive⁽³⁸⁾ and is referred to as ion scattering spectroscopy.

In this work RBS was performed using a 2MeV $^4\text{He}^+$ ion beam produced with a Van de Graaff generator. The back-scattered ions were collected by a solid state detector at a

scattering angle of $\theta = 160^\circ$ measured against the forward direction of the incident beam. The energy resolution of the detector was such that the value for dE/dx (in keV/ug/cm) for $^4\text{He}^+$ ions was subject to an error of ± 5 percent, or a depth resolution of 20 nanometers.

(3) Results

(a) Scanning electron microscope

SEM micrographs typical of the oxides formed on pure aluminum and 2024-T3 by anodization in phosphoric acid are shown in Figures 33 and 34, respectively. The anodic film on the pure metal has a uniform, continuous layer between the metal substrate and a thicker characteristic porous layer having a columnar-like structure. The thickness of the anodic oxide film as measured directly from the micrograph in Figure 33 is approximately 900 nanometers.

The micrograph in Figure 34 shows the morphology of the anodic oxide on 2024-T3 aluminum to be different from that on the pure metal. First, it does not have the uniform well-defined columnar structure. Second, there is little or no evidence of an intermediate nonporous barrier layer.

(b) Auger sputter profile analysis

Oxide thickness. Because the morphology and density of an anodic oxide are very sensitive to a number of anodization parameters, the sputter rate for electrochemically-grown aluminum oxide may differ for various anodization conditions. Table 53 shows the variation in sputter rates for anodic oxides grown in different electrolytes. The values listed in Table 53 are subject to an error of ± 10 percent.

As shown in Table 53, the sputter rates differ considerably between oxides formed with different electrolytes. The rate for the oxide formed in phthalic acid, which has a nonporous uniform structure, is more like that previously reported for Al_2O_3 .^(39,40) The rates for the porous oxides formed

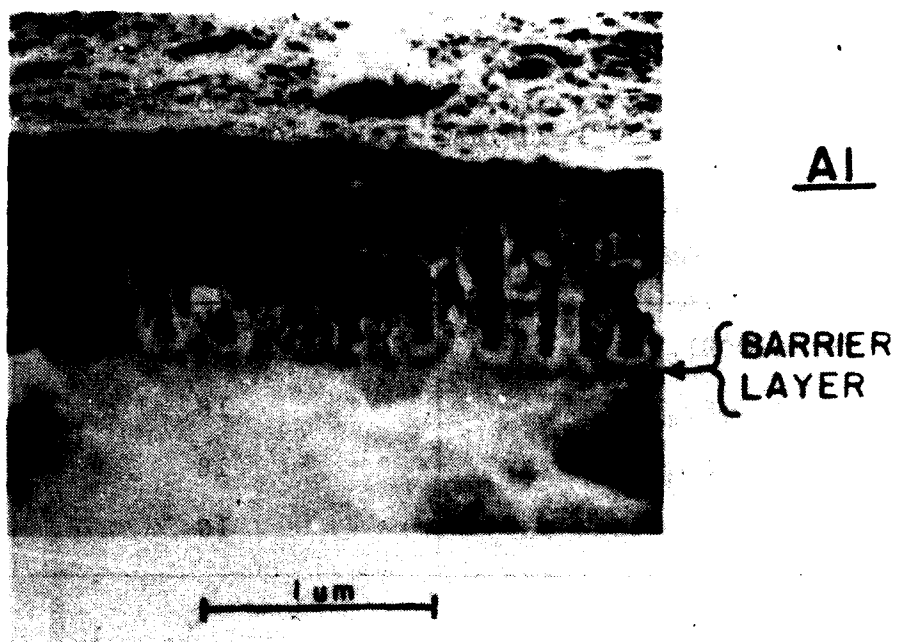


Figure 33. SEM Micrograph of Oxides on Aluminum Anodized in Room Temperature 0.05M H_3PO_4 at 60 Volts for 1 Hour.

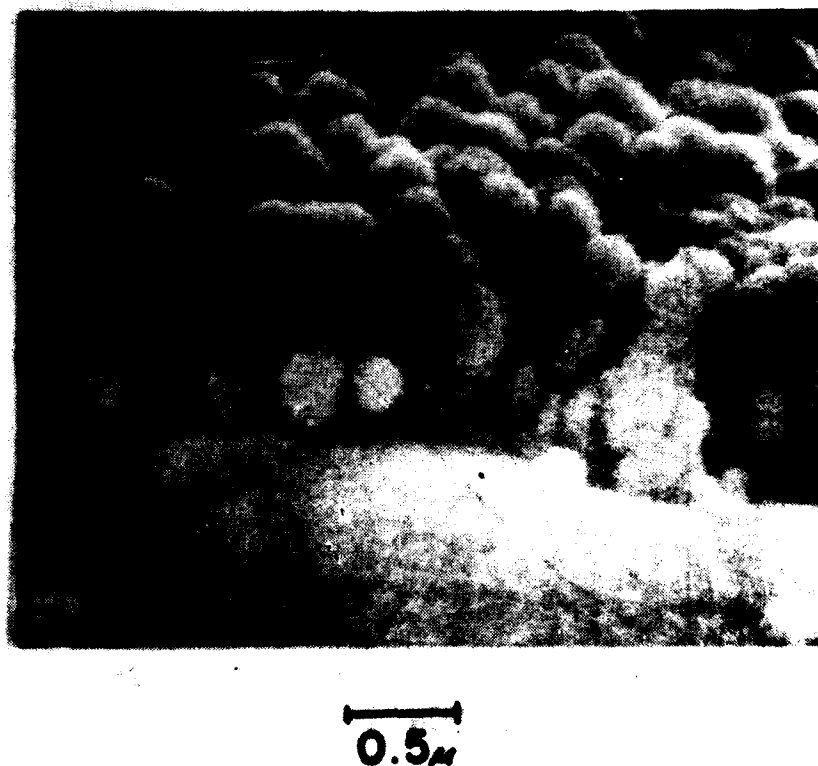


Figure 34. SEM Micrograph of Oxide on 2024-T3 Anodized in Room Temperature 1.0M H_3PO_4 at 10 Volts for 20 Minutes.

TABLE 53
SPUTTER RATES FOR ANODIC OXIDES ON AL AND 2024-T3
USING A 2keV 1.9uA/mm² ARGON ION BEAM

Specimen	Sputter Rate (nm/min)
C ₆ H ₄ (COOH) ₂ Al	6
10V 1M H ₃ PO ₄ Al	18
10V 1M H ₃ PO ₄ 2024-T3	18
10V 1M H ₂ SO ₄ 2024-T3	10

in phosphoric and sulfuric acids are greater, reflecting the porous nature of the films and, thus, a lower effective density.

The relationship of oxide thickness to anodization time for pure aluminum and 2024-T3 anodized at 10 volts in 1.0 molar phosphoric acid is shown in Figure 35.

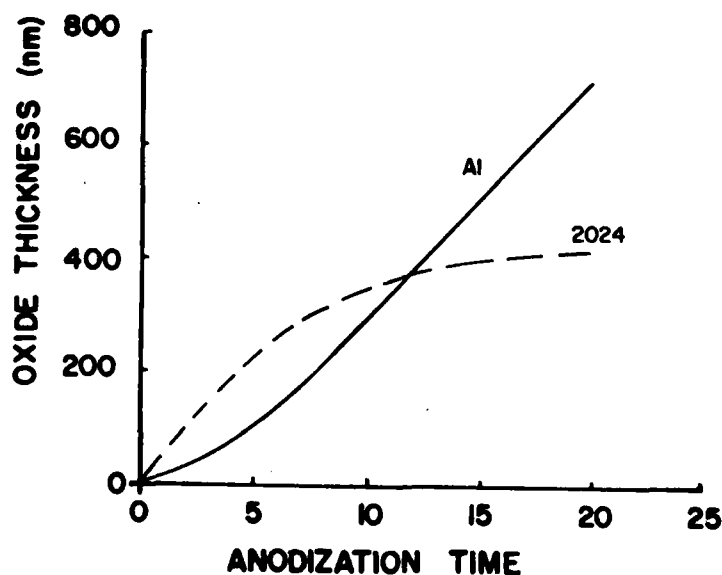


Figure 35. Oxide Film Thickness on Aluminum and 2024-T3 Plotted as a Function of Anodization Time at 10 Volts in Room Temperature 1.0M H₃PO₄.

Interface characterization. Figure 36 shows the in-depth profiles of oxygen, aluminum, and copper obtained by ASPA from the Oakite etched specimen. The oxide is approximately 5-10 nanometers thick, while the copper enrichment zone extending from the oxide-metal interface into the bulk alloy is approximately 36 nanometers thick. Copper enrichment was not observed at the oxide-metal interface of non-deoxidized or as-received specimens. Magnesium was neither detected throughout the oxide nor in the bulk etched alloy immediately below the oxide-metal interface.

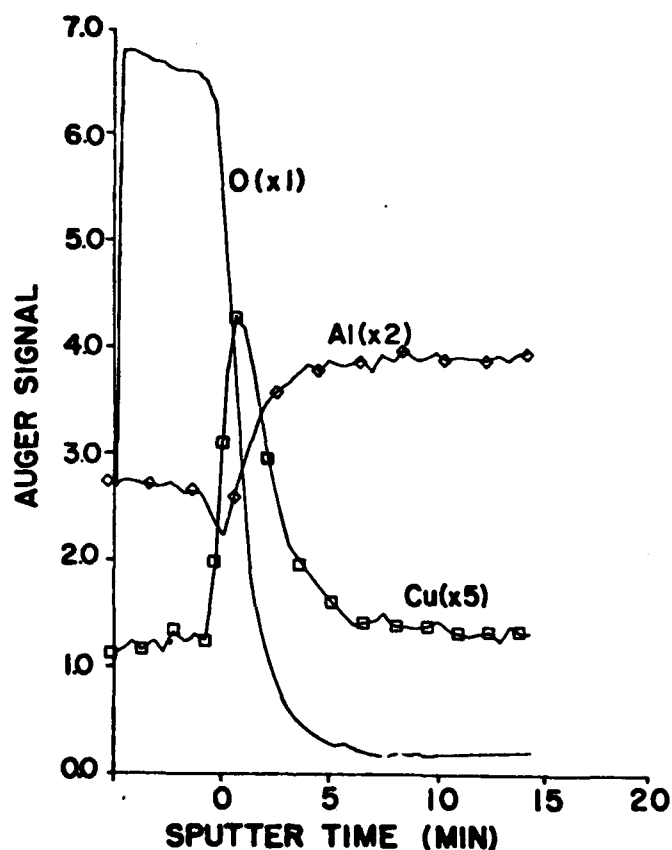


Figure 36. Oxygen, Aluminum, and Copper Auger Sputter Profiles of the Surface Oxide Layer of Oakite Deoxidized 2024-T3 Aluminum.

The copper in-depth profiles from Oakite deoxidized alloy specimens which were anodized at 10 volts for 1, 3, 5, and 10 minutes are shown in Figure 37. The profile from the 10-minute anodized specimen as well as those from specimens anodized longer than 10 minutes no longer show a copper enrichment at this interface but a concentration level equal to that in the bulk. The depth distributions of the copper-enriched zones in the 1, 3, and 5-minute anodized specimens according to Figure 37 are 34, 59, and 84 nanometers, respectively.

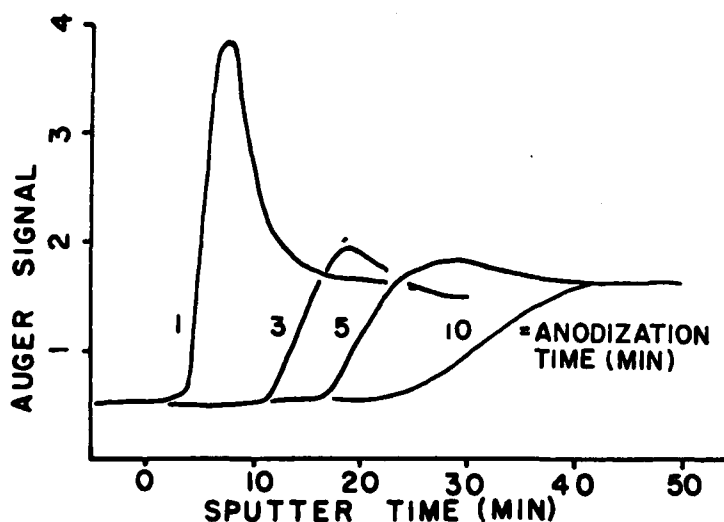


Figure 37. Auger Sputter Profiles of Copper in Anodic Oxide Films on Oakite-Etched 2024-T3 Anodized at 10 Volts in Room Temperature 1.0M H_3PO_4 .

(c) Rutherford backscattering

Figures 38 and 39 show RBS spectra from an Oakite-etched and a 20-minute anodized specimen. In both cases a copper-enriched interface is evident. Noticeably absent in Figure 38 is an oxygen peak. Oxygen was detected by Auger electron spectroscopy.

Figure 40 shows RBS spectra in the region of 1.2 to 1.8MeV for specimens etched and anodized for times up to two hours. Contrary to ASPA data, a copper interfacial

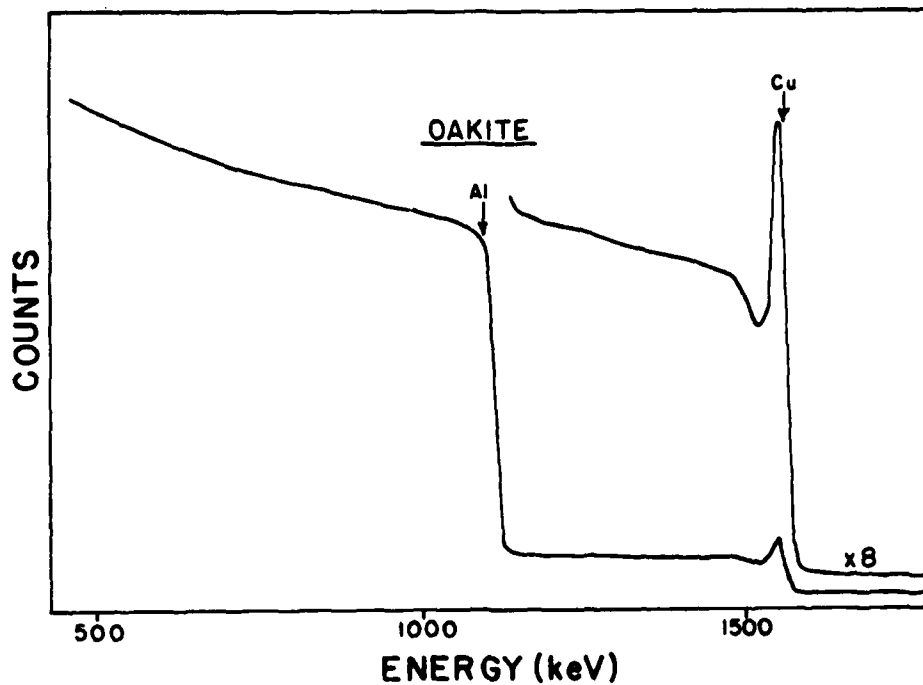


Figure 38. RBS Spectrum from Oakite-Etched 2024-T3 with a 2MeV $^4\text{He}^+$ Beam.

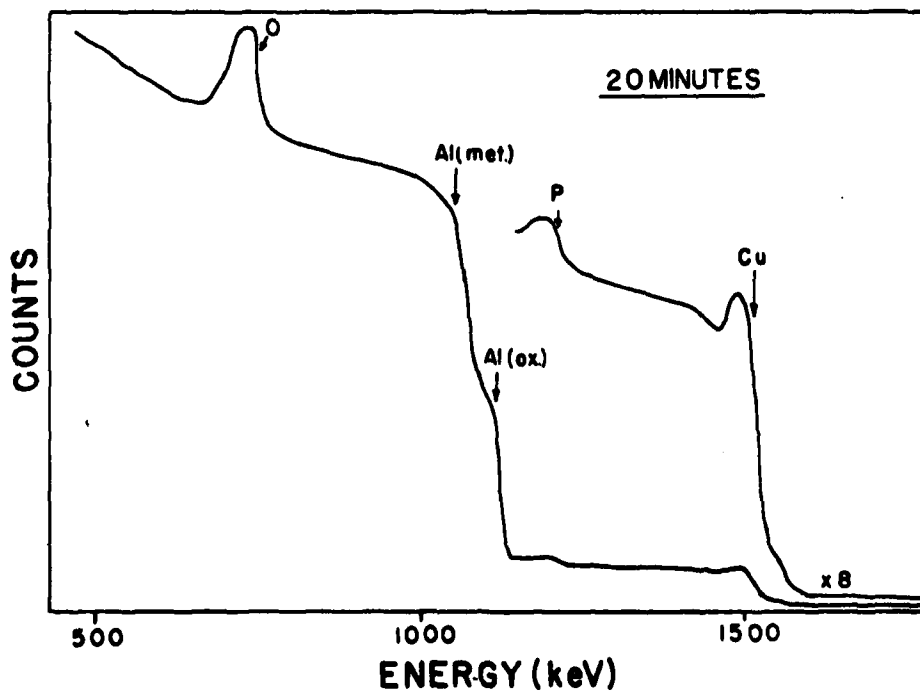


Figure 39. RBS Spectrum from Oakite-Etched 2024-T3 Anodized in Room Temperature 1.0M H_3PO_4 at 10 Volts for 20 Minutes Obtained Using a 2MeV $^4\text{He}^+$ Beam.

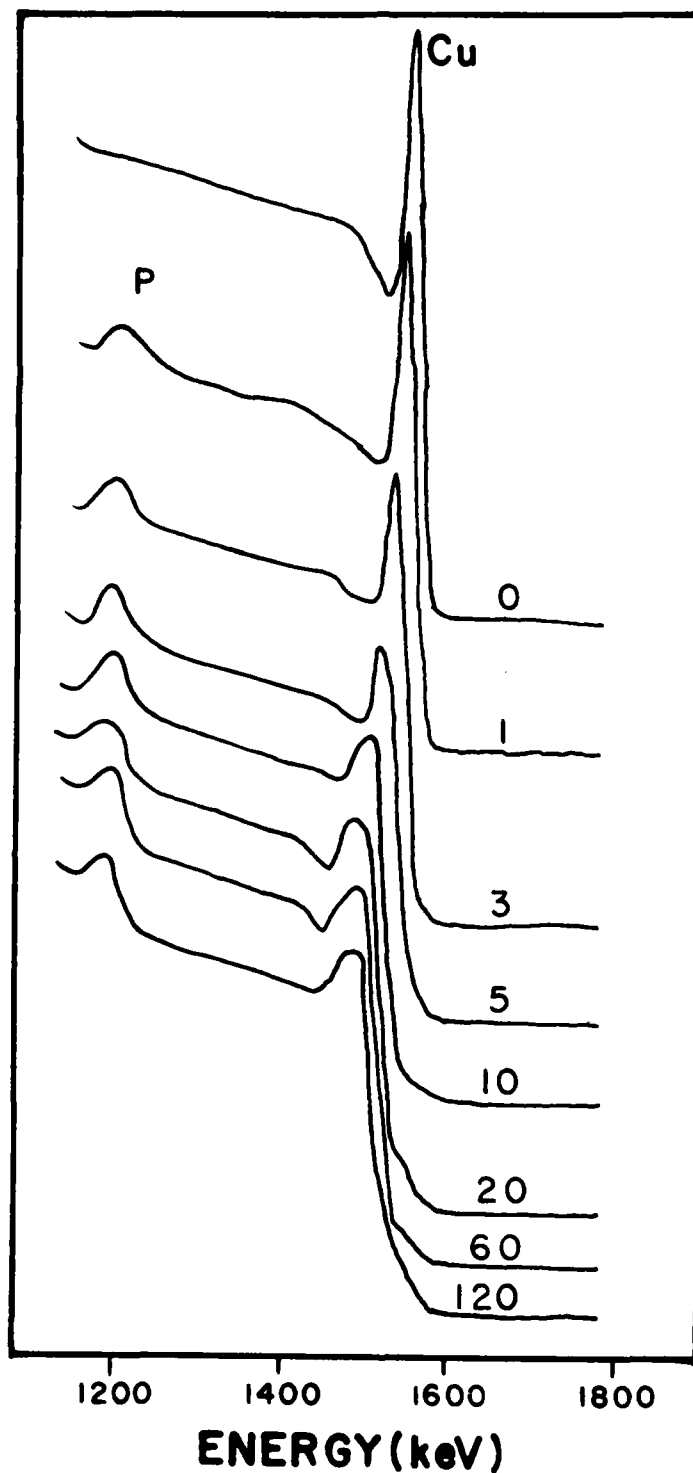


Figure 40. RBS Spectra of the Cu and P Peaks from Oakite-Etched 2024-T3 Anodized in Room Temperature 1.0M H_3PO_4 at 10 Volts for Times in Minutes, as Specified for Each Spectra, Using a 2MeV $^4He^+$ Beam.

enrichment is evident in all cases. Also evident in Figure 38 is what appears to be a copper deficient zone (compared to the bulk level) extending approximately 95 nanometers below the enrichment zone.

Table 54 lists the widths of the enrichment zone and copper concentration of the zones. The widths were calculated from the full width at half maximum (FWHM) of the copper peaks. The values in Table 54 were corrected for the measured depth resolution ($W_D = 20$ nanometers) in the following manner:

$$W^2 = W_M^2 - W_D^2$$

where W_M is the measured width at FWHM.

TABLE 54
RUTHERFORD BACKSCATTERING DATA FROM OAKITE-ETCHED AND 10 VOLT
1.0M H_3PO_4 ANODIZED 2024-T3 WITH A 2MeV $^4He^+$ BEAM

Anodization Time (minutes)	Copper Interfacial Width (nanometers)	Weight Percent Copper	
		Bulk	Interface
0	33	4.7	6.9
1	33	3.9	6.1
3	44	3.9	5.2
5	53	3.9	5.2
10	73	3.9	4.6
20	89	3.9	4.3
60	83	3.9	4.2
120	89	3.8	4.2

From the values listed in Table 54, it appears that the width of the copper-enrichment zone increases with anodization time up to approximately 10 minutes anodization, after which a constant thickness appears to be maintained.

Although the values listed in Table 54 are subject to an error of ± 0.25 weight percent, they seem to show a definite trend which indicates that there is a slight enrichment at the interface which appears to reach a steady-state value at approximately 10 minutes anodization.

(4) Discussion

(a) Interfacial phenomena

The ASPA copper profiles in Figure 37 show a copper enrichment at the oxide-metal interface to decrease in concentration with anodization time and finally disappears after approximately 10 minutes of anodization. The RBS data in Table and Figure 40, however, shows copper reaching a steady-state interfacial enrichment after 10 minutes anodization. The discrepancy in the data from the two techniques can be explained by taking into account their respective depth resolutions.

Depth resolution refers to the ability of a technique to characterize a layer of material at a particular depth in a specimen. The depth resolution of RBS or a sputter profile is normally taken to be a measurement of the deviation of a measured width, as determined from the leading and trailing edges of a RBS peak or sputter profile, from the true width.⁽⁴¹⁻⁴³⁾

The depth resolution of the RBS technique is constant throughout the backscattering range within a specimen. The depth resolution of ASPA, on the other hand, can be depth dependent.

A common convention⁽⁴²⁾ for defining depth resolution of sputter profile techniques is the rates of the difference in the sputtering time, ΔT , between the points of an interface at which 16 percent and 84 percent of a particular signal are reached to the sputtering time, T , at which 50 percent of the signal is recorded.

There are several phenomena which affect depth resolution. The loss of depth resolution has been

attributed to the sputtering process⁽⁴⁴⁻⁴⁸⁾ and the Auger process.^(49,50) According to Swartz et al, the two most significant broadening effects are ion knock-on mixing and electron escape depth.⁽⁵⁰⁾ They showed that the measured interfacial width ΔI_M is related to these two phenomena according to the following expression:

$$\Delta I_M \approx \{\Delta I^2 + (2.2L)^2 + (2R)^2\}^{1/2}$$

where I is the real interfacial width, L is the escape depth of the Auger electron and R is the mean escape depth of Cu_{LMM} and Al_{KLL} electrons to be in the range of 1-2 nanometers;⁽⁵¹⁾ and a similar range for mixing effects by a 2keV argon ion beam,⁽⁵⁰⁾ the contribution to interfacial broadening attributable to the ASPA technique, should be approximately 3 nanometers. Since the data in Table 53 shows interfacial widths for the copper-enrichment zones in the anodized 2024-T3 specimens to extend over a range of 33 to 90 nanometers, the Auger escape depth and ion beam knock-on effects do not significantly affect the ASPA interfacial resolution of data from anodized 2024-T3.

Another factor which has been reported to significantly affect depth resolution of Auger sputter profiles is surface roughness.⁽⁴⁵⁻⁴⁸⁾ Surface roughness effects have been attributed to the quality of the original surface^(47,48) as well as the sputter process,^(52,53) particularly preferential sputtering of materials.

As seen in Figures 33 and 34, the surfaces and textures of the anodic oxides formed on pure aluminum and 2024-T3 in phosphoric acid are rough and microscopically non-uniform. The $\Delta T/T$ values obtained from the oxygen profiles from 1.0M phosphoric acid anodized pure aluminum and 2024-T3 are plotted in Figure 41.

The $\Delta T/T$ values for both the pure metal and the alloy are large for films less than 100 nanometers. For

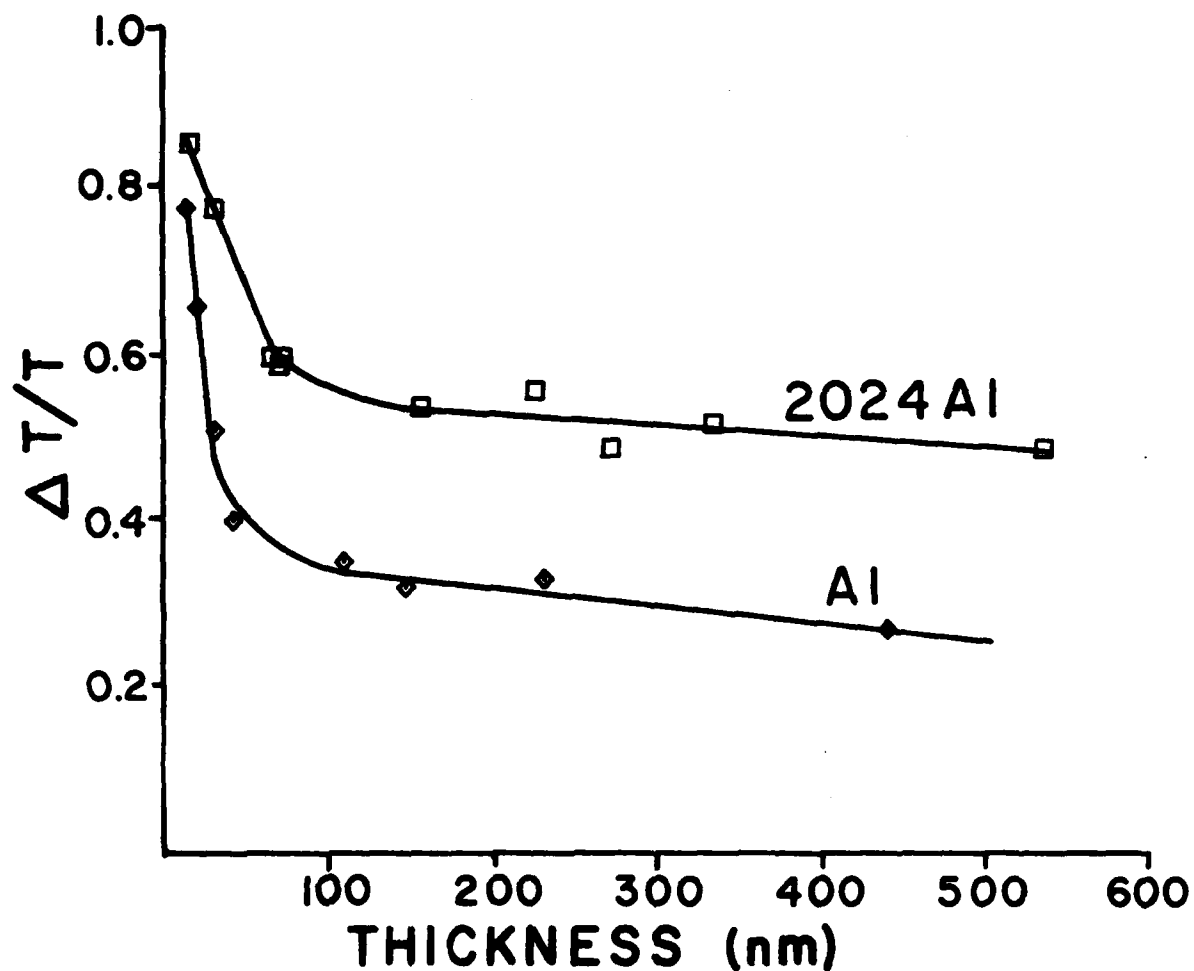


Figure 41. Depth Resolution $\Delta t/t$ (where t is Sputtering Time in Minutes) versus Anodic Oxide Thickness Sputtered on Al and 2024-T3 Anodized in Room Temperature 1.0M H_3PO_4 at 10 Volts.

oxides thicker than 100 nanometers, the respective $\Delta T/T$ values are fairly constant, although there is a small linear decrease over the measured range. Within the 100 to 600 nanometer range, $\Delta T/T$ is approximately 55 percent for 2024-T3 and 35 percent for the pure metal. Mathieu and Landolt⁽³⁹⁾ reported a $\Delta T/T$ of approximately 20 percent for oxide-metal interfaces in phthalic acid anodized aluminum using a 2keV argon ion beam. The anodic oxide grown in phthalic acid is nonporous and subsequently smoother textured than on phosphoric acid anodized aluminum.

The difference in the respective $\Delta T/T$ values for corresponding thicknesses of oxide on the alloy and pure metal is most probably related to the difference in their respective oxide layer textures which, as shown in Figure 34, is rougher on 2024-T3, particularly at the oxide-metal interface.

As a consequence of the relatively poor depth resolution for 2024-T3, interfacial features less than 55 nanometers in thickness in a specimen with a 100-nanometer thick oxide film cannot be characterized by ASPA with a high degree of confidence.

Whereas the influence of depth resolution on ASPA makes it difficult to characterize the thickness and elemental concentration of thin films with increasing depth, it has profound effects on RBS's ability to characterize thin films at any depth. When the film thickness becomes less than the system or depth resolution, the actual peak height begins to decrease; and the peak widths become significantly broader than the ideal or theoretical spectra. This twofold effect of peak broadening and peak height reduction introduces an error in quantitative calculations based on peak height or area under the peak and depth and thickness measurements.

In order to correct for the effects of depth resolution on RBS data, it is necessary to establish the relationship of film thickness to shifts in peak maxima and the broadening effects on peak height. An experimental approach to do this has been suggested by Chu et al.⁽⁵⁴⁾

If the values for interfacial copper concentration in Table 54 are not affected by depth resolution, then a simple comparison with ASPA data should reflect relatively similar amounts of copper.

The ratio of the areas of the copper enrichment contributions to the ASPA data from the one-minute versus the three-minute anodized specimen in Figure 36 shows a total copper enrichment in the one-minute anodized specimen of approximately four times above that in the three-minute anodized specimen. The area from the five-minute specimen was the same as the three-minute specimen. The areas of copper enrichment from the one and three-minute specimens in the RBS data in Figure 40 show no significant difference. This being the case, the interfacial copper concentration of the etched and one-minute anodized specimen may be much higher than listed in Table 54.

(b) Oxide thickness

Oxide growth on aluminum by electrochemical anodization in phosphoric acid is limited by both the increasing current retarding effects of the growing oxide film and the dissolving action of the acid electrolyte. The maximum oxide thickness is reached when the dissolution and growth rates become equal (continued anodization beyond this point only affects surface topography).

The presence of copper in aluminum has considerable effects on oxide growth rates.^(28,29) During anodization of copper containing aluminum alloys such as 2024-T3, there is a constant evolution of oxygen^(29,34) which is probably related to a charge transfer mechanism involving copper rather than aluminum, resulting in copper dissolution by the electrolyte. The net result is a lower concentration of Al^{+3} ions to combine with O^{-2} ions to form oxide. The consequence of this is reflected in Figure 35, which contains anodization time versus oxide thickness curves for aluminum and 2024-T3 anodized in 1.0M H_3PO_4 at 10 volts constant potential.

The curves in Figure 35 are based on ASPA and SEM data. Calculations to determine thickness from RBS data are based on the assumption that the density of the material is the ideal atomic density (for pure elements), the additive atomic density (for alloys and mixtures of pure elements), or crystalline density (for compounds). If voids or pores are present in films, such as in anodic oxides, the effective or total density of the film will be lower than the ideal density; and the measured thickness will be lower than the true thickness. Based on a density of 3.97 g/cm^3 for Al_2O_3 and a backscattering energy loss factor of 2.05 keV/ug/cm^2 , the calculated thickness from RBS data for the oxide layer on the 20-minute anodized specimen is approximately 70 nanometers; while the actual thickness, as determined from SEM data, is approximately 400 nanometers.

The oxide on 2024-T3 has a limiting thickness of approximately 400 nanometers, while growth continues on the pure metal (the maximum thickness on the metal was approximately 1000 nanometers).

An interesting subtlety with the aluminum curve in Figure 35 is its initial lower growth rate and subsequent thinner oxide for the first few minutes of anodization, compared to the alloy. This phenomenon is possibly related to the formation of the so-called barrier layer prior to columnar growth, the thickness of which is voltage-dependent according to a thickness-to-voltage ratio of 1 to 2 nanometers per volt.⁽⁵⁵⁾ This film forms in a very short period of time and causes a very rapid decrease in current density due to its electrical resistivity. Almost instantaneous with its formation, the electrolyte begins to nonuniformly dissolve the oxide creating thinner areas (pores); whereupon the oxide grows in a columnar fashion at a faster time-dependent rate.

In the case of 2024-T3 (see Figure 34), there is little evidence of barrier layer formation. According to Strehblow and Doherty,⁽³⁴⁾ the emission of oxygen during anodization prevents the formation of a continuous oxide film.

Therefore, uninhibited at the onset by the formation of a continuous oxide film, current not consumed by copper initially forms oxide on the alloy at a faster overall growth rate than on the pure metal.

(c) Oxide morphology

Another possible consequence of oxygen evolution due to the presence of copper is the effect on oxide morphology. Oxygen evolution most likely occurs at surface sites containing higher copper concentrations. Only when the copper concentration at one of these sites is decreased by the formation of a soluble compound can oxide growth begin. On the other hand, if the local copper concentration increases with anodization time, local oxide growth will be retarded or possibly stopped.

Anodization in phosphoric acid can have a twofold effect on copper in 2024-T3. First, since copper is highly soluble in phosphoric acid, it will be continually dissolved as the alloy substrate is consumed in the anodic process. Second, according to Strehblow et al, copper will diffuse to the oxide-metal interface where it will reach a steady-state enrichment at the oxide-metal interface. (35)

Both ASPA and RBS show that the etching step of the Boeing process leaves a preanodization interfacial enrichment of copper which, according to Table 53, is in excess of 2 percent above the bulk. At the onset of anodization, this enrichment is reduced by the dissolving action of the electrolyte until (as shown in Figure 40) a steady-state interfacial concentration is reached. This steady-state level of copper represents the net difference between the dissolving action of the electrolyte and the diffusion of copper. For the first few minutes of anodization, the dissolving action appears to exceed the diffusional replacement of copper because of the decrease in interfacial enrichment until approximately 5-10 minutes anodization. The initial imbalance in favor of the dissolution process most likely reflects the slower nature of the diffusion process.

Strehblow et al reported copper diffusion to the oxide-metal interface at a rate of 3.5×10^{-8} cm/sec during the anodization of Al - 0.5 percent Cu.⁽³⁵⁾ They and others⁽⁵⁶⁾ attributed this to the creation of vacancies at the oxide-metal interface.

Since copper is diffusing to the interface during anodization, it is highly probable that local diffusion rates and thus local copper concentrations will vary due to variations in local microstructure (i.e. grain size, grain boundaries, vacancy concentration, defect structure, and compound inclusion). Also, the competing mechanisms of diffusion and dissolution will effectively cause a cyclic variation in local copper concentrations. Consequently, oxide growth does not occur at fixed sites during the duration of anodization, and the oxide morphology on the alloy is not one of well-defined columns but rather that as shown in Figure 34. This does not take into account the effects of very high levels of copper present in the form of intermetallic compounds which would be randomly present at the oxide-metal interface as the Al-Cu solid solution is consumed.

(5) Conclusions

Auger sputter profile analysis and Rutherford backscattering are complementary techniques when applied to the characterization of thin films. Elemental distributions in very thin films, particularly of low mass elements such as oxygen within 200 nanometers of a surface, are best characterized by ASPA. Layers of higher mass elements such as copper or thick layers of low mass elements located at depths of 200 to 1000 nanometers are best characterized by RBS.

The combined SEM, ASPA, and RBS data from the anodic oxides on phosphoric acid anodized 2024-T3 aluminum present strong evidence for the influence of copper on anodic oxide growth and resulting thickness and morphology. SEM and ASPA showed that, at the onset of anodization, the presence of Cu can inhibit the formation of a uniform dense oxide film normally observed in the anodization of the pure metal. The result, when compared to the pure metal, is a slightly greater growth rate.

The RBS data showed that the anodization process results in the bulk diffusion of Cu to the oxide-metal alloy interface where, after a period of time, a steady-state enriched concentration zone of Cu is established. This zone broadens with longer anodization time. The steady-state enrichment of Cu is the result of the competition between the two time-dependent mechanisms of diffusion and electrolyte dissolution. Because of this cyclic process, growth rates may vary at local sites which, in turn, can result in a somewhat different oxide morphology than that produced on the pure metal.

The advantages of phosphoric acid anodization of aluminum for adhesive bonding applications are the built-in corrosion resistance offered by the barrier layer, and the large potential for good mechanical interlocking between adhesive and oxide throughout the oxide film owing to the ability of the adhesive to flow into vacant pore columns. Since the anodic oxide formed on 2024-T3 does not form a continuous uniform layer at this oxide-metal interface, it is doubtful if the oxide offers significant corrosion resistance. Also, because of its non-columnar morphology, the amount of mechanical interlocking between the oxide and adhesive may be reduced.

B. Phosphate-Fluoride Etching Effects on Titanium Alloy Surfaces

(1) Introduction

Most of the commercial and common laboratory chemical etchants for titanium and its alloys contain fluorine. The phosphate-fluoride (P-F) treatment is one which is commonly used as a conversion treatment; that is, it replaces the original natural oxide with a chemically-formed oxide layer. The problem with adhesive bond joints made with fluoride-treated titanium alloy adherends is their low strength. Bonded structures of Ti alloys which contain fluorine in their surface oxide layers usually exhibit a locus of failure at the oxide-metal interface. This reflects a lower adhesive strength between oxide and metal versus oxide and adhesive.

A study was made to determine the relationship between the presence of fluorine on a titanium alloy adherend and the low strength performance of adhesive-bonded structure of Ti alloys which were subjected to fluoride prebonding treatments. SEM, AES, ISS, SIMS, and XPS were used to characterize the treated alloy surfaces and surface layers. The combined information obtained from these techniques was used to describe the surface topography, surface chemistry, and elemental distribution within surface layers.

(2) Experimental

Titanium and its alloys listed in Table 55 were slurried in acetone, wiped dry, then ultrasonically cleaned in carbon tetrachloride for five minutes (degreased treatment). After drying, the panels were submerged for two minutes in a room temperature solution of 50g sodium ortho-phosphate (Na_3PO_4), 9g sodium fluoride (NaF), 26 ml hydrofluoric acid (HF) diluted to 1 liter with distilled water. The panels were then rinsed in tap water for one minute and soaked in deionized water for five minutes and finally dried. Some Ti-6Al-4V panels, which were only degreased, were anodized in 5 weight percent H_2SiF_6 at 30 volts for two minutes. After drying, Epon 828, cured with meta-phenylenediamine (mpda) was applied to the panels. After curing the adhesive layer was delaminated from the adherend by the application of a slight bending stress.

(3) Results

A more detailed description of the results of this study is reported elsewhere,^(57,58) and only a brief summary of these results is presented below.

Table 55 lists the Auger peak height ratios of O/Ti, C/Ti and F/Ti for all the treated panels. Except for Ti-5Al-2.5Sn and Ti-13V-11Cr-3Al which had only a small amount of F, the F/Ti ratio was nearly the same in all cases. Table 55 also specifies whether the Ti_{LMV} shape from each of the treated panels had a TiO_2 like shape or not. In those cases where the

TABLE 55
SUMMARY OF AES, SIMS, AND ASPA DATA FROM
CHEMICALLY ETCHED TITANIUM AND TITANIUM ALLOYS

Metals		AES			SIMS			ASPA
		h_O/h_{Ti}	h_C/h_{Ti}	h_F/h_{Ti}	"TiO ₂ " peak shape	TiF ⁺	TiF ₂ ⁺	oxide thickness (nm)
Ti (c.p)	D a)	2.8	1.6	—	yes	no	no	16.6
	P-F b)	1.2	0.3	0.8	no	yes	yes	82.5
Ti-8Al-1Mo-1Sn	D	2.3	0.7	—	yes	no	no	14.6
	P-F	1.6	0.5	0.7	no	yes	yes	111.8
Ti-6Al-4V	D	2.7	0.6	—	yes	no	no	5.1
	P-F	1.3	0.5	0.8	no	yes	yes	35.0
Ti-5Al-2.5Sn	D	2.1	0.1	—	yes	no	no	6.2
	P-F	2.1	1.9	0.1	yes	no	no	19.2
Ti-5Al-5Sn-2Mo -2Zr-0.25Si	D	2.5	0.6	—	yes	no	no	10.4
	P-F	0.9	0.3	0.8	no	yes	yes	112.0
Ti-3Al-2.5V	D	2.2	0.4	—	yes	no	no	1.7
	P-F	1.2	0.3	0.8	no	yes	yes	50.7
Ti-13V-11Cr-3Al	D	3.1	1.4	—	yes	no	no	9.6
	P-F	3.1	1.3	0.1	yes	no	no	6.8
Ti-8Mn	D	2.7	0.5	—	yes	no	no	7.9
	P-F	1.3	0.1	0.7	no	yes	yes	21.4

a) D = degreased, b) P-F = phosphate-fluoride treated.

peak shapes were different from TiO₂, they were identical to those from Ti and Ti-6Al-4V. In those cases where the shape was identical to TiO₂, both Na and F were detected in small amounts. The thicknesses of the oxide layers on the treated panels based on ASPA data and the sputter rate for TiO₂ are also listed in Table 55. SEM micrographs verified that the TiO₂ sputter rate was a good approximation even though the chemistry of these films differed from TiO₂.

In all cases when the AES Ti_{LMV} peak shape differed from that of TiO₂, the XPS C_{1s}, O_{1s}, and Ti_{2p} binding energies were identical to those from the P-F treated Ti-6Al-4V. The F_{1s}, when detected, had the same binding energy at the surface. However, when the AES Ti_{LMV} shape differed from TiO₂, the bulk oxide F_{1s} shifted to a slightly lower binding energy. When the Ti_{LMV} peak shape was identical to that of TiO₂, F was only

detected at the surface and not in the bulk surface oxide. In this latter case the binding energies of C_{1s} , O_{1s} , and Ti_{2p} were the same as those from degreased panels.

(4) Discussion

In all but two cases (Ti-5Al-2.5Sn and Ti-13Al-11Cr-3Al), the data strongly suggests two chemical states of F as well as a change of the natural surface oxide state of TiO_2 to one in which Ti is chemically bound to F and O. However, the chemical states of F and Ti are not necessarily related to the characteristic coarse granular structure produced by the P-F treatment, since this structure was not observed in Ti-6Al-4V where Ti was found not to be chemically bound to oxygen as TiO_2 . On the other hand, Ti-13V-11Cr-3Al, which has the granular structure, has a TiO_2 surface oxide. Perrier et al ⁽⁵⁹⁾ attributed this granular structure on Ti-6Al-4V following a P-F treatment to the presence of Na as well as F. Using an aged P-F solution, that is, one which was 300 days old and previously used to etch Ti alloys, we were able to produce the granular structure on Ti-6Al-4V; and the F_{1s} , O_{1s} , and Ti_{2p} binding energies from the surface were identical to those from the surface without the granular structure. Therefore, we feel this structure is associated with F compounds such as NaF, CaF, KF, etc. Since these compounds are easily hydrolyzed, they can be removed by a H_2O rinse following the P-F treatment which explains the randomness of the presence of this granular structure.

In trying to characterize the chemical states of Ti, O, and F, absolute binding energies, as determined by XPS, could not be used, since all peaks (including C_{1s}) were subjected to shifts which may or may not be related to charging. Consequently, binding energy differences between the respective Auger and photoelectron peaks of the same element and between various photoelectron peaks of the same scan were used to determine relative changes in chemical bonding, since a difference value between two peaks would not be affected by charging and is

characteristic of a particular chemical state. Table 56 lists the binding energy differences between a number of Auger and photoelectron peaks recorded from degreased, P-F treated, and H_2SiF_6 anodized Ti-6Al-4V. The $\text{Ti}_{\text{LMM}}\text{-Ti}_{2p_{3/2}}$ and $\text{O}_{1s}\text{-Ti}_{2p_{3/2}}$ difference values listed in Table 55 for the degreased and anodized surfaces are in agreement with the values for TiO_2 reported by Armstrong and Quinn.⁽⁶⁰⁾ The values from the P-F treated and delaminated or failed anodized surfaces differ from that for TiO_2 and the degreased and anodized surfaces. These values show that the chemical state of Ti, O, and F on the P-F treated and failed anodized surfaces are similar. Since the anodized surface oxide layer did not contain Na, the chemical states of Ti and O on the P-F treated surface are not related to the presence of that element. The values listed for Na on the P-F treated surface are in agreement with that reported for NaF.⁽⁶¹⁾ Since the value is slightly greater within the oxide layer, Na may be present within this region as Na_3PO_4 .⁽⁶²⁾

According to the data in Table 56, the binding energies of O and Ti have increased as a result of the P-F treatment. This should be expected if both are chemically bound to a more electronegative element such as F. Therefore, based only on this phenomena and the lack of stable Ti-F compound standards, XPS data alone cannot be used to identify the exact chemical state of Ti. However, if the $\text{Ti}_{2p_{3/2}}$ binding energy difference between Ti metal (453.8eV) and Ti compounds is plotted versus the actual or real charge on the Ti atom, which can be determined from its formal charge multiplied by the ionic bonding factor according to Pauling for crystalline materials,⁽⁶³⁾ a correlation can be made between the $\text{Ti}_{2p_{3/2}}$ shift and the chemical state of titanium.⁽⁶⁴⁾ This factor for the Ti atom is determined by the following Pauling expression:

$$f_{\text{Ti}} = 1 - \frac{N}{M} e^{-0.25(X_A - X_B)^2}$$

where N = valence (Ti)
 M = coordination number

TABLE 56
XPS BINDING ENERGY DIFFERENCE FROM CHEMICALLY ETCHED Ti-6Al-4V ALLOY

Treatment	E(eV)	Ti _{LMM} -Ti _{2p3/2}	O _{KLL} -O _{1s}	F _{1s} -F _{KLL}	Na _{1s} -Na _{KLL}	C _{1s}	Ti _{2p3/2}
Degrease	Surface	413.6	212.1	-	-	285.0	458.6
	Oxide	413.3	211.7	-	-	285.0	458.7
Phosphate-fluoride	Surface	415.2	215.1	86.8	806.1	286.7	461.3
	"Oxide"	414.8	213.9	86.8	806.7	285.7	460.3
Treatment	E(eV)	O _{1s} -Ti _{2p3/2}	F _{1s} -Ti _{2p3/2}	Na _{1s} -Ti _{2p3/2}	Ti _{2p3/2} -C _{1s}	O _{1s} -C _{1s}	
Degrease	Surface	71.3	-	-	173.6	244.9	
	Oxide	71.5	-	-	173.7	245.2	
Phosphate-fluoride	Surface	68.4	225.5	611.7	174.6	243.0	
	"Oxide"	69.6	225.8	612.7	174.5	244.2	
Anodization	Oxide	71.5	226.0	-	173.3	244.8	
5% H ₂ SiF ₆ (30 V)	Failure surface	69.8	226.1	-	174.4	244.2	

X_A and X_B = electronegativities of pure A and B atoms.
The real charge on each atom in a compound such as $A_n^{+q_i} B_m^{-q_i}$ is then given by

$$q_i(\text{real}) = q_i(\text{formal}) \cdot f_i$$

A compound such as TiF_4 has a calculated $q(\text{real})$ value of 3.44.

Figure 42 contains a plot of the $\text{Ti}_{2p_{3/2}}$ binding energy differences for TiO , Ti_2O_3 , and TiO_2 versus $q(\text{real})$ as reported by Demosthenous.⁽⁶⁴⁾ Also plotted in Figure 42 are the ΔE values by Ramquist⁽⁶⁵⁾ for TiO and TiO_2 and our values for the degreased and P-F treated Ti-6Al-4V panels. According to the plot in Figure 42, a compound such as TiF_4 with a $q(\text{real})$ value of 3.44 should have a ΔE value of 6.7eV. The ΔE values listed in Table 56 for the surface and bulk oxide layer on P-F treated Ti-6Al-4V are 7.5 and 6.5eV, respectively. A compound such as Na_2TiF_6 has a calculated $q(\text{real})$ value of 3.6 (assuming an average electronegativity value between Na and Ti) and, according to Figure 42, a ΔE value of 7.3eV. In other words, the bulk oxide on the P-F treated surface is most probably a mixture of TiO_2 and TiF_4 , while the surface may also contain a compound such as Na_2TiF_6 .

(5) Conclusion

In general, the P-F treatment replaces the original surface oxide of Ti and its alloys with one that is a mixture of titanium oxide and titanium fluoride and, therefore, cannot be classified as a "conversion" treatment according to strict definition. The surface topography of the P-F produced surface oxide is extremely sensitive to the formation of easily hydrolyzed non-titanium compounds of fluorine and contaminant species found in the rinse water or the P-F solution.

The poor performance of adhesive-bonded structure of P-F treated Ti alloys, which have a titanium oxide plus titanium fluoride surface layer, is probably related to the cohesive

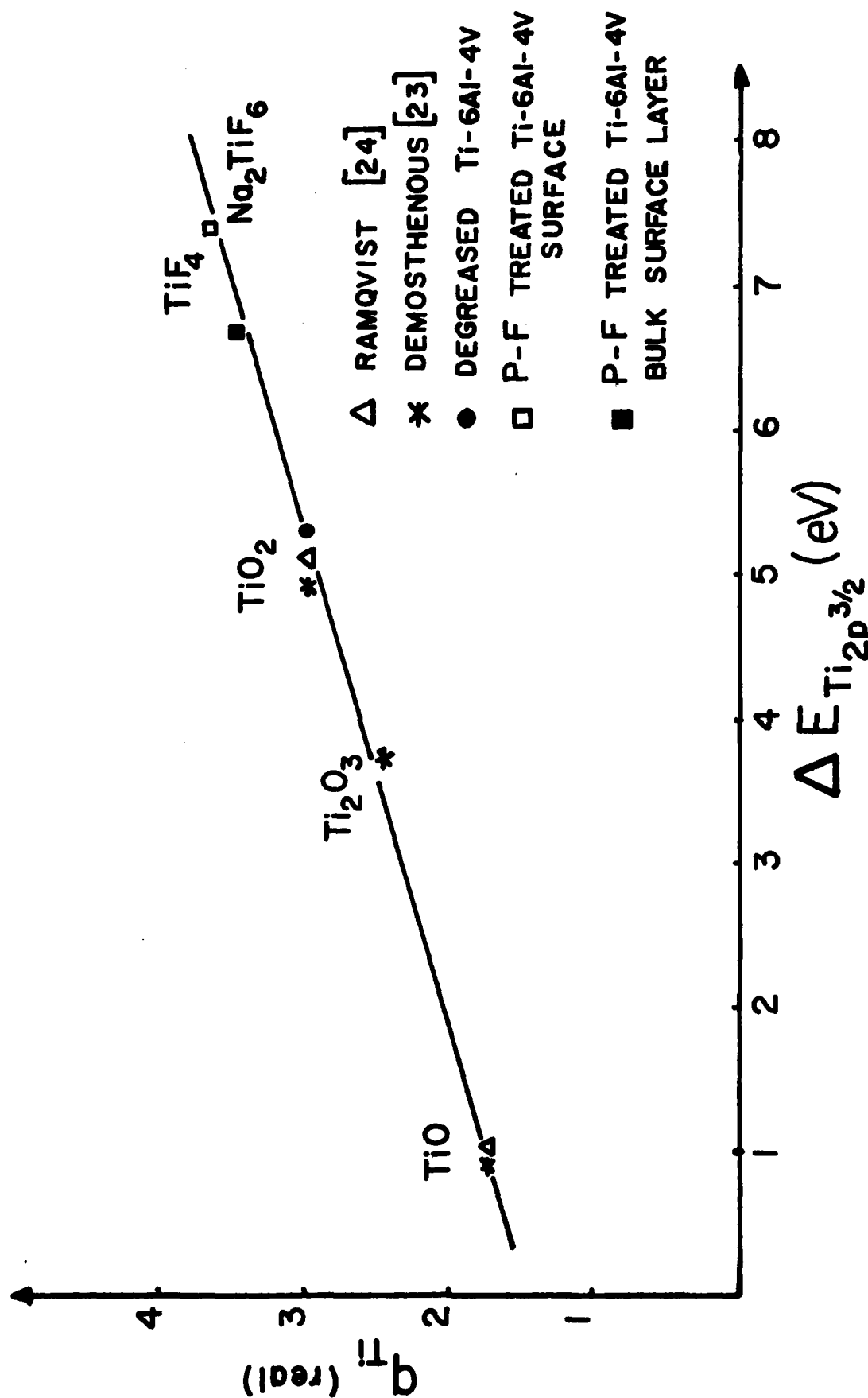


Figure 42. Real Charge on the Titanium Atom versus $Ti_{2p_{3/2}}$ Shift for Several Compounds.

strength of this mixture. The locus of failure within these structures is usually within the oxyfluoride layer, whereas the failure with a pure TiO_2 surface oxide generally occurs between adhesive and surface oxide. One can only assume that the cohesive strength of a titanium oxyfluoride mixture is lower than that of the pure oxide.

C. The Effect of Surface Treatment on Bond Line Performance of Adhesively Bonded Ti-6Al-4V

(1) Introduction

A three-point flexure test using a single adherend/adhesive structure was used to evaluate the material properties of the interphase of an adhesive bond joint. In the past the flexure test was used to characterize ultimate strength and shear stress of composites and sandwich (two adherends) adhesively-bonded structures.⁽⁶⁶⁾ However, large concentrations of both normal and shear stresses in the adhesive layer occur at locations of geometric and material discontinuities, such as the ends of a bond joint.⁽⁶⁷⁾ This can lead to mixed mode failures.

Using only one adherend and applying the load entirely to it instead of the adherend-epoxy structure, as in the case of a sandwich, eliminates the problem of residual compressive stresses within the bond joint and, thus, the stress patterns observed in a photoelastic fringe tend to be parallel to the interphase. The patterns from sandwich specimens usually show stresses proceeding from the interphase region toward and throughout the bulk adhesive⁽⁶⁸⁾ which indicates that the stress behavior during testing is not very sensitive to interphase properties but rather to bulk adhesive properties.

(2) Experimental

Figure 43 contains illustrations of a three-point flexure test configuration using a single adherend-epoxy adhesive test specimen. Figure 43a shows the specimen without an applied load. Figures 43b and 43c illustrate the specimen under applied load and after debonding along the interphase, respectively.

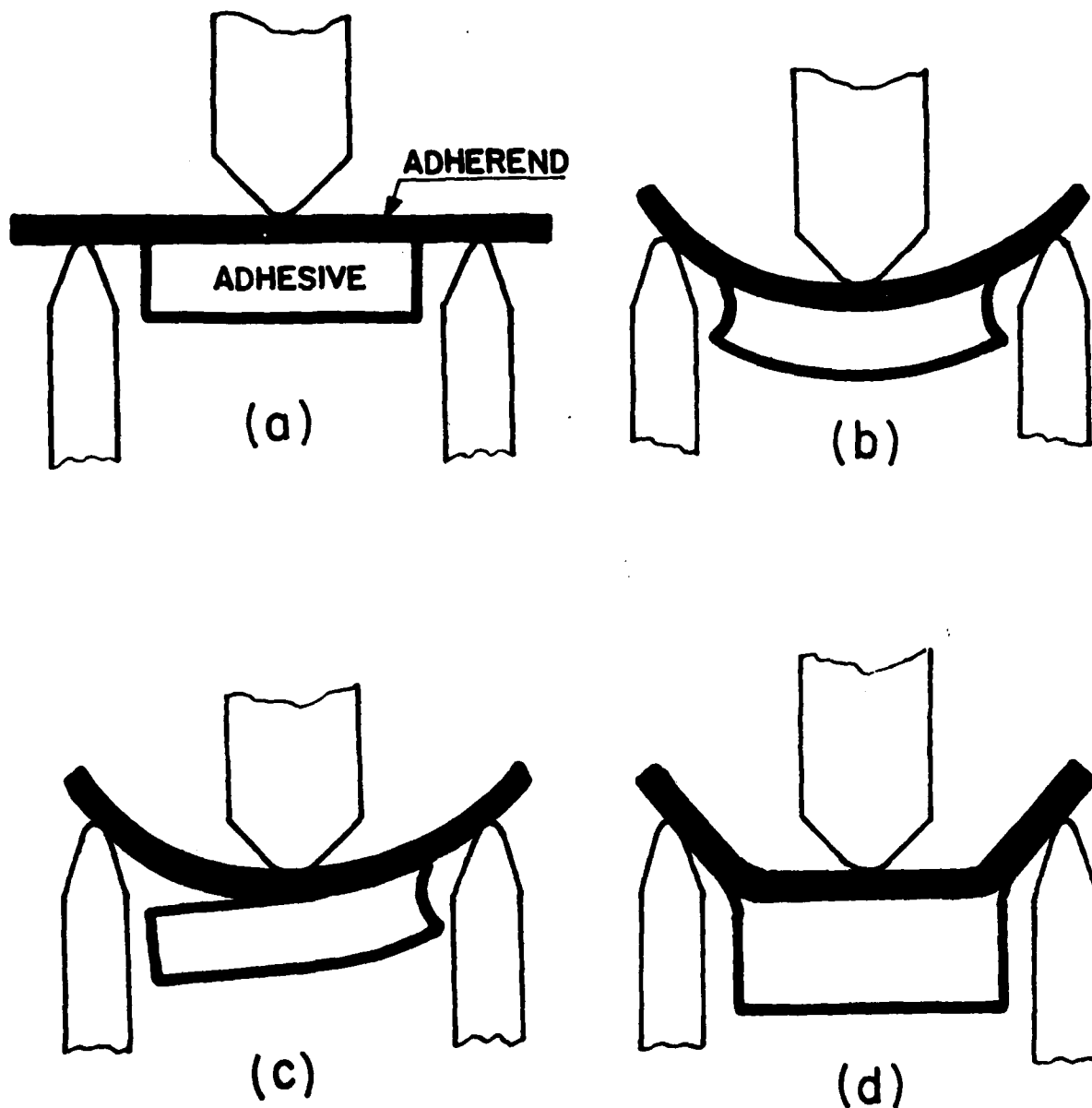


Figure 43. Illustrations of a Three-Point Flexure Test Configuration Using a Single Adherend-Epoxy Adhesive Test Specimen: (a) with No Applied Stress, (b) with Applied Stress, (c) Delamination of the Adhesive, and (d) Yielding of Thin Metal Adherend with Application of Stress.

Adherend yielding illustrated in Figure 43d can occur when the adhesive layer is too thick and becomes constrained by the sides of the static specimen mounts or the stiffness of the interphase/bulk adhesive is greater than that of the adherend. Therefore, a ratio of adherend thickness to adhesive thickness was always chosen which would produce debonding (Figure 43c) before any noticeable adherend yielding. The specimen preparation fixture is shown in Figure 44. The adhesive forming mold (Figure 44b) was made of RTV-624. It was held against the adherends by a clamping assembly (Figures 44a and 44c). An exact amount of adhesive was applied to each adherend with a syringe (Figure 44d). Care must be taken to ensure that no bubbles evolve within the adhesive near the interfacial region.

A table model 1102 Instron tester, fitted with a model G-09031 decade cross-head speed reducer and a 453.6 kg load cell, was used for testing. The cross-head speed was typically 84.6×10^{-6} m/s with a loading sensitivity as low as 11.3 kg full scale. Figure 45a shows the actual size of a bonded single adherend specimen, and Figure 45b shows the specimen mounted in the Instron tester behind a light polarizer.

Seven sets of test specimens with 0.4 mm thick Ti-6Al-4V alloy adherends were bonded with an epoxy adhesive (6 mm thick) having a modulus $E = 3.65$ GPa. The seven alloy adherends were subjected to different chemical treatments prior to bonding. These treatments are listed in Table 57. An identical set of the treated alloys were characterized for their surface chemistry and surface oxide thickness by Auger electron spectroscopy and Auger sputter profiling.

(3) Results and Discussion

Table 58 is a semiquantitative listing of the elements detected on the seven treated alloys by Auger electron spectroscopy.

Figure 46 shows a series of photoelastic isochromatic fringes recorded from the Ti-6Al-4V specimen subjected to

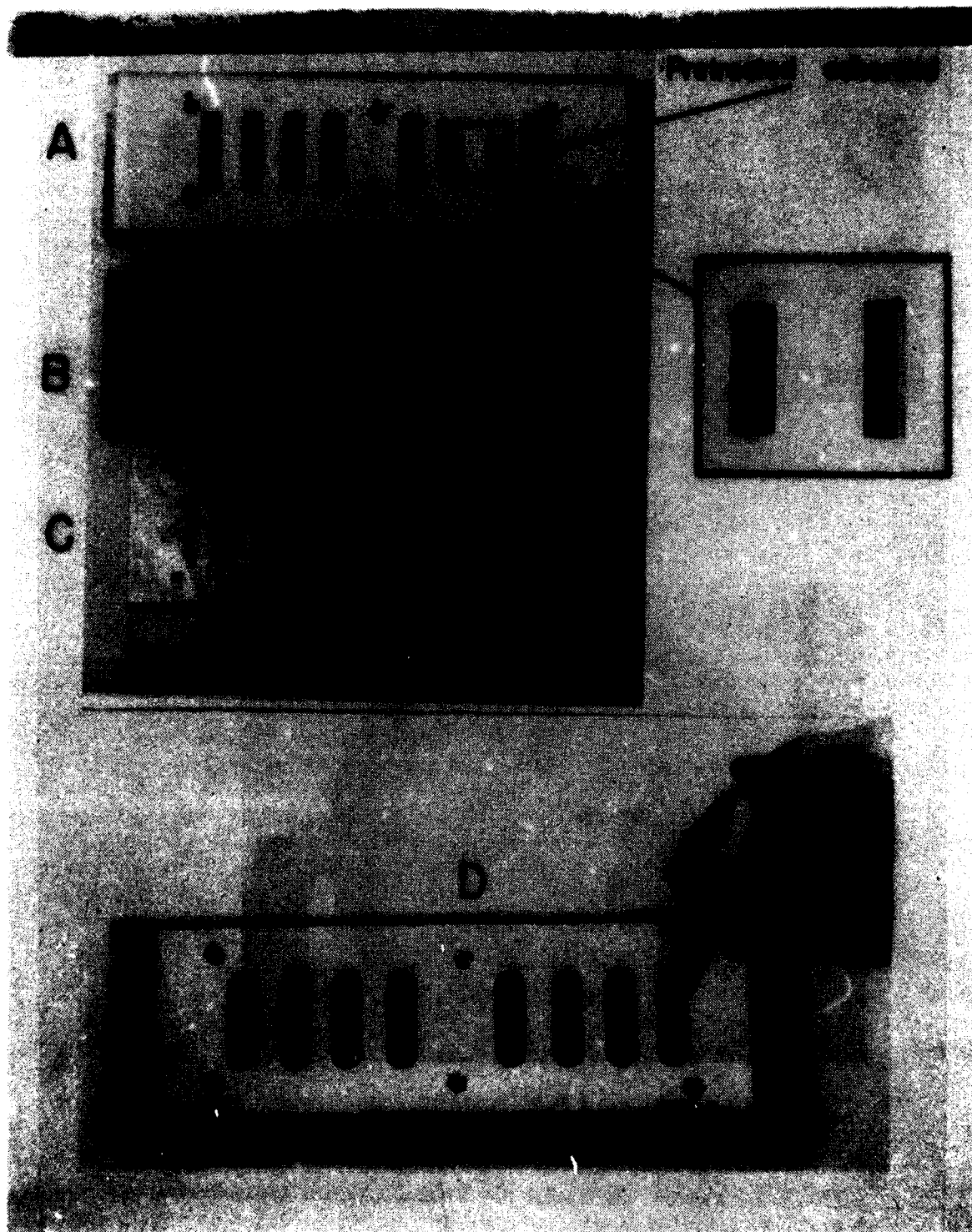
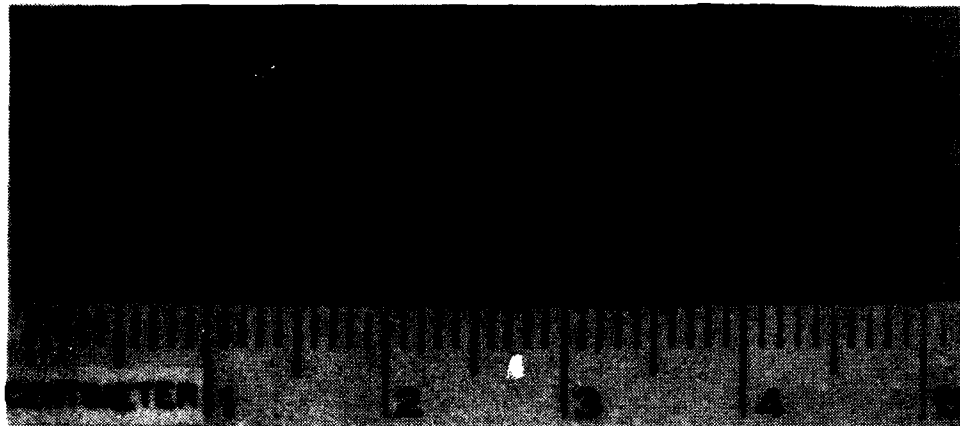
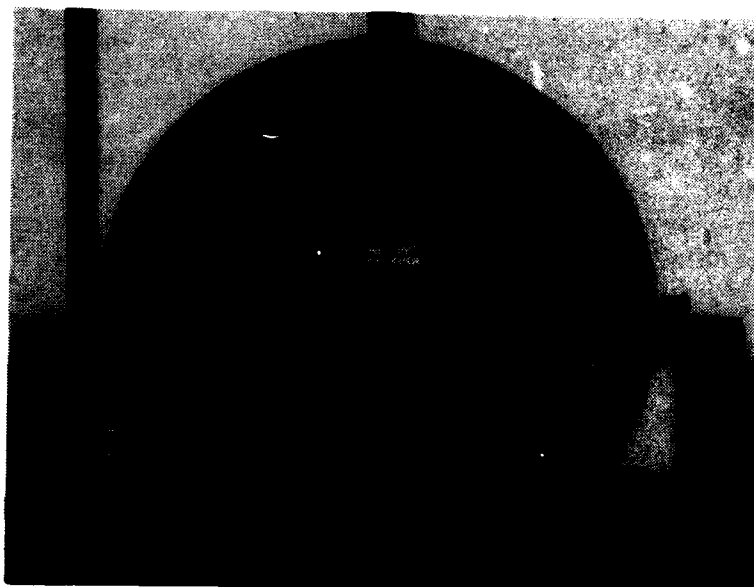


Figure 44. Specimen Preparation Fixture.



(a)



(b)

Figure 45. Bonded Single Metal Adherend Specimen (a) and Specimen Mounted in a Model 1102 Instron Tester Fitted with a Light Polarizer (b).

TABLE 57
SURFACE CHEMICAL TREATMENTS FOR TITANIUM
AND TITANIUM ALLOYS

CODE	DESCRIPTION	TREATMENT
1	Degrease	Sample slurried in acetone, wiped dry, then ultrasonically cleaned in carbon tetrachloride for 5 minutes.
2	Alkaline	Sample submerged in 0.1N sodium hydroxide, room temperature for 2 minutes. Running tap H ₂ O for 1 minute, standing deionized H ₂ O for 5 minutes.
3	HNO ₃ /HF (fluoro-nitric)	Sample submerged in a solution of 170 ml nitric acid, 30 ml hydrofluoric acid, 800 ml distilled water, room temperature for 2 minutes. Rinse as in #2.
4	Na ₃ PO ₄ /NaF/HF (fluoro-phosphate)	Sample submerged in a solution of 50g sodium ortho-phosphate, 9g sodium fluoride, 26 ml hydrofluoric acid, distilled water to 1 liter, room temperature for 2 minutes.
5	H ₂ SO ₄ /CrO ₃ (sulfo-chromium)	Sample submerged in solution of 300g sulfuric acid, 40g chromium acid, distilled water to 1 liter, room temperature for 2 minutes. Rinse as in #2.
6	HNO ₃ /HF/H ₂ O ₂ /NH ₄ F, HF (fluoro-nitro-ammonium)	Sample submerged in solution of 80 ml nitric acid, 20 ml hydrofluoric acid, 20 ml hydrogen peroxide (30%), 10 ml ammonium bifluoride (saturated), distilled water 500 ml, room temperature for 2 minutes. Rinse as in #2.
7	Hot NaOH/H ₂ O ₂ (hot alkaline)	Sample submerged in solution of 20g sodium hydroxide, 20 ml hydrogen peroxide (30%), distilled water to 1 liter, 65°C temperature (150°F) for 2 minutes. Rinse as in #2.

TABLE 58
AES ELEMENTAL I.D. OF TREATED Ti-6Al-4V

Treatment Code	ELEMENT IDENTIFICATION										
	Ti (381 eV)	O	C	P	Ca	Na	F	S	Cl	Al	V
1	1	2.7	0.6		0.2	x		x	x	x	x
2	1	2.2	0.9		x	x		x	x	x	
3	1	2.3	0.8					x	0.2	x	x
4	1	1.3	0.5	x	0.2	0.5	0.8	x	x	x	
5	1	2.2	0.5				x	x	x	x	x
6	1	2.1	0.4	x	x		x	x	x	x	x
7	1	2.1	0.4		x		x	x	x	x	x

(x: Auger peak-to-peak height ratio <0.1)

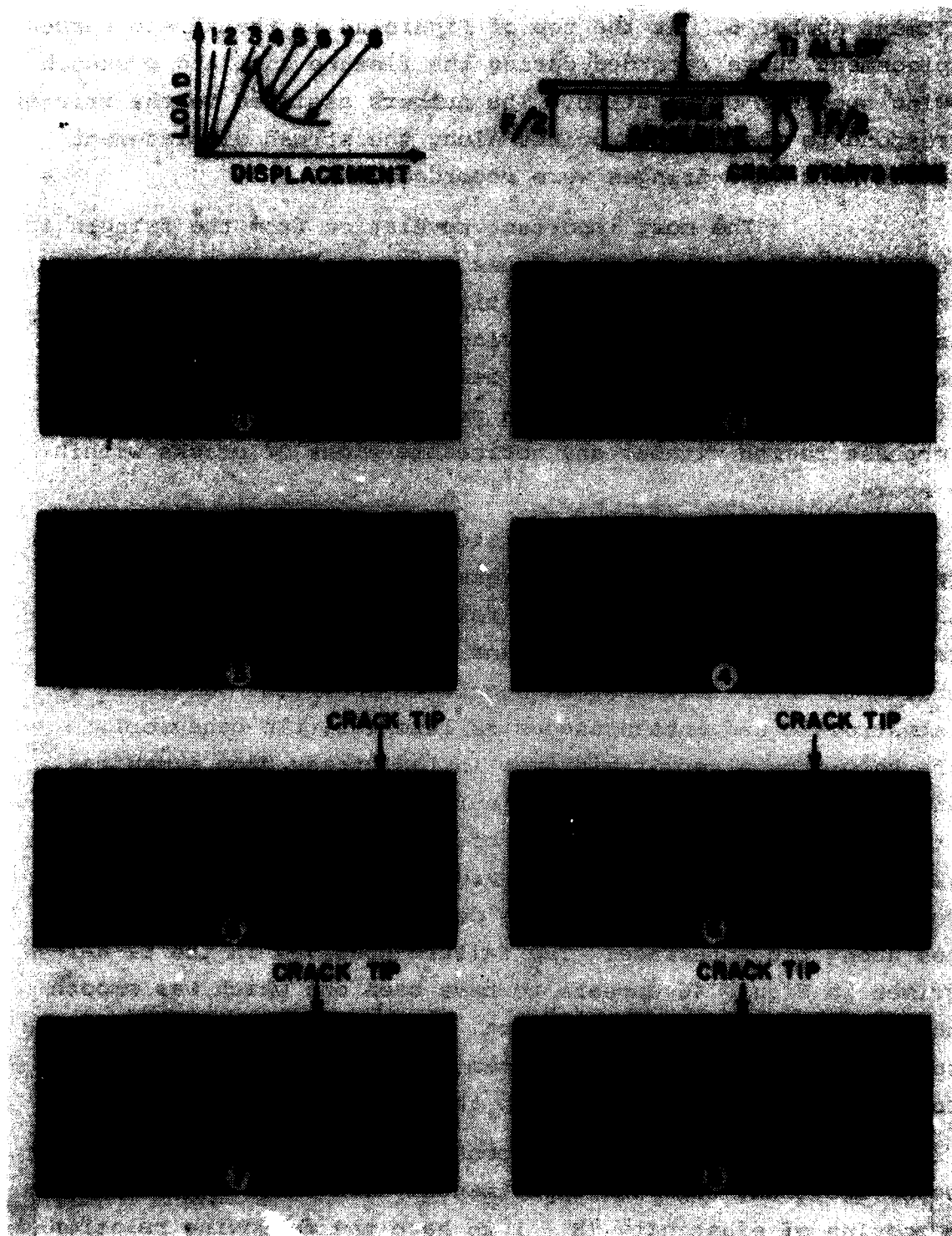


Figure 46. Photoelastic Isochromatic Fringes Recorded During the Testing of a Single Ti-6Al-4V Adherend Specimen.

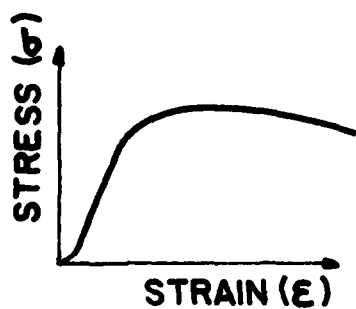
treatment number 5. At the top of Figure 46 is the stress versus displacement curve recorded during the flexure test and a sketch showing specimen orientation. The numbers assigned to the fringes correspond to the various points along the stress displacement curve at which the fringes were recorded.

The most important revelation from the fringes in Figure 46 is that except for stress concentrations at the edges, stresses within the epoxy are initially parallel to the bond joint interface and remain so during the test cycle. Starting with fringe number 5, failure or delamination is seen to have initiated. The delamination then progresses inward through the interphase region without any noticeable signs of cracks within the epoxy.

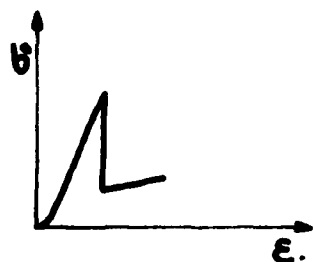
Figure 47 illustrates some examples of possible stress-strain curves that could result from various interfacial behaviors during testing. If no failure occurs, an ideal stress-strain curve with a yield point and maximum yield stress corresponding to the metal adherend should be observed. If there is a catastrophic and instantaneous failure (brittle behavior), there should be a very rapid drop in the stress from a maximum point, followed by a stress-strain relationship characteristic of the metal adherend. The rate of decrease in the stress following initial delamination can vary from smooth and rapid to an irregular stepwise progression as delamination or failure propagates along the interface. The failure observed in the Ti-6Al-4V specimen in Figure 46 appears to have been one which was smooth with slow delamination propagation. For all seven specimens, the stress level went through a maximum before failure, and the isochromatic fringes were similar to those in Figure 46.

If this test is sensitive to the material properties of the bond, then the experimental data should show the system modulus of elasticity (E_{sys}) to have the following relationship:

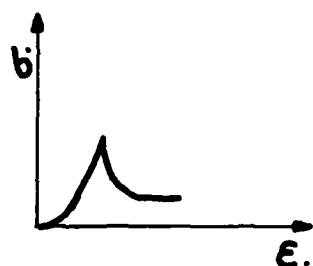
$$E_A < E_{sys} < E_M$$



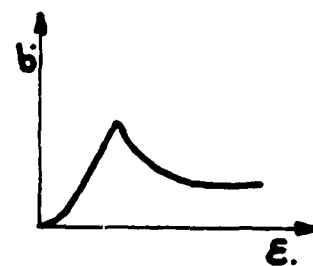
WITHOUT FAILURE



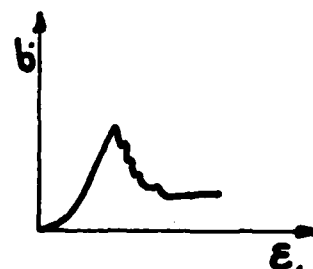
BRITTLE FAILURE



SMOOTH and RAPID
FAILURE PROPAGATION



SMOOTH and SLOW
FAILURE PROPAGATION



STEP WISE FAILURE
PROPAGATION

Figure 47. Examples of Possible Stress-Strain Curve that Could Result from Various Interfacial Failure Mechanisms.

where E_A is the modulus of the adhesive (3.65 GPa) and E_M is the modulus of the metal (113.7 GPa). A system modulus can be approximated as follows:

$$E_{\text{sys}} = \frac{E_M V_F^M + E_A V_F^A}{V_F^M + V_F^A}$$

where E_M and E_A are the respective modulus of the metal and adhesive, and V_F^M and V_F^A are the respective volume fraction of the metal adherend and adhesive. Based on this relationship, E_{sys} for the Ti alloy/epoxy system described above should be 10.5 GPa.

Table 59 lists the values of the maximum loads and experimentally determined E_{sys} for each of the seven treatments. Also listed in Table 59 are the respective surface oxide thicknesses determined from a set of identical specimens by Auger sputter profile analysis. The data in Table 59 shows an optimum value for E_{sys} for oxide thicknesses of approximately 13 to 16 nanometers. The behavior of those specimens with thinner oxide layers during testing tended to be one of very fast delamination propagation at the onset of delamination. The specimen subjected to treatment 4 had the thickest oxide layer but a lower E_{sys} . The load-displacement curve for this specimen showed failure to occur in a slow but stepwise manner. Table 58 shows the surface of this specimen to contain easily hydrolyzed species of Ca, Na, and F. As reported in section B, the oxide itself was found to be a mixture of titanium oxide and titanium fluoride, and failure was mixed mode in that delamination propagated along the oxide-adhesive interface at times, while at other times there was cohesive failure within the oxyfluoride layer.

(4) Conclusion

To characterize the material properties of an interphase is extremely difficult and may not be possible in all cases. However, using a three-point flexure test on a single metal adherend adhesive-bonded structure can be sensitive to these properties providing that load conditions and specimen size

TABLE 59
THREE-POINT FLEXURE TEST DATA AND OXIDE THICKNESSES
FOR CHEMICALLY TREATED Ti-6Al-4V
ADHEREND-EPOXY STRUCTURES

Surface Treatment Code from Table 56	Maximum Load (kg)	Modulus of Elasticity (GPa) ±0.8%	Thickness (nanometers)
1	1.0	9.09	5.1
2	1.4	11.9	14.3
3	1.6	9.6	4.0
4	1.6	10.3	35.0
5	1.6	13.2	13.0
6	1.6	11.4	4.8
7	1.1	12.6	15.8

can be adjusted to optimize experimental sensitivity to very small changes in the stress-displacement relationship.

The results reported here show that the material properties of the interphase are sensitive to the physical and chemical properties of the adherend surface. With this information it becomes possible to better understand failure mechanisms and the nature of bonding between adherend and adhesive, and better enables the prediction of performance following modifications to bonding steps.

SECTION IV

DURABILITY/LIFE PREDICTION OF COMPOSITES AND ADHESIVES

The major effort during this reporting period has been made in the area of strength of multidirectional laminates, delamination and transverse cracking, and fatigue. Three technical reports on related subjects were completed during the reporting period and are attached to this report as Appendices A, B, and C. In addition a variety of tests have been conducted on material characterization, impact, warpage of unsymmetric laminates, etc., and the results can be found in the monthly status reports.

1. STRENGTH OF MULTIDIRECTIONAL LAMINATES

Prediction of the in-plane strength of a multidirectional laminate is of great importance in design of the laminate as well as development of material systems. In this program a simple approach is employed to predict the in-plane tensile strength of a multidirectional laminate as an engineering approximation. To achieve this, we made an assumption that ultimate failure of multidirectional laminates occurs upon the strongest ply failure for a given externally-applied stress resultant, ignoring the damages incurred in the course of loading. The in-plane stress components in each constituent ply for a given laminate were calculated using laminated plate theory. The quadratic failure criterion developed by Tsai and Wu is then applied to the respective ply. The analytical results were compared with experimental results obtained from a variety of laminates including laminates showing delamination before final failure. The damage process, in terms of delamination and transverse crack, was experimentally observed for selected laminates.

Three basic families of laminates used in this work are $[0_2/\pm\theta]_s$, $[0/\pm\theta/90]_s$, and $[0/90/\pm\theta]_s$, with $\theta = 5, 10, 15, 30, 45, 60, 75$, and 90 degrees. The effect of delamination was considered by comparing the results of the last two families of laminates, since interlaminar normal stress at the free edge region

is tension in the $[0/\pm\theta/90]_s$ laminate and compression in the $[0/90/\pm\theta]_s$ laminate under applied uniaxial tensile loading. The material system used in this study was T300/5208 graphite/epoxy supplied in the prepreg form by Narmco Corporation.

The experimental results obtained from the three families of laminates were found to be in good agreement with prediction with a consistent exception. The exception is that all the laminates show delamination at the free edges which substantially reduces the load-carrying capability. The detailed results and discussion can be found in Appendix A. In addition, Table 60 lists the predicted and experimental strengths of the laminates tested for the various programs. The comparison was found to be reasonable in most cases except for those laminates containing the 15-degree layer.

2. DELAMINATION

A. Initiation of Delamination

Delamination along free edges of the laminate in the presence of in-plane loading is one of the major types of damages. This delamination often reduces load-carrying capability and stiffness of the laminates which are detrimental to the structural reliability and durability of the composite laminates. Tensile interlaminar normal stress, σ_z , usually found in the free-edge region of the laminate, has been considered to be mainly responsible for cause of delamination. Analytical works by Pagano and Pipe show that σ_z is highly localized, and its sign and magnitude vary depending upon the stacking sequence for a given laminate. Hence, delamination will occur when the magnitude of σ_z attains the ultimate transverse strength of the material system. Since the transverse strength in compression is approximately four times that of tension, those laminates having tensile σ_z may be more prone to delamination than others.

A series of tests has been conducted to insure the role of σ_z to initiation of delamination under static tension and compression. The material system used in this test was T300/5208

TABLE 60
STATIC STRENGTH OF MULTIDIRECTIONAL LAMINATES

LAMINATE	STRENGTH, KSI		NO. OF SPECIMENS TESTED
	PREDICTION	EXPERIMENT	
$[0_2/+5]_s$	200.42	206.71	6
$[0_2/+10]_s$	198.53	193.27	6
$[0_2/+15]_s$	188.42	167.04	6
$[0_2/+45]_s$	118.25	125.84	20
$[0_2/90]_s$	95.88	103.67	20
$[0_2/90_4]_s$	67.73	69.72	20
$[0/90_6]_s$	36.01	31.46	4
$[0/+15]_s$	179.62	135.92	10
$[0/+30]_s$	118.01	109.08	12
$[90/+15]_s$	112.27	86.12	8
$[0/+30/+60/90]_s$	77.97	66.81	5
$[0/+22\frac{1}{2}/+45/+67\frac{1}{2}/90]_s$	77.97	66.36	9
$[0/+45/90]_s$	77.97	69.20	6
$[0_8/+45_2/90]_s^*$	148.44	141.70	6
$[+45_2/90]_s^*$	29.41	28.55	3
$[0/+45_2]_s^*$	64.21	55.13	3
$[0/90_3/\pm 45]_s$	55.92	50.72	10
$[0/90_6/\pm 45]_s$	41.07	35.944	10

*Obtained from literature.

graphite/epoxy. A variety of laminates showing either tensile or compressive σ_z were considered. The sign of σ_z can be determined by free-body diagram of moment in conjunction with laminated plate theory. The stress level at onset of delamination was also determined by acoustic emission in tension test. In compression test, both free edges of each specimen were visually inspected with the unaided eye in the course of loading, since the antibuckling device used made it difficult to instrument an acoustic emission transducer on the specimen. Upon detection of delamination the specimen was unloaded to subject it to microscopic examination to insure delamination. Figures 48 and 49 show microphotographs of free-edge delamination under applied tension and compression, respectively.

Three families of laminates, which produce compressive σ_z in the presence of tensile in-plane loading, did not show any delamination until final failure. These laminates are: $[0/90/\pm\theta]_s$ with $\theta = 15, 30, 45, 60$, and 75 degrees; $[90_n/\pm30]_s$ with $n = 1$ and 2 ; and $[0/90_n/\pm\theta]_s$ with $n = 1, 2$, and 3 . Since these laminates produce tensile σ_z in the presence of compressive in-plane loading, the $[0/90_n/\pm\theta]_s$ laminates were only tested under compression. All specimens were delaminated as expected. The delamination threshold stresses are listed in Table 61. Table 61 also presents the delamination threshold stresses for a variety of laminates which produce tensile σ_z in the presence of tensile in-plane loading. For the laminates which show no delamination, the magnitude of σ_z appears to be small compared with the interlaminar strength of the material system. Based on experimental results, we can conclude that those laminates having tensile σ_z under in-plane loading will likely be delaminated.

The experimental results also indicate that the delamination threshold stress widely varies depending upon the number of layers for the identical laminates of $[0/\pm45/90]_s$, $[0_2/\pm45_2/90_2]_s$, and $[0_3/\pm45_3/90_3]_s$ as listed in Table 61. Analytical results obtained from the method described in Section IV, subsection 2-E show almost identical distribution of σ_z for the laminates as shown in Figure 50.

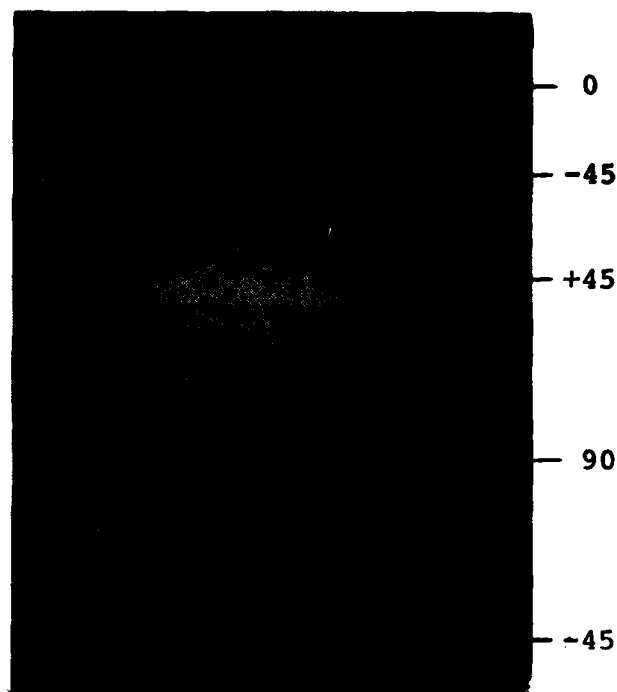


Figure 48. Microphotograph Showing Delamination of a Specimen of $[0/\pm 45/90]_s$ Laminate Under Static Tension.

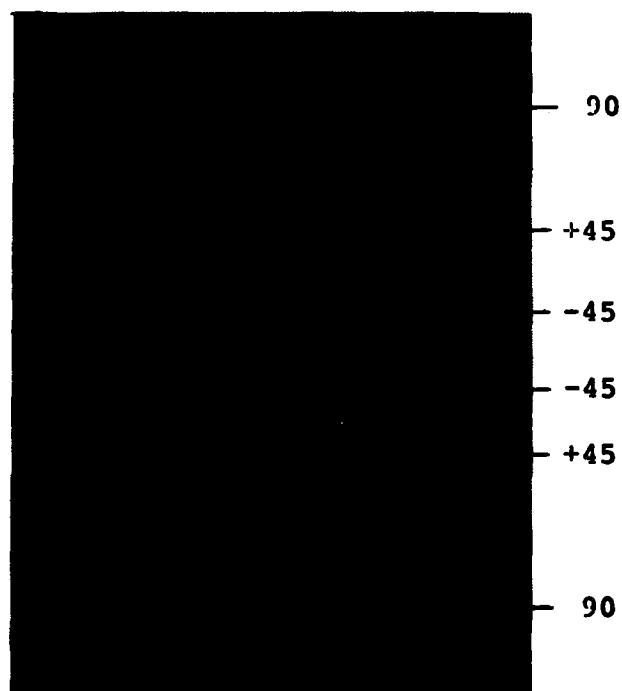


Figure 49. Microphotograph Showing Delamination of a Specimen of $[0/90_3/\pm 45]_s$ Laminate Under Static Compression.

TABLE 61
EXPERIMENTAL RESULTS OF DELAMINATION

Laminate	Type of Axial Load	Axial Stress at Onset of Delamination, ksi	No. of Specimens Tested
$[\pm 30/\overline{90}]_s$	Tension	38.77	7
$[\pm 30/90]_s$	"	30.37	6
$[\pm 30_4/90]_s$	"	20.59	10
$[\pm 30_6/90]_s$	"	18.71	10
$[\pm 45/0/90]_s$	"	39.12	13
$[\pm 45/90/0]_s$	"	52.12	11
$[0/\pm 45/90]_s$	"	53.15	10
$[0/\pm 45/90_3]_s$	"	46.40	10
$[0/\pm 45/90_6]_s$	"	24.66	10
$[0_2/\pm 45_2/90_2]_s$	"	41.99	10
$[0_3/\pm 45_3/90_3]_s$	"	27.33	10
$[0/\pm 45/90]_{2s}$	"	No delamination	8
$[0/\pm 60/90]_s$	"	"	10
$[0/\pm 75/90]_s$	"	"	10
$[0/90/\pm 45]_s$	Compression	51.76	7
$[0/90_3/\pm 45]_s$	"	40.81	10
$[0/90_6/\pm 45]_s$	"	35.43	7

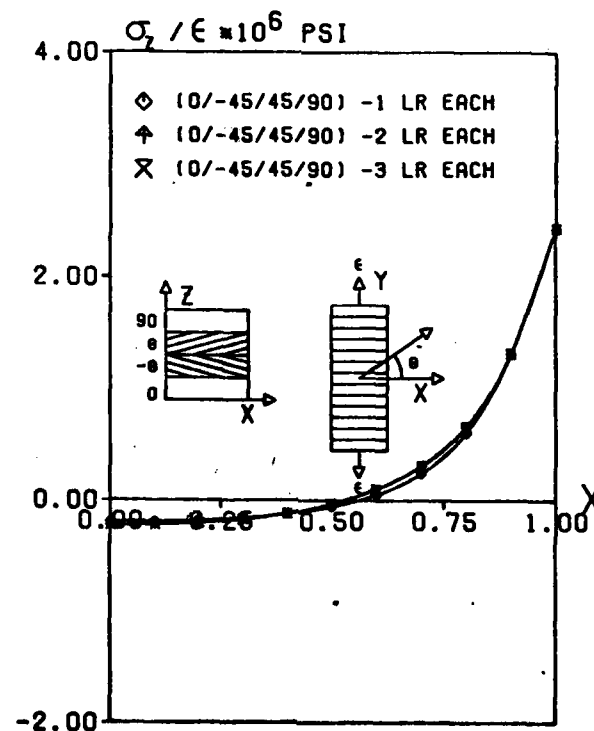


Figure 50. Distribution of Interlaminar Normal Stress in the Free-Edge Region.

B. Transverse Crack and Delamination

An experimental investigation has been conducted on damage behavior related with matrix cracking under static and fatigue loading using two stacking sequences of the $[0/90_n/\pm 45]_s$ and $[0/\pm 45/90_n]_s$ laminates for $n = 1, 3$, and 6 . The latter stacking sequence produces tensile interlaminar normal stress along free edges of a tensile coupon, whereas the other stacking sequence produces compression at the same edges. Emphasis in this study was on the interaction between transverse cracks and delamination, and effect of layer thickness on crack density and propagation. Transverse crack and delamination were periodically measured by interrupting testing until final failure. Experimental results indicate that the crack density and propagation are influenced by layer thickness, and delamination appears to be mainly governed by either or combination of tensile interlaminar normal stress and size of transverse crack. The applied force at incipient delamination can be predicted by an existing theory with a certain limitation for the laminates considered. The details can be found in Appendix B.

C. Effect of Matrix Properties

A series of static tests was conducted on three different types of material systems to study the matrix property dependency at onset of delamination. The three material systems used in this test were AS/Epon 828, AS/MY720, and AS/3502, which were fabricated with $[\pm 30_2/90_2]_s$ orientation. The AS/Epon 828 system exhibits a considerable ductility and AS/MY720 exhibits brittleness. Table 62 shows the experimental results for an average of five specimens of each material system except for longitudinal modulus, which is an average of three specimens. Table 62 clearly indicates that the delamination threshold stress and ultimate strength increase with increasing ductility. During this test, transverse cracks in the 90-degree layer were also monitored on the free edges of three specimens of each material system. The crack density, defined as number of cracks divided by measured length, is shown in Figure 51. The transverse crack

TABLE 62
SUMMARY OF TEST RESULTS

Material System	Stress Level at Onset of Delamination, ksi	Ultimate Strength, ksi	E_L 10^6 psi
AS/828	33.96	43.91	7.15
AS/3502	31.47	39.46	7.93
AS/MY720	22.49	35.55	7.34

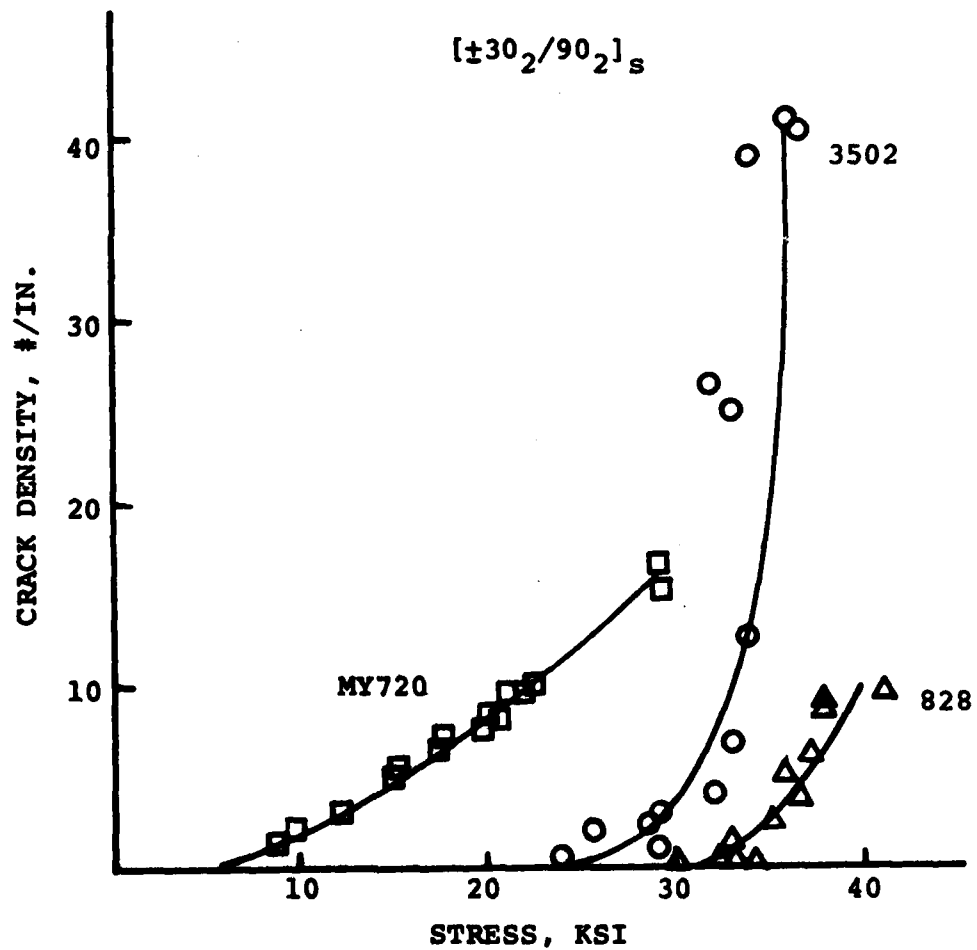


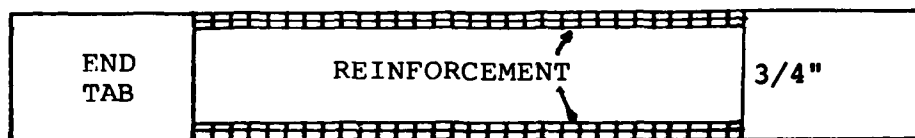
Figure 51. Crack Density vs. Applied Stress for 90-Degree Layer; Composite Data of Three Specimens for Each Material System.

threshold stress also increases with ductility. The reason for higher crack density of the AS/3502 system is not clear at present.

D. Prevention of Delamination

Since the presence of the tensile interlaminar normal stress, σ_z , at free-edge regions is mainly responsible for cause of delamination, one can prevent the delamination by suppressing σ_z with a kind of reinforcement of free edges. The main interest of this program was to develop such a reinforcement to prevent delamination under static and fatigue loading. The material system used in this test was T300/5208 graphite/epoxy with $[0/\pm 45/90]_s$ orientation which exhibits an extensive delamination before final failure. The free edges of a tensile coupon were reinforced with fiberglass woven cloth using Epon 828 adhesive. Figure 52 shows the details of the reinforced specimen. Each specimen was tested with monitoring of acoustic emission under static loading. Some specimens were unloaded at the prescribed stress level to examine the free edges under a microscope. After removing the specimen from the loading frame, the reinforcement material was removed and the free edges were polished to facilitate microscopic examination. Figure 53 shows the microphotographs of the free edge and indicates the applied stress level at the moment the photographs were taken. The reinforced specimen does not show any evidence of delamination, whereas extensive delamination occurred in the unreinforced specimen. Figure 54 shows the comparison of acoustic emission signal in the reinforced specimen with that in the unreinforced specimen. The sporadic acoustic emission signal, without a sudden increase in the reinforced specimen until final failure, indicates that the specimen failed without any delamination. Figure 55 shows the stress-strain behavior for both specimens. The strain behavior is unique up to final failure in the reinforced specimen, whereas the strain, especially transverse strain, was drastically changed after delamination in the unreinforced specimen.

To insure this technique in fatigue loading, a reinforced specimen was tested under tension-tension fatigue with the



REINFORCEMENT MATERIAL: FIBERGLASS CLOTH
ADHESIVE: EPON 828

Figure 52. Details of Reinforced Specimen.



STRESS 60 KSI
UNREINFORCED



STRESS 80 KSI
REINFORCED

Figure 53. Microphotographs Showing Delamination of
[0/±45/90]_s Laminate Under Static Tension.

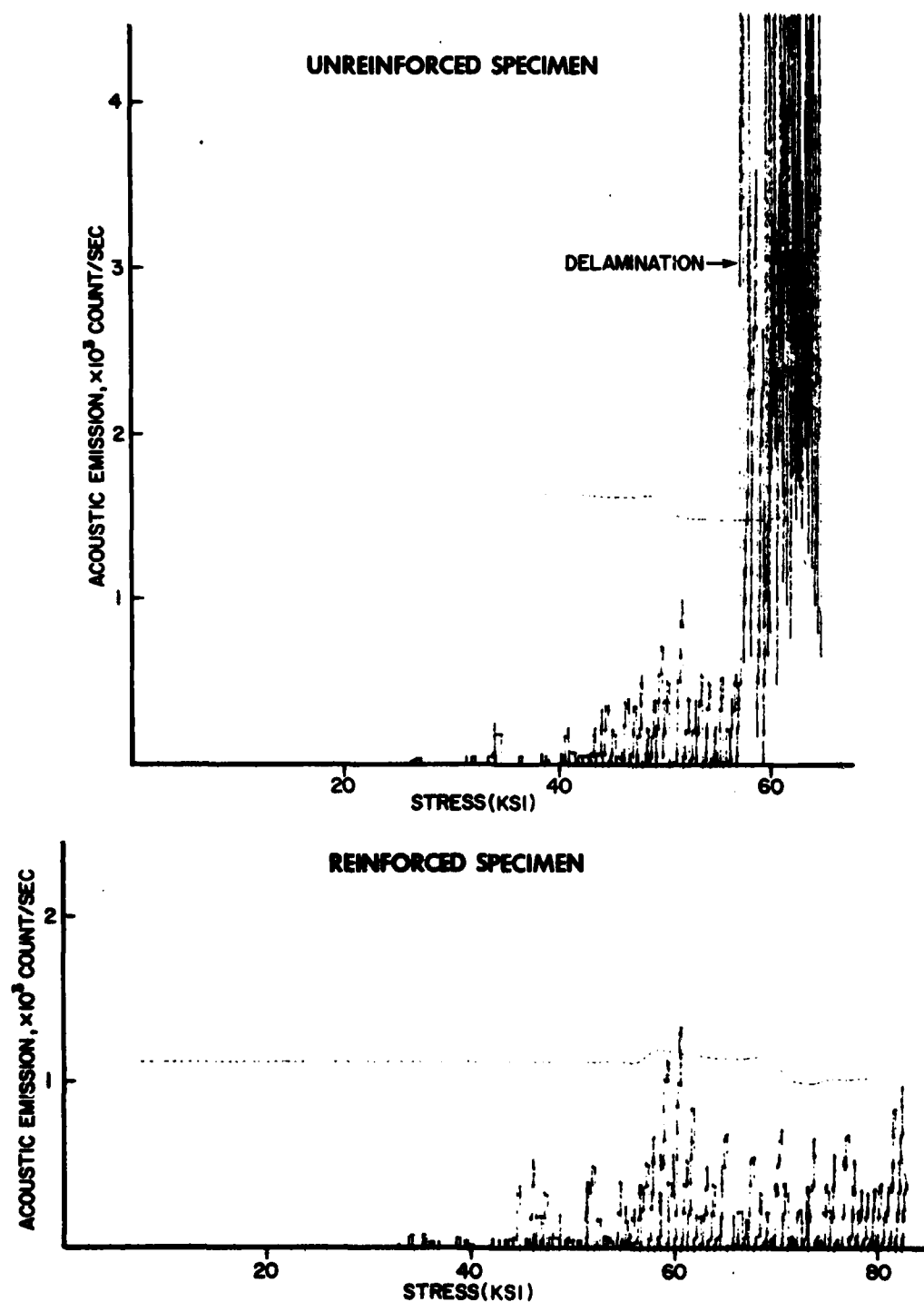


Figure 54. Comparison of Acoustic Emission Signal of an Unreinforced Specimen to a Reinforced Specimen for $[0/\pm 45/90]_s$ Laminate.

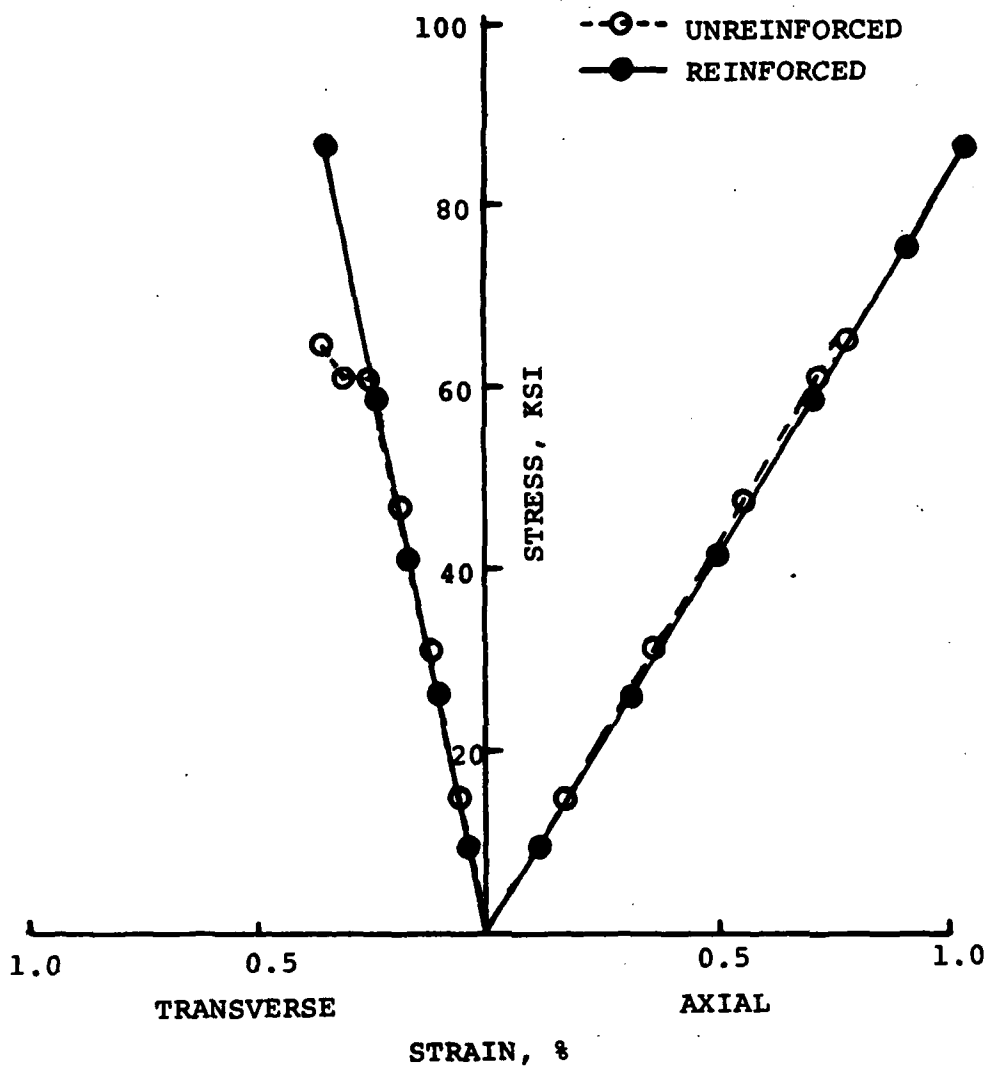


Figure 55. Stress vs. Strain for the Unreinforced and Reinforced Specimen of the $[0/\pm 45/90]_s$ Laminate.

maximum fatigue stress, $S_{\max} = 50$ ksi, up to 1.5 million cycles and removed from the loading frame to subject it to nondestructive evaluation. An unreinforced specimen was fatigued with $S_{\max} = 50$ ksi up to 10,000 cycles. Figures 56 to 58 show the comparison of microphotograph, x-ray, and stress strain behavior of these two specimens. An examination of Figures 56 to 58 reveals that the technique is also quite effective in fatigue cases. Table 63 shows the tensile strength of the reinforced and unreinforced specimens of $[0/\pm 45/90]_s$ and $[0/90/\pm 45]_s$ laminates. In the $[0/90/\pm 45]_s$ laminate, which does not reveal delamination under static loading, the strengths of both reinforced and unreinforced specimens are practically identical. In the $[0/\pm 45/90]_s$ laminate with the reinforced edges, the detrimental effect of delamination to the laminate strength was eliminated.

TABLE 63
TENSILE STRENGTH: MEAN OF 10 SPECIMENS

Laminate	Edge Reinforcement	Strength, ksi
$[0/\pm 45/90]_s$	without	64.65
	with	83.68
$[0/90/\pm 45]_s$	without	83.09
	with	85.80

E. Free-Edge Analysis: Global-Local Laminate Variational Principle

(1) Introduction

The principal problem of interest in the present investigation is the same as that treated in Reference 69, i.e. the stress analysis of a composite laminate built of anisotropic elastic layers of uniform thickness and subjected to prescribed tractions and/or displacements on its boundary surface. The body is bounded by a cylindrical edge surface and upper and lower faces



10^4 CYCLE AT $S_{\max} = 50$ KSI
UNREINFORCED



1.5×10^6 CYCLE AT $S_{\max} = 50$ KSI
REINFORCED

Figure 56. Microphotographs Showing Delamination of $[0/\pm 45/90]_s$ Laminate Under Fatigue Loading at $S_{\max} = 50$ ksi.



10^4 CYCLE AT $S_{\max} = 50$ KSI
UNREINFORCED



1.5×10^6 CYCLE AT $S_{\max} = 50$ KSI
REINFORCED

Figure 57. X-ray Pictures Showing Extension of Delamination Toward the Middle of $[0/\pm 45/90]_s$ Specimen Width Under Fatigue Loading.

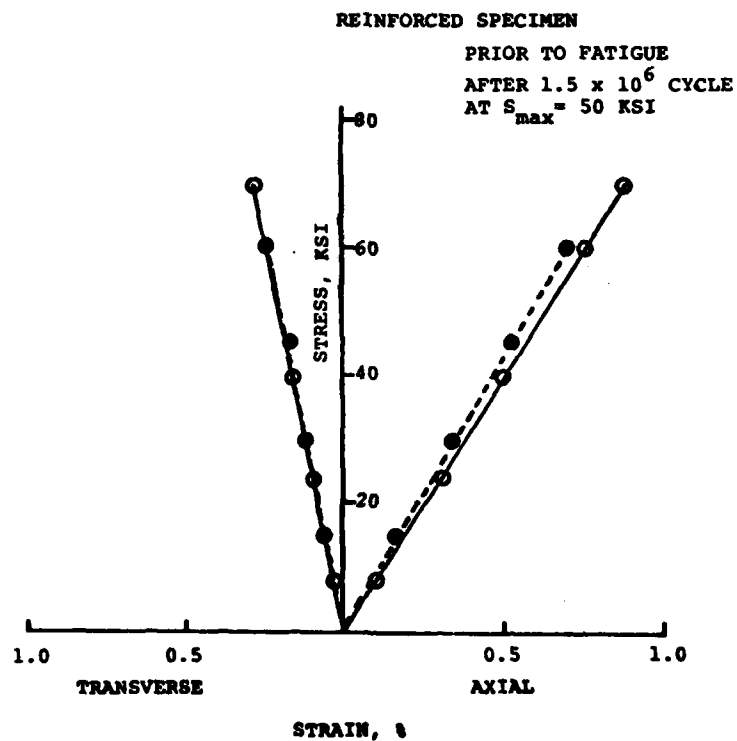
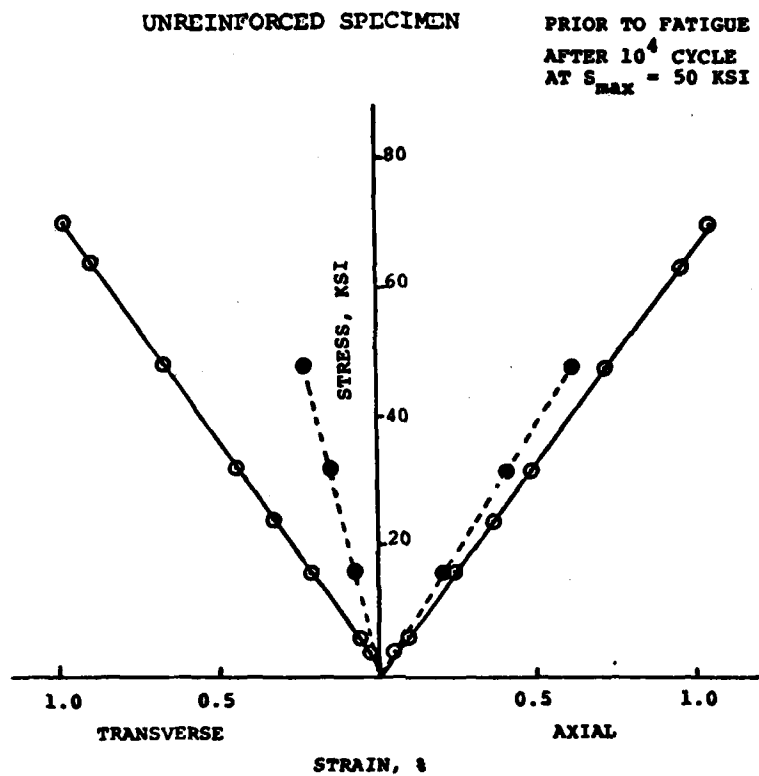


Figure 58. Stress vs. Strain Prior to and After Fatigue of $[0/\pm 45/90]_s$ Laminate.

that are parallel to the interfacial planes. This assumption is made only for convenience in writing the governing equations. There is no difficulty in extending the model to include laminates of variable thickness.

In practical applications, numerous layers may be present (use of 100 layers in aircraft structures is not unusual). Contemporary models are incapable of providing precise resolution of the local stress fields in the vicinity of stress raisers under such conditions. Global models, which follow from an assumed, usually elementary, displacement field, lead to the definition of effective (or smeared) laminate moduli and are not sufficiently accurate for stress field computation.⁽⁶⁹⁾ On the other hand local models, in which each layer is represented as a homogeneous, anisotropic continuum, become intractable as the number of layers becomes even moderately large, in some methods as few as four layers, results in technical/economic barriers to accurate stress resolution. In this work we blend these concepts into a self-consistent model which can define detailed response functions in a particular, predetermined region of interest (local), while representing the remainder of the domain by effective properties (global). Such dual representations are not without precedent in solid mechanics. For example, Gurtin⁽⁷⁰⁾ discussed this approach with reference to the solution of crack-tip stress field problems.

Wand and Crossman⁽⁷¹⁾ used an effective modulus representation of regions of a laminate; however, only the extensional response of the regions were considered, i.e., the flexural and flexural-extension coupling characteristics of laminated bodies were ignored. Hence, that approach fails to provide correct solutions to certain trivial laminate problems for which exact solutions are available. Stanton et. al.⁽⁷²⁾ used a global representation based upon a three-dimensional laminate model developed by Pagano⁽⁷³⁾ which is based upon the assumption that the stress field is only a function of one space coordinate. This is a generalization and improvement of the material model

given in Reference 71; however, this approach is not convenient for coupling with the model presented earlier.⁽⁶⁹⁾ Furthermore, it is desirable to retain the model⁽⁷⁴⁾ as a special degenerate case of a global model since that result was shown to produce very good agreement for transverse normal stress σ_z with a known elasticity solution.

There have been several investigations on the interlaminar stress fields in laminated composites. Pagano⁽⁶⁹⁾ has given a detailed description of the relevant literature in this field. A recent review article⁽⁷⁵⁾ by Salamon presents an up-to-date literature survey on related topics as of 1980. In this present discussion, reference will be made only to those publications which are not covered by References 69 and 75. Spilker and Ting⁽⁷⁶⁾ have conducted the static and dynamic analysis of composite laminates using hybrid stress finite elements. Raju et. al.⁽⁷⁷⁾ have investigated the free edge stresses in layered plates using eight node isoparametric elements. In both of these publications, the laminate idealization for a reasonably accurate finite element analysis had to be very fine; i.e. a quarter of the laminate has to be divided into about 600 elements. No more than four layers, half thickness, were considered for numerical calculations. For a moderately large number of plies, (say 10), these approaches will lead to computer storage/economic difficulties.

Blumberg et. al.⁽⁷⁸⁾ used the assumed stress fields along the thickness of each layer in the laminate. The governing equations of equilibrium for stiff lamina layers and soft binding polymeric material layers were obtained using separate theories. The resulting differential equations were solved by boundary function techniques defining these functions at three regions along the width of the laminate. An iterative procedure was developed to compute the interlaminar stress components.

Partsevskii⁽⁷⁹⁾ has presented an approximate treatment of a free-edge problem in composite laminates. It has been shown that the results computed by this technique agree with those of Reference 74.

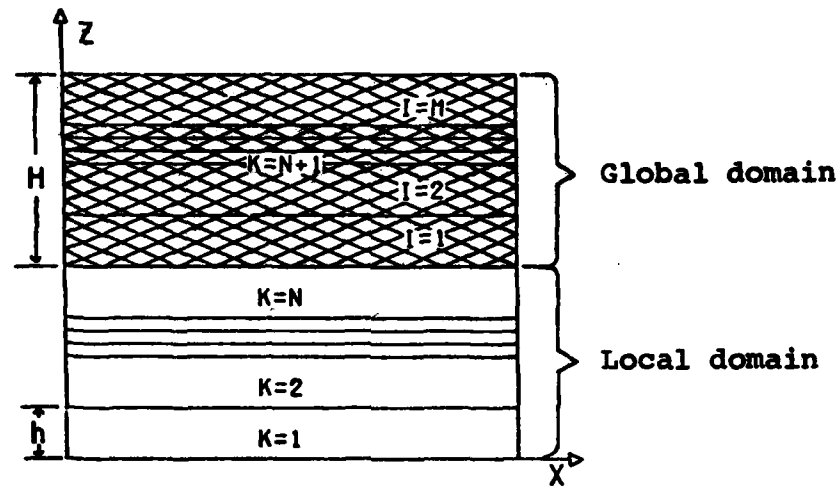
(2) Numerical Results

It has already been shown⁽⁶⁹⁾ that the model developed on the basis of Reissner functional works very well. For a limited number of layers in the laminate, the computer program gives excellent results; whereas for laminates with a moderately large number of layers, computational difficulties were encountered. In the following section the results are presented for different laminates to show that the present global-local model gives satisfactory stress fields in the region of interest for laminates consisting of any number of layers. To accomplish this a large number of laminates have been analyzed using a different number of layers in the local and the global regions. For the computation of results, T300/5208 graphite/epoxy material with the following material properties has been considered:

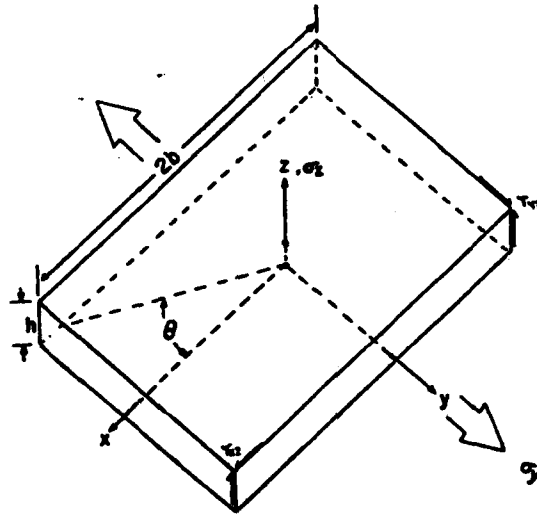
$$\begin{aligned} E_{11} &= 20 \times 10^6 \text{ psi}, E_{22} = 1.4 \times 10^6 \text{ psi} \\ G_{12} &= G_{13} = 0.8 \times 10^6 \text{ psi}, G_{23} = 0.6 \times 10^6 \text{ psi} \\ \nu_{12} &= \nu_{13} = 0.3, \nu_{23} = 0.6 \end{aligned}$$

In most of the earlier investigations, ν_{12} , ν_{13} , and ν_{23} have been taken to be of the same magnitude. Some experiments were conducted in the Materials Laboratory of the Air Force Wright Aeronautical Laboratories (AFWAL/ML), and it was found that ν_{23} was considerably higher than ν_{12} and ν_{13} , and its value turned out to be approximately 0.6.

Using the global-local model, results for a large number of laminates were computed. A comparison between the results by the present theory and the existing theory⁽⁶⁹⁾ shows that the concepts put forth herein work extremely well. A representative case of such a comparison is given in Figure 60. This figure gives the transverse normal stress component $\sigma_z / (\epsilon \times 10^6) \text{ psi}$ along the width of the laminate due to an applied strain ϵ along y-axis, for three different models of a $[0/(\pm 60)_2]_s$ -laminate. The coordinate axes, angle notation and stacking sequence notation should be clear from Figures 59a and 59b.



(a) Half of the laminate thickness showing the plies in the global domain and the local domain.



(b) Coordinate axes in each ply in the laminate.

Figure 59. Coordinate System Used for the Free-Edge Stress Analysis.

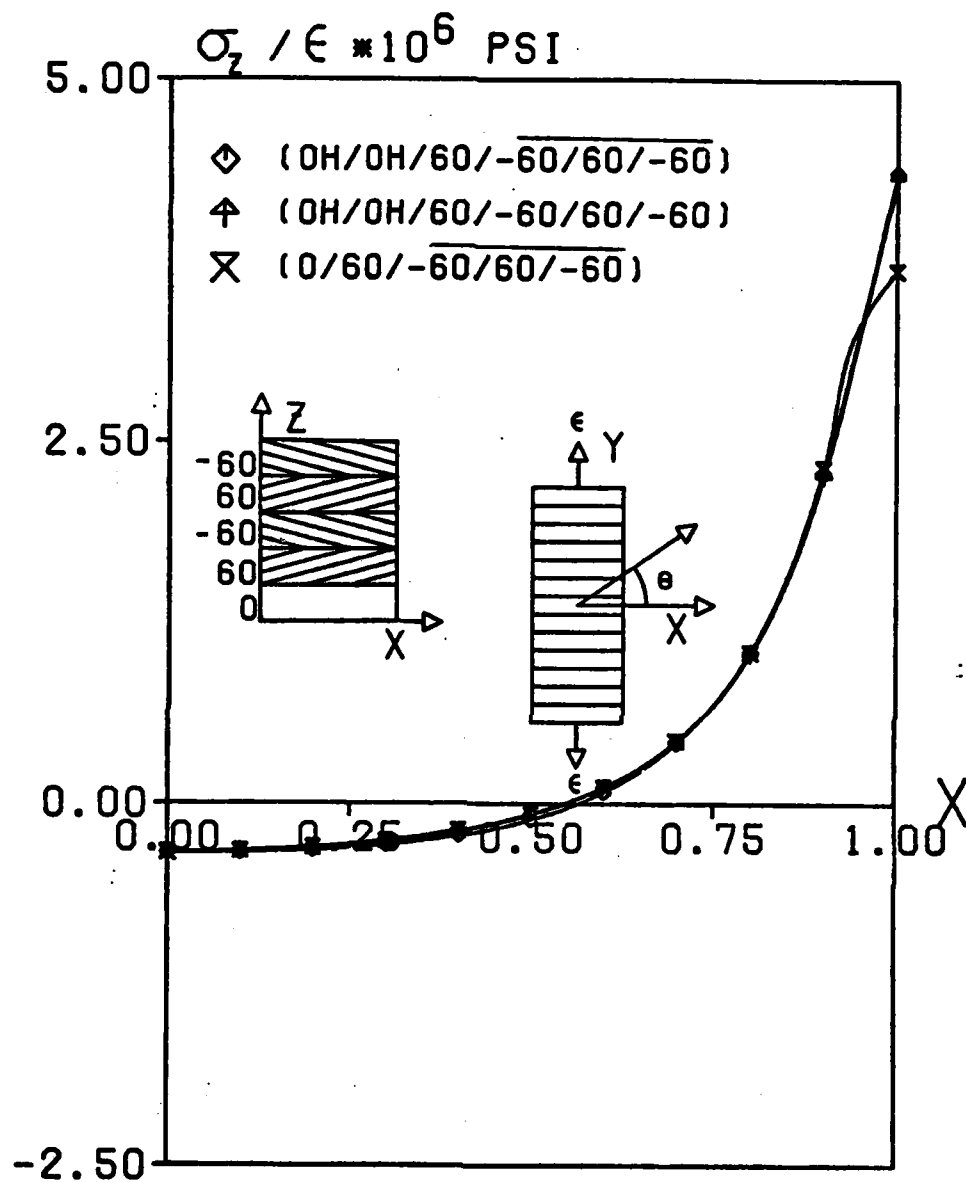


Figure 60. Distribution of Interlaminar Normal Stress in the Free-Edge Region.

In Figures 60 and 61, an H following a numeral in the description of symbols represents one-half of the layer with corresponding orientation (number) in degrees. A bar over a set of numbers represents the layers taken in the global domain. The stacking sequence for the global domain is the same as shown in Figure 59a. The width of the horizontal axis is equal to the total thickness of the laminate, so that $X = 1$ represents the free edge of the laminate. Figure 61 shows the distribution of $\sigma_z / (e \times 10^6)$ psi versus X for $[0/(\pm 60)_n]$, $n = 1, 2, 4$ laminates. A Fortran digital algorithm has been developed to conduct these computations. The program computes stress fields at different layers of the laminate at various points along the width.

Advantages of the present model are as follows:

1. The present model can give stress fields for laminates with any number of layers. The other methods run into computational/economical difficulties.
2. The present model takes considerably less time than that in Reference 69, which itself is a very effective and efficient model.

3. FATIGUE STUDY

A fatigue program has been initiated to obtain fatigue data for evaluation of the effect of delamination on fatigue life and residual strength. The tensile interlaminar normal stress at the free edge is primarily responsible for the initiation of delamination, whereas the interlaminar compression may not cause delamination. The sign and magnitude of the interlaminar normal stress is dependent upon the stacking sequence of a laminate. In this program, a quasi-isotropic laminate with two stacking sequences was chosen to produce interlaminar tension or compression. One stacking sequence was $[0/\pm 45/90]_g$, which produces interlaminar tension under applied uniaxial tension and interlaminar compression under applied uniaxial compression. Therefore, this stacking sequence specimen shows delamination under

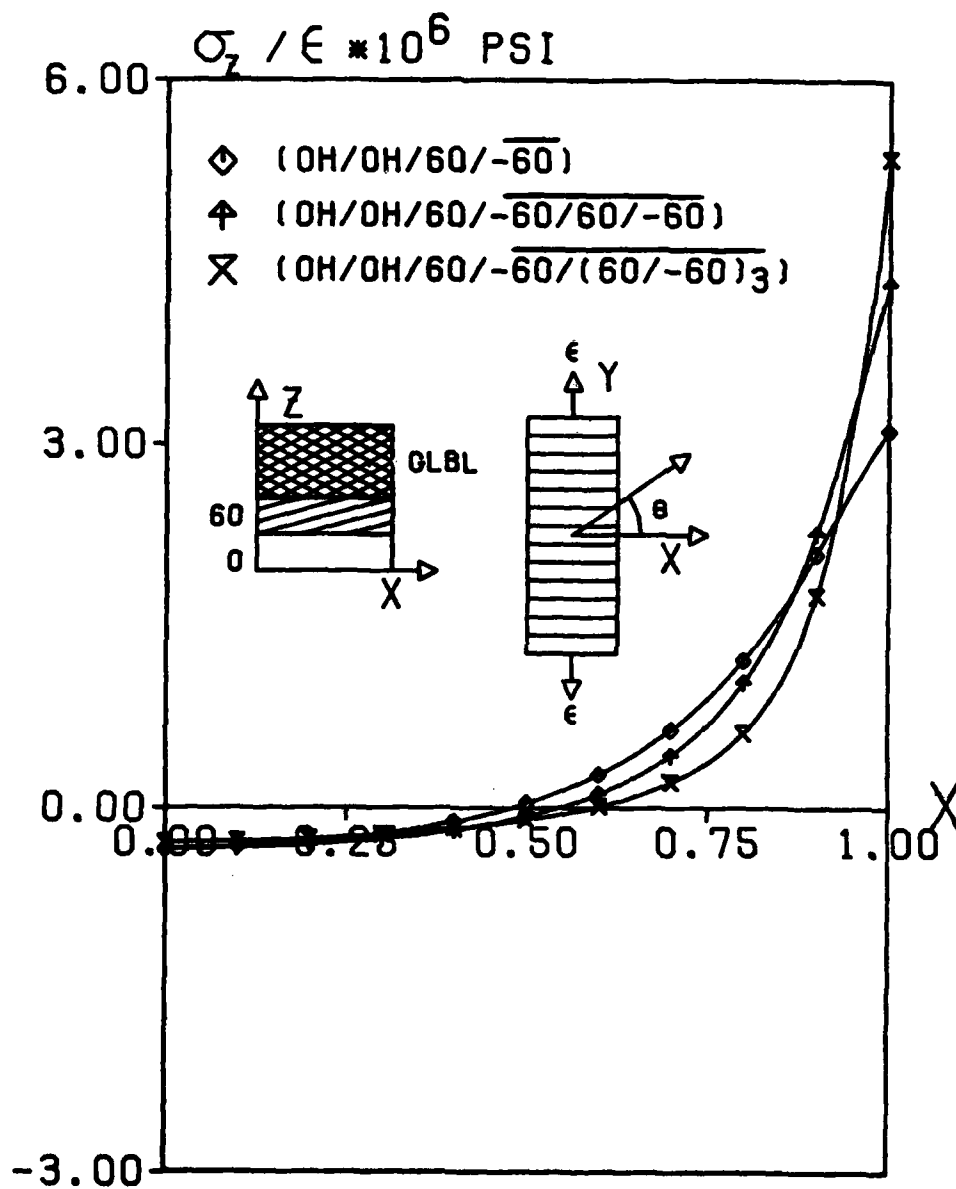


Figure 61. Distribution of Interlaminar Normal Stress in the Free-Edge Region.

tension but not under compression. The second stacking sequence was $[0/90/\pm 45]_s$, which produces interlaminar compression under applied uniaxial tension and interlaminar tension under applied compression.

The material system used in this test was T300/5208 graphite/epoxy. A straight-sided coupon specimen, $3/4$ " wide and 5" long in gage section, was adopted for static compression and compression-compression fatigue test. A side support device was used to prevent specimen buckling. All specimens were tested using MTS loading frames with 10 Hz of frequency and $R = 0.1$ in both tension-tension and compression-compression fatigue. Two fatigue stress levels considered were 50 and 60 ksi. A total of 10 specimens were tested for each condition. In the $[0/\pm 45/90]_s$ laminate, an extensive delamination occurred under static tension but did not occur under static compression as expected. In the $[0/90/\pm 45]_s$ laminate, delamination was observed only under static compression and confined to the free-edge regions without showing any further extension until final failure.

In the fatigue test, propagation of delamination varies widely depending upon signs of fatigue loading, maximum fatigue stress, and stacking sequence. All specimens of the $[0/\pm 45/90]_s$ laminate under tension-tension fatigue were completely delaminated in the early stage of fatigue life. In spite of the existence of compressive interlaminar normal stress in the $[0/90/\pm 45]_s$ laminate under tension-tension fatigue, delamination occurred in the late stage of fatigue life and its extension was relatively slow. Figure 62 shows a typical x-ray picture showing delamination in a specimen of the $[0/90/\pm 45]_s$ laminate after five million cycles at $S_{max} = 50$ ksi of tension-tension fatigue.

In compression-compression fatigue, none of the specimens of the $[0/\pm 45/90]_s$ laminate show delamination, but all specimens of the $[0/90/\pm 45]_s$ laminate show delamination which remained stationary until final failure.

AD-A114 069

DAYTON UNIV OH RESEARCH INST

F/G 11/4

IMPROVED MATERIALS FOR COMPOSITES AND ADHESIVES.(U)

DEC 81 D ASKINS, A BEHME, A BIERMANN, W CLICK F33615-78-C-5102

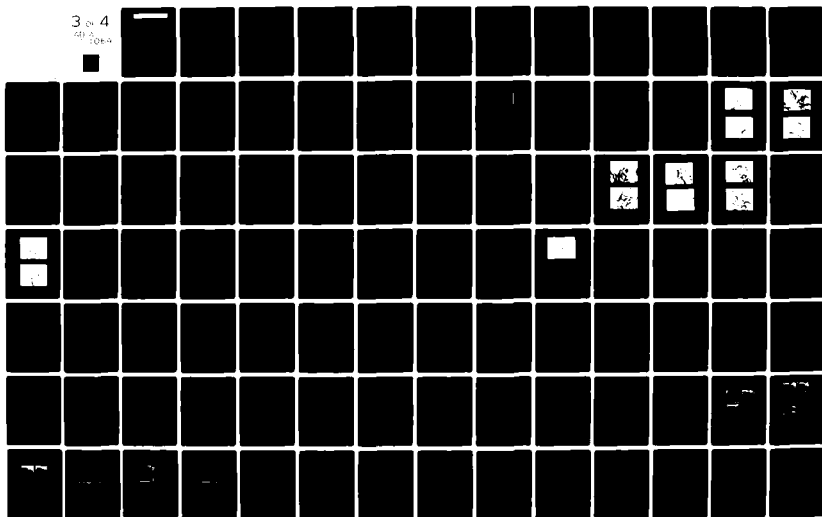
UNCLASSIFIED

UDR-TR-81-108

AFWAL-TR-81-4154

NL

3 of 4
000004





 5×10^6 cycle at $S_{\max} = 50$ ksi

Figure 62. X-ray Picture Showing Delamination of a $[0/90/\pm 45]_s$ Laminate Under Fatigue Loading.

A maximum likelihood estimation was employed to analyze static and fatigue life data. Table 64 shows the summary of static test results.

TABLE 64
STATIC TEST RESULTS

Laminate	Type of Loading	Mean Strength ksi	Weibull Parameters	
			α	β , ksi
$[0/\pm 45/90]_s$	Tension	66.07	16.5	68.61
	Compression	77.01	17.3	79.08
$[0/90/\pm 45]_s$	Tension	82.34	18.0	84.44
	Compression	81.07	12.2	84.33

In the $[0/\pm 45/90]_s$ laminate, the compressive strength is greater than the tensile strength; whereas in the $[0/90/\pm 45]_s$ laminate, the static strengths in tension and compression appear to be practically identical.

In fatigue data, those specimens which survived after five million cycles were subjected to residual strength tests and included in Weibull parameter estimation using a censoring technique. Table 65 shows the summary of fatigue test results. Average of the residual strength after five million cycles at $S_{\max} = 50$ ksi was found to be 70.13 ksi for the $[0/\pm 45/90]_s$ laminate and 74.50 ksi for the $[0/90/\pm 45]_s$ laminate.

TABLE 65
FATIGUE TEST RESULTS

Laminate	Type of Loading	Maximum Fatigue Stress, ksi	Weibull Parameters	
			α	β , cycle
[0/ \pm 45/90] _s	Tension-Tension	50	0.56	15,444,000 ⁽⁶⁾
	Tension-Tension	60	0.43	32,100
	Compression-Compression	50	1.21	20,500
	Compression-Compression	60	1.07	2,306
[0/90/ \pm 45] _s	Tension-Tension	50	1.29	3,467,000 ⁽²⁾
	Tension-Tension	60	1.40	65,100
	Compression-Compression	50	0.97	59,600
	Compression-Compression	60	0.97	9,000

Note: The numerals in the last column in parentheses indicate the number of specimens which survived after 5×10^6 cycles.

Scatter of fatigue life data appears to be severe for those specimens showing an extensive delamination. Based on the scale parameters estimated from the experimental data, the detrimental effect of delamination on fatigue life is inconclusive. The experimental results also show a drastic reduction in fatigue life under compression-compression fatigue. It is noted that most of the specimens were broken at the unsupported area under compression-compression fatigue.

4. ADHESIVE BONDED JOINT

A finite element technique is used to conduct the stress analysis of adhesively-bonded scarf joints. Both three-dimensional linear analysis and two-dimensional nonlinear analysis are conducted using the NASTRAN, a general purpose finite element computer code. The analytical results were compared with the experimental results obtained previously. An aluminum specimen, 1 in. (2.54 cm) wide and 0.25 in. (0.54 cm) thick, was bonded

using FM123-2 structural adhesive film. It is observed that a stress concentration in both normal and shear components of less than six percent exists in the adhesive layer near the ends of the scarf. The detailed results and discussion are given in Appendix C.

SECTION V

TRAVELING WAVE TUBES

1. CHARACTERIZATION OF CATHODES

Impregnated dispenser cathode construction is based on a matrix of tungsten particles which are sintered to a density of approximately 80 percent. The resulting porous body is impregnated with a mixture of BaO, CaO and Al_2O_3 . At operating temperatures, a monolayer of barium on the outermost surface of the cathode acts to lower the work function and thereby enables the cathode to sustain useful electron emission. During the useful life of the cathode, loss by evaporation is overcome by the dispensing action of the porous tungsten which continuously replenishes the surface from the BaO supply stored in the impregnant.

The work during this period was aimed at the determination of failure modes of the interior parts of traveling wave tubes, in particular those of cathodes. This was accomplished with studies of the barium evaporation rate from cathodes, and the elemental distribution in the outer surface of cathodes during an activation cycle. The instrument used for this purpose was a combination of a Physical Electronics Industries Auger electron spectrometer (AES) and an Extranuclear Laboratories secondary ion mass spectrometer (SIMS) with a 3M minibeam ion gun. Both spectrometers were placed in an Ultek belljar and ion pump system which is illustrated schematically in Figure 63. Residual gas analysis was also available.

The following cathode activation studies and other tasks were completed:

- a) The Philips M dispenser cathode (AES-RGA)
- b) Sample preparation and oxide cathode mounting for ion scattering spectroscopy (ISS)
- c) The Semicon 3:1:1 dispenser cathode (SIMS)
- d) The WJ#3 oxide cathode (SIMS)
- e) Cathode alloy D429, Cathode alloy 200 (Ni-Mn) (SIMS)

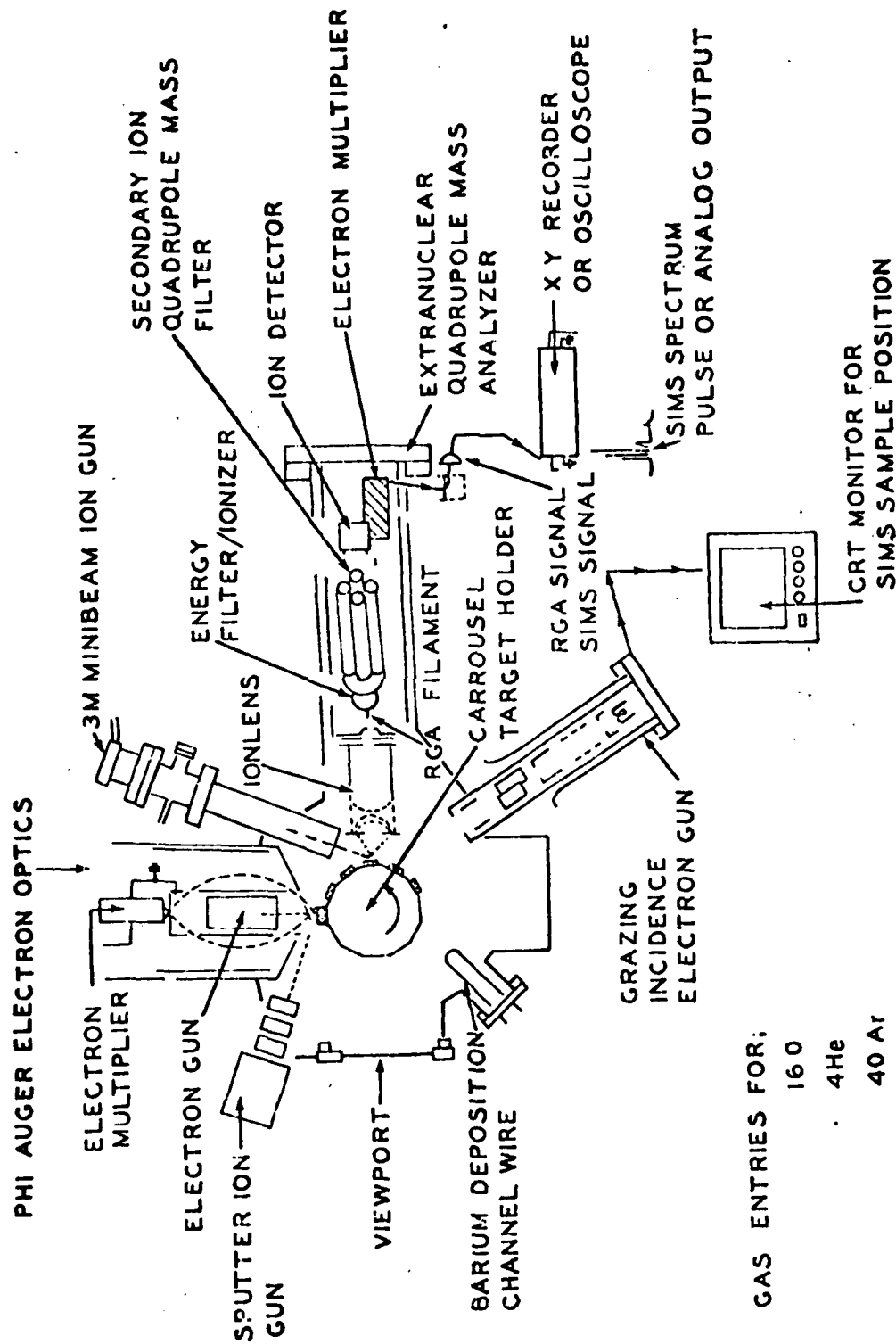


Figure 63. Schematic of Combined AES and SIMS Instrument for the Characterization of TWT Components.

- f) Semicon 1:1:1 dispenser cathode (SIMS)
- g) Spectra-Mat 5:3:2 dispenser cathode (SIMS)
- h) Cathode surface imitations by Ba and BaO depositions on tungsten foils (AES-SIMS)
- i) AEG Telefunken 6:1:1 dispenser cathode (SIMS)
- j) Sputter rate determinations of an argon beam (SIMS)

The operating characteristics of a cathode rely on its surface properties during activation and, therefore, SIMS was used primarily to monitor the Ba/BaO ratio since Ba is thought to migrate to the surface during activation. Because the Ba layer was thought to be only one atom thick, a low damage He ion probing beam was used. This technique was originally called "static SIMS" and later referred to as "low damage SIMS". This technique is designed to analyze the first atomic layer on a surface. Since the impregnant of a dispenser cathode also contains BaO, the low damage technique should be capable of distinguishing between the state of Ba on the surface versus the bulk. The conditions established for low damage ion beam bombardment were:

- a) ^4He as the sputter gas in a static vacuum of 1×10^{-5} to 1×10^{-6} torr partial pressure of He
- b) Beam currents less than 30 nA
- c) Rastering the ion beam while gating a pulse signal in order to overcome signal contributions of crater walls produced by the ion beam

The low damage ion beam SIMS technique was applied to the characterization of Semicon 5:3:2 and AEG Telefunken 6:1:1 cathodes. In the latter case Ba^+ ($m/e = 138$) and BaO^+ ($m/e = 154$) peaks were monitored for one hour with the cathode at room temperature. During this time the BaO^+/Ba^+ ratio had a value of 0.5. Single step heating to 1100°C changed this ratio to 0.013 within a few minutes. Soon after the BaO^+ signal was no longer detected. At the same time the Ba^+ signal increased by four.

The BaO^+ signal did not disappear when an argon beam (40 nA beam current) was used to probe the surface during activation.

These results indicate that the cathode has a monolayer coverage of Ba metal during activation which fits the currently accepted model of an impregnated tungsten cathode illustrated in Figure 64.

A. Evaporation Rates

One factor which effects TWT life is the evaporation rate of barium from the cathode surface. A method of studying evaporation rates is the vapor collect method which relies upon the attenuation of the Auger peak intensity of a collector due to the presence of barium from the cathode.

Plotting the ratio of the Auger peak height of the adsorbate to the substrate as a function of time of deposition permits determination of the growth mechanism and the determination of the monolayer growth point. In some cases the number of breaks in the plot gives the growth mechanism while the first break point gives the time at which a monolayer has been achieved.

The presence of more than one break point indicates a layer by layer growth (Franck-van der Merwe mechanism). The presence of one and only one break point indicates a crystalline growth on top of a monolayer (or Stranski-Krastanov mechanism). The last mechanism is a crystalline growth directly on the substrate or a Volmer-Weber mechanism where no break points exist. Figure 65 illustrates the three growth mechanisms.

In the calculation of evaporation rates, it is necessary to have either a Franck-van der Merwe or a Stranski-Krastanov growth mechanism to determine the time for the growth of the first monolayer.

The configuration of the vapor collect method is illustrated in Figure 66.

The collection of the evaporant occurs in ultrahigh vacuum (UHV) which eliminates any residual gas effects. In this work the ultrahigh vacuum system was that of a Physical Electronics model 545 scanning Auger microprobe. An assumption is made that the radiant flux density of atoms is omni-directional (diffuse radiation).

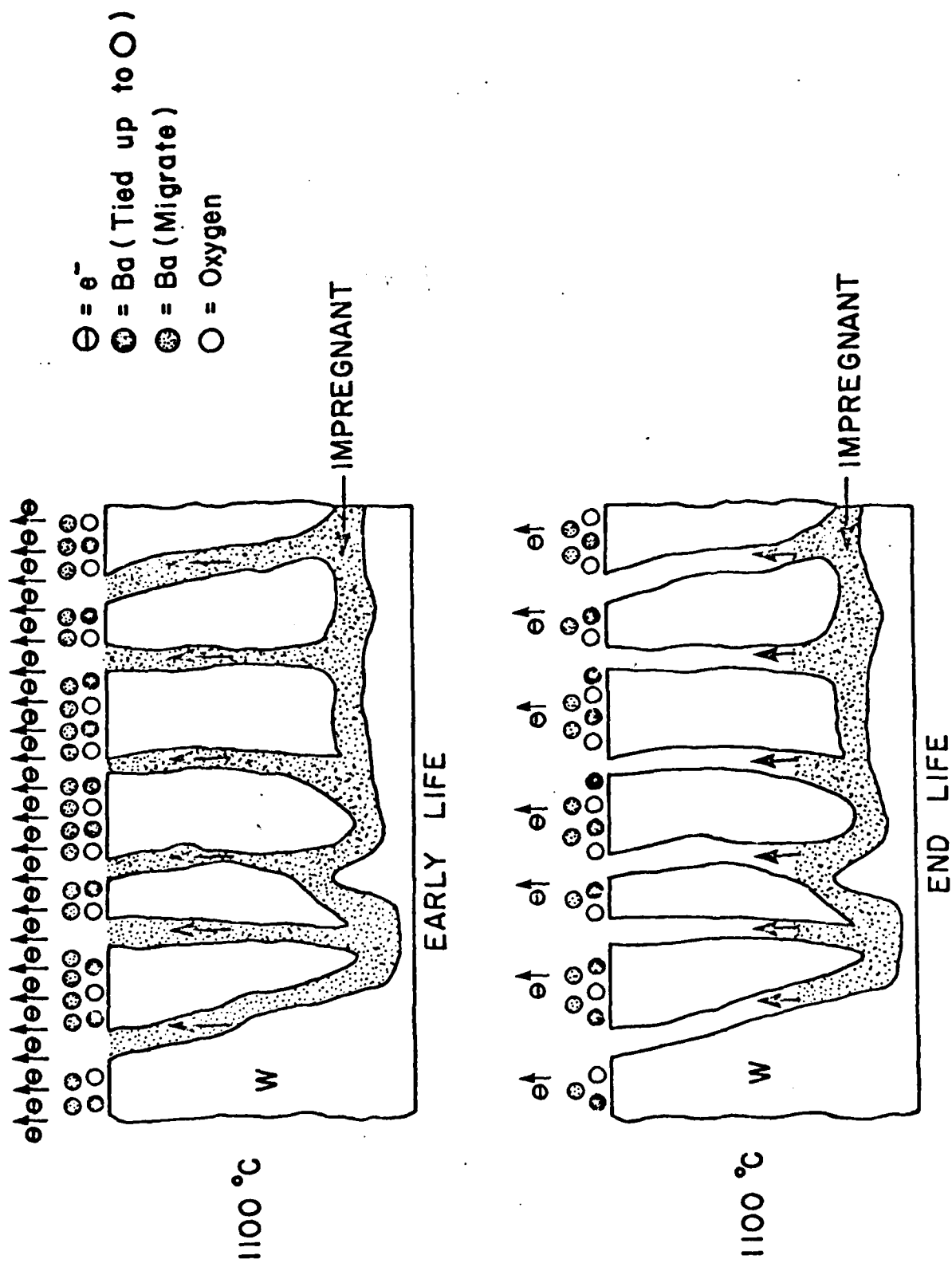


Figure 64. Model of Impregnated Tungsten Cathode According to Forman. (80)

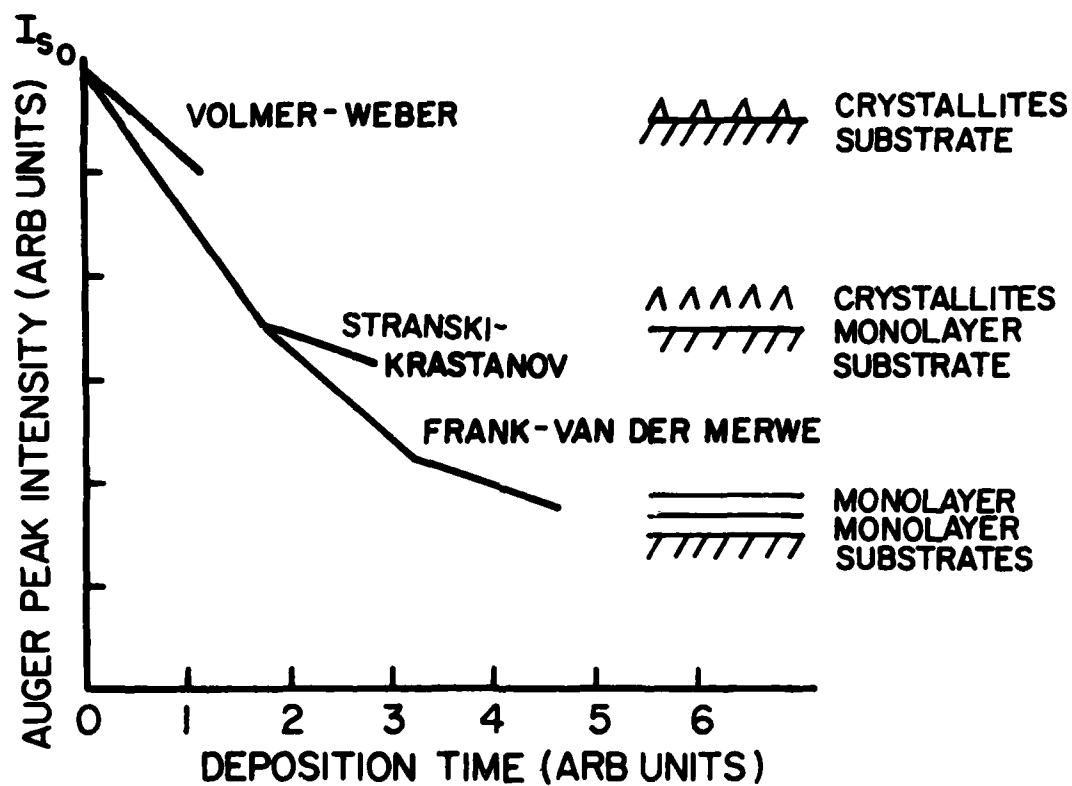


Figure 65. Three Possible Growth Mechanisms of Adsorbate on Substrate.

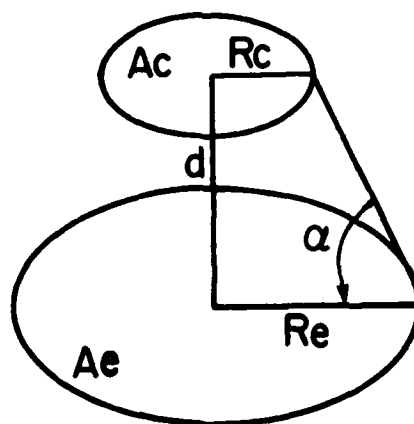


Figure 66. Assumed Collector - Cathode Configuration.

The total quantity of atoms $N_{E,C}^i(t, t + \Delta t; T)$ emitted from the surface in a time t to $t + \Delta t$ is given by Verhoeven and Doveren⁽⁸¹⁾ as

$$N_{E,C}^i(t, t + \Delta t; T) = F(E,C)A_E \int_{\Delta t} \dot{n}_E^i(t, T) \beta^i dt$$

where \dot{n}_E^i is the number of particles i emitted per cm^2 per second at time t from the cathode area A_E . To account for the configuration of the best apparatus, an angle factor, $F(E,C)$, must be included. β^i is the sticking probability. Generally β^i is assumed to be unity for those methods.

Since Auger analysis gives the concentration C_C^i of materials on the collector rather than $N_{E,C}^i$, the factor which modifies the relationship is the collected area A_C . With this modification the relationship becomes

$$C_C^i = \frac{N_{E,C}^i(t, t + \Delta t, T)}{A_C} = \text{Fac}(E,C) \int \dot{n}_E^i(t, T) \beta^i dt$$

where $\text{Fac}(E,C) = F(E,C) \frac{A_E}{A_C}$

In the experimental geometry maintained in the tests, the latter factor $\text{Fac}(E,C)$ can be written

$$\text{Fac}(E,C) = \frac{R_E^2}{R_E^2 + d^2} = \cos^2 \alpha$$

Now the evaporation rate $\dot{n}(T)$ of the metal i can be described in terms of the maximum evaporation rate at the equilibrium vapor pressure p in Torr, the molecular mass m in grams, the absolute temperature T and the evaporation coefficient. In metals which form atomic vapors the evaporation coefficient is approximately unit. Now relating the vapor pressure to the standard heat of evaporation ΔH_v^o (cal mole^{-1}) and the standard entropy of evaporation ($\text{cal mole}^{-1} \text{ deg}^{-1}$),

$$\log p = \frac{-1}{4.524} \left(\frac{\Delta H_v^o}{T} - \Delta S_v^o + 2.88 \right)$$

The above form can be viewed as satisfying the following relation

$$\log p = A - \frac{B}{T} \text{ where}$$

$$A = \frac{\Delta S_{V0} - 2.88}{4.524} \text{ and } B = \frac{\Delta H_{V0}}{4.524}$$

From a plot of $\log p$ versus $1/T$ the value of $\Delta H^{\circ}v$ can be determined from the slope of the line by using the relationship

$$\Delta H_{V0} = 4.574 \text{ or } \frac{d(\log p)}{d(1/t)} = 4.574B$$

Several different collector materials were tried. Among these were polycrystalline Ni foil, W foil, polished polycrystalline Ta and finally a single crystal of W (110).

The nickel foil suffered extreme deformation when heated by electron bombardment. This deformation prevented a uniform surface for collection of evaporants. The initial use of polycrystalline W foil was suspended because of the concern for evaporation of tungsten from the cathode surface. The polished Ta surface appeared to be an ideal collecting surface except the observed growth mechanism was Volmer-Weber type which gave no break points. However, the Ta collection flag did serve a useful function by indicating the lack of W as a evaporation product from the cathodes. The final collector flag material was a single crystal of W (110) which was successful.

Cathodes used for the evaporation rate studies were from two manufacturers, Semicon and Spectra-Mat. Three different impregnant mixtures were analyzed. They were 5:3:2, 4:1:1, and 1:1:1 where the ratio A:B:C indicates the mole ratio of BaO, CaO and Al₂O₃.

After activating the cathode according to the manufacturer's procedure, data was collected at 1050, 1100, and 1150°C as measured by a Pt/6 percent Rh versus Pt/30 percent thermocouple connected to an Omega Model 299 digital readout. A summary of the cathodes analyzed is presented in Table 66. It

TABLE 66
EVAPORATION RATES
(Atoms/cm²/sec)

Cathode	Temperature					Comments
	950	1000	1050	1100	1150	
Semicon 5:3:2	--	--	2.9×10^{11}	5.1×10^{11}	1.5×10^{12}	
Spectra-Mat 5:3:2	--	--	5.3×10^{11}	1.6×10^{12}	2.5×10^{12}	
Spectra-Mat 5:3:2	--	--	--	7.5×10^{12}	2.1×10^{13}	
Semicon 1:1:1	--	--	4.8×10^{11}	1.6×10^{12}	2.6×10^{12}	
Spectra-Mat 1:1:1	--	--	--	--	--	Failed to activate
Spectra-Mat 4:1:1	7.4×10^{12}	1.4×10^{13}	3.7×10^{13}	5.2×10^{13}	--	Defective
Semicon 1:1:1	--	--	--	--	--	

should be noted that several cathodes failed to activate properly; therefore, a complete sequence of evaporation rate studies was not performed.

Figures 67, 68, 69, 70 present plots of the ratio of adsorbate/substrate Auger peaks versus time. Generally, the adsorbate was considered to be just Ba; however, in the case of the Semicon 1:1:1 cathode the adsorbate was taken to be both Ca and Ba. In all cases the substrate was considered to be W.

It is evident that the Semicon 5:3:2 cathode required less time to achieve monolayer coverage compared to the two Spectra-Mat 5:3:2 cathodes. However, the heat of evaporation for the Semicon 5:3:2 was about 12 kcal/mole higher than the Spectra-Mat 5:3:2.

The 1:1:1 behaved as expected. It emitted a higher concentration of Ca from the surface. It should be noted that Al was not observed as an evaporation product from any cathode.

A Semicon 1:1:1 and Spectra-Mat 1:1:1 dispenser cathode failed to activate properly. The W collection flag was in place during the activation procedure for the Semicon 1:1:1 cathode. The Auger analysis showed Ag, C, S, O, Ba, Ca, K, Cu and W. The Cu, Ag, and S were not expected. Cu had been observed in some earlier cathode studies and was thought to come from small Cu deposits left behind on the cathode sleeve after spot welding thermocouple leads to the Mo sleeve with Cu electrodes. This problem has been resolved by using W insert electrodes. A possible source of the Cu could be the W billet which holds the impregnant. Cu is used to make machining of the W billet easier but is supposed to be completely removed following machining. Ag and S have not previously been observed following activation, so it appears that the Cu, Ag, and S found came from the cathode surface. These impurities are cathode poisons, and, indeed, no significant emission was obtained from this cathode.

As this particular cathode was defective, it was remounted for Auger analysis. The aperture and a new Semicon 1:1:1 cathode (unpotted, whereas the defective one was potted, but

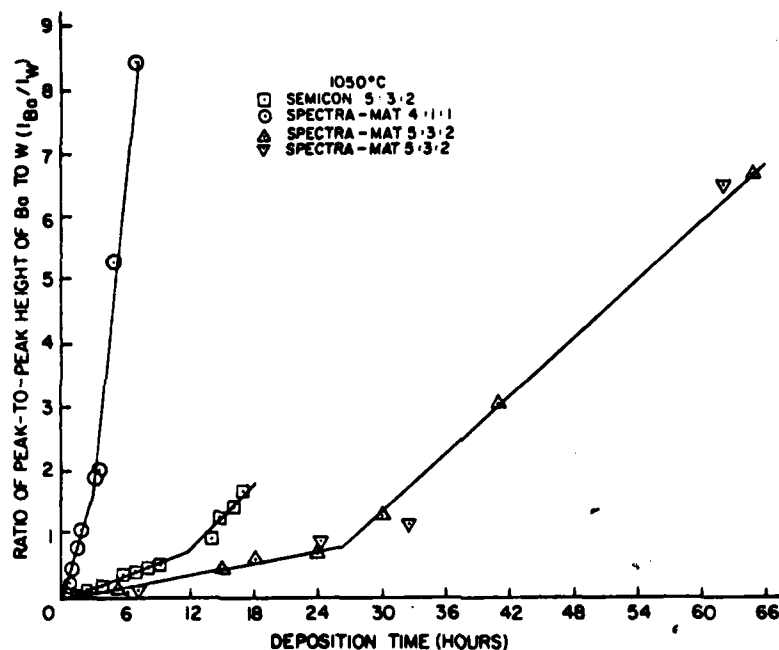


Figure 67. Ratio of Adsorbate to Substrate versus Deposition Time for a Cathode Temperature of 1050°C.

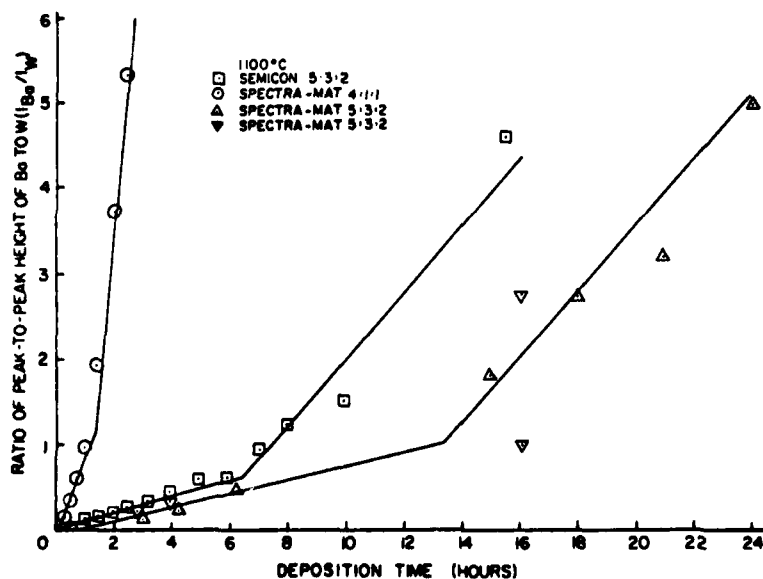


Figure 68. Ratio of Adsorbate to Substrate versus Deposition Time for a Cathode Temperature of 1100°C.

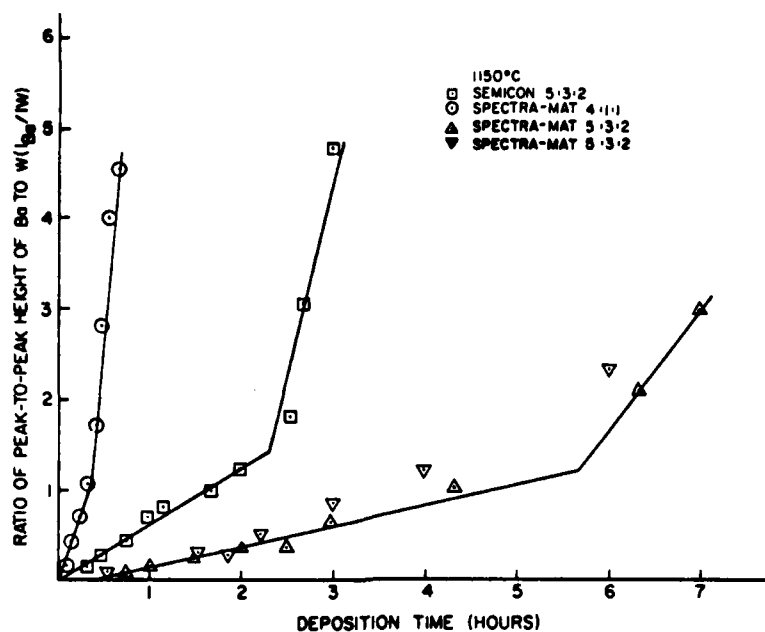


Figure 69. Ratio of Adsorbate to Substrate versus Deposition Time for a Cathode Temperature of 1150°C.

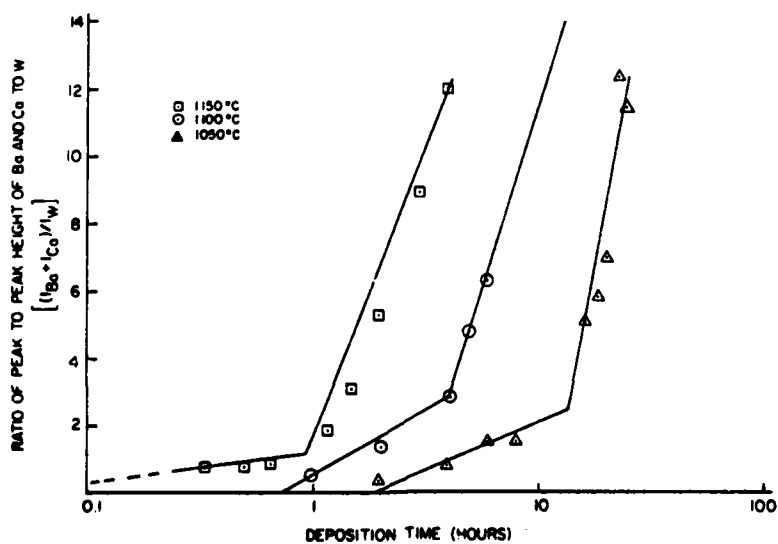


Figure 70. Ratio of Adsorbate to Substrate versus Deposition Time for a Semicon 1:1:1.

having the same lot number) were mounted for Auger analysis. The surface of the defective cathode showed S, C, O, Ba and W, but no Ca, Cu, or Ag were observed. The new unpotted cathode showed C, O, Ca, and W on the surface. The aperture showed S, Cu, C, O, Ba, and Ca on its surface. The proposed evaporation of Cu and Ag from the cathode could not be confirmed from this analysis. However, it appears that the sulfur observed was definitely from the defective cathode surface. The Spectra-Mat 1:1:1 which had failed showed erratic evaporation behavior. A consistent amount of evaporation products could not be obtained. The cathode failed to show significant emission. One possible explanation for this behavior is that this particular molar ratio cathode is not a standard production item for Spectra-Mat, therefore, it had to be compounded specifically.

Another significant problem which arose in the use of Spectra-Mat heater filaments was their high failure rate. Approximately two out of three heater filaments failed. There were generally two modes of failure. The first involved the breakage of the uninsulated pigtail of the two ends of the heater filament. The second mode was a shorting of the filament upon application of current. Upon closer examination of the coating on the heater filaments, it was determined that most of the filaments had very thin coating of insulating material. Some appeared to be bare in certain areas. The Semicon heater filaments did not appear to be plagued with these problems.

As evident from the summary table, a clear pattern as to the evaporation rate and molar concentration cannot be ascertained. Also, there appears to be very small agreement among the same molar concentration cathodes. These discrepancies may be the result of other factors not considered. These factors may be the porosity of the tungsten billet, contamination of the surface, and purity of material used as impregnant.

Future studies should deal with the control of the aforementioned factors. Also, residual gas analyses studies will be performed to discover which species are coming from the cathode surface.

B. Scanning Low Energy Electron Probe

Most surfaces do not have the same work function at every point on the surface. These variations in work function can affect the functioning of electronic devices. A method of studying the variation of the work function across a surface is the scanning low energy electron probe (SLEEP). The basic principle of the SLEEP technique is similar to the method used by Anderson⁽⁸²⁾ to measure contact potential between two surfaces.

Figure 71 illustrates schematically the operation of a SLEEP unit; however, the exact electronics to be used in the SLEEP unit attached to the scanning Auger microprobe (SAM) have not been finalized.

Figure 72 illustrates the idealized potential profile through which the electron beam has to travel from the electron source to the target. The electron beam travels from a surface with a work function ϕ_c on the electron source to an area of work function ϕ_{T1} on the target. Generally, ϕ_c will be the space-charge barrier in front of the electron source; V_c the external voltage applied between Fermi levels E_{fc} and E_{ft} of the electron source and target, respectively. The quantity $E_B = (\phi_c - V_c)$ is the energy that an electron leaving the electron source with zero kinetic energy has with respect to the Fermi level of the target. As E_B is reduced and becomes less than ϕ_{T1} , some electrons in the beam are repelled, and the beam is in the "retarding field region". Now assuming an ideal half-Maxwellian distribution of normal velocities, and if no perturbations exist in the normal velocity distribution, the current I vs. E_B for electrons incident on an area of work function ϕ_{T1} would follow the relation,

$$I = \begin{cases} I_m \exp \left[\frac{E_B - \phi_{T1}}{KT_c} \right], & \text{for } E_B < \phi_{T1} \\ I_m & , \text{for } E_B \geq \phi_{T1} \end{cases}$$

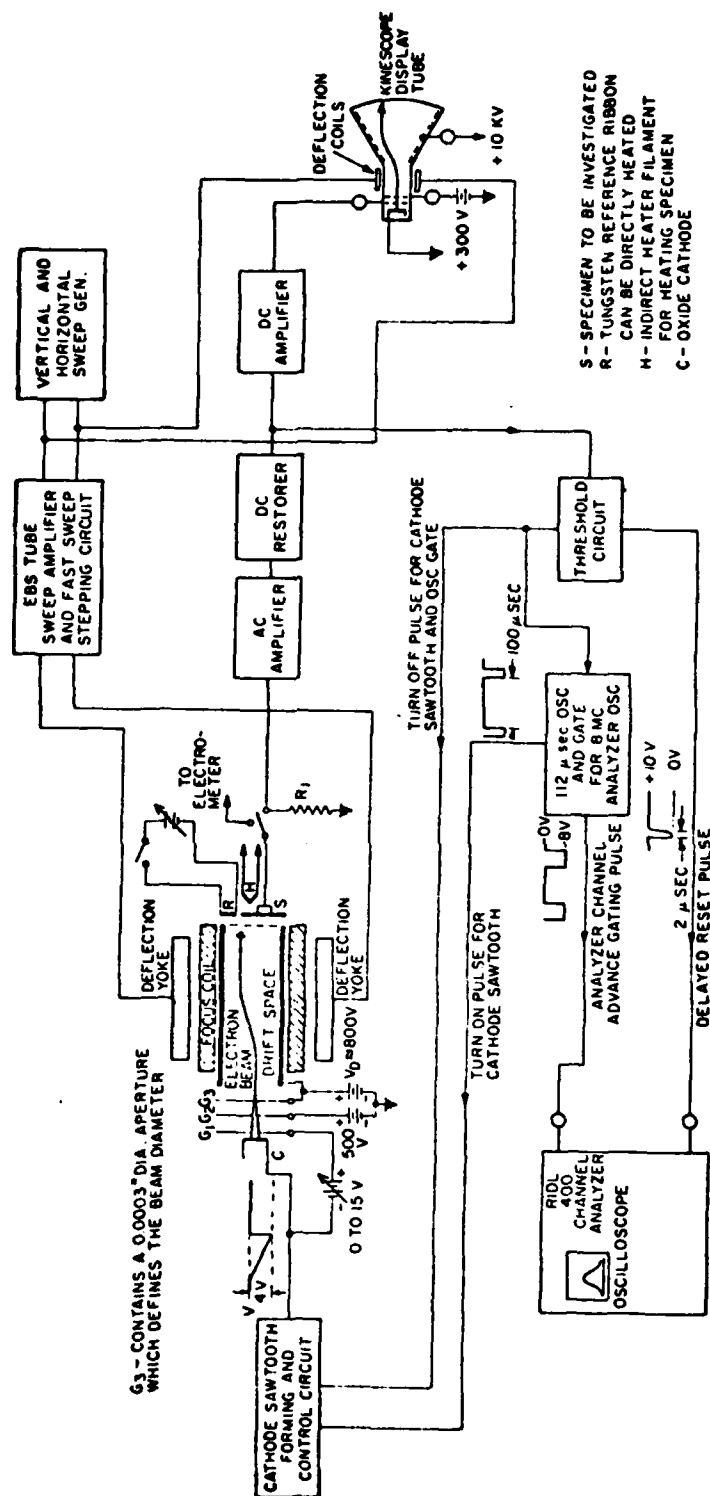


Figure 71. Schematic of Electron-Beam Scanning Tube and Associated Circuitry.

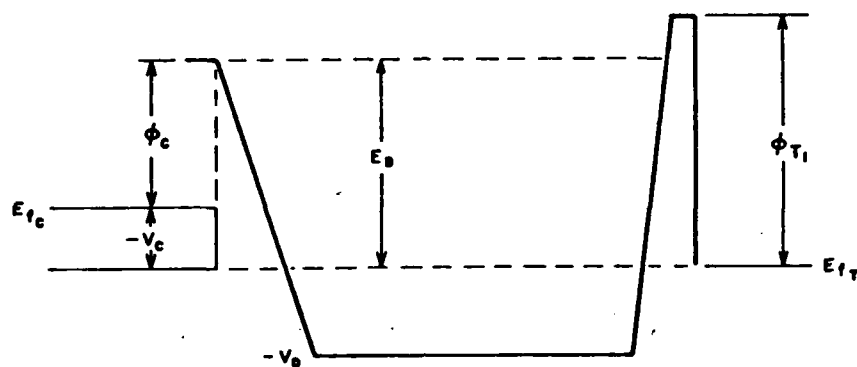


Figure 72. Idealized Potential Profile Over the Electron-Beam Path in the Electron-Beam Scanning Tube.

where k is Boltzmann's constant and T_c is the temperature of the electron source. Figure 73 illustrates the physical configuration of the SLEEP unit which will be attached to the system of the scanning Auger microprobe. The electron gun configuration is illustrated in Figure 74.

C. BaCO₃, BaO, and Ba Metal Studies

Few studies have been done to establish the binding energies of the Ba_{3d} or Ba_{M₄N_{4,5}N_{4,5}} levels in Ba metal, BaO, or BaCO₃. These values are important to our work on characterizing cathode surfaces, both before and after activation. This study was therefore undertaken to obtain relative measurements of these compounds in our instrument and an attempt was made to relate these values to absolute values of binding and kinetic energies. The instrument used for these determinations was a KRATOS ES300 X-ray photoelectron spectrometer. The base pressure was 3×10^{-10} Torr (4×10^{-8} Pa).

The procedure was as follows:

The first method that was used involved the decomposition of BaCO₃ to BaO. This transition occurs upon heating to 1000°C for 20 minutes.⁽⁸³⁾ The BaCO₃ powder (ultrapure, ALFA) was slurried in distilled water to the consistency of a thick milk. It was then transferred to two tungsten ribbons (0.0005" x 0.040") using a glass stirring rod. The ribbons had previously been spotwelded to niobium wires and the entire assembly placed in a 10^{-6} Torr vacuum, where the tungsten ribbons were outgassed at about 1250°C using 5 1/2 - 6 amps of current for 30 minutes.

Scans were taken of the BaCO₃ powder both before and during heating to 1000°C. Before heating, the Ba_{3d} and O_{1s} peaks were seen as doublets with about 4eV separation. This was probably due to sample charging. Because of this charging phenomenon, Ba_{3d} and O_{1s} peak positions could not be accurately measured, but the Ba_{3d}-Ba_{M₄N_{4,5}N_{4,5}} peak separation was found to be 123.5eV with a standard deviation of 0.2eV.

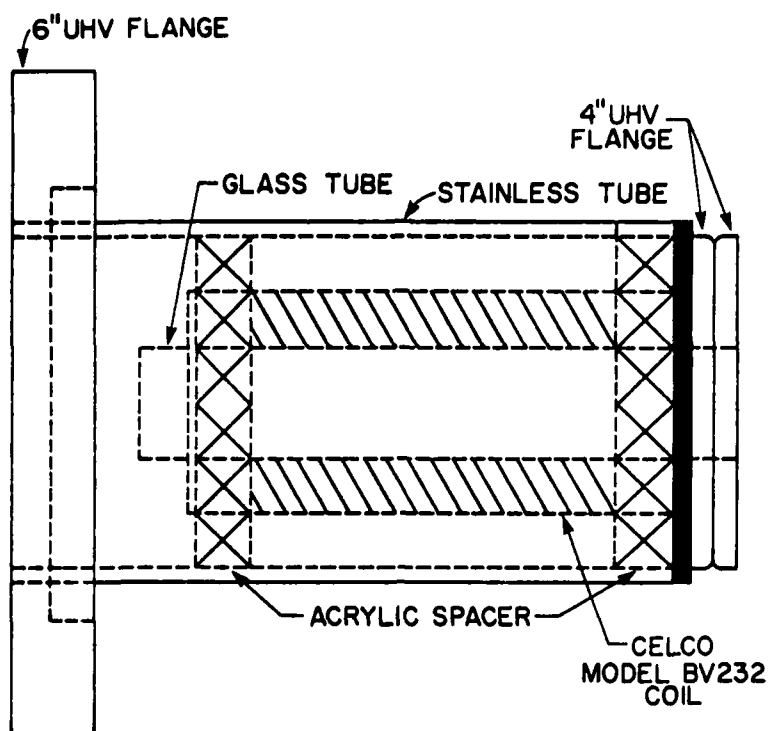


Figure 73. Vacuum Mounting Hardware for Scanning Low Energy Electron Probe (SLEEP).

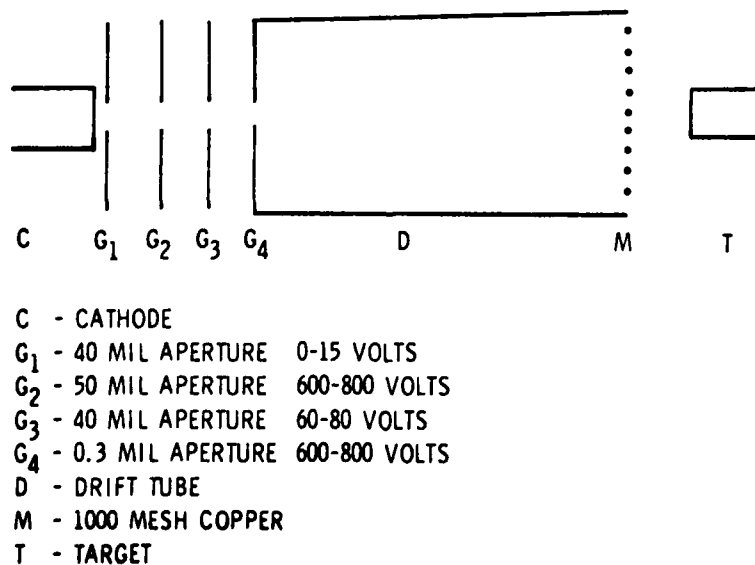


Figure 74. Electron Gun Configuration for SLEEP.

A second method of producing BaO was then utilized. The same type of tungsten ribbon was used as a sample holder and flashed repeatedly to high temperature (1300°C) in the vacuum chamber until no pressure rise was noticed. High resolution scans of O_{1s} showed oxygen starting to build up 5 minutes after flashing. A commercial barium source, consisting of a barium-metal alloy held in an iron channel, was then heated to about 700°C for 1-3 minutes to deposit barium metal onto the tungsten ribbons. Scans were taken immediately after the barium source was heated to insure that no oxygen would react with the Ba metal before analysis was complete. Scans were taken of Ba_{3d} , Ba_{MNN} , O_{1s} , W_{4f} , and then the Ba_{3d} scan was repeated to see if the peak had shifted. More barium was then evaporated, scans of Ba_{3d} were taken, the high voltage power supplies were placed on standby, and the chamber was backfilled with research grade O_2 to 5×10^{-7} Torr. Since the diffusion pump cannot be valved off from the main chamber, a continuous flow of oxygen was maintained for 5 minutes. Scans of Ba_{3d} , Ba_{MNN} , O_{1s} , W_{4f} and a wide scan were then repeated. This entire procedure was repeated three times, the third time, however, only the Ba_{3d} peaks were monitored.

To calibrate the instrument and convert the measured kinetic energies to binding energies, gold and palladium metal foils were used as standards. The foils were heated to 400°C for one hour prior to analysis and analyzed while still hot. The values obtained for the barium data were identified using either of these standards, i.e., assigning the $Au_{4f_{7/2}}$ peak to 83.8eV BE,⁽⁸⁴⁾ or setting the Pd_{4d} edge to 0.0eV BE,⁽⁸⁵⁾ giving a value for the $PD_{3d_{5/2}}$ of 335.2eV BE. As a check of the linearity of the analyzer supply, a copper foil was analyzed at 400°C. The values obtained for the copper peaks were as follows:
 $Cu_{2p_{3/2}}$, 932.8eV BE, $Cu_{L_{3M_{4,5}M_{4,5}}}$ 918.4eV KE.

The modified Auger parameter (α') is defined as α' and $\alpha' BaO = BE_{XPS \text{ peak}} + KE_{Auger \text{ peak}}$.⁽⁸⁶⁾ From this work, α'_{Ba}

metal (1381.7eV) and α' BaO (1378.0eV) are within 0.5eV of those reported by van Doveren⁽⁸⁷⁾ (1381.3eV) and Lampert et al⁽⁸⁸⁾ (1381.7eV) for barium metal and within 0.7eV for the BaO measurements of van Doveren (1377.5eV) and Wagner et al⁽⁸³⁾ (1377.35eV). Lampert et al found a value of 1378.2eV for the oxidized thin films, but a different value (1377.2eV) for BaO pressed powders.

The values obtained for the $Ba_{3d_{5/2}}$ peak positions of Ba metal ($780.65 \pm 0.15\text{eV}$) and BaO ($779.75 \pm 0.15\text{eV}$) are in good agreement with those of Wagner et al (779.65eV for BaO) and Sinharoy⁽⁸⁹⁾ (779.4eV for BaO), but are quite different from the others (van Doveren: Barium metal 779.1eV, BaO 778.9eV; Lampert et al: barium metal 779.8eV, BaO 779.0eV). This is no doubt due to a difference in linearity of the analyzer power supplies used by each investigator, since each group referenced the $Au_{4f_{7/2}}$ peak to 83.8eV. The magnitude of the metal-oxide shift was found to be -0.9eV BE, compared with -0.5eV reported by Lampert et al and -0.2eV reported by van Doveren.

D. SEM Studies

The SEM studies extended from tungsten powders used in the making of billets to the examination of impregnated dispenser cathodes. The first phase of this work was to examine the particle shapes and measure the particle sizes of tungsten powders. The next phase was to observe the particle shapes in porous green billets of tungsten. The last phase was to examine the emitter surface of impregnated dispenser cathodes.

E. Phase 1

It is believed that the sizes and shapes of the particles affect the quality of cathodes by controlling the effluence rate of barium from the cathode and the quantity of barium that can be emitted by the interconnectivity of the pores. More simply stated, it is believed that the particle size affects the emission rate and lifetime of the cathode. For these reasons, it is logical to size the particles and to see the effects of sorting, to determine the particle size distribution,

their average size, and the standard deviation. Also, particle shapes need to be determined because presently the particles are sized by a sedimentation method. This method is not accurate in sizing particles if their shapes are different. This is because the spherically shaped particles have a larger surface area than box shaped particles, hence during sedimentation will settle more slowly and would be measured larger than box shaped particles. Four tungsten powders were analyzed for particle shape changes caused by the sorting and deconglomeration process. Two of the tungsten powders were not sorted or deconglomerated, the other two tungsten powders were processed through different sorting and deconglomeration processes. Figure 75 is a micrograph of G.E. tungsten powder before sorting and deconglomeration. Figure 76 is a micrograph of G.E. sorted tungsten powder after deconglomeration and sorting to 5.5 - 6.5 μm . Comparing Figures 75 and 76 it can be seen that particle shapes have not been affected but that a few of the fine particles have been sorted out. Figure 77 is a Sylvania tungsten powder before sorting and deconglomeration. Figure 78 is the powder after the same process. Comparing Figures 77 and 78 it can be seen that the particle shapes have changed to rougher rounded edges and most of the fine particles have been removed in sorting. Table 66 lists the measured average particle size of 79 powders sorted to various expected values. It can be seen from the table that the average particle size of the G.E. 5.5-6.5 μm nominal size powder is actually 5.2 μm and that for the Sylvania 5.5-6.5 μm nominal size is 4.5 μm . This discrepancy in sorting is due to a greater boundary layer around the rough rounded edges of the particles in the Sylvania powder (Figure 78) than around the sharp edges of the G.E. powder (Figure 75). Powder samples 1-8 and 21-25 will be made into cathodes and tested for correlations between particle shapes and sizes, and their performance.

The particle sizes in Table 67 are reported as the average length of the maximum and minimum dimensions of the particles on the micrographs. The data was fitted to Weibull



Figure 75. Micrograph of G.E. Tungsten Powder
As Received, 5000X.

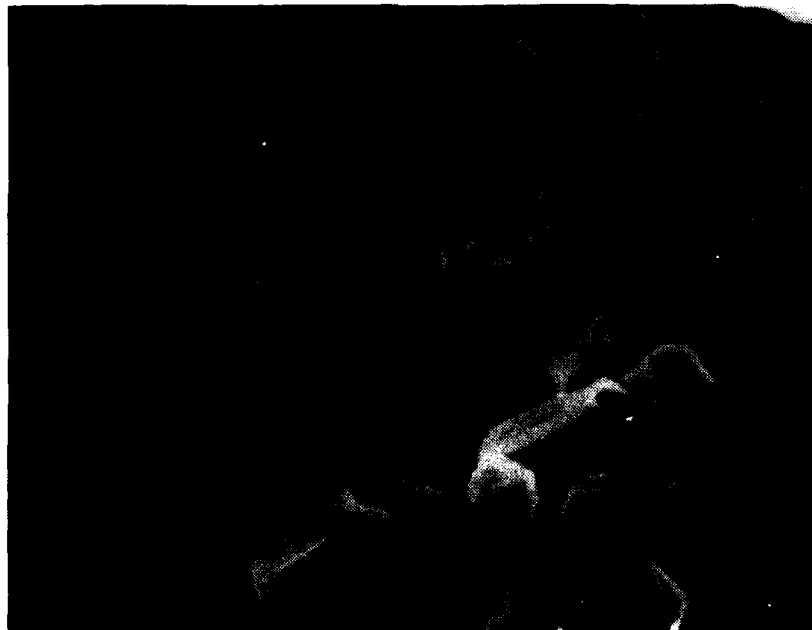


Figure 76. Micrograph of G.E. Tungsten Powder After Sorting
and Deconglomeration 5.5-6.5 μm Nominal Size.



Figure 77. Micrograph of Sylvania Tungsten Powder As Received.



Figure 78. Micrograph of Sylvania Tungsten Powder After Sorting and Deconglomeration 5.5-6.5 μm Nominal Size.

TABLE 67
 PARTICLE SIZE DISTRIBUTIONS OF 15 SORTED TUNGSTEN
 POWDERS AND EXPECTED SIZE FOR 10 OF THE POWDERS

Sample	Expected Sorting Size (μm)	Type of Distri- bution	Distribution Shape Parameters for Weibull		Number of Particles Sized	Average Particle Size (μm)	Standard Deviation (μm)
			α	β			
Syl- vania	5.5-6.5	Normal	---	---	431	4.5	1.2
G.E.	5.5-6.5	Normal	---	---	257	5.2	1.4
1	<4.5	Weibull	1.8	2.1	97	1.8	1.1
2	4.5-7.5	Weibull	2.4	3.3	125	2.9	1.4
3	7.5-10.5	Weibull	3.0	5.7	275	5.1	1.9
4	>10.5	Normal	---	---	96	7.9	2.6
5	<4.5	Normal	---	---	136	2.8	1.1
6	4.5-7.5	Weibull	4.2	5.7	256	5.2	1.4
7	7.5-10.5	Weibull	7.1	8.5	109	8.0	1.3
8	>10.5	---	---	---	77	10.7	4.8
21	---	Weibull	2.2	6.6	236	5.8	2.8
22	---	---	---	---	322	4.6	1.2
23	---	---	---	---	180	5.6	1.6
24	---	---	---	---	128	7.2	1.2
25	---	Normal	---	---	115	7.8	1.4

and normal distributions using a computer program written by Dr. Dale Ford of the University of Dayton. The program also gives a plot of the data in histogram form, the Weibull function (the solid line), and the normal function (the dotted line). The program also gives the values of alpha (α) and beta (β) the curve shaping parameters for the Weibull distribution, the average value (μ) and standard deviation (σ) of the normal distribution, as well as the Chi-squared goodness-of-fit values for both distributions. The Chi-squared goodness-to-fit test is used to determine whether or not a hypothesis is statistically acceptable. In this case the hypothesis is that the Weibull or normal distribution fit the data at 97.5 per cent confidence level. Table 66 lists the results from the data reduction and Figures 79 through 93 are plots of the data with all graphs on the same scale. Samples 1, 2, 3, 7 and 21 fit the Weibull distribution. Samples 4, 5 Sylvania 5.5-6.5 μm nominal size, and 25 fit the normal distribution. Samples 8, 22, 23, and 24 fit neither distributions at 97.5 per cent confidence level, and the average value and standard deviation are given for the normal distribution.

F. Phase 2

This phase involved particle shape variations between six porous green billets of tungsten. Tungsten powder samples 1, 2, 3, 6, 7 and 8 were made into green tungsten billets. These billets were examined by the SEM for porosity and particle shapes. The billets are very porous as seen in Figures 94 and 95. Micrographs of the corresponding powders are shown in Figures 96 and 97. It can be seen that the particle shapes have changed in forming the billets. For sample 3 the particle shapes have changed from sharp edges to more rounded edges (Figures 96 and 94). For sample 6 (Figures 95 and 97) the shapes have changed from rough rounded edges to smooth rounded edges.

G. Phase 3

The last step was to examine the topography of the emitting surfaces of some impregnated dispenser cathodes. Figure

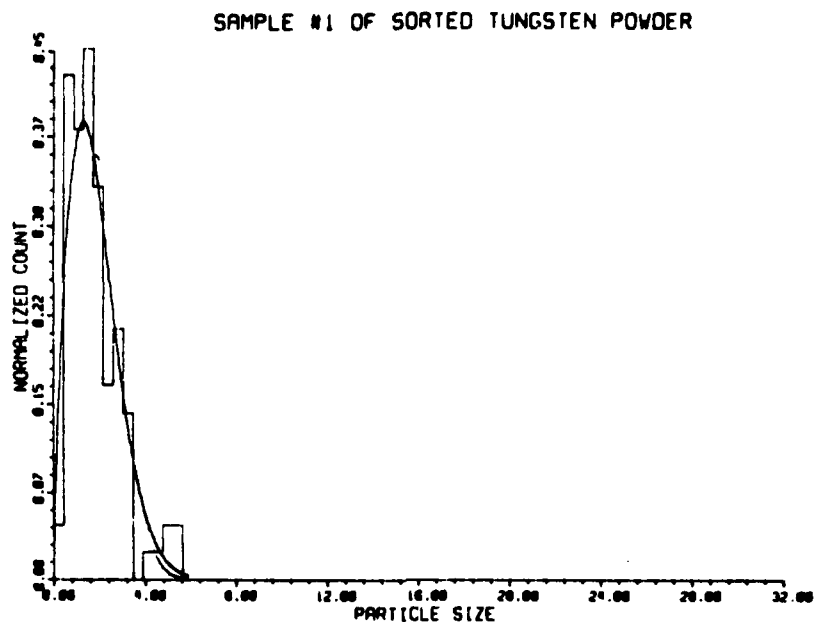


Figure 79. Particle Size Distribution Plot of Sample #1 Sorted Tungsten Powder.

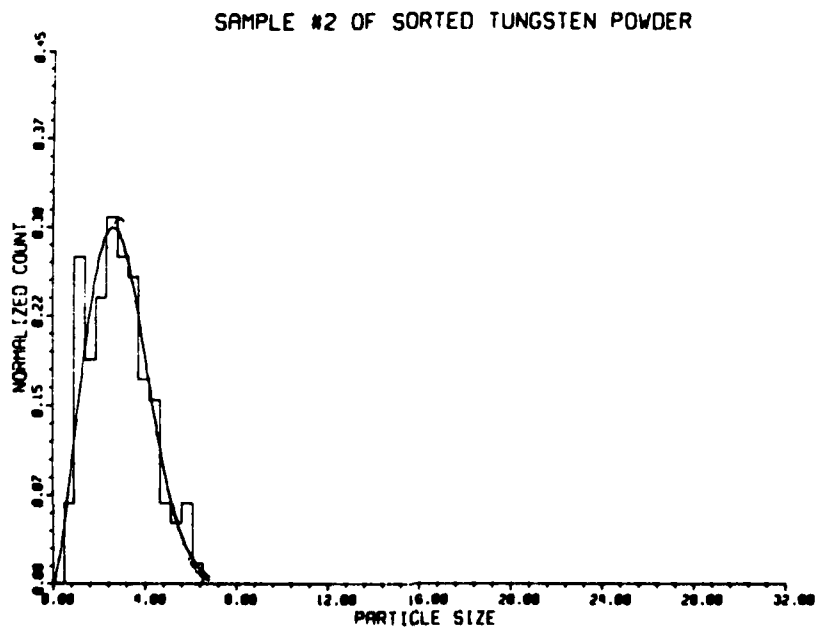


Figure 80. Particle Size Distribution Plot of Sample #2 Sorted Tungsten Powder.

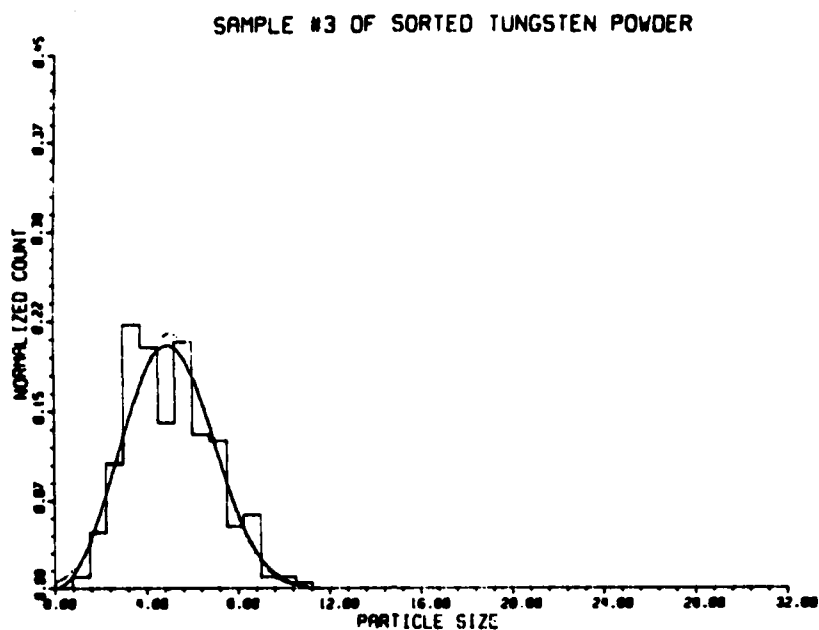


Figure 81. Particle Size Distribution Plot of Sample #3 Sorted Tungsten Powder.

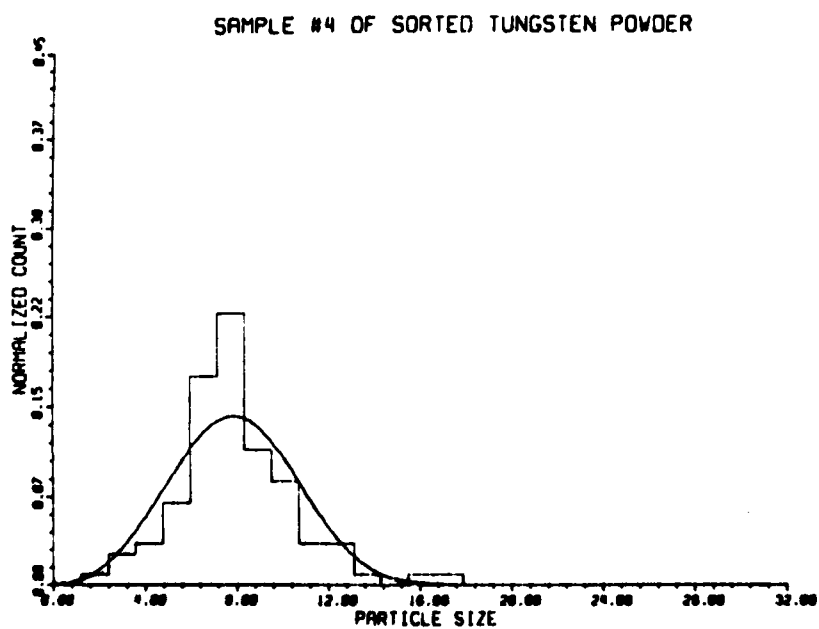


Figure 82. Particle Size Distribution Plot of Sample #4 Sorted Tungsten Powder.

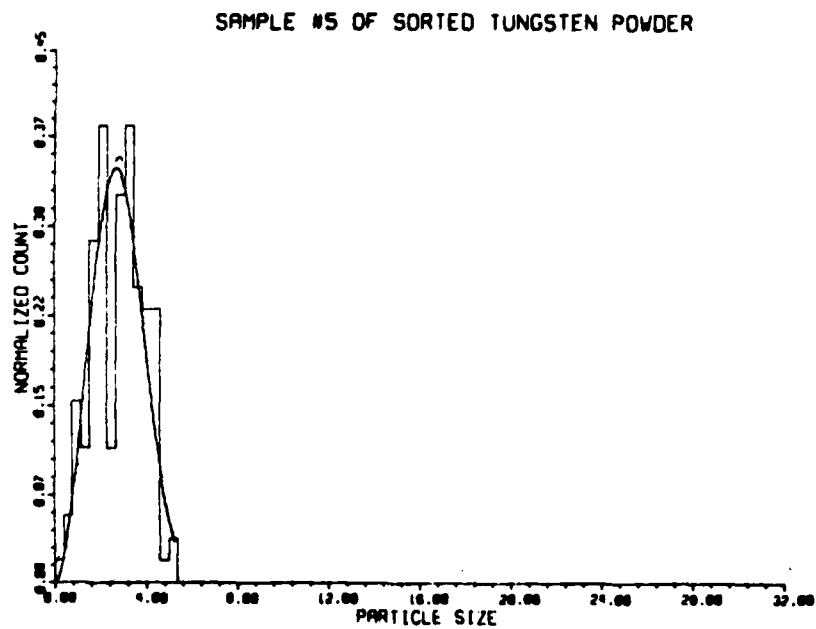


Figure 83. Particle Size Distribution Plot of Sample #5 Sorted Tungsten Powder.

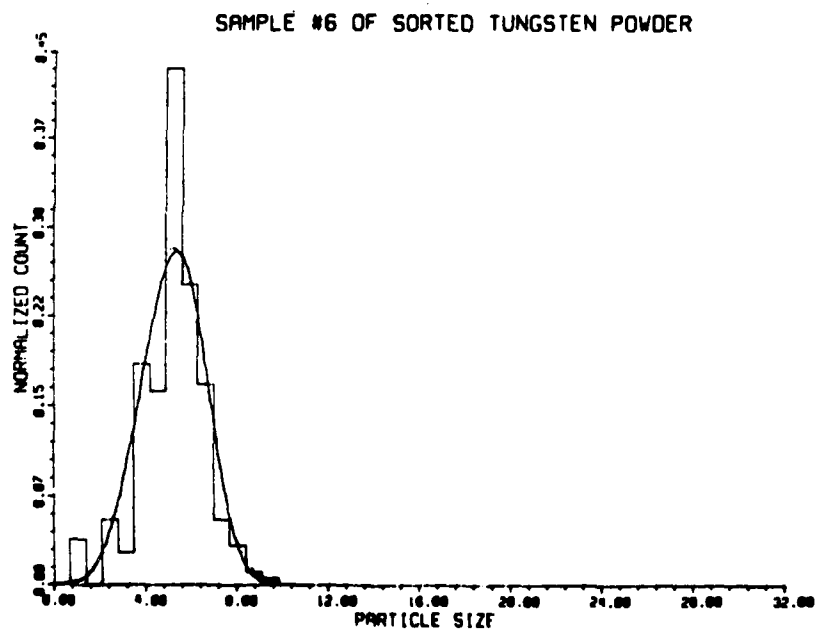


Figure 84. Particle Size Distribution Plot of Sample #6 Sorted Tungsten Powder.

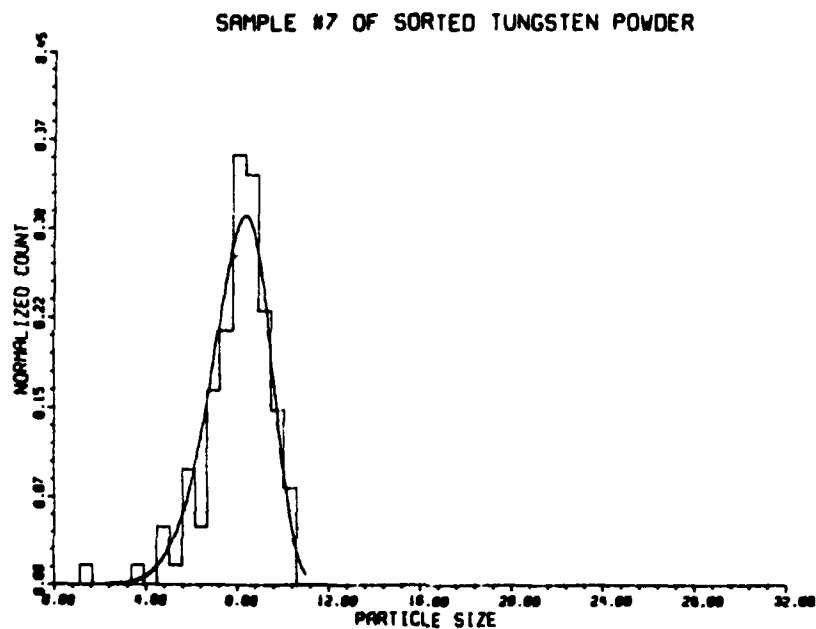


Figure 85. Particle Size Distribution Plot of Sample #7 Sorted Tungsten Powder.

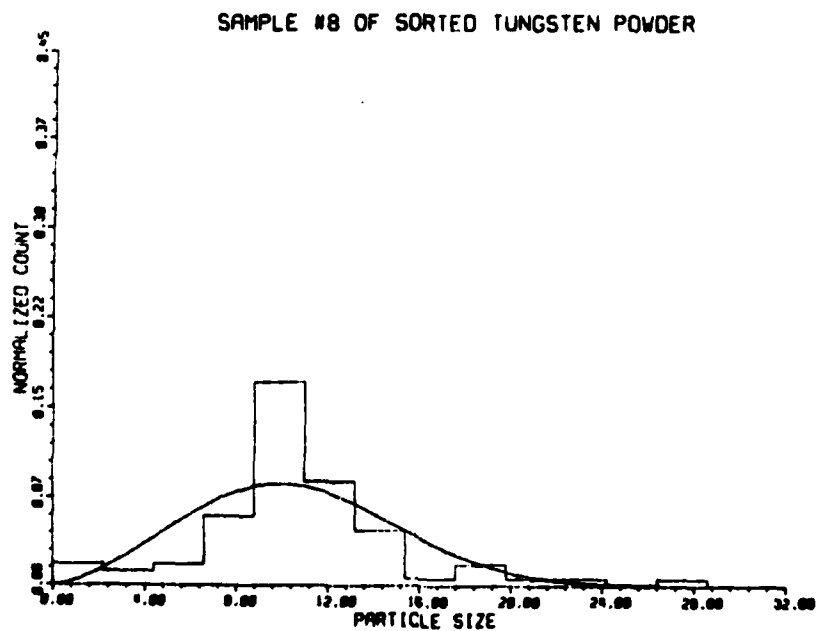


Figure 86. Particle Size Distribution Plot of Sample #8 Sorted Tungsten Powder.

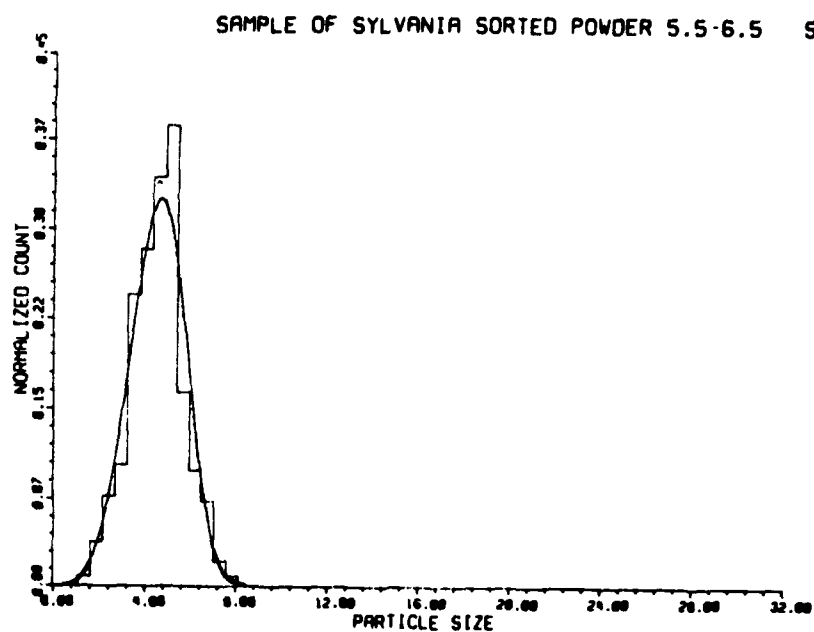


Figure 87. Particle Size Distribution Plot of Sylvania Sorted Powder 5.5-6.5 μm Nominal Size.

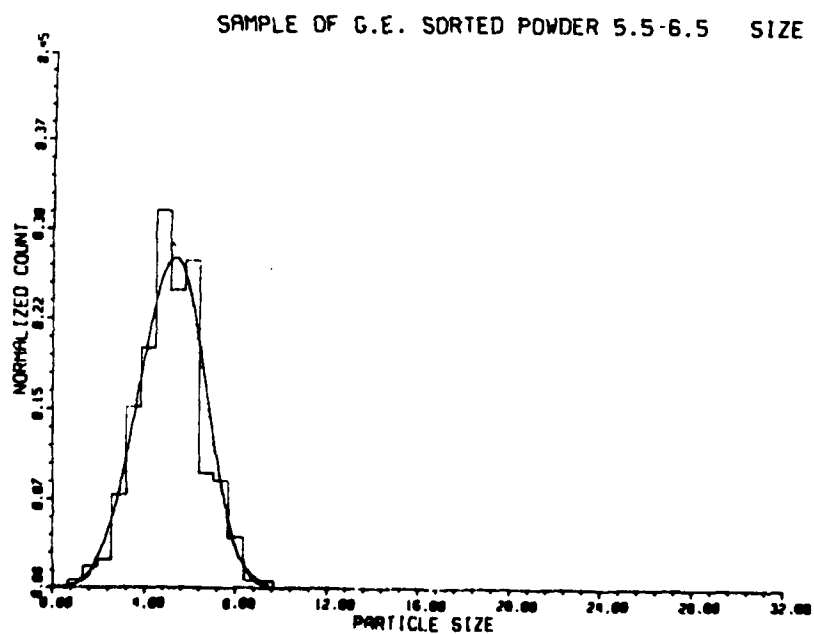


Figure 88. Particle Size Distribution Plot of G.E. Sorted Tungsten Powder 5.5-6.5 μm Nominal Size.

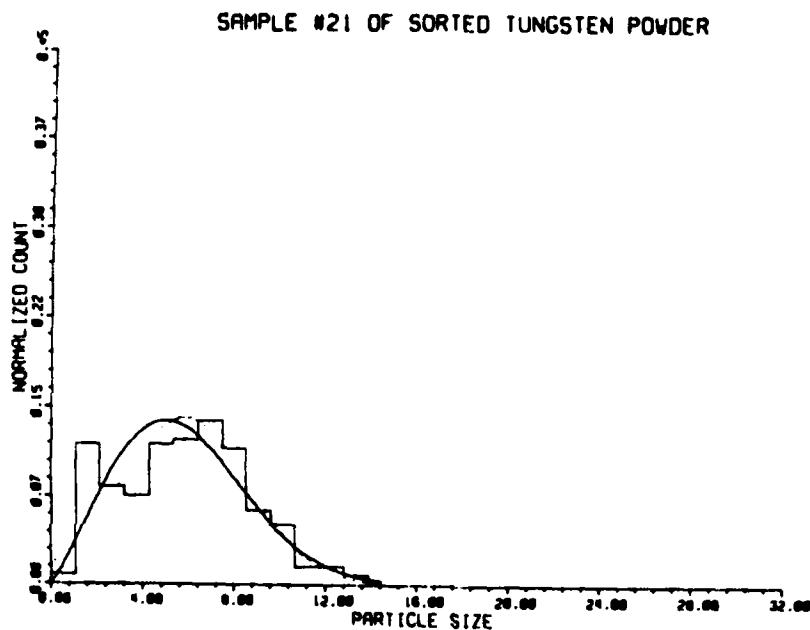


Figure 89. Particle Size Distribution Plot of Sample #21 Sorted Tungsten Powder.

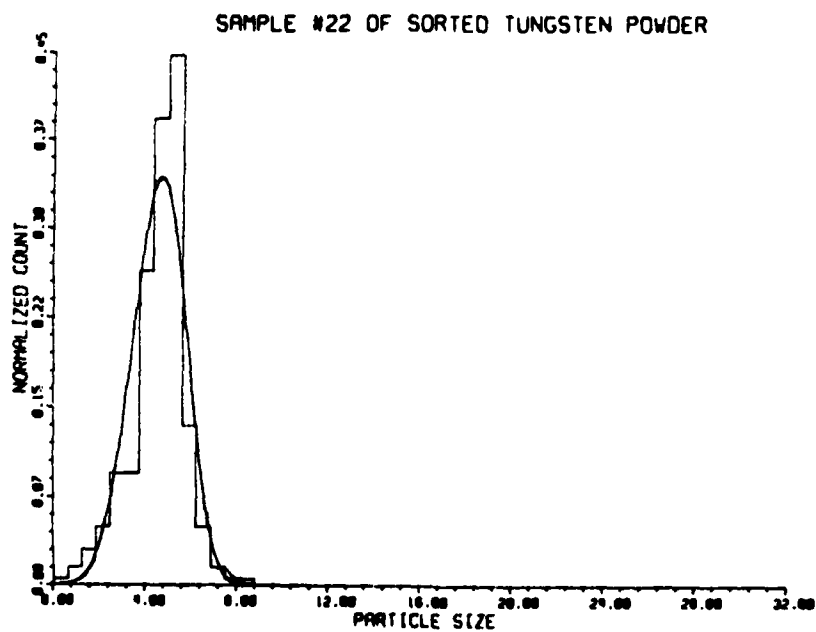


Figure 90. Particle Size Distribution Plot of Sample #22 Sorted Tungsten Powder.

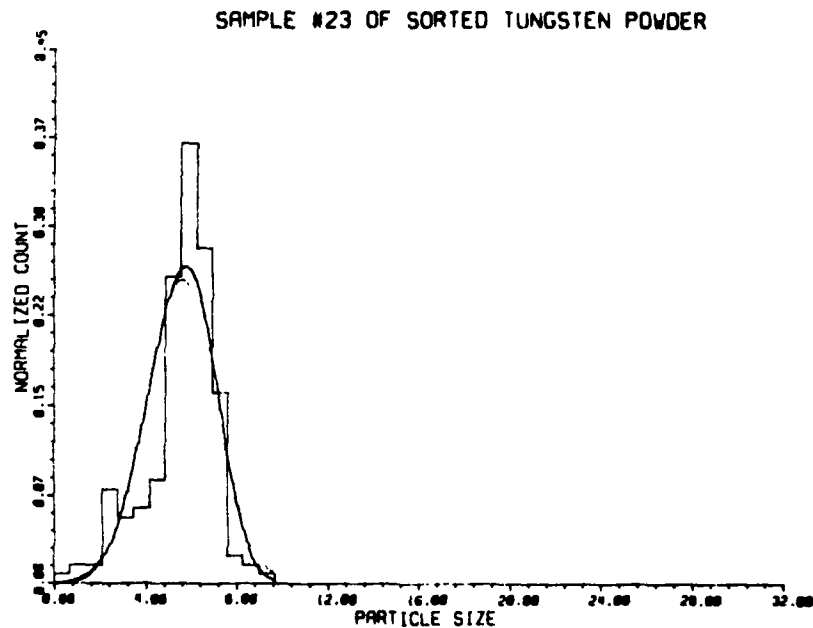


Figure 91. Particle Size Distribution Plot of Sample #23 Sorted Tungsten Powder.

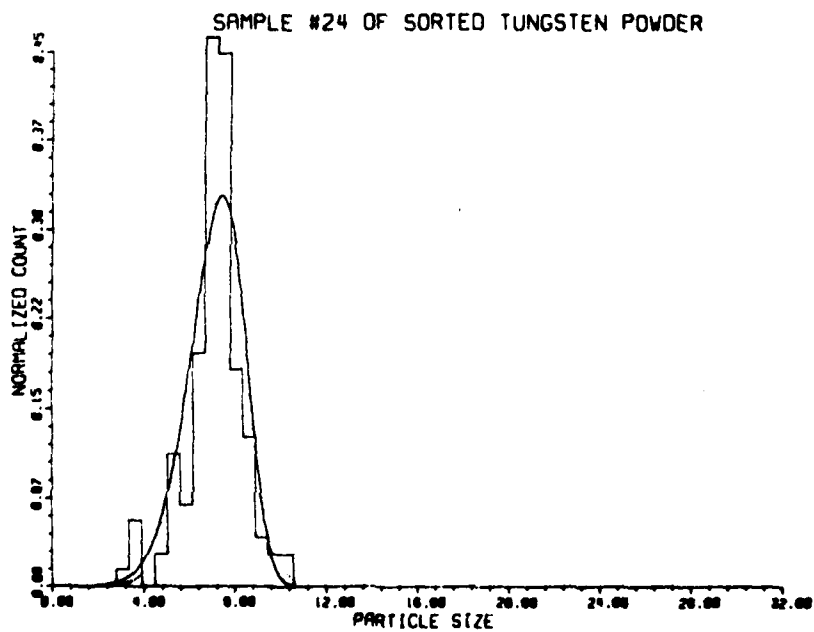


Figure 92. Particle Size Distribution Plot of Sample #24 Sorted Tungsten Powder.

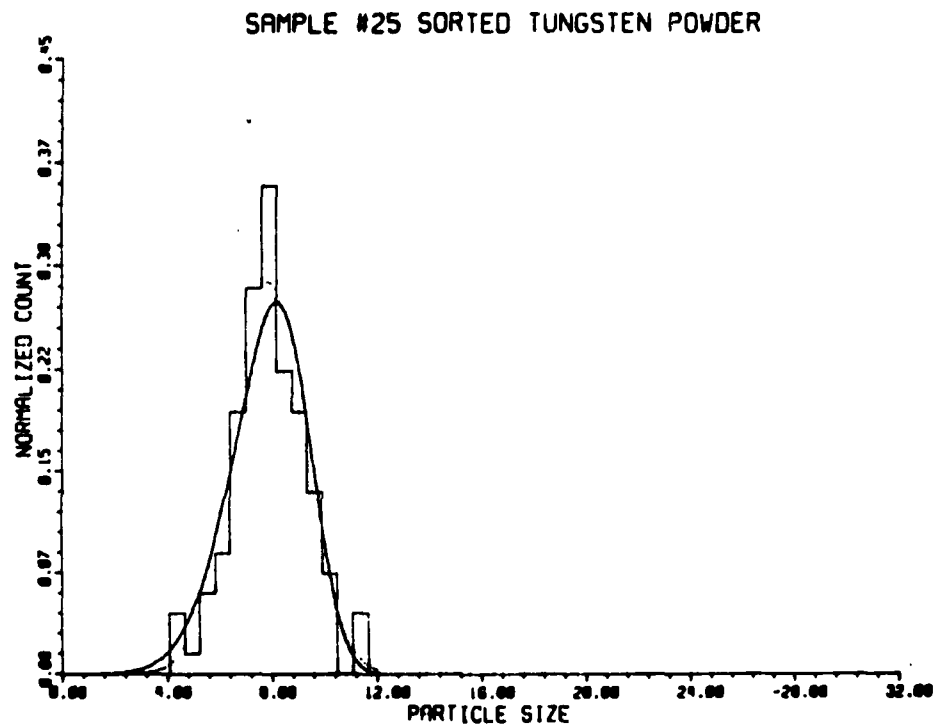
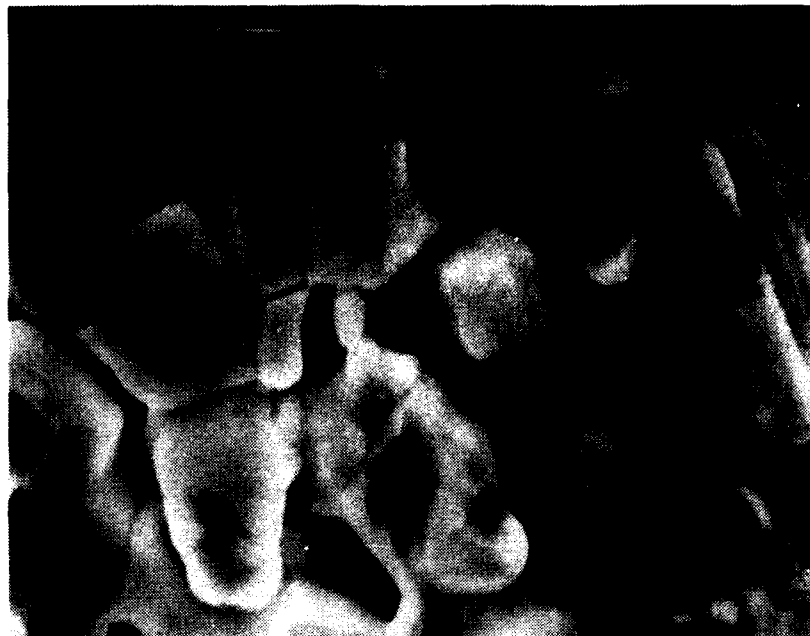


Figure 93. Particle Size Distribution Plot of Sample #25 Sorted Tungsten Powder.



Sample 3 W billet on end 5.0kX 1 μ m



Sample 3 W billet axially 5.0kX 1 μ m

Figure 94. Tungsten Billet of Sample #3 Sorted Powder.



Sample 6 W billet on end 5.0kX 1 μ m



Sample 6 W billet axially 5.0kX 1 μ m

Figure 95. Tungsten Billet of Sample #6 Sorted Powder.



B Sample #3 5.0kX 1 μ m

Figure 96. Micrograph of Sample #3 Tungsten Sorted Powder.



B Sample #7 5.0kX 1 μ m

Figure 97. Micrograph of Sample #6 Tungsten Sorted Powder.

98 is a micrograph of a Semicon 5:3:2 cathode which had been activated for 72 hours at 1190°C. The bulk of the emitting surface appeared to be an impregnated tungsten billet with some areas of contamination. Figure 99 is a micrograph of a Semicon 1:1:1 cathode. This cathode was activated at 1190°C and operated at 1150°C for 1100 hours. Note that the surface has lost the tungsten billet appearance completely.

2. STUDIES OF COMPONENTS OF TRAVELING WAVE TUBES

Components from various traveling wave tubes were Auger analyzed to ascertain the elements on the surface. Below is listed the components and a brief description of the component if available.

263HA SN242 collector

SN97 focus electrode

SN97 anode

SN10 Sample 23 alumina insulator with braze material

SN101 Sample 23 alumina cylindrical insulator with braze material and discoloration

271H TWT SN25 oxide cathode with blotches in certain areas

288H SN85 focus electrode

265H SN201 focus electrode from TWT which had leaked

A typical scan of 263HA SN242 is illustrated in Figure 100. The collector was machined from copper; the carbon and oxygen are due to exposure to atmosphere.

288H SN85 focus electrode had a large variety of elements on the surface. These elements included S, C, N, Cr, O, Fe, Na, Mg, and Si. The focus electrode was constructed of a stainless steel which could explain the presence of Fe, Cr, and Si on the surface.

SN97 focus electrode showed Cl, K, C, Ca, N, O, and Na present on the surface. The peak identified as Cl may in reality be due to the 180 volt electrons which are used in the ionizer of the ion gun. Another area of the focus electrode gave



Figure 98. Semicon 5:3:2 Dispenser Cathode Near Center
5.0 kX 1 μ m.



Figure 99. Semicon 1:1:1 Dispenser Cathode Near Center
5.0 kX 1 μ m.

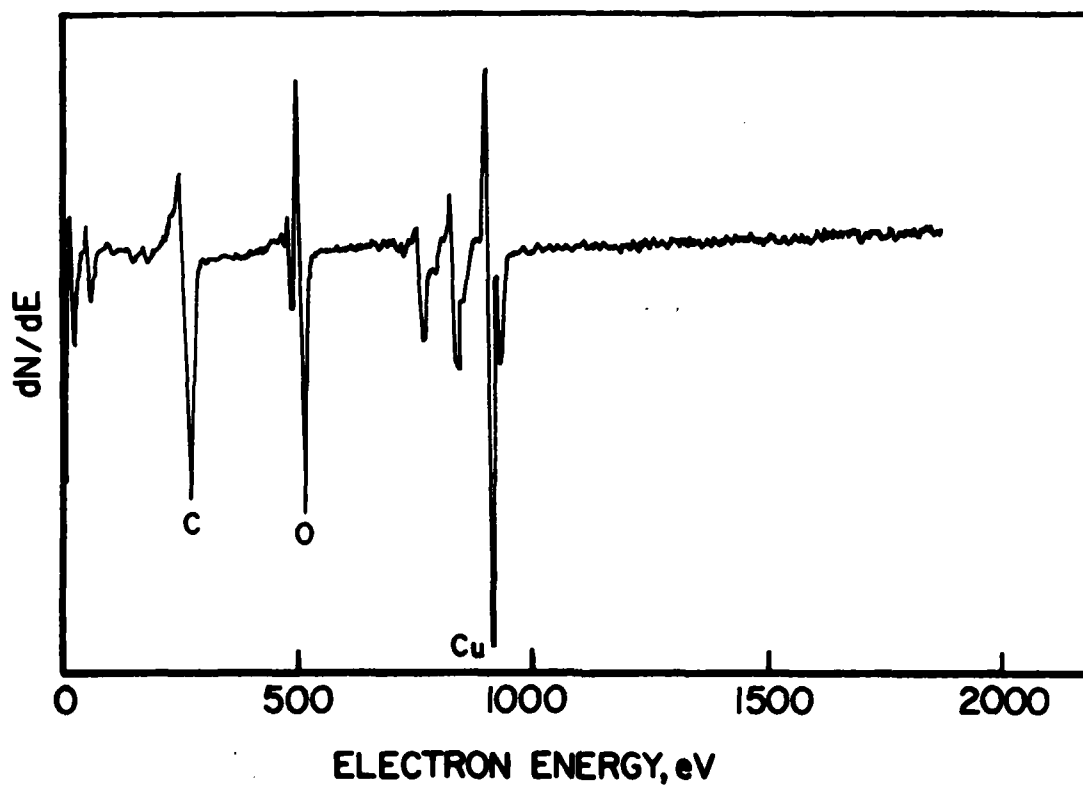


Figure 100. Typical Auger Scan from Collector 263 HA
S/N 242.

an Auger spectrum indicating the presence of S, Cl, Mo, C, Ca, O, F, and Si. The presence of fluorine could be due to the use of microdusters which has freon as the propellant. The Si may be due to the quartz tube which is the exterior envelope of the TWT.

SN10 Sample #23 is a cylindrical-shaped insulator with braze material present on the surface. The braze material was Auger analyzed to ascertain the elements present. It was determined from the Auger spectrum that S, Cl, O, Fe, Co, Ni, Cu, and Al were present. The S, Cl, and O could be from exposure to atmosphere.

SN97 anode had a typical Auger spectrum with Cl, K, C, Ca, O, Ba, F, and Al being observed.

SN101 Sample #23 was a cylindrical alumina insulator with braze material about its circumference. Below the braze material the insulator had a gray color region. The discolored region showed in the Auger spectrum Cl, C, O, Fe, Cu, Na, Al, Au, and Ta. The Fe, Cu, and Au probably were components of the braze material. The Cl, C, and O were picked up from exposure to the atmosphere. The Ta proved to be the most interesting element observed. It had to come from the Ta heated shield around the cathode.

The half-moon shaped insulator SN10 cut #1 had an Auger spectrum which showed the presence of Cl, C, O, Fe, Co, Ni, Al, and Si. These elements are to be expected from construction material and exposure to atmosphere.

263HA SN242 was a collector from a TWT. It was machined from high purity copper. The Auger spectrum showed Cu, O, and C.

271H TWT SN25 oxide cathode had a patchy surface which showed the presence of C, N, O, and Ni, but not Ca or Ba which are the active materials of the cathode. It appears that the patches were regions where the active material had flaked or sputtered off the surface. The Ni observed would be from the substrate.

Focus electrode 265 H SN 201 came from a TWT which had leaked. It was hoped that a large amount N would be implanted in the surface, however, no substantial amount of N was recorded. An anode from a Telefunken test diode was analyzed across its surface. The anode was a circular button of Mo approximately 25mm in diameter. It was mounted on the end of a heavy copper rod. In the absorbed current image of the scanning Auger microprobe, distinct regions could be observed. Auger spectra were recorded in eleven different regions across the surface.

Region 1 approximately 1mm in from the edge showed the presence of Ba, K, Ca, C, Mo, O, and Cu. The Auger spectrum for this region is illustrated in Figure 101. Region 2 approximately 5mm in from the edge showed the presence of Ba, K, C, Ca, O, Mo and Na. The Auger spectrum for this region is presented in Figure 102.

Figure 103 is the Auger spectrum of Region 3 which was approximately 8mm from the edge. It showed the presence of Ba, K, Mo, and O.

Region 4, 5, and 6 showed mostly Ba, Ca, and O with the Mo substrate being completely covered.

Region 7 through 11 were effectively mirror images of Regions 1 through 5.

None of the elements detected on the surface were unexpected.

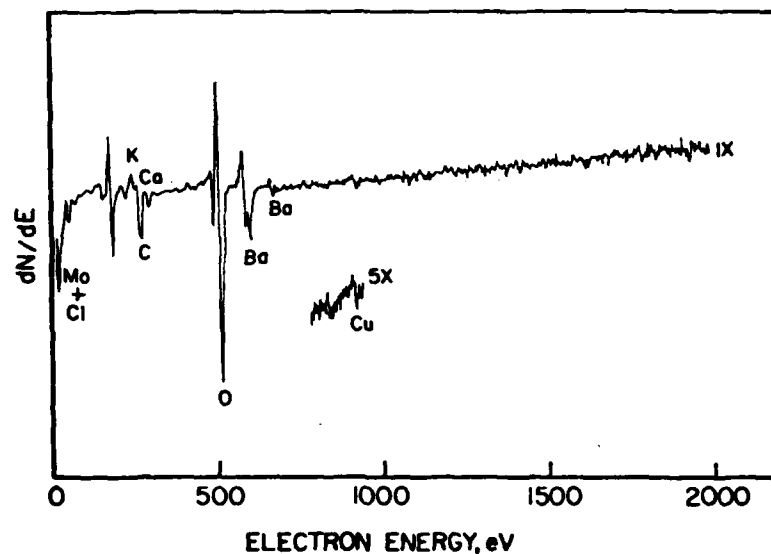


Figure 101. Auger Spectrum of Spot Approximately 1 mm from Edge of a Telefunken Anode.

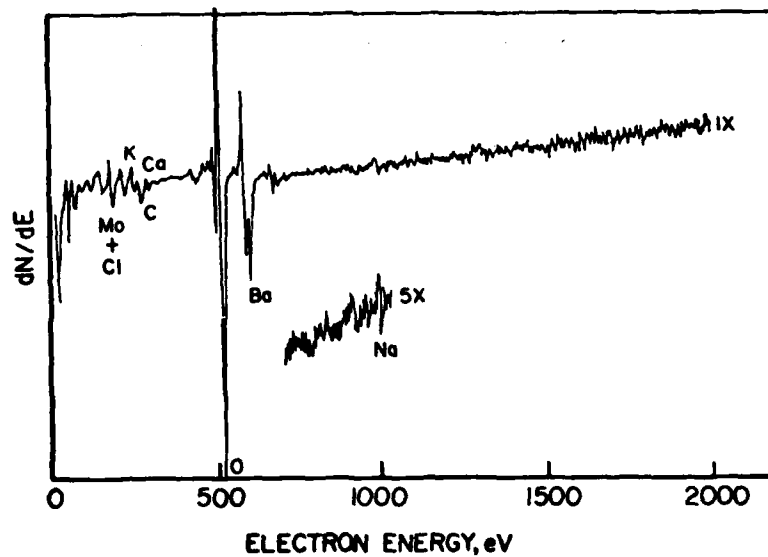


Figure 102. Auger Spectrum of Spot Approximately 5 mm from Edge of a Telefunken Anode.

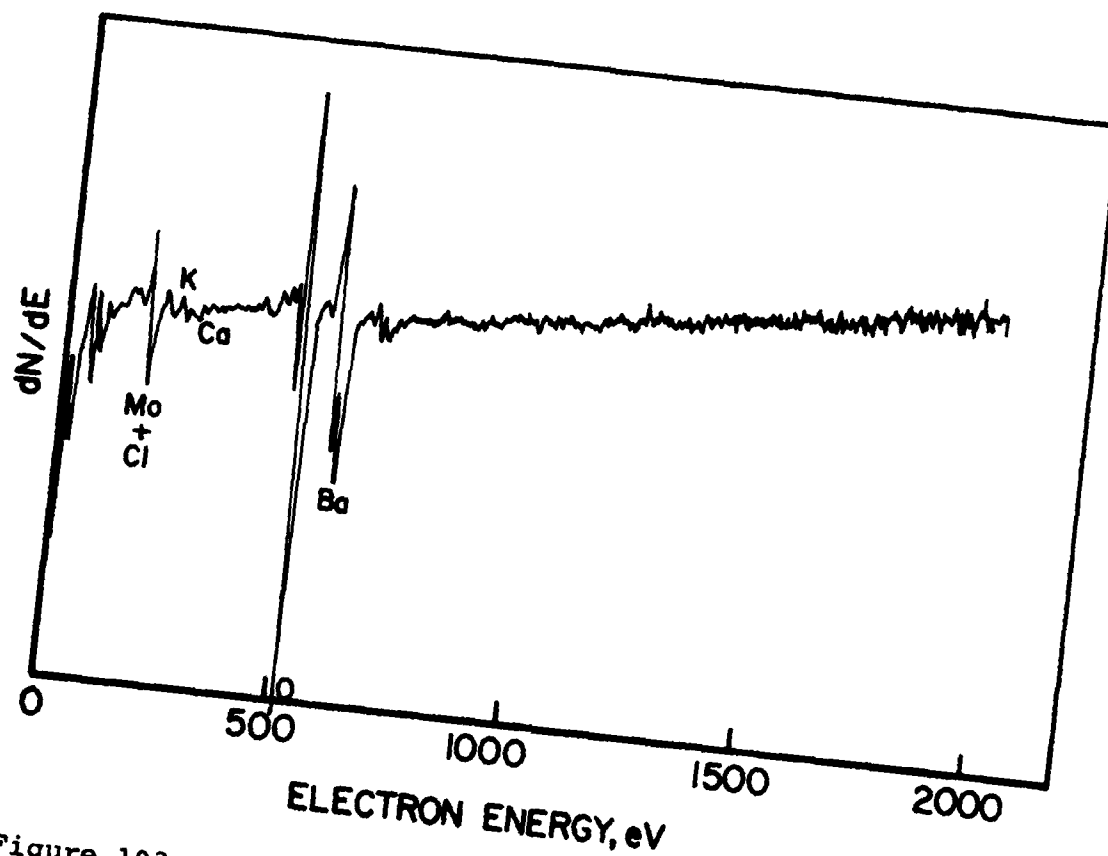


Figure 103. Auger Spectrum of Spot Approximately 8 mm from Edge of a Telefunken Anode.

SECTION VI
SURFACE ANALYSIS

1. PRATT AND WHITNEY NICKEL ALLOY SPECIMENS

A. Fracture Specimens

Seven rod-shaped specimens from Pratt and Whitney Aircraft Group were fractured at reduced temperature in the ultra-high vacuum system of a PHI 545 scanning Auger microprobe. These specimens were made from alloys used or proposed to be used in turbine blades.

The fracture surfaces were Auger analyzed to ascertain elements present on the surface. The fracture surface showed the presence of sulfur at approximately one percent atomic concentration. It was also observed that the concentration of sulfur varied over different regions of the fracture surface. This is an important result as sulfur is detrimental to the required properties of the alloys.

A typical Auger analysis, e.g. on specimen number 533, showed the following atomic percent concentration on the fracture surface.

Ni	Mo	Al	W	S
70	7.7	18	2.7	1.6

The listed weight percent concentrations for specimen 533 are:

Ni	Mo	Al	W	C
73.5	13.0	7.3	6.2	0.1

The corresponding atomic percent concentrations for this specimen are:

Ni	Mo	Al	W	C
73.7	8.0	15.9	2.0	0.3

It can be seen that the measured concentrations of Ni, Mo, Al, and W are close to the expected values. Carbon was not detected at a freshly fractured surface, but it did accumulate

with time from the residual gases in the vacuum chamber (1×10^{-9} torr). It would not be expected to be able to detect bulk carbon as the detectability of carbon using Auger spectroscopy is about one percent atomic concentration.

Auger spectra from the other six specimens were very similar to number 533. Sulfur was also present on all fractured surfaces and varied across the fracture surface. The minor alloy additives (Hf, Y, Zr, Si) were not detected in the Auger spectra as they were below detectability levels. Representative Auger spectra are presented in Figures 104 and 105.

Two additional rod-shaped specimens of nickel alloy with Hf added were subsequently analyzed. It was proposed that Hf should keep sulfur in suspension and not permit it to migrate to the grain boundaries.

The two specimens were fractured and analyzed for sulfur. It was ascertained that sulfur was evident on the fracture surface. This result indicates that the added Hf failed to keep the sulfur in suspension. A SEM photograph of the fracture surface is presented in Figure 106.

B. Nickel Alloy Wafers

Four RSR 105 radial wafers from Pratt and Whitney Aircraft Group were submitted for Auger analysis. The wafers carried a number etched on the back. The description of the wafers is as follows:

- 1 = As received
- 2 = Pre-clean
- 3 = MECL electro clean (stored in air)
- 4 = MECL electro clean (stored in vacuum)

Several Auger scans of each specimen were performed. The initial scan was of the surface before ion bombardment etching. The following briefly reviews the results of the Auger analysis.

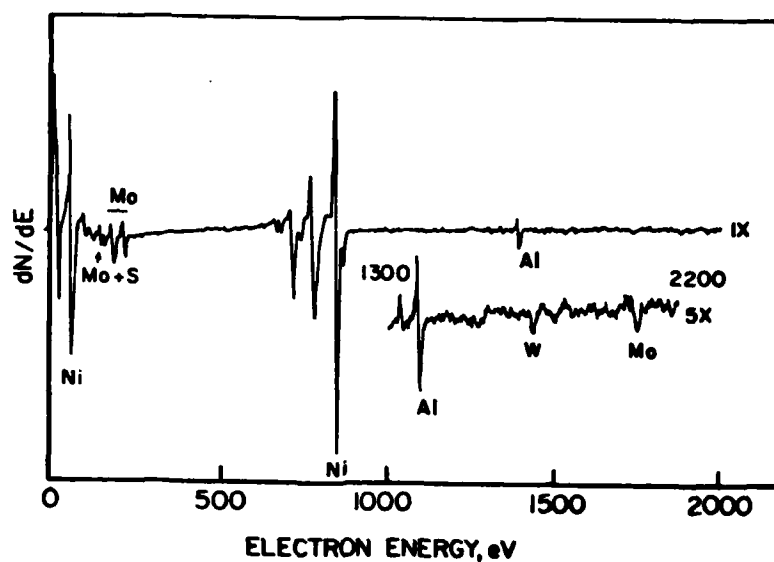


Figure 104. Auger Scan of Fracture Surface of Nickel Alloy Specimen RSR 533.

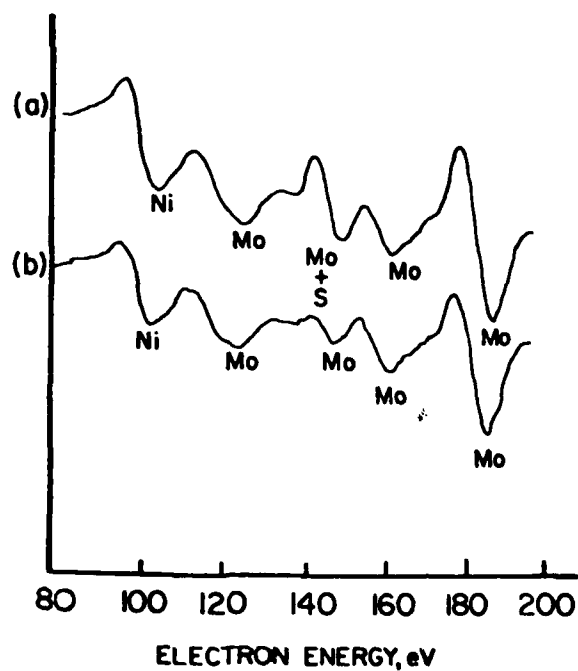


Figure 105. Auger Scans of Nickel Alloy Specimen RSR 533 Taken from Two Different Regions on the Fracture Surface.

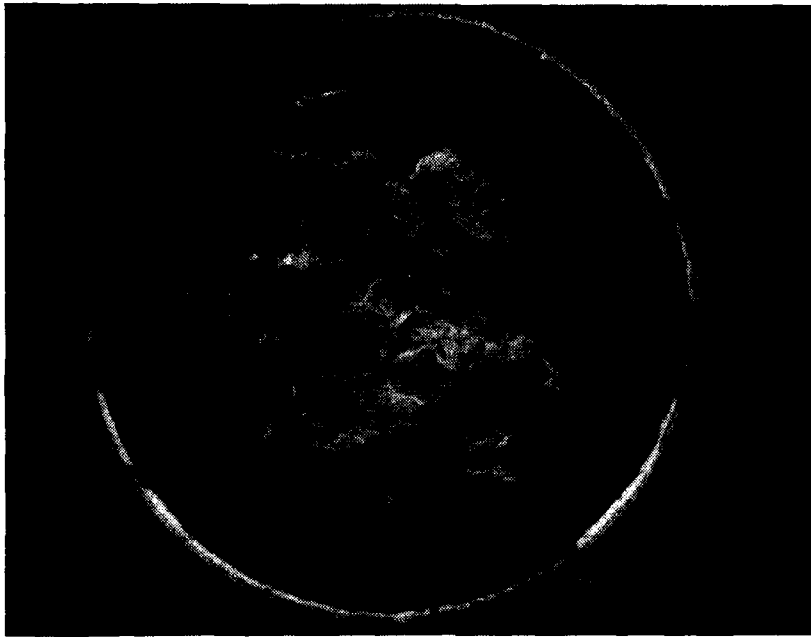


Figure 106. SEM of Fracture Surface on Nickel Alloy Rod.
The longer white marker is 100 μm .

(1) Specimen #1

This specimen was described as being the "as received" specimen. The initial Auger analysis showed carbon, calcium, oxygen, nickel, and to a lesser extent, aluminum. Thirty seconds of ion bombardment did not produce a significant change in the Auger spectrum. After 45 minutes of ion bombardment, tungsten and molybdenum could be observed along with the previously mentioned elements.

(2) Specimen #2

This specimen showed phosphorous, carbon, calcium, oxygen, nickel, and aluminum in the normal sensitivity scan. A higher sensitivity scan demonstrated the presence of tungsten and molybdenum. Thirty seconds of ion bombardment reduced the carbon and oxygen signals considerably. The molybdenum, tungsten, aluminum, and nickel signals increased their peak-to-peak heights. The carbon signal peak shape changed from an amorphous form to a

carbide. It cannot be said with certainty as to whether the carbide form existed under the amorphous carbon layer or was created through ion beam interaction with the carbon and metals in the nickel alloy.

(3) Specimens #3 and #4

These two specimens were electro cleaned. The major difference between these two specimens was that specimen #4 was stored in an evacuated mason jar. Specimen #3 showed carbon, oxygen, nickel, aluminum, tungsten, and molybdenum before ion bombardment. After 30 seconds of ion bombardment, Auger analysis showed carbon, oxygen, nickel, aluminum, tungsten, and molybdenum. The Auger scan of specimen #4 was similar to specimen #3 except calcium and nitrogen were also present in the initial scan of specimen #4.

In conclusion, there appeared to be little difference in specimens #2, #3, and #4. The specimen marked #1 had the most difference, in that the carbon layer was fairly thick.

2. ULTRAPURE SILICON WAFER

A wafer of ultrapure silicon had been heated in an oven. Upon removal from the oven, a burnt region was observed on the wafer. EDAX scans were performed upon this region and other regions that contained minor eruptions in the surface. The EDAX scans did not show any unexpected elements in the burnt region. This particular EDAX instrument was not sensitive to elements lighter than sodium. Therefore, Auger analysis was enlisted to ascertain the light elements present in the burnt region.

Five points were analyzed inside the burnt area. Typical scans that were obtained before and after 30 seconds of ion bombardment are shown in Figures 107 and 108, respectively. It can be observed that the before ion bombardment Auger scans show carbon, oxygen, and silicon present on the surface. Nitrogen, sulfur, and chlorine were also observed in some areas. After

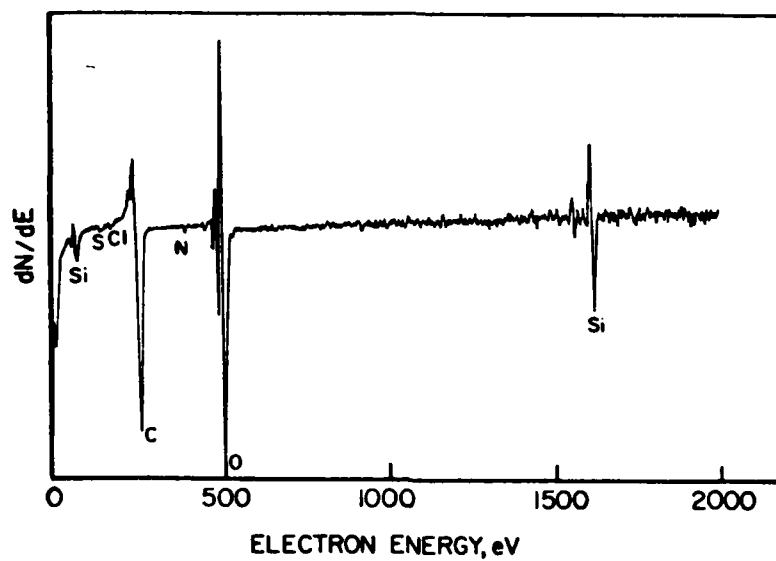


Figure 107. Auger Scan of Burnt Area on Ultrapure Silicon Wafer Before Ion Bombardment.

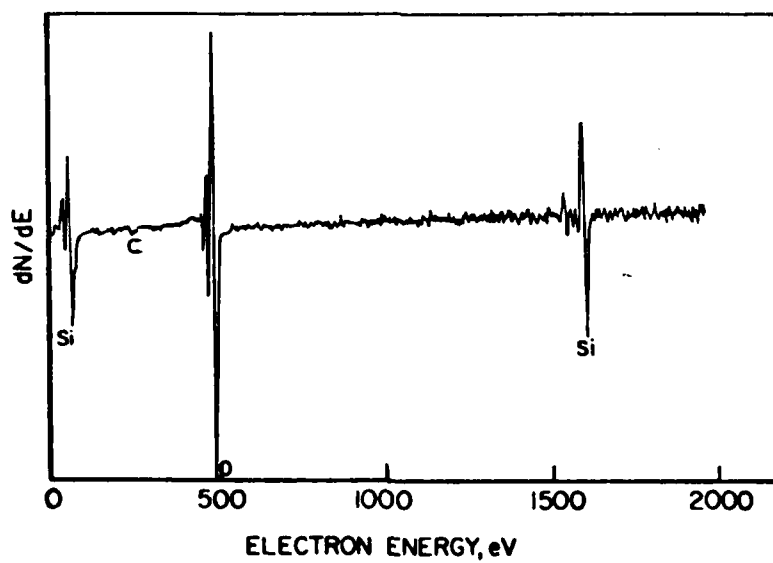


Figure 108. Auger Scan of Burnt Area on Ultrapure Silicon Wafer After 30 Seconds of Ion Bombardment.

ion bombardment oxygen and silicon were present with nitrogen, sulfur, and chlorine completely removed and carbon reduced to approximately one percent.

The silicon peak shape and energy position indicated that the silicon was combined with the oxygen.

The atomic percent concentrations of the elements observed are listed below.

Before Ion Bombardment:

Si	57.3	C	27.4	O	14.5	N	0.6	Cl	0.1	S	0.1
----	------	---	------	---	------	---	-----	----	-----	---	-----

After Ion Bombardment:

Si	82.2	C	1.2	O	16.6	N	0	Cl	0	S	0
----	------	---	-----	---	------	---	---	----	---	---	---

3. TITANIUM CARBIDE

A. Graphoil Cover Plates

Four graphoil specimens were submitted for Auger analysis. Graphoil is used as a crucible cover during the heating of TiC powder to drive off impurities in the commercially-available TiC powder.

The specimen designations are as follows:

- 1 - Graphoil (graphite foil) - standard
- 2 - Graphoil cover from crucible with "as received" HP-25 TiC powder which had been heated to approximately 2000°C
- 3 - Graphoil cover from crucible with leached HP-26 TiC powder which had been heated to approximately 2000°C
- 4 - Graphoil cover from crucible with "as received" HP-27 TiC powder, with silicon added, which had been heated to approximately 2000°C

The rationale behind the Auger analysis of the graphoil was to ascertain whether the same impurities observed on fracture surfaces of TiC specimens prepared in the crucibles could be observed on the graphoil crucible covers. The impurities were Co and Fe.

All the used graphoil covers exhibited similar Auger spectra of Ti, C, O, and S. The graphoil standard showed only C in a normal Auger scan. No peaks from Co or Fe were detected on any of the specimens.

The graphoil specimens produced considerable outgassing. The lowest pressure obtained during analysis was approximately 4×10^{-8} torr. With the ion pumps off, the pressure in the vacuum system would rise. It was decided that it would not be feasible to perform any ion bombardment which could have shown possible Co or Fe below the Ti layer.

Representative Auger spectra are presented in Figures 109, 110, 111, and 112.

B. Titanium Carbide Fracture Specimen

Two rectangular cross-section rods of TiC were fractured in the scanning Auger microprobe. The fracture surface was Auger analyzed to ascertain elements present on the surface. The rods bore the designations STC-19 at 2600°C and STC-19 at 2150°C, respectively.

The Auger spectra of the fracture surfaces showed the presence of chlorine, carbon, titanium, oxygen, cobalt, sodium, and silicon.

4. SiO₂ SPUTTER RATE DETERMINATION

The sputter rate of SiO₂ from a SiO₂/Si wafer was determined. A well-characterized SiO₂/Si wafer was provided by C. C. Chang of Bell Telephone Laboratories in Murray Hill, New Jersey. The wafer carried a designation of BTL-1-0045.

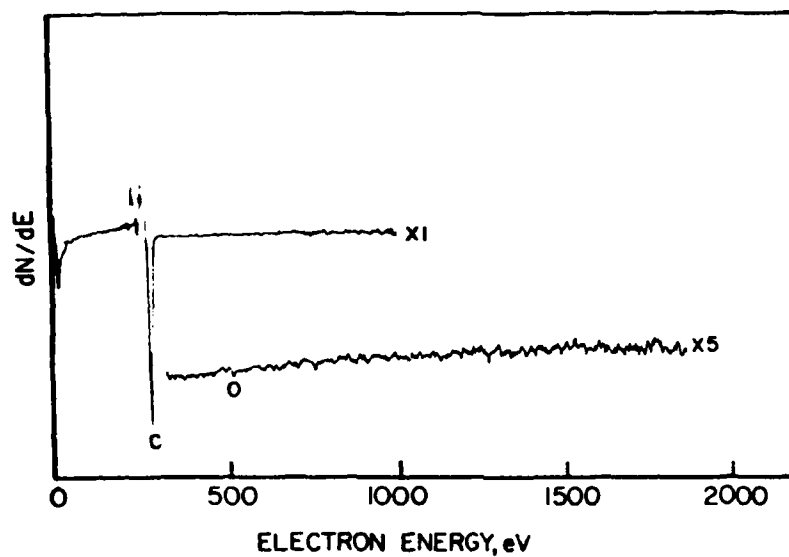


Figure 109. Auger Scan Graphoil Standard.

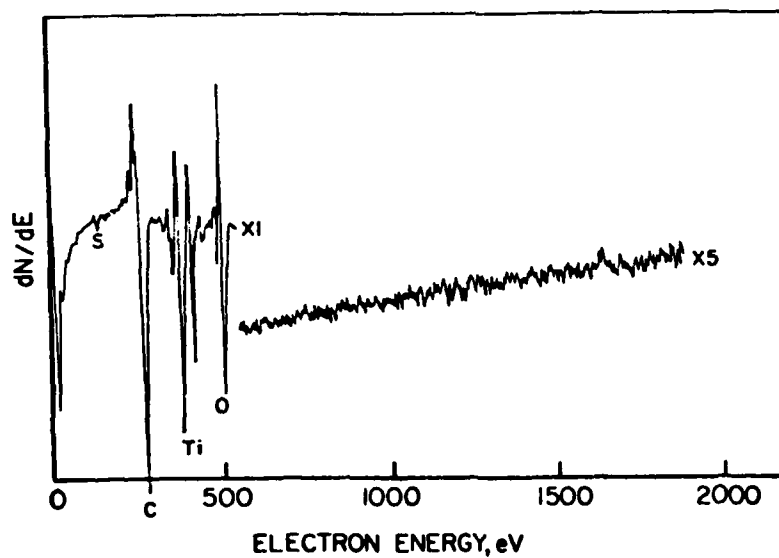


Figure 110. Auger Scan Graphoil Specimen HP-25.

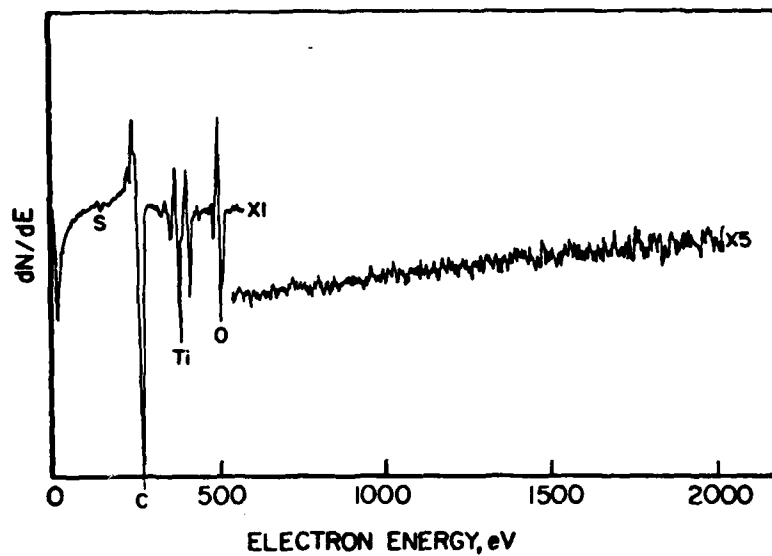


Figure 111. Auger Scan Graphoil Specimen HP-26.

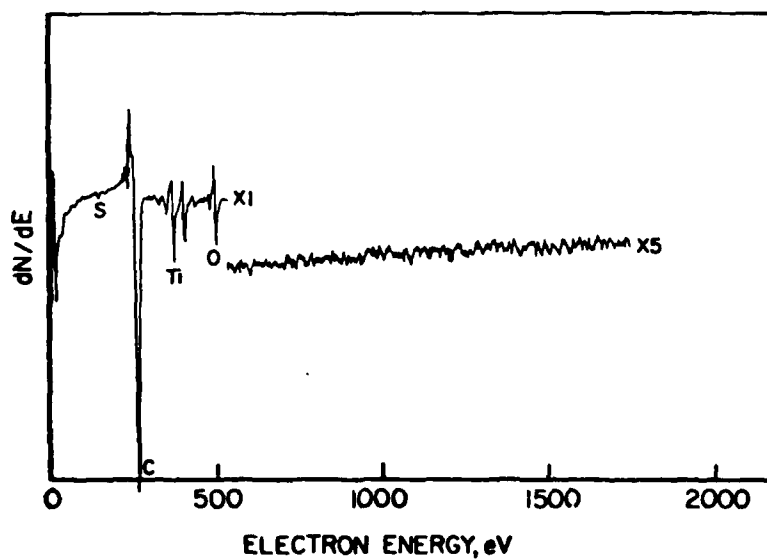


Figure 112. Auger Scan Graphoil Specimen HP-27.

The wafer was fractured according to the recommended procedure of Chang. The small segments were mounted on a carousel and placed in the scanning Auger microprobe. The ion gun was operated at 3 kV and current densities of 110 A/cm^2 and 210 A/cm^2 . The sputter rates determined under these conditions were 11 nm/min and 24 nm/min, respectively.

5. ALUMINUM PANELS

Five anodized aluminum alloy (2024) panels were Auger analyzed to ascertain the nature of the material present in the corrosion pits. Three of the specimens were treated with an alodized process (CrO_4) and then anodized; the remaining two were anodized in phosphoric acid. The specimens were corroded in a NaCl solution. Listed below are the panel designations and treatment received by them.

P190-5A Phosphoric acid anodized

AP190-21A Alodized with CrO_4 ; then phosphoric acid anodized

P190-1A Phosphoric acid anodized

AP190-9A Alodized with CrO_4 ; then phosphoric acid anodized

AP190-3A Alodized with CrO_4 ; then phosphoric acid anodized

Since the alodized specimens were similar, only one representative specimen was analyzed, this being specimen AP190-21A. Similarly, only one of the anodized specimens, P190-1A, was analyzed.

Specimen P190-1A showed areas with a large amount of corrosion pits. A typical Auger spectrum before and after ion bombardment etching is presented in Figure 113. It should be noted that generally copper was found at the sight of corrosion.

Specimen AP190-21A showed an interesting characteristic of having a scab over a pit. The Auger spectrum of a scab area is presented in Figure 114. The scab material appeared to consist of minor components of the aluminum alloy. Chromium was found in regions away from the scabs.

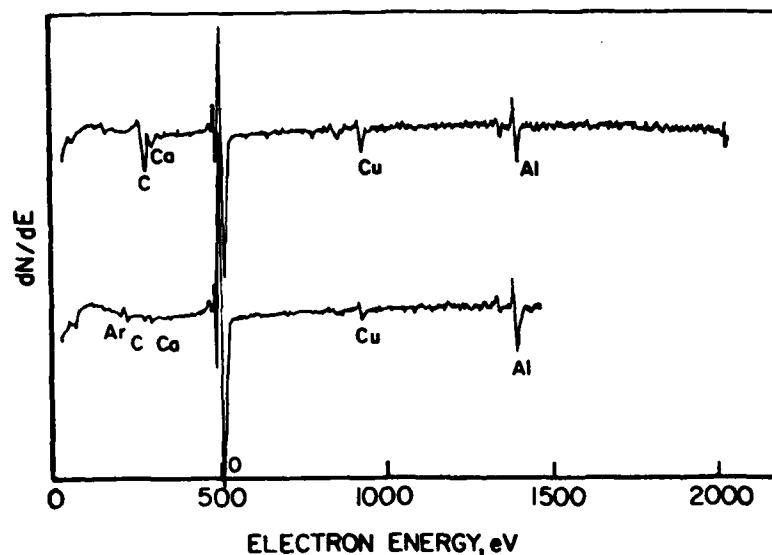


Figure 113. Auger Scan of Phosphoric Acid Anodized 2024 Aluminum Alloy Panel P190-1A, (a) Before Ion Bombardment and (b) After 30 Seconds of Ion Bombardment.

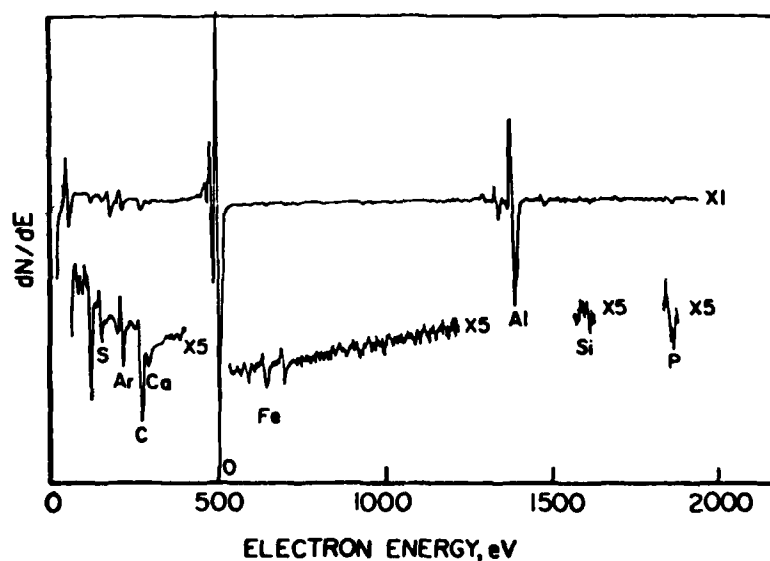


Figure 114. Auger Scan of Scab Area on Corroded 2024 Aluminum Alloy Panel AP190-21A.

In general, the panels which had been alodized showed less corrosion.

6. ALUMINUM ALLOY (7075) PANELS AND TITANIUM-6ALUMINUM-4VANADIUM ALLOY PANELS

Two panels each of 7075 Al alloy and Ti-6Al-4V alloy had been fractured previously. The fracture surface of each panel had Auger analysis performed on it. Listed below is the designation given to each panel and a brief description of the panel.

The first Al alloy panel was designated as 7 Al 7075. It had been fractured. The fracture surface before ion bombardment etching showed S, C, O, Mg, and Al. After etching, the Mg signal had disappeared. The second Al panel, designated as 15 Al 7075, which had been heat-treated, showed signs of blistering on the surface. The presputter Auger spectrum showed S, C, O, F, and Al. The post-sputter Auger spectrum showed S, C, O, Mg, Cu, and Al.

The two Ti-6Al-4V alloy panels showed similar Auger spectra to each other. The elements observed were C, O, and Ti but no Al or V.

7. GAS BEARINGS USED IN THE GUIDANCE SYSTEM OF THE MX MISSILE

Five gas bearings used in the guidance system for the MX missile were analyzed to determine the elements on the surface. A description of these bearings is given below.

ML-23	Cleaned and processed up through wheel balance - scattered spots all over
ML-33	Cleaning completed - acid cleaned to remove calcium spots at ends of grooves
ML-35	Large spot at middle
ML-044	As received from storage - no grooves machined in bearing

The above gas bearings had an aluminum oxide coating over a beryllium substrate. The results are as follows.

A typical Auger spectrum of the surface of ML-23 indicated aluminum, carbon, and oxygen.

ML-33 showed the same elements on the surface as ML-23 with the addition of fluorine. It was discovered that the specimens had been cleaned with toluene and then blown dry with a freon microduster. It had been previously observed that certain porous specimens tended to trap freon in them; since freon is a fluorocarbon, the fluorine could have come from it. A respective spectrum is illustrated in Figure 115.

ML-34 and ML-044 appeared to have a similar surface as ML-23. There did not appear to be any signs of calcium being present on the surface.

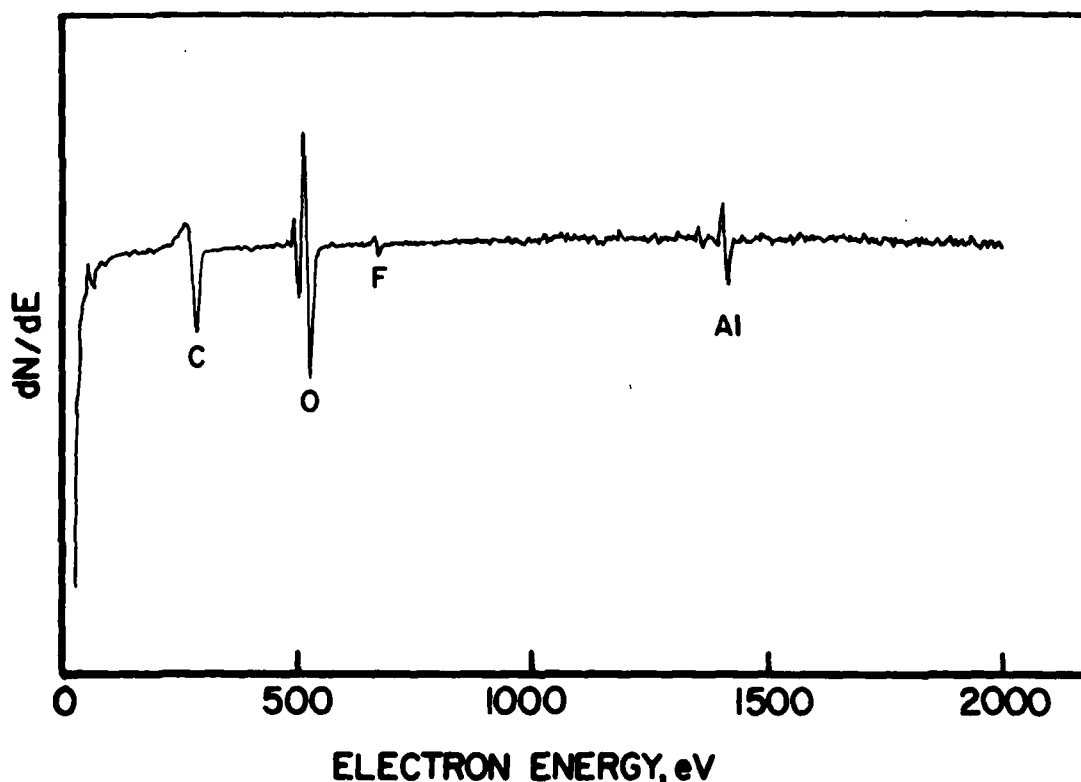


Figure 115. Auger Scan of Typical Area on Gas Bearing Number ML-33.

SECTION VII
LIST OF PUBLICATIONS AND PRESENTATIONS

The following publications and presentations cover work carried out under this contract. They were either prepared or appeared publicly during this reporting period.

Presentations

1. Soni, S. R. and Kim, R. Y., "Stress and Failure Analysis of an Adhesively Bonded Scarf Joint," 1981 ASME Failure Prevention and Reliability Conference, Hartford, CT, September 1981.
2. Drzal, L. T., Rich, M. J., and Hall, D. L., "Structure Property Relationships at the Composite Interphase," 15th Carbon Conference, The University of Pennsylvania, June 1981.
3. Soni, S. R., "A New Look at the Stress Fields in Multidirectional Composite Laminates with a Fastener Hole," American Institute of Aeronautics and Astronautics (Dayton-Cincinnati Section) Mini Symposium, Dayton, OH, March 1981.
4. Kim, R. Y. and Aoki, R. M., "Transverse Crack and Delamination in Composite Materials," 3rd National and 1st International Conference on Composite Materials, Milano, Italy, November 1980.
5. Husman, G. and Hartness, J. T., "Acetylene Terminated Sulfone Resin Development," 12th National SAMPE Technical Conference, Seattle, WA, October 1980.
6. Kim, R. Y., "Experimental Assessment of Static and Fatigue Damage of Graphite/Epoxy Laminates," 3rd International Conference on Composite Materials, Paris, France, August 1980.

Publications

1. Kim, R. Y., "On the Off-Axis and Angle Ply Strength of Composites," Test Methods and Design Allowables for Fibrous Composites, ASTM STP 734 (1981).
2. Drzal, L. T., Rich, M. J., Camping, J. D., and Park, W. J., "Interfacial Shear Strength and Failure Mechanisms in Graphite Fiber Composites," AFWAL-TR-81-4003, January 1981.
3. Ford, D. and Hall, D. L., "Modifications and Extensions to the Computer Program ADDES," UDR-TM-80-43, October 1980.

Publications (Concluded)

4. Kim, R. Y., "Experimental Assessment of Static and Fatigue Damage of Graphite/Epoxy Laminates," Advances in Composite Materials, Proceedings of the Third International Conference on Composite Materials, Paris, France (1980).
5. Fowler, C. C., Browning, C. E., and Von Kuzenko, M., "Dynamic Mechanical Characterization of Advanced Composite Epoxy Matrix Resins of Altered Composition," ACS Symposium Series Book, Resins for Aerospace (1980).

REFERENCES

1. Hoggatt, J. T. and Von Volki, A. D., "Evaluation of Reinforced Thermoplastic Composites and Adhesives," Naval Air Systems Command Final Report, Contract N00017-7A-C-0026, March 1975.
2. May, L. C. and Goad, R. C., "Manufacturing Methods for Fabrication and Assembly of Advanced Composite Primary Aircraft Structure," U.S. Air Force Materials Laboratory Report, AFML-TR-75-111, July 1975.
3. Laakso, J. H. and Hoggatt, J. T., "Development of a Low-Cost Graphite Reinforced Composite Primary Structural Component," Naval Air Development Center Final Report, Contract N62269-74-C-0368, December 1976.
4. Husman, G. and Hartness, J., "Polyphenyl Sulfone Matrix Composites," 24th National SAMPE Symposium and Exhibition, Volume 24, Book 2, p. 21 (1979).
5. Hartness, J., "Polyphenylene Sulfide Matrix Composites," 25th National SAMPE Symposium and Exhibition, Volume 25, p. 376 (1980).
6. Gardner, R. J. and Martin, J. R., "Effect of Relative Humidity on the Mechanical Properties of Poly(1,4-Butylene Terephthalate)," Journal of Applied Polymer Science, Vol. 25, pp. 2353-2361 (1980).
7. "Improved Materials for Composites and Adhesives," University of Dayton Research Institute Annual Progress Report, AFML-TR-79-4176, May 1979.
8. Drzal, L. T., Rich, M. J., Camping, J. D., and Park, W. J., Proceedings of 35th Society for the Plastics Industry RP/C Technical Conference, Paper 20-C, 1980.
9. Hercules, Inc., Wilmington, Delaware.
10. Trademark, Shell Chemical Company, Houston, Texas.
11. Pfaltz and Bauer, Inc., Stamford, Connecticut.
12. Aldrich Chemical Company, Inc., Milwaukee, Wisconsin.
13. Instron Corporation, Canton, Massachusetts.
14. McMahon, P. E., SAMPE Quarterly, Vol. 6, No. 1, 7 (1974).
15. Techne (Princeton) Limited, Princeton, New Jersey.

16. Drzal, L. T., Rich, M. J., and Lloyd, P. F., Proceedings ACS Convention, Poly. Preprints Vol. 22, No. 2, 1981.
17. Kim, S. L., Skibo, M. D., Manson, J. A., Hertzog, R. W., and Janiszewski, J., Poly. Eng. Sci., 18, 1093 (1978).
18. Selby, K. and Miller, L. E., J. Math. Sci., 10, 12 (1975).
19. Kelly, A. and Tyson, W. R., J. Mech. Phys. Solids, 13, 329 (1965).
20. Drzal, L. T., Rich, M. J., and Hall, D. L., Proc. 15th Biennial Carbon Conference, Paper FC-14, 1981.
21. Alfa Products, Danvers, Massachusetts.
22. California Fine Wire Company, Grover City, California.
23. Drzal, L. T. and Mescher, J. A., "A Volumetric Gas Adsorption System for the Characterization of the Surfaces of Adherends and Reinforcing Fibers," Air Force Materials Laboratory Technical Report, AFML-TR-76-84, 1976.
24. Brunauer, S., Emmett, P. H., and Teller, E., J. Am. Chem., 60, 309 (1938).
25. Wagner, C. D., et. al., Handbook of X-ray Photoelectron Spectroscopy, 1979.
26. The Boeing Aircraft Company, Seattle, Washington.
27. Schwartz, H. S., Journal of Applied Polymer Science: Applied Polymer Symposium, 32, 65 (1977).
28. Keller, F., Wilcox, G. W., Tosterud, M., and Slunder, C. J., Metals and Alloys, 10, 219 (1939).
29. Kissin, G. H., Deal, B. E., and Paulson, R. V., in The Finishing of Aluminum, G. H. Kissin, ed. (New York: Reinhold Publishing Corp., 1963), p. 13.
30. Solomon, James S. and Hanlin, D. E., Applications of Surface Science, 4, 307 (1980).
31. Hennemann, O. D., "A Comparison of Anodized Processes on the Strength and Durability of Adhesively Bonded Aluminum," Third Annual Meeting of the Adhesion Society, Savannah, Ga., February 1980.
32. Schwartz, H. S., SAMPE Journal, 13, 2 (1977).
33. Sun, T. S., McNamara, D. K., Ahern, J. S., Chen, J. M., Ditchek, B., and Venables, J. D., Applications of Surface Science, 5, 406 (1980).

34. Strehblow, H.-H. and Doherty, C. J., Journal Electrochemical Society, 125, 30 (1978).
35. Strehblow, H.-H., Millian-Smith, C. M., and Augustyniak, W. M., Journal Electrochemical Society, 125, 915 (1978).
36. Golubev, A. I. and Ignatov, N. N., Zashchita Metallov, 1, 445 (1965).
37. Spooner, R. C., Journal Electrochemical Society, 125, 127 (1978).
38. Smith, David P., Surface Science, 25, 171 (1971).
39. Mathieu, H. J. and Landolt, D., in Proceedings of the 7th International Vacuum Congress and 3rd International Conference on Solid Surfaces, Vienna 1977, R. Debrozemy, F. Rudenauer, F. Viehbock, and A. Breth, eds. (Debrozemy, Vienna, 1977), p. 2023.
40. Kelly, R. and Lam, N. Q., Radiat. Eff., 19, 39 (1973).
41. Chu, W. K., Mayer, J. W., and Nicolet, M.-A., Backscattering Spectrometry (Academic Press, New York, 1978), pp. 120-122.
42. Kirchner, J. and Etzkorn, H. W., in Proceedings of the 7th International Vacuum Congress and 3rd International Conference on Solid Surfaces, Vienna 1977, R. Debrozemy, F. Rudenauer, F. Viehbock, and A. Breth, eds. (Debrozemy, Vienna, 1977), p. 2213.
43. Honig, R. and Harrington, V., Thin Solid Films, 19, 43 (1973).
44. Röhl, Klaus and Hammer, Christoph, Thin Solid Films, 57, 209 (1979).
45. Anderson, H. H., Applied Physics, 18, 131 (1979).
46. Mathieu, H. J., McClure, D. E., and Landolt, D., Thin Solid Films, 38, 281 (1976).
47. Mathieu, H. J. and Landolt, D., Le Vide Les Couches Minces, Numero special Mars, 273 (1979).
48. Hofmann, S. and Erlewein, J., Thin Solid Films, 43, 275 (1977).
49. Coburn, J. W. and Kay, Eric, Critical Review of Solid State Science, 4, 561 (1974).
50. Swartz, S. A., Helms, C. R., and Spicer, W. E., Journal of Vacuum Science and Technology, 15, 227 (1978).

51. Brundle, C. R., Journal of Vacuum Science and Technology, 11, 212 (1974).
52. Navinšek, Boris, Progress in Surface Science, 7, 49 (1975).
53. Kistemaker, J. and Roosendaal, H. E., Japan Journal of Applied Physics, Supplement 2, 571 (1974).
54. Chu, W. K., Mayer, J. W., and Nicolet, M-A., Backscattering Spectrometry (Academic Press, New York, 1978), pp. 328-331.
55. Furneau, R. C., Thompson, G. E., and Wood, J. C., Corrosion Science, 18, 853 (1978).
56. Mackintosh, W. D., Brown, F., and Plattner, H. H., Journal of the Electrochemical Society, 121, 1281 (1974).
57. Roche, A. A., Solomon, J. S., and Baun, W. L., Appl. Surf. Sci., 7, 83 (1981).
58. Roche, A. A., Solomon, J. S., and Baun, W. L., Air Force Wright Aeronautical Laboratories Technical Report, AFWAL-TR-80-4105, August 1980.
59. Perrier, R., Bodu, J. J., and Brunin, M., Surface Techn., 8, 463 (1979).
60. Armstrong, N. R. and Quinn, R. K., Surf. Sci., 67, 451 (1977).
61. Wagner, C. D., Riggs, W. N., Davis, L. E., Moulder, J. F., and Muilenberg, G. E., Handbook of X-ray Photoelectron Spectroscopy, G. E. Muilenberg, ed., Perkin-Elmer Co., Physical Electronics Division, Minnesota, 1979.
62. Dalard, F., Montella, C., and Gandon, J., Surf. Tech., 8, 203 (1979).
63. Pauling, L., The Nature of the Chemical Bond, 3rd Ed., Cornell University Press, Ithica (1960).
64. Demosthenous, M., These, Lyon (1978).
65. Ramquist, L., Hamrin, K., Johansson, G., Fahlman, A., and Nordling, A., J. Phys. Chem. Solids, 30, 1835 (1969).
66. Fowler, C. C., Jr., "Testing and Machining Techniques for Reinforced Plastic Test Specimens," Air Force Materials Laboratory Technical Report, AFML-TR-70-73, 1970.
67. Yuceoglu, U. and Updike, D. P., J. Engineering Mechanics Division, Proceedings of the American Society for Civil Engineers, 106, No. EMI, 1980.

68. Kemochi, K. and Uemura, M., Experimental Mechanics, p. 80, March 1980.
69. Pagano, N. J., "Stress Fields in Composite Laminates," Int. J. Solids Structures, 14, 385-400 (1978).
70. Gurtin, M. E., "Continuum Theory of Fracture," Mechanics of Composites Review, Bergamo Center, Dayton, Ohio, 83-86 (1977).
71. Wang, A. S. D. and Crossman, F. W., "Some New Results on Edge Effect in Symmetric Composite Laminates," J. Composite Mat., 11, 92 (1977).
72. Stanton, E. L., Crain, L. M., and Neu, T. F., "A Parametric Cubic Modelling System for General Solids of Composite Material," Int. J. Num. Meth. Engg., 11, 653 (1977).
73. Pagano, N. J., "Exact Moduli of Anisotropic Laminates," in Composite Materials, Mechanics of Composite Materials (edited by G. P. Sendeckyj, Vol. 2, pp. 23-44, Academic Press, New York (1974)).
74. Pagano, N. J., "On the Calculation of Interlaminar Normal Stress in Composite Laminates," J. Composite Mat., 8, 65-82 (1974).
75. Salamon, N. J., "An Assessment of the Interlaminar Stress Problem in Laminated Composites," J. Composite Matl., Supplement 14, 177-194 (1980).
76. Spilker, R. L. and Ting, T. C. T., "Stress Analysis of Composites," Army Materials and Mechanics Research Center, Watertown, Mass., Technical Report #AMMRC-TR-81-5 (1981).
77. Raju, I. S., Whitcomb, J. D., and Goree, J. G., "A New Look at Numerical Analyses of Free Edge Stresses in Composite Laminates," NASA Tech. Paper 1751 (1981).
78. Blumberg, N. N. and Tamuzh, V. P., "Edge Effects and Stress Concentrations in Multilaminate Composite Plates," Mechanics of Composite Materials, 298-307 (1980). Translated from Russian Jl. Mekh. Kompositn. Mater., 3, 424-435 (1980).
79. Partsevskii, V. V., "Approximate Analysis of Mechanisms of Fracture of Laminated Composites at a Free Edge," Mechanics of Composite Materials, 179-185 (1980). Translated from Russian Jl. Mekh. Kompositn. Mater., 2, 246-253 (1980).
80. Forman, R., Applications of Surface Science, Vol. 2, No. 2, 258 (1979).
81. Verhoeven, J. A. Th. and van Doveren, H., Mikrochimica Acta, 331-334 (1979).

82. Anderson, P. A., Phys. Rev., 47, 958 (1935).
83. Verhoeven, J. and van Doveren, H., Applications of Surface Science, 5, 361-373 (1980).
84. Wagner, C., et. al., Handbook of X-ray Photoelectron Spectroscopy, Perkin-Elmer Corporation, Eden Prairie, Minnesota, 1979.
85. Johansson, G., et. al., J. Electron Spec. Related Phen., 2, 295-317 (1973).
86. Wagner, C. D., Gale, L. H., and Raymond, R. H., Anal. Chem., 51, 466-482 (1979).
87. van Doveren, H. and Verhoeven, J., J. Electron Spec. Related Phen., 21, 265-273 (1980).
88. Lampert, W. V., et. al., to be published in J. Electron Spec. Related Phen..
89. Sinharoy, S. and Wolfe, A. L., J. Electron Spec. Related Phen., 18, 369-371 (1980).

APPENDIX A

UDR-TR-81-84

IN-PLANE TENSILE STRENGTH OF
MULTIDIRECTIONAL COMPOSITE LAMINATES

R. Y. Kim

August 1981

UNIVERSITY OF DAYTON
RESEARCH INSTITUTE
DAYTON, OHIO 45469

FOREWORD

This report was prepared by the University of Dayton Research Institute, Dayton, Ohio under U.S. Air Force Contract No. F33615-78-C-5102. The work was administered under the direction of the Nonmetallic Materials Division, Materials Laboratory, Air Force Wright Aeronautical Laboratories, Wright-Patterson Air Force Base, Ohio.

ABSTRACT

A simple approach using quadratic failure theory has been employed to predict the in-plane tensile strength of multidirectional laminates as an engineering approximation. The experimental result obtained from various types of laminates of T300/5208 graphite/epoxy was found to be in good agreement with predictions except for those laminates revealing delamination.

TABLE OF CONTENTS

Section		Page
I	INTRODUCTION	1
II	EXPERIMENTAL PROCEDURE AND DATA ANALYSIS	3
III	RESULTS AND DISCUSSION	5
IV	CONCLUSIONS	24
	REFERENCES	25

LIST OF ILLUSTRATIONS

Figure		Page
1	Photomicrographs Showing Transverse Crack Under Static Loading	6
2	Photomicrographs Showing Transverse Crack and Delamination for $[0/\pm\theta/90]_s$ Under Static Loading	7
3	Photomicrographs Showing Transverse Crack for $[0/90/\pm\theta]_s$ Under Static Loading	9
4	X-ray Pictures Showing Delamination Under Static Loading: Dark Area Indicates Delamination	11
5	Longitudinal Modulus Predicted by Laminated Plate Theory	15
6	Longitudinal Poisson's Ratio Predicted by Laminated Plate Theory	15
7	Stress-Strain Curves Predicted by Laminated Plate Theory	16
8	Comparison of Calculated In-Plane Tensile Strength with Experiment	18
9	Comparison of Calculated In-Plane Tensile Strength with Experiment	19
10	Typical Acoustic Emission Signals Indicating Onset of Delamination	22
11	Typical Acoustic Emission Signals Indicating Onset of Delamination	23

LIST OF TABLES

Table		Page
1	Crack Density	13
2	Stress Level at the First-Ply Failure in MPa	20
3	Stress Level at Onset of Delamination	20

SECTION I

INTRODUCTION

Most composite laminates for structural application consist of multidirectional layers to meet the structural integrity. Prediction of the in-plane strength of a multidirectional laminate is of great importance in design of the laminate as well as development of material systems. Most laminates reveal a progressive type of failure when subjected to an applied stress. The final failure of a laminate is usually followed by the weaker ply failure in the form of matrix cracking along fiber direction. In certain laminates delamination is also initiated at the free edges and propagated toward the middle of the test specimen. The type and degree of these damages vary widely depending upon lamination including stacking sequence, layer thickness, and material properties.

In view of this progressive failure process in multidirectional laminates, a variety of approaches have been reported to develop a reliable methodology to predict the in-plane tensile strength.^(1,2,3) These approaches are based on the damage caused by only transverse cracking and can be divided into two groups, depending upon complete elimination of damaged ply or employing damage functions in calculation of strength. Therefore, success of these approaches appears to remain in question until one has a proper understanding of the damage process and its influence on the strength change, including other failure modes such as delamination and fiber break, etc. Furthermore, one of the main obstacles in accepting these approaches in strength prediction is complexity in the calculation process with the uncertainty of gaining any improvement.

In this work a simple approach is employed to predict the in-plane tensile strength of a multidirectional laminate as an engineering approximation. To achieve this, we made an assumption that ultimate failure of multidirectional laminates occurs upon the strongest ply failure for a given externally-applied

stress resultant ignoring the damages incurred in the course of loading. The in-plane stress components in each constituent ply for a given laminate were calculated using laminated plate theory. The quadratic failure criterion developed by Tsai and Wu is then applied to the respective ply.⁽⁴⁾ The analytical results were compared with experimental results obtained from a variety of laminates including laminates showing delamination before final failure. The damage process, in terms of delamination and transverse crack, was experimentally observed for selected laminates; and its influence on final failure was briefly given.

SECTION II

EXPERIMENTAL PROCEDURE AND DATA ANALYSIS

Three basic families of laminates used in this work are $[0_2/\pm\theta]_s$, $[0/\pm\theta/90]_s$, and $[0/90/\pm\theta]_s$, with $\theta = 5, 10, 15, 30, 45, 60, 75$, and 90 degrees. The effect of delamination can be considered by comparing the results of the last two families of laminates, since interlaminar normal stress at the free edge region is tension in the $[0/\pm\theta/90]_s$ laminate and compression in the $[0/90/\pm\theta]_s$ laminate under applied uniaxial tensile loading.

The material system used in this study was T300/5208 graphite/epoxy supplied in the prepreg form by Narmco Corporation. Tensile coupons, $3/4$ " wide and 5" long in gage section, were prepared from the panels fabricated in an autoclave according to the manufacturer's recommended cure cycle. The fiber volume was 66% by volume and density was 1.6. The side edges of some specimens of several laminates were polished with 5 and 0.5 micron polishing powder in order to facilitate microscopic examination for assessing damages incurred during loading. The stress level at initiation of delamination was determined by acoustic emission. It was found that the rate of acoustic emission signal was rapidly increased with onset of delamination and virtually remained in the same level until final failure. Some specimens were unloaded after delamination to delineate the delamination area by x-ray. Some specimens were also instrumented with longitudinal and transverse strain gages in order to compare the stress-strain behavior predicted by laminated plate theory. All specimens were stored in a desiccator until being tested and then subjected to uniaxial tension using an MTS testing machine in the load control mode, with the loading rate corresponding to 16.7 to 33.4 m/m.s of the strain rate.

Following is a list of the ply properties and the strength of unidirectional laminate used in calculation.

$$\begin{aligned}
E_x &= 137.9 \text{ GPa} & E_y &= 9.7 \text{ GPa} \\
E_s &= 5.5 \text{ GPa} & \nu_{xy} &= 0.3 \\
X = X' &= 1,380 \text{ MPa} & S = S' &= 90 \text{ MPa} \\
Y &= 48 \text{ MPa} & Y' &= 192 \text{ MPa}
\end{aligned}$$

where

X, X' = tensile and compressive strength in the longitudinal direction;

S, S' = positive and negative shear strength in the longitudinal direction; and

Y, Y' = tensile and compressive strength in the transverse direction.

Because of experimental difficulty in determination of longitudinal compressive strength, we assumed that the compressive strength equaled the tensile strength for the T300/5208 graphite/epoxy. These material strengths allow determination of all the strength parameters, F'_s , except F_{xy} in the quadratic failure criterion given in equation (1).

$$F_{xx}\sigma_x^2 + F_{yy}\sigma_y^2 + 2F_{xy}\sigma_x\sigma_y + F_{ss}\sigma_s + F_x\sigma_x + F_y\sigma_y + F_s\sigma_s = 1 \quad (1)$$

In view of the difficulty in experimental determination of the F_{xy} term, Tsai introduced the following relation.⁽⁵⁾

$$F_{xy} = F_{xy}^* \sqrt{F_{xx}F_{yy}} \quad (2)$$

F_{xy}^* is bounded by a negative to positive unit to insure that the failure surface will intercept each stress axis. Tsai assigned negative 1/2 to the value of F_{xy}^* based on a generalization of the Von Mises yield criterion for isotropic material. Details can be found in Reference (5).

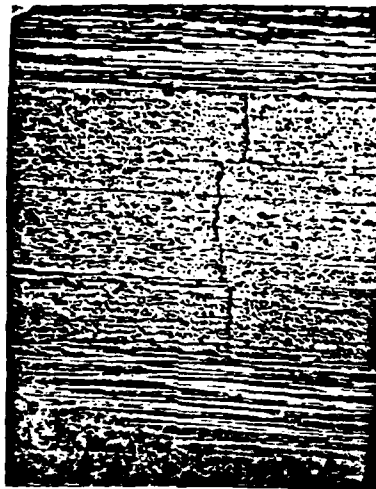
SECTION III

RESULTS AND DISCUSSION

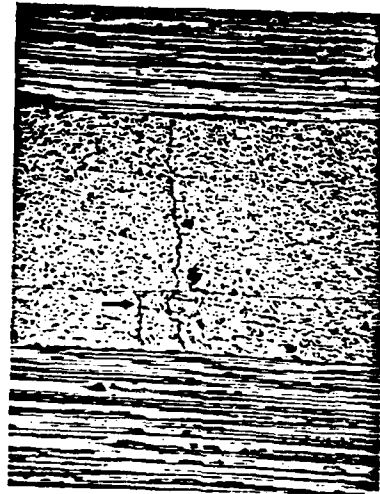
Damage in the form of transverse cracks in each off-axis layer and delamination between interfaces was observed at the free edges of a typical specimen of $[0_2/\pm\theta]_s$, $[0/90/\pm\theta]_s$, and $[0/\pm\theta/90]_s$ laminates under incremental step loading. Figures 1 to 3 show photomicrographs of the damage, along with the stress level at which it was taken. In the $[0_2/\pm\theta]_s$ laminate for $\theta \leq 45$, no transverse crack was found until the last loading step which was in the range of 92 to 98% of the ultimate strength. However, in both $[0_2/\pm 60]_s$ and $[0_2/\pm 75]_s$ laminates, most cracks were extended to the entire off-axis layers as shown in Figure 1. As the load is further increased, additional cracks, which usually occurred near the previous cracks, were found in the $\pm\theta$ layer as indicated by the arrow in Figure 1(b). In the $[0/90/\pm\theta]_s$ and $[0/\pm\theta/90]_s$ laminates, transverse cracks were found in the 90-degree layer for all laminates and in the $\pm\theta$ layer for $\theta \geq 45$. Most cracks in the $\pm\theta$ -degree layers were located at or near the tip of the 90-degree layer crack as shown in Figures 2 and 3. When θ is small, say less than 30 degrees, transverse cracks were hardly found in the $\pm\theta$ layers.

An extensive delamination has been observed in the $[0/\pm\theta/90]_s$ laminate for $\theta \leq 45$ as shown in Figure 2 (a,b,c,d). No delamination has been observed in the $[0/\pm 60/90]_s$ and $[0/\pm 75/90]_s$ laminates in spite of the presence of interlaminar normal stress at the free edges, as predicted by theory in Reference (6). The reason for this appears to be that the magnitude of the interlaminar stress is too small to induce delamination. The extent of delamination toward the middle of the specimen was obtained by x-ray and is shown in Figure 4. The stress level at the moment the picture was taken is also indicated.

The crack data observed in each test was reduced in terms of number of cracks per centimeter in the respective off-axis layer obtained from the total number of cracks divided by the

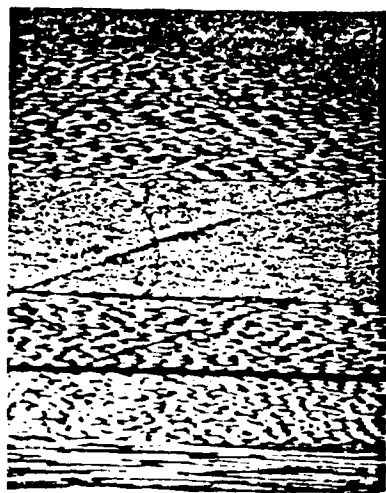


$[O_2/\pm 60]_s$ 586 MPa



$[O_2/\pm 75]_s$ 580 MPa

Figure 1. Photomicrographs Showing Transverse Crack Under Static Loading.



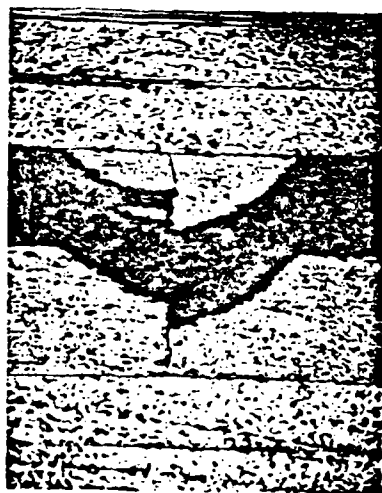
$[0/\pm 10/90]_s$ 800 MPa

(a)



$[0/\pm 15/90]_s$ 656 MPa

(b)



$[0/\pm 30/90]_s$ 397 MPa

(c)



$[0/\pm 45/90]_s$ 440 MPa

(d)

Figure 2. Photomicrographs Showing Transverse Crack and Delamination for $[0/\pm\theta/90]_s$ Under Static Loading.



$[0/\pm 60/90]_s$ 430 MPa

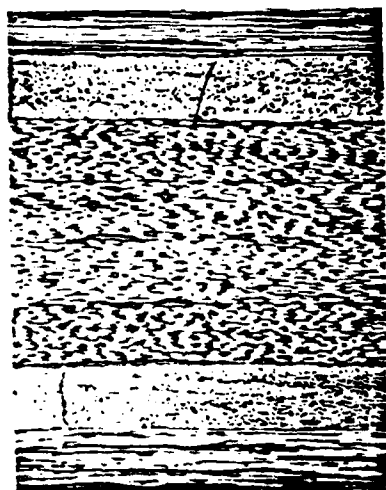
(e)



$[0/\pm 75/90]_s$ 414 MPa

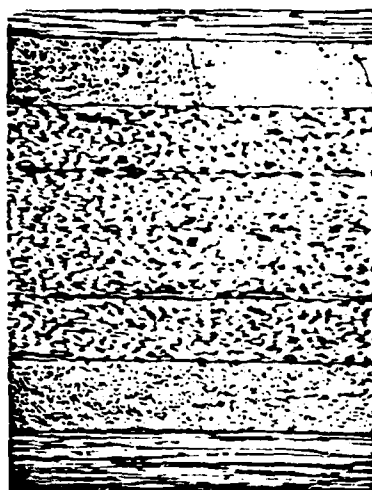
(f)

Figure 2. (Concluded) Photomicrographs Showing Transverse Crack and Delamination for $[0/\pm\theta/90]_s$ Under Static Loading.



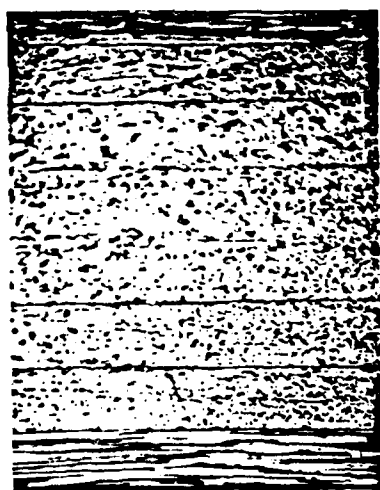
$[0/90/\pm 10]_s$ 931 MPa

(a)



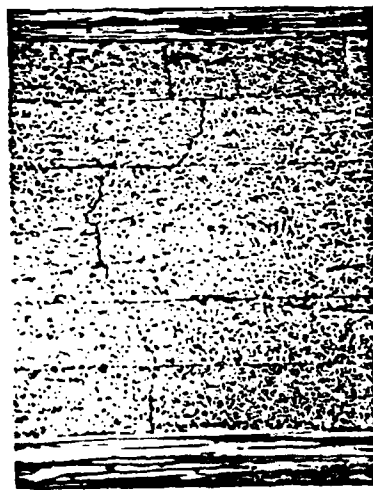
$[0/90/\pm 15]_s$ 738 MPa

(b)



$[0/90/\pm 30]_s$ 676 MPa

(c)



$[0/90/\pm 45]_s$ 552 MPa

(d)

Figure 3. Photomicrographs Showing Transverse Crack for $[0/90/\pm\theta]_s$ Under Static Loading.



$[0/90/\pm 60]_s$ 286 MPa

(e)



$[0/90/\pm 75]_s$ 165 MPa

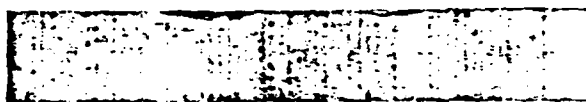
(f)

Figure 3. (Concluded) Photomicrographs Showing Transverse Crack for $[0/90/\pm \theta]_s$ Under Static Loading.



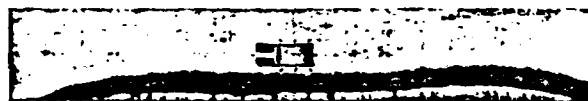
$[0/\pm 10/90]_s$ 800 MPa

(a)



$[0/\pm 15/90]_s$ 656 MPa

(b)



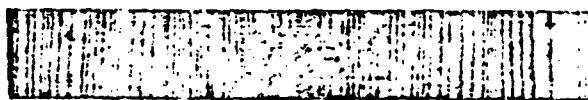
$[0/\pm 30/90]_s$ 448 MPa

(c)



$[0/\pm 45/90]_s$ 440 MPa

(d)



$[0/\pm 60/90]_s$ 430 MPa

(e)

Figure 4. X-ray Pictures Showing Delamination Under Static Loading: Dark Area Indicates Delamination.

measured length (12.7 cm). This quantity is referred to as crack density and listed in Table 1. The stress level, in terms of fraction of ultimate strength, is also indicated. Some specimens were broken before reaching the previous stress level. Although the data in Table 1 is obtained from one specimen, it indicates general trends of transverse cracking behavior which vary widely depending upon lamination and thickness for a given layer.

Figures 5 and 6 show the in-plane elastic constants (longitudinal modulus and Poisson's ratio) for the laminates of $[0_2/\pm\theta]_s$, $[0/90/\pm\theta]_s$, and $[0/\pm\theta/90]_s$ as a function of angle θ . Solid lines represent calculated results obtained by laminated plate theory, and experimental results are indicated by triangles for the $[0_2/\pm\theta]_s$ laminate and circles for the combined data of the $[0/90/\pm\theta]_s$ and $[0/\pm\theta/90]_s$ laminates. Each data point represents a mean of two specimens. The experimental data are compared well with the prediction for all angles.

In order to examine damage influence on the overall strain behavior of the laminates, Figure 7 presents the entire stress-strain curves for the $[0/90/\pm\theta]_s$ and $[0/\pm\theta/90]_s$ laminates, which show more damage than the $[0_2/\pm\theta]_s$ laminate. The straight line represents the result of linear analysis, and solid and open circles represent experimental data for the $[0/90/\pm\theta]_s$ and $[0/\pm\theta/90]_s$ laminates, respectively. The ordinate of the last data point corresponds to the ultimate strength of the specimen. The experimental data indicate fairly linear stress-strain behavior until final failure in most cases with a few exceptions. Slight non-linear strain behavior in the specimen of the $[0/\pm 30/90]_s$ laminate is mainly attributed to the delamination which was extended to the strain gage area. Delamination in the other laminates appears to be confined to near the free edge region until final failure. This is based on the previous work, indicating that axial strain change only occurred when either delamination or transverse cracking develops in the gage area.⁽⁷⁾ The small amount of strain jumps at a higher stress level in the specimen of the $[0/90/\pm 60]_s$ and $[0/\pm 60/90]_s$ laminates is attributed to the transverse cracks

TABLE 1
CRACK DENSITY

Laminate	Stress		Ply Orientation	Crack Density #/cm
	MPa	Fraction of Ultimate		
[0 ₂ /±60] _s	817	.95	+60	23.0
			-60/-60	12.5
[0 ₂ /±75] _s	758	.93	+75	22.3
			-75/-75	14.6
[0/90/±10] _s	931	1.02	90	3.7
			+10	0
			-10/-10	0
[0/±10/90] _s	800	1.01	+10	0
			-10	0
			90/90	20.4
[0/90/±15] _s	758	.96	90	0.4
			+15	0
			-15/-15	0
[0/±15/±90] _s	656	1.01	+15	0
			-15	0.2
			90/90	12.0
[0/90/±30] _s	715	1.00	90	6.5
			+30	0
			-30/-30	0
[0/±30/90] _s	489	.98	30	0
			-30	2.8
			90/90	13.6
[0/90/±45] _s	552	1.04	90	10.4
			+45	1.9
			-45/-45	0.1
[0/±45/90] _s	453	.91	+45	0.3
			-45	8.7
			90/90	10.8
[0/90/±60] _s	400	.84	90	21.5
			+60	21.3
			-60/-60	13.0
[0/±60/90] _s	474	.91	+60	9.1
			-60	14.3
			90/90	8.9

TABLE 1
CRACK DENSITY
(Concluded)

Laminate	Stress		Ply Orientation	Crack Density #/cm
	MPa	Fraction of Ultimate		
[0/90/±75] _s	441	.91	90	15.4
			+75	18.0
			-75/-75	12.0
[0/±75/90] _s	405	.96	+75	19.5
			-75	18.3
			90/90	13.1

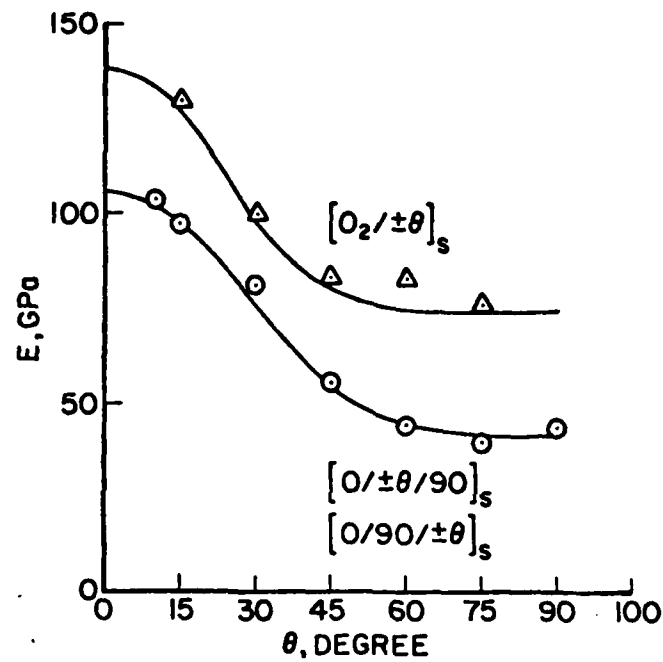


Figure 5. Longitudinal Modulus Predicted by Laminated Plate Theory. Symbols represent experimental results.

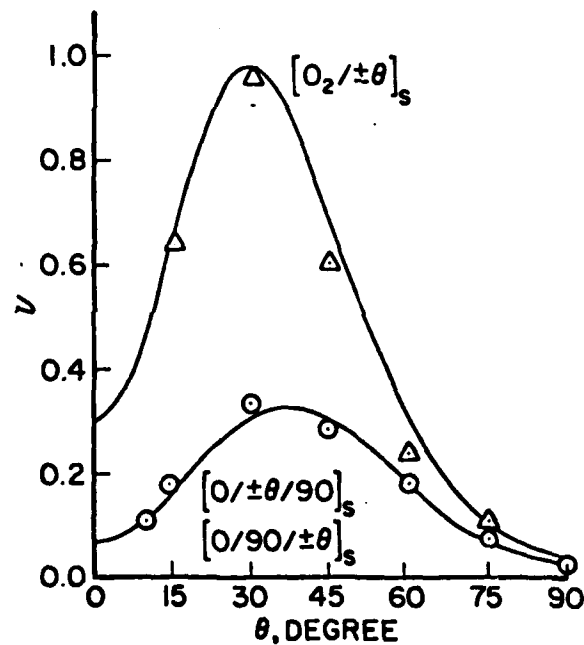


Figure 6. Longitudinal Poisson's Ratio Predicted by Laminated Plate Theory. Symbols represent experimental results.

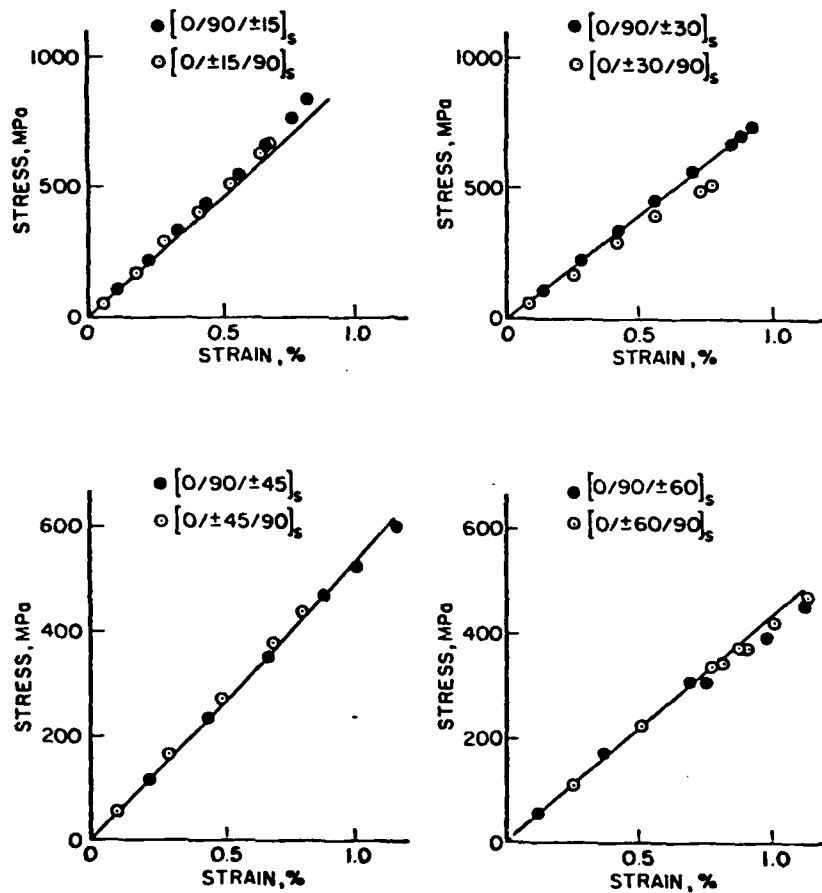


Figure 7. Stress-Strain Curves Predicted by Laminated Plate Theory. Solid and open circles represent experimental data.

which occurred in the strain gage area. Similar jumps were observed in the laminates of $\theta = 75$. It remains in question at present how this small amount of the observed strain change will contribute to the final failure of the laminate.

Figures 8 and 9 show analytical prediction of the failure stress of the respective layers for the laminate family of $[0_2/\pm\theta]_s$, $[0/90/\pm\theta]_s$, and $[0/\pm\theta/90]_s$ as a function of angle θ . The curing residual stresses are not included in this calculation. Various symbols in Figures 8 and 9 are experimental results which represent the mean of 10 to 11 specimens for a given laminate.

In the $[0_2/\pm\theta]_s$ laminate, the experimental results are fairly well compared with the analytical results of the 0-degree layer. Analysis gives a little conservative prediction in all cases except for $\theta = 10$ and 15 degrees. Analytical prediction shows almost identical strength for the 0-degree and off-axis layers up to approximately 30 degrees and, thereafter, the difference increases as increasing angle θ as shown in Figure 8. This implies that the laminates for $\theta \leq 30$ will fail without revealing progressive failure; that is, no off-axis ply failure will be preceded by final failure. On the other hand, off-axis ply failure will be anticipated before final failure when θ is greater than 30 degrees. The results of crack observation described earlier appear to support this analytical prediction except for the specimen of the $[0_2/\pm45]_s$ laminate. Three more specimens of the $[0_2/\pm45]_s$ laminate were examined to find transverse crack before failure. None of the specimens show any evidence of crack until the last loading step, which was in the range of 92 to 98% of the ultimate strength. A similar difference in off-axis layer failure between prediction and experiment was observed for the $[0_2/\pm60]_s$ and $[0_2/\pm75]_s$ laminates as shown in Table 2. The experimental result is the mean of five specimens. The theory also appears to underestimate the off-axis ply failure for the family of the $[0_2/\pm\theta]_s$ laminate. In spite of the numerous cracks extended to the entire off-axis layers in the $[0_2/\pm60]_s$ and $[0_2/\pm75]_s$ laminates, the experimentally-determined strengths are greater than those of prediction.

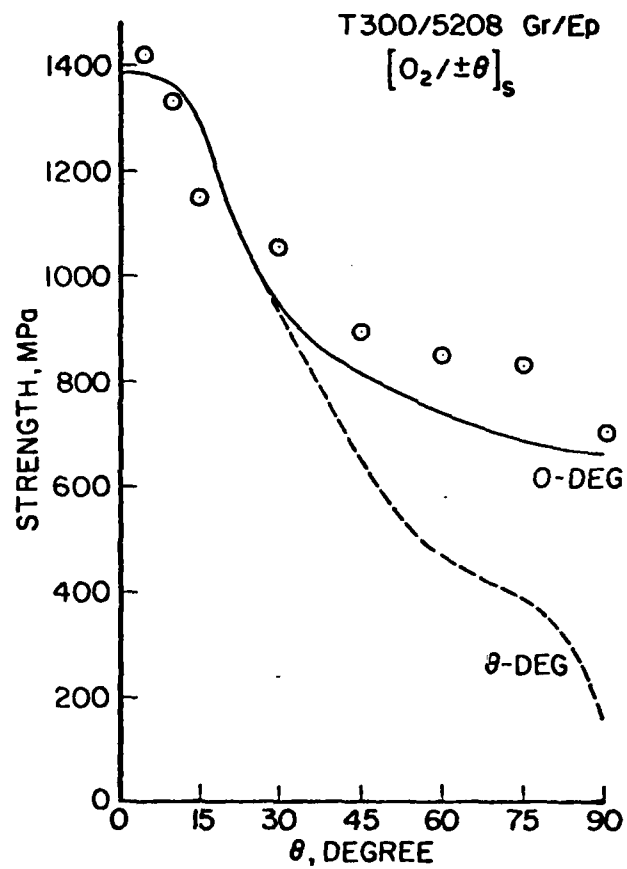


Figure 8. Comparison of Calculated In-Plane Tensile Strength with Experiment.

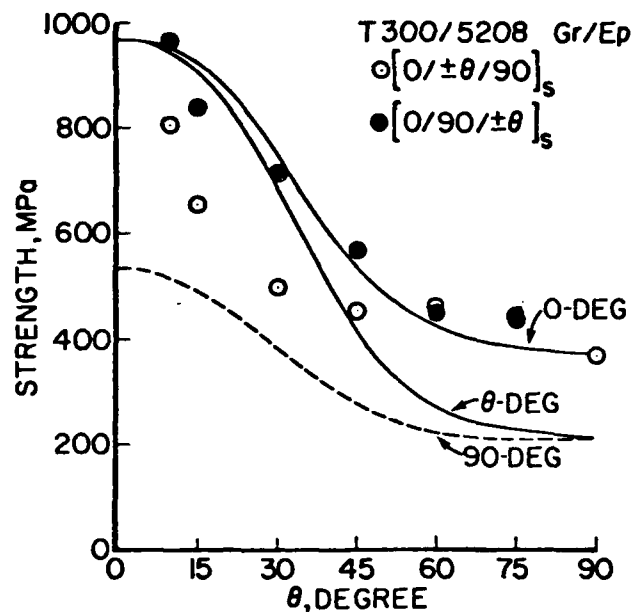


Figure 9. Comparison of Calculated In-Plane Tensile Strength with Experiment.

TABLE 2
STRESS LEVEL AT THE FIRST-PLY FAILURE IN MPa

Laminate	Prediction	Experiment
$[0_2/\pm 60]_s$	465	544
$[0_2/\pm 75]_s$	390	471

Experimentally-determined strength is significantly different between two families of the $[0/90/\pm\theta]_s$ and $[0/\pm\theta/90]_s$ laminates for $\theta \leq 45$ in spite of identical prediction as shown in Figure 9. For those laminates which did not show any delamination until final failure, the experimental results are fairly well compared with the analytical results of the 0-degree layer. Experimentally-determined strength for the laminates experienced in delamination is markedly smaller than the predicted strength. Table 3 shows the stress level at onset of delamination determined by acoustic emission for seven to eight specimens of each laminate except for the $[0/\pm 10/90]_s$ laminate (two specimens).

TABLE 3
STRESS LEVEL AT ONSET OF DELAMINATION

Laminate	Stress, MPa
$[0/\pm 10/90]_s$	800
$[0/\pm 15/90]_s$	652
$[0/\pm 30/90]_s$	413
$[0/\pm 45/90]_s$	400

Figure 10 shows raw data of typical acoustic emission rate versus applied load for the $[0/\pm 15/90]_s$ and $[0/\pm 30/90]_s$ laminates. Sudden increase of acoustic emission signal is indicative of onset of delamination, and this signal remained practically at the same level until final failure. This is indicative of continuous propagation of delamination as a function of applied stress. A similar acoustic emission pattern was observed for the specimens of the $[0/\pm 45/90]_s$ laminate. However, for the $[0/\pm 10/90]_s$ laminate, two types of typical acoustic emission patterns were observed as shown in Figure 11. The acoustic signal in Figure 11(a) shows strong indication of delamination upon failure, whereas Figure 11(b) does not show any indication of delamination. It is not clear whether or not delamination occurred from the acoustic emission signals in Figure 11. However, during examination of the free edges under step loading described previously, delamination was found in two specimens showing a similar acoustic emission pattern in Figure 11(b). The reason for this appears to be that the specimen fails upon delamination, which is limited to a very small area, as shown in Figure 4(a).

Experimental observation of transverse cracking shows quantitatively the similar trend predicted by analysis on the off-axis ply failure in Figure 9. Although a number of transverse cracks were found in the respective off-axis ply in both families of laminates, especially for $\theta \geq 45$, there is no evidence of strength degradation due to these cracks, as there was in the case of $[0_2/\pm \theta]_s$. Further study needs to be done for a variety of laminates, especially considering larger size of cracks.

AD-A114 069

DAYTON UNIV OH RESEARCH INST

F/G 11/4

IMPROVED MATERIALS FOR COMPOSITES AND ADHESIVES.(U)

DEC 81 D ASKINS, A BEHME, A BIERMANN, W CLICK F33615-78-C-5102

UNCLASSIFIED

UDR-TR-81-108

AFWAL-TR-81-4154

NL

4 x 4

4 x 4

■



END

DATE

FORM

5-B

DTM

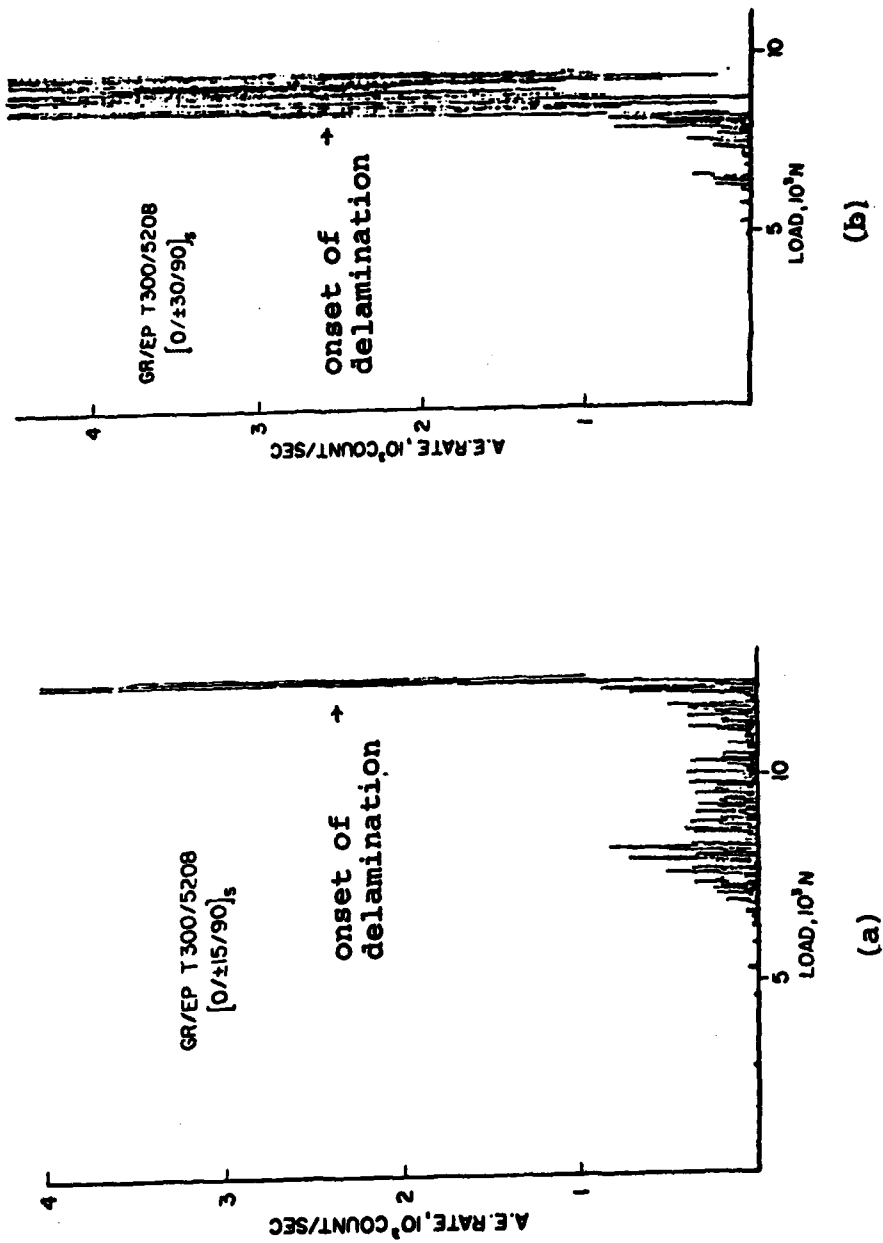
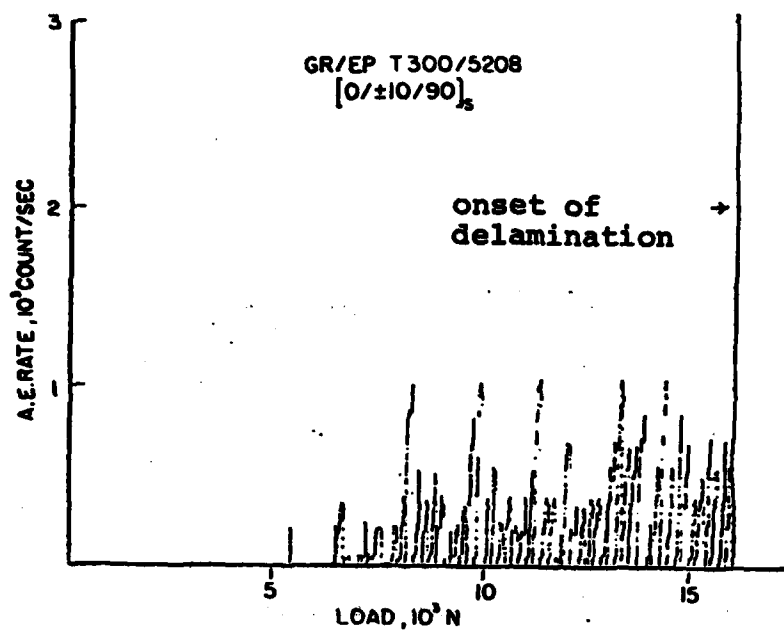
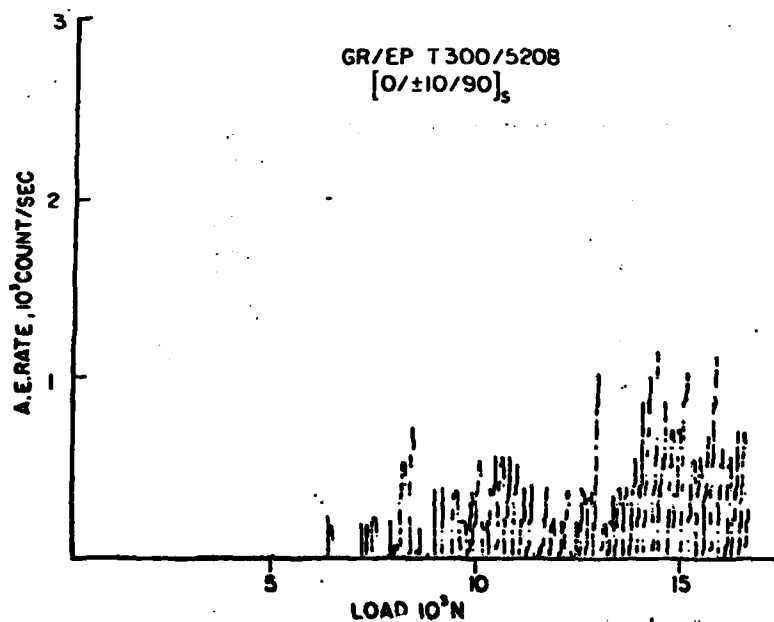


Figure 10. Typical Acoustic Emission Signals Indicating Onset of Delamination.



(a)



(b)

Figure 11. Typical Acoustic Emission Signals Indicating Onset of Delamination.

SECTION IV CONCLUSIONS

Quadratic failure theory in conjunction with laminated plate theory has been applied to predict the in-plane tensile strength of multidirectional composite laminates. In analytical prediction, the ultimate failure of a laminate is assumed to occur upon the failure of the strongest ply in the laminate by ignoring the contribution of interlaminar stresses and transverse cracks preceded by final failure. The experimental result obtained from various types of laminates of T300/5208 graphite/epoxy was found to be in good agreement with prediction with consistent exceptions. The exceptions are all the laminates show delamination at the free edges which substantially reduces the load-carrying capability. The experimental result indicates that the effect of transverse cracking on the strength appears to be insignificant for those laminates considered in this study. This approach has the advantage of simplicity and quickness in approximation of the in-plane tensile strength of multidirectional laminates.

REFERENCES

1. Nuismer, R. J., "Predicting the Performance and Failure of Multidirectional Polymeric Matrix Composite Laminates: A Combined Micro-Macro Approach," ICCM3, Vol. 1.
2. Rowlands, R. E., "Analytical-Experimental Correlation of Polyaxial States of Stress in Thornel-Epoxy Laminates," Experimental Mechanics, Vol. 18, No. 7, July 1978.
3. Yeow, Y. T. and Brinson, H. F., "An Experimental Investigation on Tensile Moduli and Strengths of Graphite/Epoxy Laminates," Experimental Mechanics, Vol. 17, No. 11, November 1977.
4. Tsai, S. W. and Wu, E. M., "A General Theory of Strength for Anisotropic Materials," J. Composite Materials, Vol. 9, January 1971.
5. Tsai, S. W. and Hahn, H. T., Introduction to Composite Materials, Chapter 7, Technomic, 1980.
6. Pagano, N. J. and Pipes, R. B., "Some Observations on the Interlaminar Strength of Composite Laminates," Int. J. Mech. Sci., Vol. 15, 1973.
7. Kim, R. Y. and Hahn, H. T., "Effect of Curing Stresses on the First-Ply Failure in Composite Laminates," J. Composite Materials, Vol. 13, January 1979.

APPENDIX B

TRANSVERSE CRACK AND DELAMINATION IN
COMPOSITE MATERIALS

by

R. Y. Kim

University of Dayton
Research Institute
Dayton, Ohio U.S.A.

and

R. M. Aoki

DFVLR
Stuttgart, West Germany

ABSTRACT

An experimental investigation has been conducted on damage behavior related with matrix cracking under static and fatigue loading using two stacking sequences of the $(0/90_n/\pm 45)_s$ and $(0/\pm 45/90_n)_s$ laminates for $n=1, 3$, and 6 . The latter stacking sequence produces tensile interlaminar normal stress along free edges of a tensile coupon, whereas the other stacking sequence produces compression at the same edges. Emphasis in this study was on the interaction between transverse cracks and delamination, and effect of layer thickness on crack density and propagation. Transverse crack and delamination were periodically measured by interrupting testing until final failure. Experimental results indicate that the crack density and propagation are influenced by layer thickness, and delamination appears to be mainly governed by either or combination of tensile interlaminar normal stress and size of transverse crack. The applied force at incipient delamination can be predicted by an existing theory with a certain limitation.

INTRODUCTION

Transverse cracking is one of the major types of damage which is frequently observed in multi-directional composite laminates subjected to a certain load history. The transverse crack develops first in a weaker ply within a laminate and multiplies progressively throughout the specimen volume before final failure. These transverse cracks often extend to the adjacent off-axis layer and in some cases along layer interfaces resulting in reduction of load carrying capability as well as stiffness of the laminate. Thus, the better understanding of mechanisms related to formation and propagation of crack appears to be very useful for developing a reliable life prediction methodology for composite materials. Previous works indicated that the transverse cracks appear to play a significant role in initiation of delamination in addition to tensile interlaminar normal stress [1,2]. The interlaminar normal stress at free edge has been considered as a key factor for causing delamination [3]. However, the laminate which produces compressive interlaminar stress at free edge under uniaxial tension also exhibited a considerable amount of delamination under uniaxial tension-tension fatigue loading [1].

The main objective of this study was to improve our understanding of crack formation including delamination in composite laminate under static and fatigue loading. Scope of this paper is limited to interaction between transverse crack and delamination, effect of layer thickness on crack density and propagation of a crack into the adjacent off-axis layers. To accomplish this objective, the transverse cracks and delamination developed on the free edges of each specimen were observed in the various stages of loading using a microscope, acoustic emission, and ultrasonic C-scan.

Experimental results are presented for two stacking sequences of T300/5208 graphite/epoxy, $(0/90_n/\pm 45)_s$ and $(0/\pm 45/90_n)_s$. The interlaminar normal stresses at various interfaces along thickness direction were calculated by the method developed in Ref. [3] to delineate the interlaminar normal stress under uniaxial tensile loading. The calculated stress levels for initiation of delamination were compared with experimental results for the $(0/\pm 45/90_n)_s$ laminates of which free edge interlaminar normal stress is tension.

EXPERIMENTAL PROGRAM

The material system chosen in this study is T300/5208 graphite/epoxy supplied in prepreg form by Narmco Corporation. Two quasi-isotropic laminates, $(0/90_n/\pm 45)_s$ and $(0/\pm 45/90_n)_s$ with $n=1, 3$, and 6 were fabricated in an autoclave according to the manufacturer's recommended cure cycle. None of the panels received postcure. Straight-sided coupon specimens were prepared from the panels using a diamond-impregnated saw. All specimens were 12 cm long and 1.9 cm wide in gage section. The side edges of the specimens were ground with sand paper and then polished with 5 and 0.5 micron polishing powder in order to facilitate microscopic examination. All specimens were inspected under a microscope prior to each test to examine any fabrication-induced cracks and then stored in a dry-cabinet to prevent moisture absorption from the laboratory environment.

A microscope equipped with a viewing screen was employed to document all the number of cracks of each off-axis layer developed in 10 cm along the free edges during static and fatigue loading. In static test, the specimen was initially loaded to a predetermined level, unloaded, and then removed from the loading frame to examine the cracks. This procedure was repeated with incremental loading until final failure. The stress level at the first occurrence of transverse crack in the 90-degree layer for all the specimens was determined by acoustic emission which was developed in Ref. [4]. The stress level at initiation of delamination for the $(0/\pm 45/90)_s$ laminates was also determined using acoustic emission. It was found that the rate of acoustic emission signal was rapidly increased with onset of delamination and remained until final failure.

In fatigue test, all specimens were tested under tension-tension fatigue loading with frequency, 10 Hz and $R=0.1$. The damage in the form of transverse cracks and delamination was periodically observed by interrupting fatigue testing. The major effort in fatigue test was made to look at the delamination mechanisms. Ultrasonic C-scan was employed for delineating the extension of delamination toward the middle of specimen width. In both static and fatigue test, all specimens were tested using a closed-loop testing machine with friction type of jaw grips under load control mode at laboratory environment.

The analytical model proposed in Ref. [3] is used to calculate interlaminar normal stress in boundary region at the midplane of the laminates. In this calculation, we assumed, as an approximation, the distribution of interlaminar normal stress across the width as shown in Figure 1 with dotted line. Figure 2 shows the magnitude of σ_z at midplane for both laminates. The laminates with the 90-degree layers positioned in the midplane produce interlaminar tension at the free edges under uniaxial tension, but the other stacking sequence produces interlaminar compression as illustrated in Figure 2. The following mechanical properties were used to obtain the results in Figure 2.

$$\begin{aligned} E_L &= 137.9 \text{ GPa} & E_T &= 9.7 \text{ GPa} \\ G_{LT} &= 7.1 \text{ GPa} & \nu_{LT} &= .3 \end{aligned}$$

where L = fiber direction
T = transverse direction

RESULTS AND DISCUSSION

Damage in the forms of transverse crack in each off-axis layer within the laminate and delamination between interfaces was observed at the free edges of specimens under static and fatigue loading. Microscopic examination reveals that the first transverse crack occurred in the 90-degree layers and arrested at the layer interfaces in all the cases of the $(0/90/\pm 45)_s$, $(0/90_3/\pm 45)_s$, and $(0/\pm 45/90)_s$ laminates. As further increasing load, new cracks occurred in the 45-degree layers adjacent to the 90-degree layers. Most of these cracks appeared at the tip of cracks in the 90-degree layers. However, for the other laminates, $(0/90_6/\pm 45)_s$, $(0/\pm 45/90_3)_s$, and $(0/\pm 45/90_6)_s$,

the crack in the 90-degree layer was instantly extended into the adjacent 45-degree layer without being arrested at the interface.

The crack data observed in each test was reduced in terms of number of cracks per centimeter in the respective off-axis layer obtained from the total number of cracks divided by the measured length. Hereafter, this quantity will be referred to as crack density. We used an approximate curve fitting method to study the manner of the first crack occurrence in the 45-degree layers since the direct determination of the stress level at the moment of the first crack occurrence in the 45-degree layer was not successful by means of acoustic emission and other NDI techniques used in this study. The crack densities in the respective layer for the $(0/90_n/\pm 45)_s$ under static loading are plotted as a function of the applied stress as shown in Figure 3. Each curve was drawn by a least square fit to the set of crack data obtained from five specimens for each laminate. The stress in Figure 3 represents the differential stress obtained by subtracting the stress at the moment of the first crack occurrence in off-axis layer from the applied stress for simplification of presentation. The data points are also omitted for the same reason. It should be noted that the symbols at the end of each curve represent the maximum value of crack densities among the five specimens. The solid curves and dotted curves represent the 90-degree layer and +45-degree layer, respectively.

The stress difference at initiation of crack between the +45-degree layer and 90-degree layer does appear dependent upon the type of laminates. In order to look at this difference in detail, the failure stress for the two layers was calculated by using laminate plate theory in conjunction with tensor polynomial failure criteria considering curing residual stresses [7]. The calculated result is compared with experimental result in Table 1.

TABLE 1
FAILURE STRESS DIFFERENCE BETWEEN THE +45-DEGREE AND 90-DEGREE LAYER

Laminate	Calculation MPa	Experiment MPa
$[0/90/\pm 45]_s$	101	120
$[0/90_3/\pm 45]_s$	56	85
$[0/90_6/\pm 45]_s$	45	0

For the first two laminates, the experimental value is greater than the calculated one; whereas for the last laminate the experimental result indicates that cracks in both layers appear to occur simultaneously in spite of the stress difference of 45 MPa by calculation. It is also significant noting that there is a marked difference in the crack density between the 90-degree and 45-degree layer for $n=1$. To the contrary, the difference is very minimal

for $n=3$ and 6. In addition, any crack was hardly observed in the -45 -degree layers which is positioned apart from the 90 -degree layer until near the final failure for all three laminates. This difference in onset of the transverse crack between two layers oriented at opposite angle cannot be adequately explained by a simple laminate analysis. Since the laminate theory will provide identical stress magnitude for each of two layers, $+45$ -degree and -45 -degree, a failure theory based on stress or strain magnitude will predict the same level for onset of transverse crack for a given laminate.

Based on the above observation, the cracks in the $+45$ -degree layer are believed to be caused by the cracks in the 90 -degree layer for the $(0/90_3/\pm 45)_s$ and $(0/90_6/\pm 45)_s$. The difference of crack density between the 90 -degree and 45 -degree layer within the $(0/90/\pm 45)_s$ laminate suggests that all the cracks in the $+45$ -degree layer were not linked with the cracks in the 90 -degree layer. Therefore, the amount of strain energy released is considered to play a significant role in crack extension to the adjacent layer across the interface because the available energy for crack extension will increase as increasing crack length corresponding to the thickness of the 90 -degree layer. Analytical models have been reported to describe the thickness dependency on cracking behavior based on the concept of strain energy release rate [5,6].

In static case, the number of cracks increased monotonically until ultimate failure without revealing a limiting state where no further cracks occur thereafter in spite of increasing load. Thus, to determine the crack density at the limiting state, specimens of the $(0/90_n/\pm 45)_s$ laminates were fatigued, and cracks were periodically measured until final fatigue failure. The last data taken in each specimen was used for calculation of crack density. The last measurement taken in each specimen varies widely dependent upon fatigue life and was in the range of 80% to 99% of total cycle to failure. Hence, the measured number of cracks prior to failure may not precisely represent the number that would have presented at final failure. Since most cracks occurred in the early stage of fatigue life [1], the effect of measurement time on the total number of cracks appears to be very minimal. The results are summarized in Table 2.

TABLE 2
CRACK DENSITY FOR THE $(0/90_n/\pm 45)_s$ LAMINATES

Laminate	Layer Orientation, degree		
	90	+45	-45
$(0/90/\pm 45)_s$	38.1	21.3	6.4
$(0/90_3/\pm 45)_s$	16.4	20.7	5.8
$(0/90_6/\pm 45)_s$	11.5	17.3	7.7

The number of cracks in each layer was found to be dependent upon the layer thickness and orientation. Crack density for the 90-degree layer is plotted as a function of layer thickness as shown in Figure 4. The crack density at limiting state for cross ply laminates in Ref. [1] is also shown for comparison purposes.

The effect of layer thickness on the crack density is clearly indicated. The crack density difference in the 90-degree layer for the $(0/90_n)_s$ and $(0/90_n/\pm 45)_s$ is very minimal as shown in Figure 4. Thus, the crack density of a layer does not seem to be affected by the degree of constraint of the adjacent layer in these two laminates. The other laminates $(0/\pm 45/90_n)_s$ are not included here because the crack does not increase after delamination.

The magnitude of the interlaminar normal stresses at free edge as shown in Figure 2 allow us to make a prediction of the axial stress at initiation of delamination for the $(0/\pm 45/90_n)_s$ by means of a simplified approximation. We assumed that interlaminar failure (delamination) occurs when the maximum value of interlaminar normal stress, σ_z , attains the ultimate transverse strength of the laminate. The approach described in the previous section depends upon the σ_y determined by classical laminate theory. In this calculation the curing residual stresses were considered using the method described in Ref. [8].

$$\sigma_i^R = Q_{ij} A_{jk}^{-1} N_k^T - Q_{ij} e_j^T$$

where Q_{ij} = reduced stiffness at the final temperature of interest

A_{ij} = laminate stiffness

N_k^T = thermal stress resultant

e_j^T = thermal strains measured from the stress-free state

The following values in conjunction with the material constants given in the previous section were used for the calculation of the curing residual stresses; longitudinal thermal expansion coefficient, $-0.22/^\circ\text{C}$, transverse thermal expansion coefficient, $7.15/^\circ\text{C}$, and the temperature difference in cure, $97.2/^\circ\text{C}$.

Figure 5 shows the predicted stress at initiation of delamination for various thicknesses of the 90-degree layer based on the transverse strength of 52 MPa. The solid line and dotted line are predicted value with and without presence of curing residual stresses, respectively. Circle represents average of five specimens. The experimental results are fairly well compared with the calculated value for $n=1$ and 3. However, there is a large discrepancy between the experimental result and the calculated value for $n=6$. Typical microphotographs and ultrasonic C-scan pictures of the delamination pattern under static loading for the $(0/\pm 45/90_3)_s$ and $(0/\pm 45/90_6)_s$ laminates are presented in Figures 6 and 7, respectively. Each figure shows delamination patterns of two progressively increased loadings. The pictures of Figures 6(a) and 7(a) were taken at the moment delamination occurred. Photomicrograph and C-scan picture indicate an edge view (free edge) and a plane view (surface), respectively. The two boldface lines in C-scan picture correspond to the boundary region of

the intact specimen and the white region represents the delaminated area. The magnification is indicated in each case. It appears that delamination is initiated at central plane for $n=1, 3$ and at $90/+45$ interface for $n=6$. This may account for the observed difference in delamination failure stress.

Under static loading, the formation of the delamination in the $(0/\pm 45/90)_s$ and $(0/\pm 45/90_3)_s$ occurs in the following manner. Upon a further increase in applied load after transverse cracking, several delaminations in the form of axial cracks form at the midplane or interfaces between the $+45/-45$ layers or the $-45/90$ layers. However, the major delamination appears to occur at the midplane as shown in Figure 6(a). At this stage, delamination hardly propagates toward the middle of the specimen as shown in C-scan picture in Figure 6(a). As load increases further, the delamination opens up further and either continues to run along the same interface or changes to other interfaces normally at transverse crack. At this time the delamination also propagates rapidly toward the middle of the specimen as shown in C-scan picture in Figure 6(b). The interlaminar tensile stress appears to be responsible for the rapid propagation. Unlike the $(0/\pm 45/90_3)_s$ laminate, in the $(0/\pm 45/90_6)_s$ laminate all the delaminations in the forms of axial cracks occur at the tip of transverse crack at the applied stress below the expected stress as indicated in Figure 5, and failure occurs without revealing any appreciable growth of delamination as shown in Figure 7(a) and (b). Hence, this premature delamination appears to be mainly influenced by size of transverse crack.

In the $(0/90_n/\pm 45)_s$ laminates of which interlaminar normal stress is compression, no delamination has been observed under static loading until final failure except for $n=6$. In the $(0/90_6/\pm 45)_s$ laminate, most of the axial cracks occurred at the tip of transverse crack and remained stationary until final failure.

In fatigue test, however, all specimens of the $(0/90_n/\pm 45)_s$ laminates revealed a considerable delamination in spite of the presence of compressive interlaminar normal stress at free edge. Photomicrographs and C-scan pictures of a typical specimen of the $(0/90_6/\pm 45)_s$ for two progressive fatigue cycles are shown in Figure 8. All the delaminations appear to be initiated at the tip of transverse crack and propagated along interfaces and toward the middle of the specimen. The degree of opening and propagation of delamination is quite different from the case of the $(0/\pm 45/90_6)_s$ laminate in Figure 9. These specimens were tested at the same maximum fatigue stress level, 173 MPa. The specimen shown in Figure 9 was completely delaminated after 2,000 cycle endured, whereas no evidence of delamination revealed at 2,000 cycle and very small delaminations were extended at 100,000 cycle as shown in Figure 8(a) and (b). This is believed to be due to the presence of compressive σ_z at free edge tending to close the axial crack. The similar results have been observed for $n=1$ and 3.

CONCLUSIONS

An experimental investigation has been conducted on the damage related with transverse crack and delamination under static and fatigue loading using

two stacking sequences of quasi-isotropic laminates, $(0/90_n/\pm 45)_s$ and $(0/\pm 45/90_n)$ for $n=1, 3$, and 6 . Based on the experimental results, the following conclusions can be drawn for this specific class of laminates:

(1) Layer thickness plays an important role in crack density and crack extension into the adjacent off-axis layers as well as along interfaces. With increasing layer thickness, crack density decreases, and for crack extension, lower stress and fatigue cycle are required.

(2) The delamination load can be predicted reasonably well in certain laminates (Figure 5) under static loading using the theory developed in Ref. [3].

(3) When interlaminar normal stress is compressive in a tensile coupon, no delamination occurs under static loading while a considerable delamination occurs in fatigue test following transverse cracking.

(4) Delamination appears to be mainly controlled by either or combination of tensile interlaminar normal stress and size of transverse crack.

REFERENCES

1. Kim, R. Y., "Experimental Assessment of Static and Fatigue Damage of Graphite/Epoxy Laminates," ICCM 3, Paris, France, 1980.
2. Sendekyj, G. P., "Fatigue Damage Accumulation in Graphite Epoxy Laminates," Failure Modes in Composite III, Ed. by Chiao, T. T. and Schuster, D. M., 1976.
3. Pagano, N. J. and Pipes, R. B., "Some Observations on the Interlaminar Strength of Composite Laminates," Int. J. Mech. Sci., Vol. 15, 1973.
4. Kim, R. Y. and Hahn, H. T., "Effect of Curing Stresses on the First Ply-Failure in Composite Laminates," J. Composite Materials, Vol. 13, January 1979.
5. Wang, A. S. D., "Growth Mechanisms of Transverse Cracks and Ply Delamination in Composite Laminates," ICCM 3, Paris, France, 1980.
6. Bader, M. G., Bailey, J. E., Curtis, P. T., and Parvizi, A., "The Mechanisms of Initiation and Development of Damage in Multi-Axial Fiber-Reinforced Plastics Laminates," Mechanical Behavior of Materials, 1979.
7. Tsai, S. W. and Hahn, H. T., Introduction to Composite Materials, Technomic Publishing Co., 1980.
8. Pagano, N. J. and Hahn, H. T., "Evaluation of Composite Curing Stresses," Composite Materials: Testing and Design, ASTM STP 617, 1977.

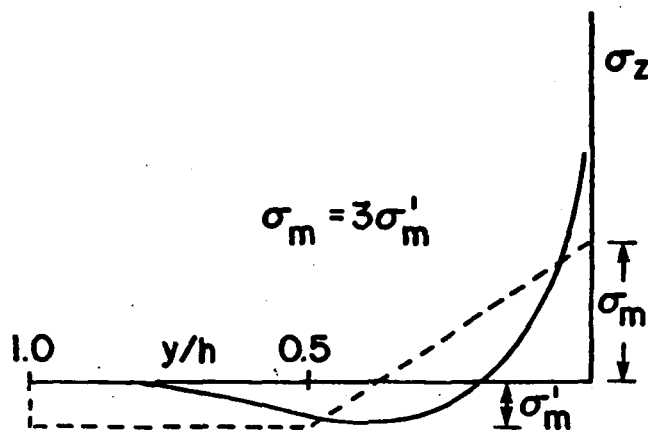


Figure 1. Distribution of Midplane Interlaminar Normal Stress at Free Edge Region: - Elasticity Solution [Ref 3] - Alternate Model Assumed in this Paper.

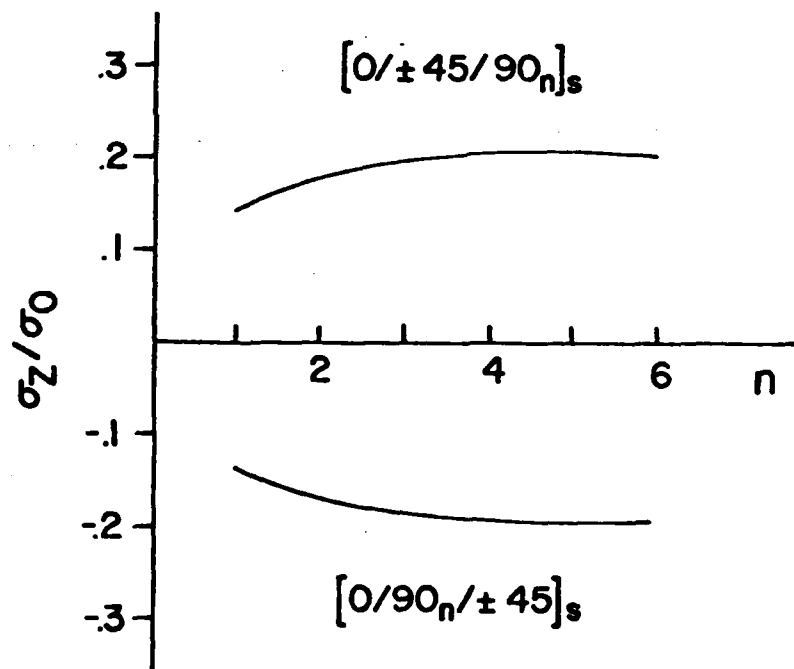


Figure 2. Midplane Interlaminar Normal Stress at the Free Edges: σ_0 = Applied Axial Stress.

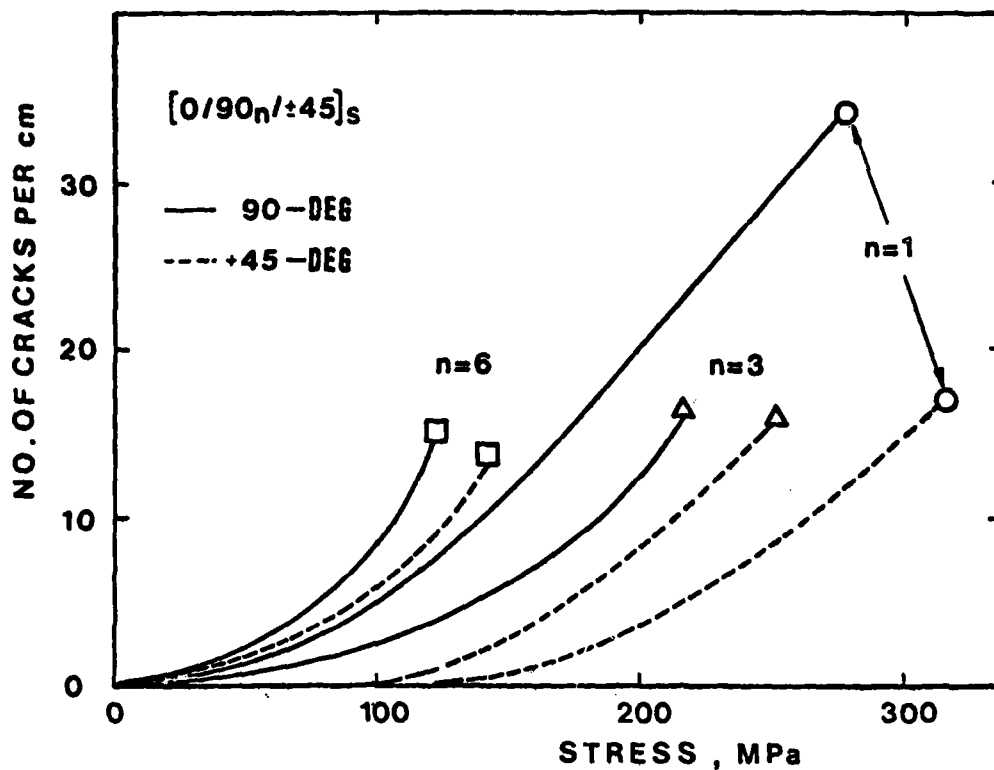


Figure 3. Applied Differential Stress vs. Number of Cracks. Each curve was obtained by a least square fit to a set of experimental data.

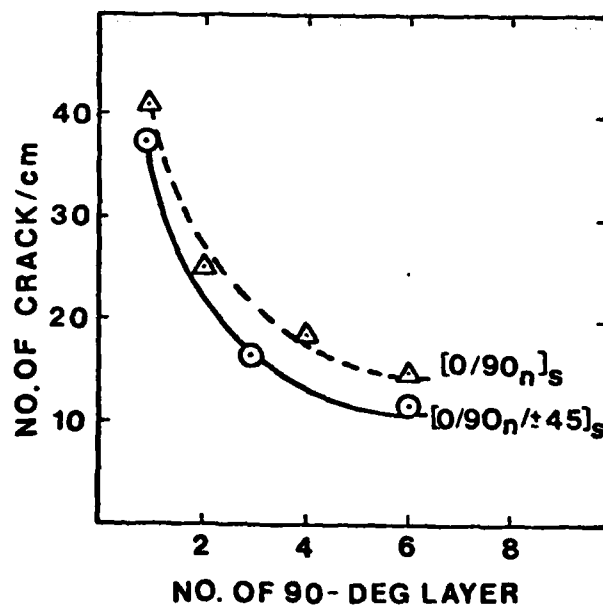


Figure 4. Effect of the 90-deg Layer Thickness on the Crack Density at Limiting State.

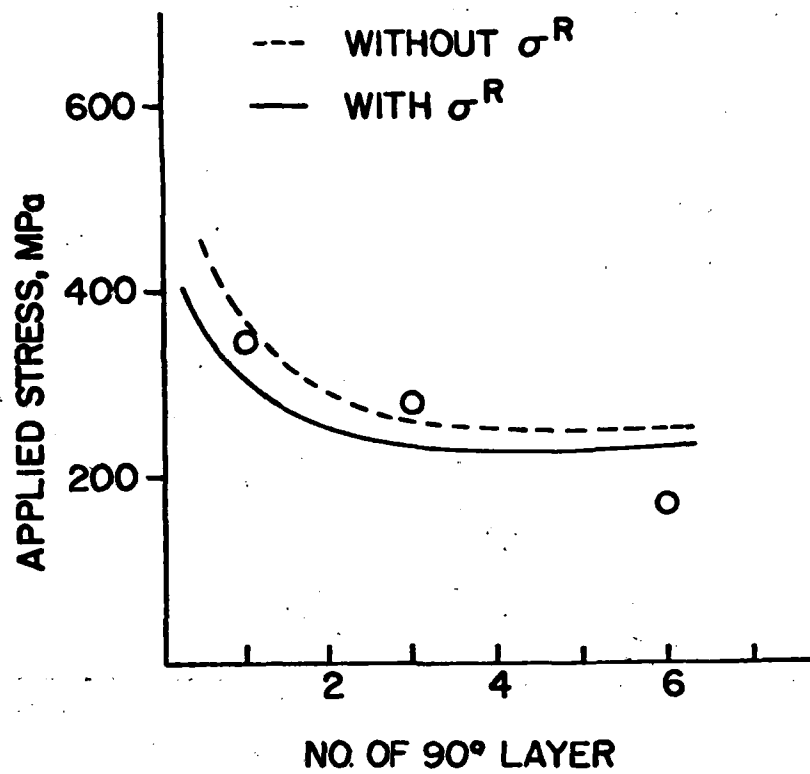
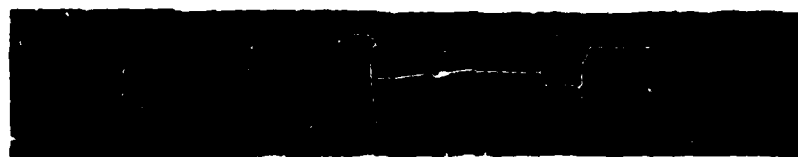


Figure 5. Comparison of Calculated and Experimental Result for Initiation of Delamination.



12X



1X

(a) 267 MPa



12X



1X

(b) 293 MPa

Figure 6. Photomicrographs and C-scan Pictures Showing Crack and Delamination Under Static Loading for $(0/\pm 45/90)_3$.



12X



1X

(a) 168 MPa



12X



1X

(b) 202 MPa

Figure 7. Photomicrographs and C-scan Pictures Showing Crack and Delamination Under Static Loading for $(0/\pm 45/90)_6$ s.

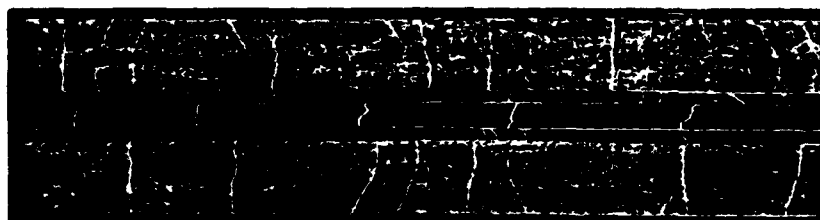


12X



1X

(a) $n = 2,000$ cycle



12X



1X

(b) $n = 100,000$ cycle

Figure 8. Photomicrographs and C-scan Pictures Showing Crack and Delamination Under Fatigue Loading for $(0/90_6/\pm 45)_s$: $S_{MAX} = 173$ MPa.



12X



1X

Figure 9. Photomicrograph and C-scan Picture Showing Crack and Delamination Under Fatigue Loading for $(0/\pm 45/90_6)_S$:
 $S_{MAX} = 173 \text{ MPa}$, $n = 2,000 \text{ cycle}$.

APPENDIX C

STRESS AND FAILURE ANALYSIS OF
AN ADHESIVELY BONDED SCARF JOINT

by

Som R. Soni*
Universal Energy Systems
3195 Plainfield Road
Dayton, Ohio 45432

and

Ran Y. Kim
University of Dayton
Research Institute
Dayton, Ohio 45469

*Effective 1 June 1981 affiliated with University of Dayton Research Institute.

ABSTRACT

A finite element technique is used to conduct the stress analysis of adhesively bonded scarf joints. Three-dimensional linear and two-dimensional nonlinear (piecewise linear) formulations are presented to investigate the effect of axial load on adhesive joints. Experiments are conducted to see the accuracy of theoretical predictions. It has been found that the comparison between the predicted and experimental stress strain histories is very good.

INTRODUCTION

Bonded scarf joints have a higher efficiency than uniform lap joints as the latter are unsuitable for joining thicker sections and have strength limitations. A great deal of work has been reported on lap joints, whereas the scarf joints are not treated much, probably because of the geometric complexity in mathematical modeling for stress analysis. Reference (1) gives a survey of literature in this field. The objective of the present paper is to apply the finite element technique for investigating the scarf joints with similar adherends. Both three-dimensional linear analysis and two-dimensional nonlinear (piecewise linear) analyses are conducted using the NASTRAN, a general purpose finite element computer code. Experimental results are obtained to compare with the analytical results. The numerical results for normal and shear stress components in the adhesive layer axis are plotted for various scarf angles. It is observed that a stress concentration, in both normal and shear stress components, less than six percent exists in the adhesive layer near the ends of the scarf. A similar observation was made by the authors of reference (2). The stress strain plots for scarf joints using piecewise linear adhesive material behavior is given for few scarf angles. Experimental results are close to predicted values.

STRESS ANALYSIS

Figure 1 shows the general arrangement of the scarf joint considered in this investigation. Both the adherends and the adhesive are assumed as isotropic materials. Adherends are of the same material. The joint is deformed by a unit tensile load per unit cross-section area of the joint. Systems of Cartesian axis $o(x,y,z)$ and $o(n,t,z)$ are chosen with origin at the center of the joint as shown in Figure 1 with z -axis normal to the plane of the paper having positive values in the outward direction.

The NASTRAN program is used to conduct the stress analysis of the adhesive joint. Three-dimensional linear and two-dimensional nonlinear analyses are conducted to simulate the realistic behavior of a scarf joint. (Nonlinear 3-D capability is not available in NASTRAN.) The material nonlinearity of adhesive is taken into account by considering it as a piecewise linear material. The stress components σ_n , σ_t , and τ_{nt}

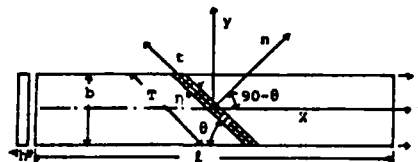


Fig. 1 General arrangement of the scarf joint

at various points of the adhesive layer are computed for different scarf joints. In the structural adhesive joint, the properties and behavior of the polymer within the joint are assumed to be the same as those of neat adhesive specimens. Also, it is assumed that a proper joint exists in which the joint strength is not limited by poor interfacial bonding. In general, the behavior of the material in the joint will depend on (i) the range of adhesive material properties, (ii) the specimen preparation method, and the thickness of the adhesive layer. In the analytical investigations, it has been assumed that a continuity in the deformations exists at the interface between the adhesive and adherend.

THREE-DIMENSIONAL ANALYSIS

The isoparametric solid hexahedron elements allow the user to define accurately a structure with fewer elements and grid points than might otherwise be necessary with simple constant strain elements. Three types of isoparametric solid hexahedron elements are available with NASTRAN. These elements are linear, quadratic and cubic. Linear elements generally give best results for problems involving mostly shear deformation, while the higher order elements give good results for situations involving both shearing and bending deformations. Therefore, eight node linear isoparametric hexahedron elements and six node wedge elements, each node defining a corner of the element, are used to discretize the three-dimensional model. Each edge of the element forms a straight line and each nodal point has three degrees of freedom (u, v, w). The structure is modeled using 120 of these elements; an idealized joint specimen is shown in Figure 2. This plot is obtained during NASTRAN computations and thus checks the proper discretization of the structure.



Fig. 2 Finite element grid of 3-D specimen

A computer program was written to generate grid points and element topology for all the 120 elements. The punched output from this program was used in the NASTRAN for conducting the finite element analysis. Numerical experiments showed that the above idealization gives reasonably accurate results.

Stress components at eight points on t-axis of the Cartesian reference frame $O(n, t, z)$ (i.e. central line of the adhesive layer) are computed for all the scarf angles taking adhesive layer thickness $\eta = 0.02$ in. Because nonlinear capabilities for solid elements are not available in NASTRAN, a two-dimensional model was made to incorporate material nonlinearity.

TWO-DIMENSIONAL ANALYSIS

For two-dimensional analysis, an assumption was made that the deformation pattern in the joint satisfies plane stress conditions. Four noded quadrilateral elements and three noded triangular elements were used to discretize the structure. Each node of the element represents a corner of the element and has two degrees of freedom (u, v). The model was idealized by using 402 of these elements (Figure 3). For comparison, results for a unit tensile load per unit cross-section area of the joint were obtained for a linear adhesive material. After that, results were computed at various loads for a nonlinear material by using the piecewise linear formulation. Stress components of various points in the adhesive layer are obtained through this formulation for three angles 30, 45 and 60 degrees. Throughout the finite element analysis, one edge of the joint was kept fixed and the tensile force was applied at the other parallel edge.



Fig. 3 Finite element grid for 2-D piecewise linear analysis

The material properties of the adhesive layer were obtained from the experiments conducted with the neat adhesive test coupons in the laboratory. There is a likelihood of a change in adhesive layer material properties, when used in a joint specimen. However, this change is assumed to be negligible in order to be able to run the analytical computations. The inplane stress components calculated through the finite element analysis are utilized in the scheme proposed by Swedlow (3) for plastic materials, to obtain the strain components ϵ . The strain increment $\Delta\epsilon$ for a stress increment $\Delta\sigma$ in the piecewise linear analysis are given by (3)

$$\Delta\epsilon = ([D^P] + [G]^{-1}) \Delta\sigma \quad (1)$$

Where $[G]$ is the normal elastic material matrix and $[D^P]$ is a matrix relating the plastic deformation of the material, and is of the following form

$$[D^P] = \frac{1}{\sigma_{T_0}^2 M_T(\tau_0)} \begin{bmatrix} S_{11}^2 & S_{11}S_{22} & 2S_{11}S_{12} \\ & S_{22}^2 & 2S_{22}S_{12} \\ & & \text{SYM.} & 4S_{12}^2 \end{bmatrix} \quad (2)$$

where

$$\tau_0 = \frac{1}{3} \sqrt{2(S_{11}^2 + 2S_{12}^2 + S_{22}^2 + S_{33}^2)}$$

$$S_{11} = \frac{1}{3} (2\sigma_x - \sigma_y)$$

$$S_{12} = \tau_{xy}$$

$$S_{22} = \frac{1}{3} (2\sigma_y - \sigma_x)$$

$$S_{33} = -\frac{1}{3} (\sigma_x + \sigma_y)$$

$$M_T(\tau_0) = E_0 E^1(\epsilon_x) / 3 [\tau_0 - E^1(\epsilon_x)]$$

In the above relations, E_0 is the Young's modulus for the elastic part of the stress-strain curve, and E^1 is the approximate slope of the stress-strain curve at each increment.

Once $\Delta\epsilon$ is obtained through equations (1) and (2), the total axial strain ϵ_x can be calculated as

$$\epsilon_x = \Delta\epsilon_x + \frac{\sigma_x}{E_0} \quad (3)$$

where σ_x is the axial stress for the elastic part of the stress-strain curve.

In the experimental determination of stress-strain curve of the adhesive joint, only average axial strain over the length of the strain-gage covering the scarf joint is obtained. The corresponding theoretical strains due to adhesive and adherend portions of the joint are averaged according to the following equation:

$$\epsilon_x^A = \left\{ \frac{\eta}{\sin\theta} \epsilon_x^{AS} + (G_L - \frac{\eta}{\sin\theta}) \epsilon_x^{AR} \right\} / G_L \quad (4)$$

where ϵ_x^A , ϵ_x^{AS} and ϵ_x^{AR} are average axial strain over the gage length, adhesive and adherend axial strain components, respectively; G_L is the strain gage length, η is the thickness of the adhesive layer, and θ is the scarf angle.

RESULTS AND DISCUSSION

The elastic constants used in this study were determined by experiment and are listed in Table 1.

TABLE 1
ELASTIC CONSTANTS

	Young's Modulus, GPa	Poisson's Ratio
Adhesive	2.66	0.36
Adherend	76.60	0.25

The adhesive considered in this study was FM 123-2 structural adhesive film supplied by American Cyanamid Company. The adhesive specimen was cast in a vacuum bag for characterization of mechanical properties. The specimens were tested under static tension, and the axial and transverse strains were recorded. A typical stress-strain curve shown in Figure 4 reveals a considerable nonlinearity with increasing stress. This stress-strain curve was utilized in piecewise linear analysis of the two-dimensional problem. Results of the tensile tests showed that the Poisson's

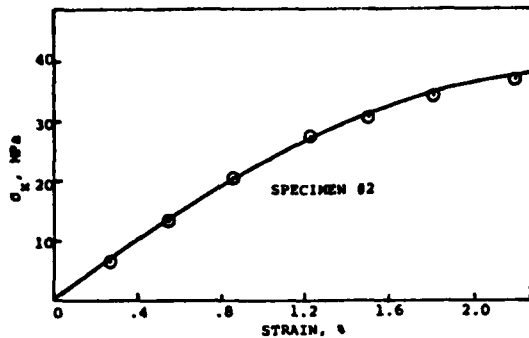


Fig. 4 Stress-strain curve for the adhesive material ratio varied linearly with the applied load (Figure 5). However, in this study, we have assumed the Poisson's ratio to be a constant. The effect of this assumption is considered to be very minimal since the variation is so small.

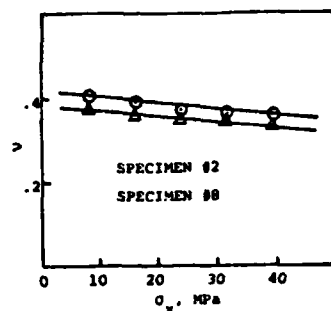


Fig. 5 Poisson's ratio of the adhesive material at various stress levels

Two adhesive thickness values (0.25 mm and 0.50 mm) have been considered in finite element analysis. It was found that the effect of adhesive layer thickness on the stress level was negligible in all the cases considered in this study.

Figures 6-8 depict the variation of normal and shear stress components along the scarf angle in $\sigma(n,t,z)$ axis. A stress concentration less than six percent has been observed near the ends of the joint. Reference (2), where the authors came across a similar situation, supports this analysis. In these figures, results are also presented using the simple approach of Lubkin (4), which compares very well with the present calculations. Figure 9 shows the comparison between 3-D and 2-D linear analyses computations and Lubkin (4) approach results. Here again, the agreement is very good. Figure 10 presents the results for σ_n and τ_{nt} for various values of scarf angles θ .

Figures 11-14 are the stress-strain behavior of the adhesive joints with 30 deg, 45 deg, 60 deg and 90 deg scarf angles. The strains plotted are average strains over the strain gage length covering the adhesive and adherend portions. Experimental results for the same angles and adhesive layer thicknesses are

also presented which show a very good agreement with the predicted results.

Figure 15 shows a comparison between the experimental and predicted strengths. The predicted failure strength was computed by using Von Mises criterion for isotropic materials. The comparison appears to be fairly good for the scarf angles considered in this study.

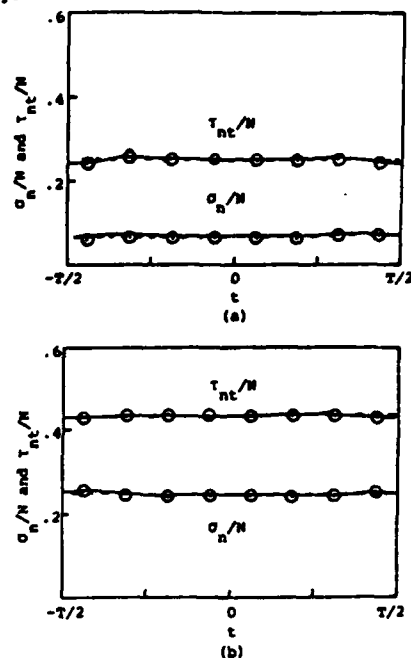


Fig. 6 Variation of normal and shear stresses along the scarf joint. (a) $\theta=15^\circ$, $l=19.8$ cm, (b) $\theta=30^\circ$, $l=13.7$ cm. ---- Ref (4), \bigcirc Present.

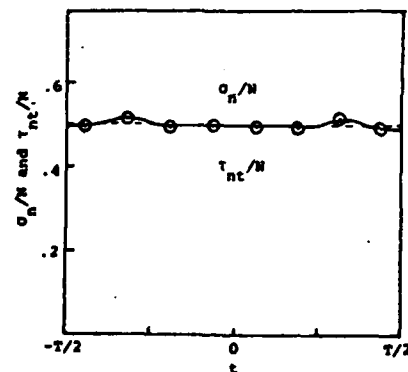


Fig. 7 Variation of normal and shear stresses along the scarf joint. $\theta=45^\circ$, $l=13.7$ cm. \bigcirc Present, ---- Ref (4).

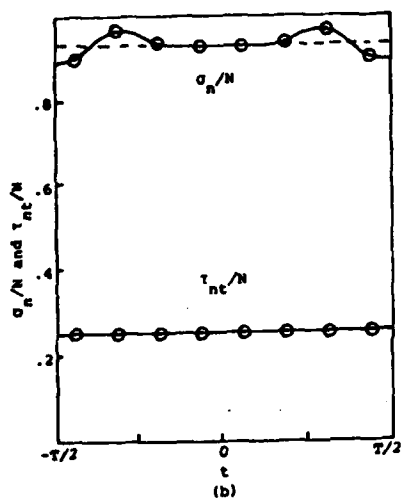
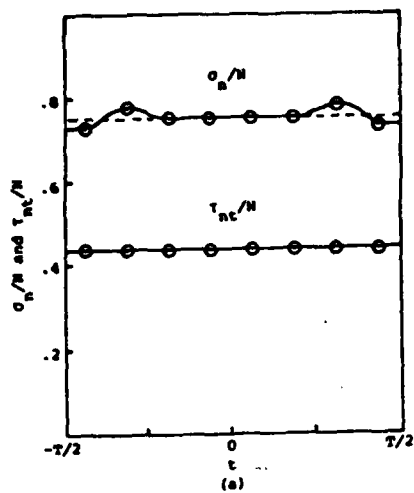


Fig. 8 Variation of normal and shear stresses along the scarf joint. (a) $\theta=60^\circ$, $l=13.7$ cm, (b) $\theta=75^\circ$, $l=13.7$ cm. \odot Present, ---- Ref (4).

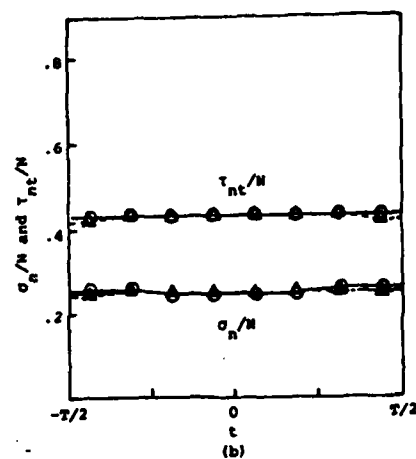
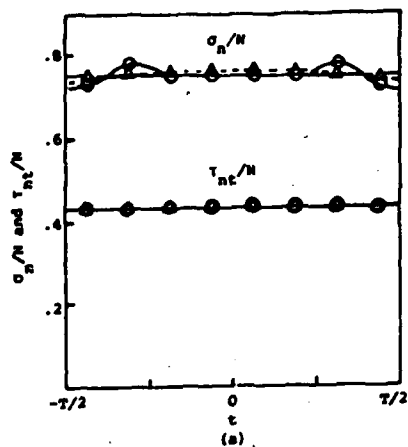


Fig. 9 Variation of normal and shear stresses along scarf joint. (a) $\theta=60^\circ$, (b) $\theta=30^\circ$, $l=13.7$ cm. ---- Ref. (4), \odot 3D, \triangle 2D.

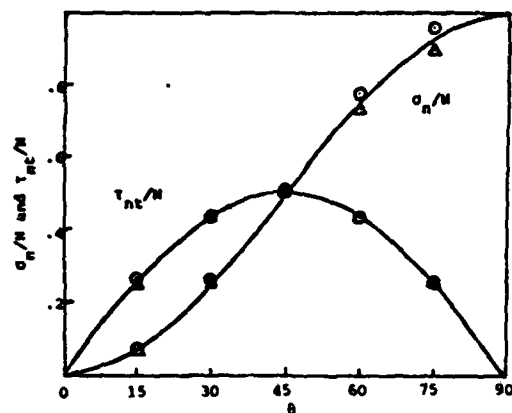


Fig. 10 Variation of normal and shear stresses for the angle. — Ref (4), \odot Maximum 3D, Δ Minimum 3D.

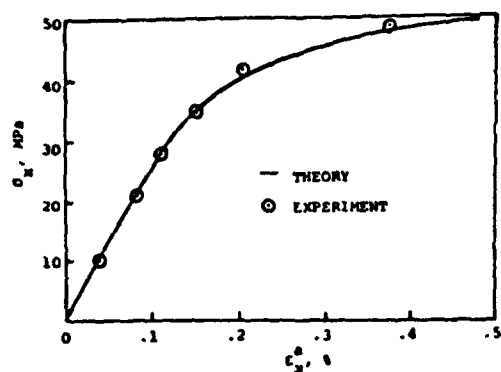


Fig. 11 Stress vs. average strain over the strain gage length covering the scarf joint. $\theta=30^\circ$, $\eta=.13$ mm.

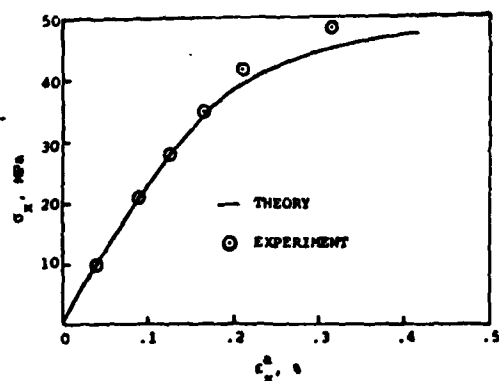


Fig. 12 Stress vs. average strain over the strain gage length covering the scarf joint. $\theta=45^\circ$, $\eta=.18$ mm.

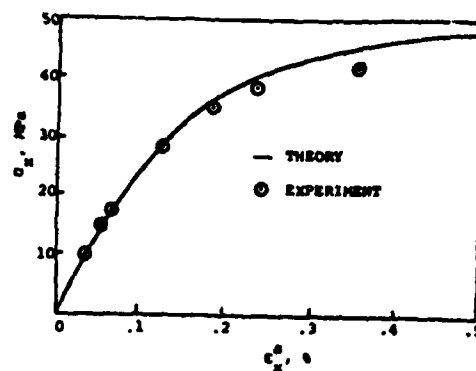


Fig. 13 Stress vs. average strain over the strain gage length covering the scarf joint. $\theta=60^\circ$, $\eta=.18$ mm.

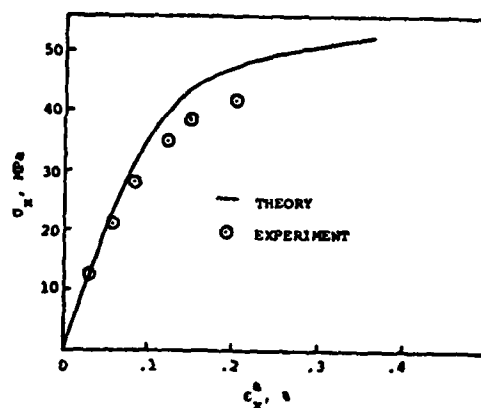


Fig. 14 Stress vs. average strain over the strain gage length covering the scarf joint. $\theta=90^\circ$, $\eta=.1$ mm.

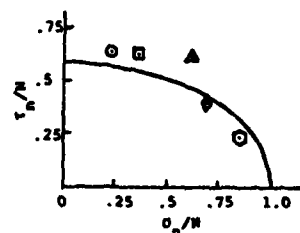


Fig. 15 Failure surface of scarf joint. $\odot=20^\circ$, $\square=30^\circ$, $\Delta=45^\circ$, $\diamond=60^\circ$, and $\odot=75^\circ$.

ACKNOWLEDGMENTS

One of the authors (S. R. Soni) is grateful to the National Research Council for a Senior Postdoctoral Research Associateship at the Air Force Wright Aeronautical Laboratories/Materials Laboratory. Constant encouragement and useful suggestions rendered by Dr. Stephen W. Tsai, AFVAL/MLBM, Wright-Patterson Air Force Base, Ohio are gratefully acknowledged.

REFERENCES

1. J. L. Hart-Smith, "Adhesive-Bonded Scarf and Stepped-Lap Joints," Douglas Aircraft Company, NASA Langley Research Report NASA-CR-112237, January 1973.
2. G. M. Lehman, et al, "Investigation of Joints and Cutouts in Advanced Fibrous Composites for Aircraft Structures," Douglas Aircraft Company, AFDD Contract F33615-67-C-1582, Third Quarterly Progress Report DAD-61566, January 1968.
3. J. L. Swedlow, "The Thickness Effect and Plastic Flow in Cracked Plates," Aerospace Research Laboratories, Wright-Patterson Air Force Base, Ohio, ARL-GS-216, October 1965.
4. J. L. Lubkin, "A Theory of Elastic Scarf Joints," Journal of Applied Mechanics, 824, June 1957, pp 255-260.